# Nanostructured Materials for the Removal of Inorganic Pollutants from Water and Subsequent Applications

Report to the
**Water Research Commission**

by

**Arjun Maity[1,2], Thembisile Mahlangu[3], Iviwe Arunachellan[1], Venkata Satya Narayana Sypu[1] and Lindiwe Skosana[1]**
[1]University of Johannesburg
[2]Council of Scientific and Industrial Research
[3]Tshwane University of Technology

**WRC Report No. 2732/1/20**
**ISBN 978-0-6392-0184-9**

**August 2020**

**Obtainable from**
Water Research Commission
Private Bag X03
Gezina
PRETORIA, 0031

orders@wrc.org.za or download from www.wrc.org.za

# EXECUTIVE SUMMARY

Water is commonly regarded as the most vital of natural resources, yet freshwater systems are directly threatened by human activities and stand to be further affected by anthropogenic climate change. Considerable parts of South Africa, for example, are now facing severe to extreme drought crises each year. According to the World Health Organization (2005), around 1.8 million people die every year from drinking contaminated water which spreads sickness and waterborne diseases such as typhoid and cholera. Certainly, we can’t think about progress in human civilization without industrialization, but its rapid pace and the resulting impacts have seriously impaired fresh water quality, globally. Sustainability is the primary concern for process industries in the present competitive era. Industrial development has led to the generation of hazardous waste such as heavy metals, dyes, pharmaceuticals, petroleum products, pesticides and fertilizer into the environment. Discharge of these hazardous pollutants into water bodies (river, lakes and ocean) without proper treatment causes serious damage to the aquatic life as well as health-related problems. Among the various toxic pollutants, in this report we have identified metal ions, fluorides and microbial contaminants. Our focus was to achieve their effective removal from aqueous medium and in some instances, subsequently reuse the waste materials after adsorption for further environmental application, as shown in the schematic below.

The aims of the project were as follows:

1. To synthesize polymer based nanostructured materials.
2. To characterize the synthesized nanomaterials with various characterization techniques.
3. To test removal efficiency of inorganic ions by means of batch studies varying several parameters such as dose, pH, initial concentration, time, temperature.
4. To test removal efficiency of inorganic ions by means of continuous column dynamic studies varying several parameters such as initial concentration, bed height, flow rate.
5. To examine desorption and regeneration capabilities of the nanomaterials using adsorption desorption cycles.
6. To test antimicrobial activity using metal loaded material obtained from aim #3.
7. To test catalytic activity using metal loaded material obtained from aim #3.
8. To test gas sensing activity using metal loaded material obtained from aim #3.

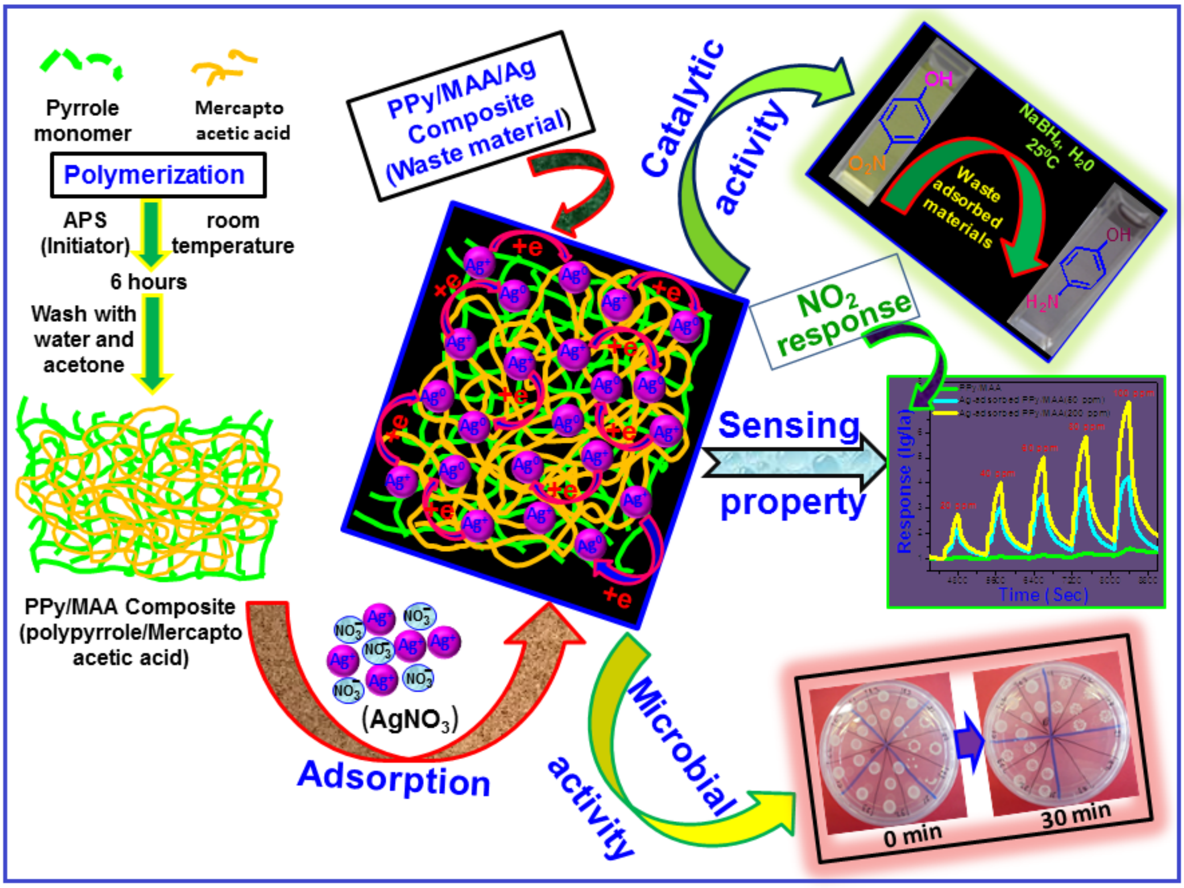

Scheme represents the synthesis of adsorbents, adsorption of pollutants and subsequent use of metal laden adsorbent for antibacterial agent, catalyst and/or gas sensor.

In this regard, a new hybrid material comprising hydrous zirconium oxide ($HZrO_2$) supported onto polyaniline (PANI) nanofibres ($HZrO_2$@PANI NFs) was prepared via precipitation of $HZrO_2$ onto as-synthesized PANI NFs and tested for its defluoridation capabilities. $HZrO_2$@PANI NFs achieved 2-fold BET surface area ~ 86.64 $m^2/g$ as compared to PANI NFs ~ 44.72 $m^2/g$, implying that the incorporation of $HZrO_2$ onto the PANI nanofibres enhanced the available surface area for effective fluoride adsorption. Moreover, $HZrO_2$@PANI NFs was found to be effective over a wide pH range (3-9) as designated by its high pHpzc ~ 9.8. The adsorption kinetics obeyed the pseudo-second-order model well with equilibrium attainment in 30 min. Adsorption isotherm was best described by the Langmuir model and the maximum adsorption capacities obtained were 83.23 and 28.77 mg/g at pH 3 and 6.5, respectively, which is superior to most $ZrO_2$ based adsorbents reported in the literature and better than that of native PANI. Furthermore, the developed adsorbent manifested quite a selective fluoride uptake at pH 3 as compared to pH 6.5 ±0.1 wherein significant chemical affinity competition was presented by phosphate ions followed by bicarbonate and sulfate. The recyclability of $HZrO_2$@PANI NFs for four cycles and its applicability to fluoride spiked ground water has also been demonstrated.

Mercapto-functionalized polypyrrole composites ((PPy/MAA) were synthesized via in situ oxidative polymerization method. The synthesis was a one-pot method, which yielded a fine, black powder. The material was applied in the removal of heavy metals (mercury and silver) from the aqueous medium, where the effect of adsorbent dose, pH, initial metal concentration and temperature were investigated. The synthesized polypyrrole with mercapto-functionalized chelating groups (PPy/MAA), exhibited high Hg(II) and Ag(I) adsorption capacities. To understand the adsorption properties of this developed polymer composite, a series of batch adsorption experiments were performed by varying the adsorption parameters. Maximum adsorption capacity of 1736.8 and 714.28 mg/g at 25°C was obtained using a Langmuir isotherm model for Hg(II) and

Ag(I) uptakes, respectively. The adsorption data showed better fitting to pseudo-second-order model. A plausible adsorption mechanism is suggested on the basis of XRD, XPS and HR-TEM analyses. With regard to the applications tested, the transformation of phenylacetylene was achieved in the presence of 5 mol% Hg-loaded PPy/MAA as a catalyst at 90°C after 6 h and afforded the corresponding acetophenone in 55% yield. Likewise, the Ag-loaded waste nanocomposite showed good catalytic activity for the reduction of nitroarenes to aniline derivatives in the presence of sodium borohydride ($NaBH_4$) as an easily accessible reducing agent. The corresponding aniline derivatives were obtained in good to excellent percentage yields. In addition, this Ag-loaded waste was also found to exhibit antimicrobial activity, as it inhibited the growth of *Escherichia coli* (*E. coli*), while pure adsorbent without Ag(I) showed no killing effect towards *E. coli.* Furthermore, Ag-loaded PPy/MAA exhibited good sensitivity towards NO2 in gas sensing applications. Based on these findings, the developed PPy/MAA composite achieved two-fold environmental benefits, not only remediating Ag+ from polluted waterways but also opened a new window for subsequently acting as antibacterial agent, catalyst and/or gas sensor (Please see the scheme).

Mercapto-acetic acid Magnetic thiol-modified nanocomposites ($Fe_3O_4$@PPy-MAA NC) were synthesized via in situ oxidative polymerization method. The same procedure was used, with the addition of iron oxide nanoparticles ($Fe_3O_4$) to introduce magnetic properties to the PPy-MAA composite. In that regard, the performance of the developed $Fe_3O_4$@PPy-MAA NC for Ag(I) adsorption was carried out through batch studies as a function of pH, adsorbent dose, temperature and initial Ag(I) concentration. The maximum adsorption capacity of Ag(I) was determined to be 806 mg/g at 25°C using Langmuir adsorption isotherm at a solution pH of 5.6 and adsorbent dose of 0.5 g/L. The kinetics studies indicated that the Ag(I) adsorption onto the $Fe_3O_4$@PPy-MAA NC surface was rapid within the initial 40 min and was well described by the pseudo-second-order kinetics equation. Also, the present study emphasised the reusability of Ag-loaded waste ($Fe_3O_4$@PPy-MAA/Ag) material for the disinfection of microorganisms, which was demonstrated through the excellent antimicrobial activity of the NC against *Escherichia coli* and *Salmonella enterica*, in both synthetic and natural water samples. Therefore, the as-prepared $Fe_3O_4$@PPy-MAA NC has an excellent ability to successfully remove Ag(I) ions from aqueous solutions and subsequently, the Ag-loaded waste material could be used as a potential candidate disinfectant.

Furthermore, $Fe_3O_4$@PPy-MAA/Ag was tested in fixed-bed column studies for *E. coli* disinfection. At an *E. coli* concentration of 1.82 x 102 CFU/mL, 2 g bed mass and a flow rate of 2 mL/min, 20 L of water were treated before the column reached breakthrough (where 1 viable colony is observed). It was established that the performance of the column is reliant on the bed mass, flow rate and initial contaminant concentration. The performance of the packed column (1.82 x 102, 1 g, 2 mL/min) was tested using groundwater and the performance was still adequate. 21 L of water were treated with only 1 g of spent adsorbent. The experimental data for synthetic and groundwater experiments were fitted to sigmoidal models (Boltzmann, Logistic and Gompertz) and the empirical data fit the data accurately, as confirmed by the high correlation factor values (R2> 97).

In addition, exploration of innovative technologies for an efficient treatment of wastewater containing toxic organic pollutants is of particular importance worldwide. Also, in the past few years, the removal of organic contaminants from aqueous medium through chemical reduction processes, using noble metal-based nanocatalysts in the presence of the reducing agent $NaBH_4$, has been established as a significant strategy. Herein, a simple straightforward approach was presented for the use of Ag+-adsorbed waste ($Fe_3O_4$@PPy-MAA/Ag) material as a promising catalyst for the reduction of organic pollutants. Magnetized and modified PPy was well-deposited with Ag NPs by the reduction of silver salt precursor ($AgNO_3$) without the need for neither any reducing agent nor a stabilizer. The successful embedment and growth of Ag NPs onto the surface of the as-described catalyst was systematically investigated using FE-SEM, TEM, XRD, XPS, BET and ATR-FTIR characterisation techniques. To demonstrate the catalytic performance of the developed nanocatalyst, the reduction of 4-nitrophenol (4-NP) and organic dyes, namely, methylene blue (MB) and methyl orange (MO), was tested in aqueous medium at 25°C. The $Fe_3O_4$@PPy-MAA/Ag catalyst exhibited excellent catalytic activity for the reduction of all three targeted organic pollutants (4-NP, MO and MB). The pseudo-first-order rate constants were estimated as 0.5-14.3 × 10-2 $min^{-1}$, 0.52-24.2 × 10-2 $S^{-1}$ and 10.1-46.8 × 10-3 $S^{-1}$ for the reduction of 4-NP, MO and MB, respectively. The catalyst was separated from the reaction medium and recycled without significant loss of catalytic activity up to eight successive cycles. The above research findings revealed that $Fe_3O_4$@PPy-MAA/Ag NC has the potential to efficiently act as an auspicious candidate for environmental applications via chemical reduction of toxic contaminants from wastewater.

Hydrous $CeO_2$-$Fe_3O_4$ (HCeFe) decorated polyaniline nanofibers (HCeFe NFs) were obtained through a simple co-precipitation deposition approach on pre-synthesised polyaniline nano-fibers (PANI NFs), and evaluated as adsorbents for fluoride removal from synthetic and real water samples. FE-SEM/EDS, HR-TEM, BET, XRD, FTIR, TGA-DTA, XPS and dynamic mechanical analysis (DMA) techniques were used to characterise the hybrid nanomaterials. The optimised HCeFe NFs adsorbent with specific surface area 66 $m^2$/g, exhibited excellent adsorption efficiency towards fluoride ions (F-) via both electrostatic interaction and ion exchange mechanisms. F- adsorption followed the pseudo-second-order rate model and best fitted the Langmuir isotherm, with the maximum capacities within 93.46-117.64 mg/g over a broad pH range 3-10, respectively. The determined thermodynamic parameters, including enthalpy (ΔH° -15.1 kJ/mol) and Gibbs free energies change (ΔG° < 0) indicated to the exothermic as well as spontaneous nature of the sorption process. The regeneration of HCeFe NFs showed a considerable adsorption-desorption efficiency over three consecutive cycles. Ultimately, the adsorbent was tested on spiked F- containing groundwater and the obtained results demonstrated its potential utility for defluoridation of natural water.

In the efforts to develop new, functional adsorbents for the removal of fluoride ions in aqueous medium, bimetal-oxides-based adsorbents were synthesised. A simple co-precipitation method was used to prepare a series of eco-friendly hydrous cerium-magnesium bimetal oxides (HCeMgO1:2, HCeMgO1:3, HCeMgO1:1 and HCeMgO2:1) adsorbents at different Ce/Mg molar ratio for fluoride removal from aqueous solution. The ideal adsorbent, HCeMgO1:1, not only demonstrated high adsorption efficiency but also rapid kinetics. Comprehensive characterisation of HCeMgO1:1 before and after fluoride adsorption was performed using FE-SEM, HR-TEM, XPS, FTIR, Point-of-zero charge, TG-DTA, BET and XRD techniques. The BET surface area of HCeMgO1:1 was around 34.06 $m^2$/g. The effect of various parameters such as adsorbent dosage, contact time, initial concentration, initial pH and co-existing ions was investigated in batch mode. The reusability of the HCeMgO1:1 as an adsorbent was explored with the aid of a desorption study. A pseudo-second-order model described the adsorption kinetics best with 5-20 minutes rapid equilibrium adsorption. Fluoride uptake followed Langmuir model, with maximum adsorption capacities in the range of 66.23-80.00 mg/g from 25-45°C at pH value 5.5. Both ion exchange and electrostatic interactions were found to dictate the process. The sorption was spontaneous and endothermic in nature. The revival study of the fluoride laden HCeMgO1:1 exhibited a high desorption efficiency of up to four adsorption-desorption cycles. Further assay on underground water samples deep-rooted the potential use of HCeMgO1:1 as suitable candidate for defluoridation.

Also, the presence of Co(II) and Ni(II) in water is a major concern owing to their non-biodegradable, carcinogenic and mutagenic nature. In recent years, diverse techniques have been applied in their removal from water and upon careful evaluation of some of these techniques; adsorption seemed to be a desirable technique of choice owing to its favourable characteristics as well as its benefits in Co(II) and Ni(II) removal. By virtue of the efficacy of adsorption being governed by an adsorbent, Hollow Carbon Nano Spheres (HCNS) have emerged as attractive adsorbents of choice due to their favourable characteristics in comparison to the adsorbents which have previously been applied in the removal of Co(II) and Ni(II) from water. In the present study, HCNS were synthesized using a hard templating method and these HCNS were characterized by techniques such as Fourier-transform infrared spectroscopy (FT-IR), X-ray diffraction analysis (XRD), scanning electron microscopy (SEM), energy dispersive X-ray (EDX) analysis, transmission electron microscopy (TEM), thermogravimetric analysis (TGA), Brunauer-Emmet-Teller (BET) surface area analyser, seta sizer and X-ray photo electron (XPS) analysis.

The adsorption properties of these HCNS towards Co(II) and Ni(II) were evaluated using batch adsorption method by varying adsorbent dosage, initial pH, and contact time. Maximum adsorption was observed at a

dosage of 0.03 g and pH 4 for $Co_{2+}$ while the maximum adsorption was observed at a dosage of 0.03 g and pH 5 for $Ni_{2+}$. Pseudo-first-order and pseudo-second-order kinetic models were used to describe the kinetic data and the constants were evaluated. The results obtained from the kinetic study showed that the adsorption of both Co(II) and Ni(II) by HCNS was best described by the pseudo-second-order kinetic model. The adsorption of both Co(II) and Ni(II) was found to be controlled by both surface and pore-diffusion, with surface diffusion occurring at the earlier stages and followed by pore diffusion at the later stages. The effect of coexisting ions, in the removal of Co(II) and Ni(II) was also evaluated and it was observed that the HCNS adsorbent was not selective to either Co(II) or Ni(II) in the presence of other competing metal ions. Furthermore, the neat-HCNS, Co-HCNS and Ni-HCNS were applied in the sensing of gases such as $SO_2$, $CH_4$, C3H6O, $NO_2$ and $H_2S$. These adsorbents were found to be successful in the sensing of these various gases. However, the Co-HCNS were observed to have the highest response to most gases. The effect of temperature on the response of these materials was also evaluated. It was observed that response decreased with increasing temperature, with maximum response observed at 50°C.

# ACKNOWLEDGEMENTS

The project team wishes to thank the following people for their contributions to the project.

| Reference Group | Affiliation |
|---|---|
| Dr N Kalebaila | Water Research Commission (Research Manager) |
| Dr M Hato | University of Limpopo |
| Dr L Seru | North West University |
| Dr V Masindi | Magalies Water |
| Dr K Pillay | University of Johannesburg |
| Dr HG Brink | University of Pretoria |
| Dr Esper Ncube | Rand Water |
| Prof O Oluwafemi | University of Johannesburg |
| Prof A Mishra | University of South Africa |

# CONTENTS

# LIST OF FIGURES

# LIST OF TABLES

# ACRONYMS & ABBREVIATIONS

| | |
|---|---|
| ACC | Clothe |
| BET | Brunauer-Emmet-Teller |
| BSE | Back-Scattered Electronsyeah OK |
| C3H6O | Acetone |
| CaS | Calcium Sulphide |
| CH4 | Methane |
| CNTs | Carbon Nanotubes |
| DFAFC | Direct Formic Acid Fuel Cell |
| EDX | Energy Dispersive X-ray |
| ESCA | Electron Spectroscopy for Chemical Analysis |
| FAC | Fibrous Activated Carbon |
| $Fe_3O_4$@PPy/MAA | Thiol-modified magnetic polypyrrole |
| FeS | Iron Sulphide |
| FT-IR | Fourier Transform Infrared Spectroscopy |
| GAC | Granular Activated Carbon |
| $H_2S$ | Dihydrogen Sulphide |
| HCNS | Hollow Carbon Nano Spheres |
| HCS | Hollow Carbon Spheres |
| HPS | Hollow Polyaniline Spheres |
| HR-TEM | High-Resolution Transmission Electron Microscope |
| HTC | Hydrothermal Carbonization |
| ICP-MS | Inductively-Coupled Plasma Mass Spectrometer |
| MWCNTs | Multi-Walled Carbon Nanotubes |
| Na2S | Disodium Sulphide |
| NaHS | Sodium Hydrogen Sulphide |
| NO2 | Nitrogen dioxide |
| PANI | Polyaniline |
| PEMFC | Proton Exchange Membrane Fuel Cell |
| PNHCS | Porous Nitrogen-doped Hollow Carbon Spheres |
| PPy | Polypyrrole |
| PS | Polystyrene Spheres |
| Py | Pyrrole |
| SDS | Sodium Dodecyl Sulfate |
| SE | Secondary Electrons |
| SEM | Scanning Electron Microscopy |
| Silver | Ag |
| SO2 | Sulphur dioxide |
| SO3H | Sulfonic acid |
| SPS | Sulfonated Polystyrene |
| SWCNTs | Single-Walled Carbon Nanotubes |
| TEM | Transmission Electron Microscopy |
| TGA | Thermogravimetric analysis |
| VOCs | Volatile Organic Compounds |
| XPS | X-ray Photoelectron Spectroscopy |
| XRD | X-ray diffraction analysis |

This page was intentionally left blank

# CHAPTER 1: BACKGROUND

## 1.1 INTRODUCTION

Water quality and environmental pollution have become a growing concern globally. Anthropogenic practices and climate change have put a strain on the availability of safe and clean water resources. The rapid growth urbanization and industrialization have led to an increase in demand and contamination of water resources, respectively [1, 2]. In this chapter, the toxic health effects and environmental dangers of heavy metals silver and copper are reviewed. Various water treatment technologies are briefly explained and the adsorption technology is further explained comprehensively. Research that was carried out on the removal of silver and coper in water is also summarised in this chapter. Since waste minimization is of importance in the overall study, the application of silver and copper as bactericidal agents is also reviewed alongside conventional water disinfection methods.

## 1.2 AIMS AND OBJECTIVES

The aims of the project were as follows:

9. To synthesize polymer based nanostructured materials
10. To characterize the synthesized nanomaterials with various characterization techniques.
11. To test removal efficiency of inorganic ions by means of batch studies varying several parameters such as dose, pH, initial concentration, time, temperature
12. To test removal efficiency of inorganic ions by means of continuous column dynamic studies varying several parameters such as initial concentration, bed height, flow rate
13. To examine desorption and regeneration capabilities of the nanomaterials using adsorption desorption cycles.
14. To test antimicrobial activity using metal loaded material obtained from aim #3
15. To test catalytic activity using metal loaded material obtained from aim #3
16. To test gas sensing activity using metal loaded material obtained from aim #3

## 1.3 WATER POLLUTION BY INORGANIC CONTAMINANTS

### 1.3.1 Overview

Heavy metals are elements with an atomic weight in the range of 63.5-200.6 and a specific gravity above 5.0 [3]. Heavy metals are released to the environment naturally and by anthropogenic activities, ending up in various water resources, as seen in Figure 1-1 [4]. Heavy metals are also non-biodegradable, thus having potentially adverse health and environmental effects [5]. Some examples of heavy metals include silver, copper, lead, cadmium, mercury and chromium. Heavy metals may be important for human bodily functions; hence there are permissible limits set by the World Health Organisation (WHO) [6, 7] and United States Environmental Protection Agency (US EPA) [7] (Table 1-1).

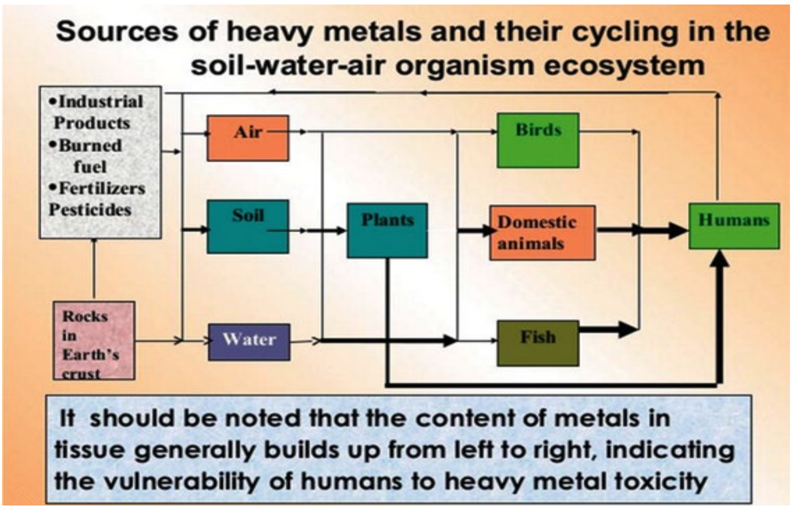

**Figure 1-1: A schematic diagram illustration the sources and paths of heavy metals in the environment [4].**

**Table 1-1: Guidelines of permissible limits for some heavy metal ions in drinking water.**

| Heavy Metal Ions | **Permissible limit (mg/L)** | |
|---|---|---|
| | **US EPA** [7] | **WHO** [6] |
| Silver | 0.1 | 0.1 |
| Copper | 1.3 | 1.5 |
| Zinc | 5 | 5 |
| Chromium | 0.05 | 0.05 |
| Lead | 0.015 | 0.05 |
| Arsenic | 0.01 | 0.05 |

### 1.3.2 Silver

Silver (Ag) is a natural constituent of the earth's crust and it is an attractive metal because of its malleability, photosensitivity and excellent thermal properties [9]. Silver has numerous uses in various industries. Silver has been historically used as an antibiotic in the healthcare industry. It has been developed for use in cardiac devices, water purification, wound care, catheters, bone prostheses and reconstructive orthopaedic surgery and in surgical appliances [10]. Ag is currently added in consumer products such as home appliances, textiles, food supplements and personal care products because of its bactericidal properties [11, 12]. The escalating use of Ag in basic consumer products, has led to an increase in its release into the environment, particularly water sources [13]. Also, silver is usually found in industrial effluent from electroplating, printing and photo processing industries [14].

Figure 1-2: A pictorial of a silver ore [8].

Although the minimal exposure of silver causes no harm to humans, chronic exposure to silver (especially in its colloidal form) leads to undesirable health effects such as argyria (skin) and argyriosis (eyes) [15-17]. Due to the toxicity associated with the excessive consumption of Ag [18], the United States Environmental Protection Agency has set the maximum contaminant level of Ag to 0.1 mg/L for drinking water [7].

### 1.3.3 Copper

Copper (Cu) is the 3rd most used commodity in the world and this attributes to its chemical and physical properties [20]. Cu is mostly used in fungicides and as an antifouling agent in paint. It is also used extensively in the electrical industry [21]. Cu is also used in construction, transportation and machinery [22]. Copper is one of the essential elements in the human body because of its role in the biological processes. However, Cu is carcinogenic if ingested at high concentrations whilst also promoting oxidation [23-25]. The United States Environmental Protection Agency has set the maximum contaminant level of Cu to 1.3 mg/L for drinking water [7].

Figure 1-3: A representative image of native copper [19].

### 1.3.4 Mercury

Mercury (Hg) is recognised as one of the most hazardous metal pollutant. Burning of petrochemical oil and coal, discharge of waste effluents from mining plant, printing industries, cement processing and batteries manufacturing are the main sources of mercury pollution in waterway. Mercury exists in several physical and chemical forms: elemental mercury ($Hg^0$), divalent mercury ($Hg^{2+}$) and monomethyl mercury cation ($CH_3Hg^+$)10. Divalent inorganic mercury ($Hg^{2+}$) has been found to be a serious contaminant due to its high solubility and stability. It is reported that divalent mercury ($Hg^{2+}$) may be easily transferred into higher toxic organometallic forms via biological methylation [26]. Alkylmercury ($CH_3Hg^+$) has received considerable attention because of its low biodegradability and greater toxicity to biological system than other chemical forms [27]. Trace amounts of mercury can affect the central nervous system and also cause serious damage to kidney and lung tissues [28]. Based on the best available science to prevent potential health problems, the United States Environmental Protection Agency (EPA) has set 0.002 mg/L (2 ppb) as the maximum allowable limit for mercury in drinking water [29].

### 1.3.5 Cobalt

Cobalt is a natural earth element which may be found in soil, plants and in our diets in trace amounts. It exists as $Co^{2+}$ and $Co^{3+}$, which forms a number of organic and inorganic salts. Cobalt is a steel-grey to black shiny metal in its pure form and usually occurs in association with other metals such as copper, nickel, manganese and arsenic [3]. Sources of environmental cobalt are both natural and anthropogenic. The natural sources include continental and marine biogenic emissions, extraction by plants, the weathering of rocks and soil as well as seawater spray and emission. The major anthropogenic sources of cobalt include the use of cobalt-containing sludge or phosphate fertilizers on soil and the disposal of cobalt containing waste. Atmospheric deposition of cobalt may arise from activities such as the burning of fossil fuels as well as the smelting and refining of metals, all of which falls under the mining and processing of cobalt-bearing ores [4]. Cobalt may be essential in trace amounts for human life because as a part of vitamin B12, it plays a key role in the body's synthesis of this essential vitamin. Cobalt also promotes the production of red blood cells and this has led to its use in the treatment of anaemia [3]. Although cobalt may be essential in trace amounts, exposure to very high levels of cobalt can result in harmful effects to human health as its toxicity is reported to cause gastrointestinal problems, mutations in living cells, asthma as well as damage to the thyroid gland [3].

### 1.3.6 Nickel

Nickel is a naturally occurring silvery-white element that can exist in various mineral forms. Nickel is resistant to corrosion by air, water and alkali but readily dissolves in dilute oxidising acids. The prevalent oxidation state of nickel is $Ni^{2+}$ [3, 5]. Nickel is widely distributed in the environment and it is released from both natural and anthropogenic sources. It is present in the air, water, soil as well as in biological material. By virtue of nickel and its compounds having many industrial and commercial uses, anthropogenic sources of nickel include the production of stainless steel and other nickel alloys with high corrosion and temperature resistance. Nickel and its alloys are also used in the metallurgical, chemical and food processing industries as catalysts and pigments [4]. Natural sources of atmospheric nickel include wind-blown dust which is derived from the weathering of rocks and soils, volcanic emissions as well as forest fires and vegetation [5]. Nickel is classified as very carcinogenic and toxic in high doses as its exposure is reported to be resulting in health effects such as asthma, chronic bronchitis, heart disorders, respiratory failures and lung embolism. Information obtained from the South African National Standards (SANS) report has been tabulated to indicate the standard limit of the heavy metals such as cobalt and nickel according to the World Health Organization (WHO) as follows:

**Table 1-2: Major sources of heavy metals and their standard limits according to WHO**

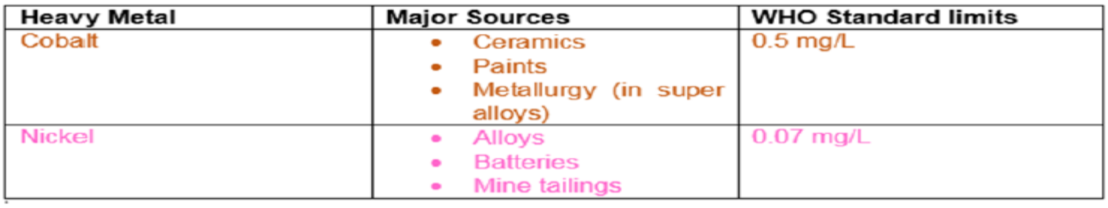

| Heavy Metal | Major Sources | WHO Standard limits |
|---|---|---|
| Cobalt | • Ceramics<br>• Paints<br>• Metallurgy (in super alloys) | 0.5 mg/L |
| Nickel | • Alloys<br>• Batteries<br>• Mine tailings | 0.07 mg/L |

However, its toxicity has been reported in the literature to result in abnormal thyroid and artery, polythermia, overproduction of red blood cells as well as problems of the right coronary artery [6]. Nickel is identified as an important component in a number of enzymes as it forms part of the so called “essential metals”. It participates in essential metabolic reactions such as urolysis, hydrogen metabolism and methane biogenesis as well as acidogenesis. However, nickel toxicity results in lung, bone and nose cancer. In fact, nickel exposure through coins and jewellery has been reported in the literature to be one of the leading causes of dermatitis [6, 7].

### 1.3.7 Fluoride

Fluoride enters the earth’s ecosystem through various sources which can be broadly classified as naturogenic and anthropogenic based on their origin. Naturogenic sources also known as geogenic sources are mainly natural or geological in origin and include various natural activities such as weathering of fluoride containing mineral rocks, gaseous emissions from volcanic eruptions and aerosols produced from marine activities. When fluoride containing mineral rocks are exposed to the weathering agents, a series of chemical processes occur due to which fluoride leaches out and permeates through earth’s crust and infuses to the groundwater. Sedimentary stones, sandstones and limestones are some fluoride rich rocks which specifically contain fluorspar ($CaF_2$) as fluoride mineral whereas igneous rocks and granite contain cryolite ($Na_3AlFPO_6$) and fluorapatite ($Ca_5(PO_4)_3F$) [30]. On the contrary, anthropogenic sources are mainly human-made in origin and comprise various human activities such as combustion of coal in coal-fired plants, industrial wastes from aluminium and steel manufacturing, fertilizer production, ore processing, glass and ceramic manufacturing, nickel and copper production, glue and adhesive producing industries. Besides, agricultural use of fluoride containing pesticides, fluorinated pharmaceuticals and addition of fluoride to public water supplies are some other anthropogenic sources of fluoride in water [31]. Fluorosis is a most evident manifestation of the chronic fluoride intoxication where the duration of fluoride exposure as well as the amount ingested play a decisive role in determining its severity [32].

## 1.4 WATER TREATMENT BY ADSORPTION

### 1.4.1 Overview

Degradation of water quality and the reduction of fresh water resources are posing a threat to human health and aquatic life. Deterioration of water quality has led to the development and refinements of water treatment technologies, which restore water and afford the environment reduced exposure to toxins [5]. Several water treatment technologies are applied in the daily running of water/wastewater treatment plants. Table 1-3 provides a description of the current methods used for wastewater and water treatment. There is a vast selection of contaminant separation techniques for wastewater treatment; however the major challenge always remains the high operational costs [56] and the incompetence at low metal ion concentrations (≤ 100 mg/L) [57]. Adsorption technology comes out superior when compared to the other technologies, because it is relatively inexpensive and easy to apply [58]. Adsorption, as described in the table above, is a technique that involves the accumulation of compounds (adsorbate) at the surface of solid state materials (adsorbent). The adsorbate is usually in gaseous or liquid state [59]. Adsorption is divided into two types, namely: physisorption and chemisorption. Physisorption takes place through weak Van der Waal’s forces, thus it is a reversible process. Chemisorption involves chemical bonding, i.e. covalent bonding; therefore it is an irreversible process [59].

Adsorption is driven by the kind of adsorbents used for the particular application (Fig. 1-4). Therefore, adsorbent characteristics play a pivotal role in adsorbent engineering and understanding the adsorption processes [61-62]. The typical adsorbent properties that are of importance in adsorption are shown in Figure 1-5. Some of the most important characteristics rising from this list of properties are surface chemistry, surface area, density, porosity and pore-size distribution [63]. This alludes to the reasons why nano adsorbents have been found to be increasingly attractive. Nanoadsorbents possess high specific surface areas which translate to a high availability of active sites, adjustable pore sizes and short intraparticle diffusion distances. The surface chemistry is also easily modified [64]. The adsorption process is assessed by obtaining the equilibrium data, which forms the basis of determining design parameters for adsorbers (fix-bed reactors, batch or flow through adsorbers). The ability for the contaminant to be adsorbed by the designed adsorbent is also determined by the adsorption equilibrium data, obtained from mathematical models. Also, the relationship between the adsorbent and adsorbate is further described by adsorption isotherms. Energies associated with adsorption processes and mechanisms are also important in designing effective adsorbers; hence there is a need to know thermodynamic parameters [61, 63-64]. The detailed explanations of the different models and isotherms are described in the chapters to follow.

**Table 1-3: Description of technologies used in the removal of inorganic contaminants.**

| Treatment process | Description | Ref |
|---|---|---|
| Chemical precipitation | This technique is based on the use of lime combined with an iron or aluminium salt to form precipitates. It is then followed by flocculation and sedimentation, generating toxic concentrated metal-ion secondary waste. The most common processes include hydroxide and sulphide precipitation. | [33-38] |
| Ion exchange | Ion exchange is the most used technique in water and wastewater treatment and other separation processes. This process involves the use of a resin possessing a similar ion to the ion of interest, immobilized on a solid support/particle. Ion exchange is either cationic or anionic. Ion exchange resins eventually reach exhaustion. They therefore, require regeneration with chemical reagents, thus having to dispose or treat large quantities of secondary waste. | [39-43] |
| Membrane filtration/separation | Membrane filtration is a separation technique that is pressure-driven that makes use of a membrane to separate particles and molecules (Benjamin&Lawler, 2013).There are different types of membrane filtration such as microfiltration, ultra-filtration, nano-filtration and reverse osmosis. The membranes used are specific to their applications (Graff, 2012). Although membrane technology is said to be effective for heavy metal removal, it is prone to fouling (possibly irreversible) (Ning, 2002). It comes with high operational costs due to fouling and high energy requirements and there is a need for skilled personnel to operate the process (Slater et al., 1983). | [44-51] |
| Adsorption | This technique, in simple terms, is the enrichment of a component(s) in the vicinity of an interface (Rouquerol et al., 2013). Adsorption can take place in a chemical or physical form. The adsorbent material used for the component of interest determines the efficacy of the technology (Cantuaria et al., 2016). The simplicity in operation, convenience and relatively low cost are what makes adsorption attractive (De Gisi et al., 2016). | [2,52-55] |

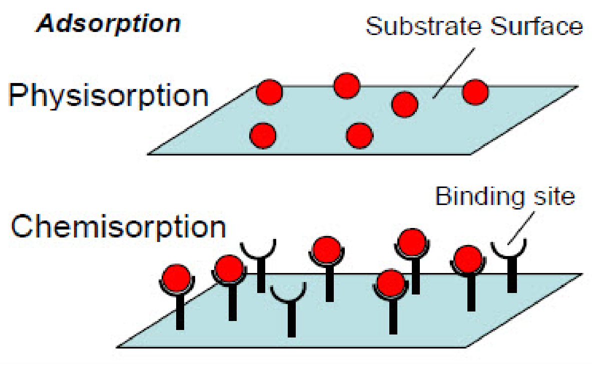

**Figure 1-4: A pictorial representation of the difference between physisorption and chemisorption (Image adapted from [60]).**

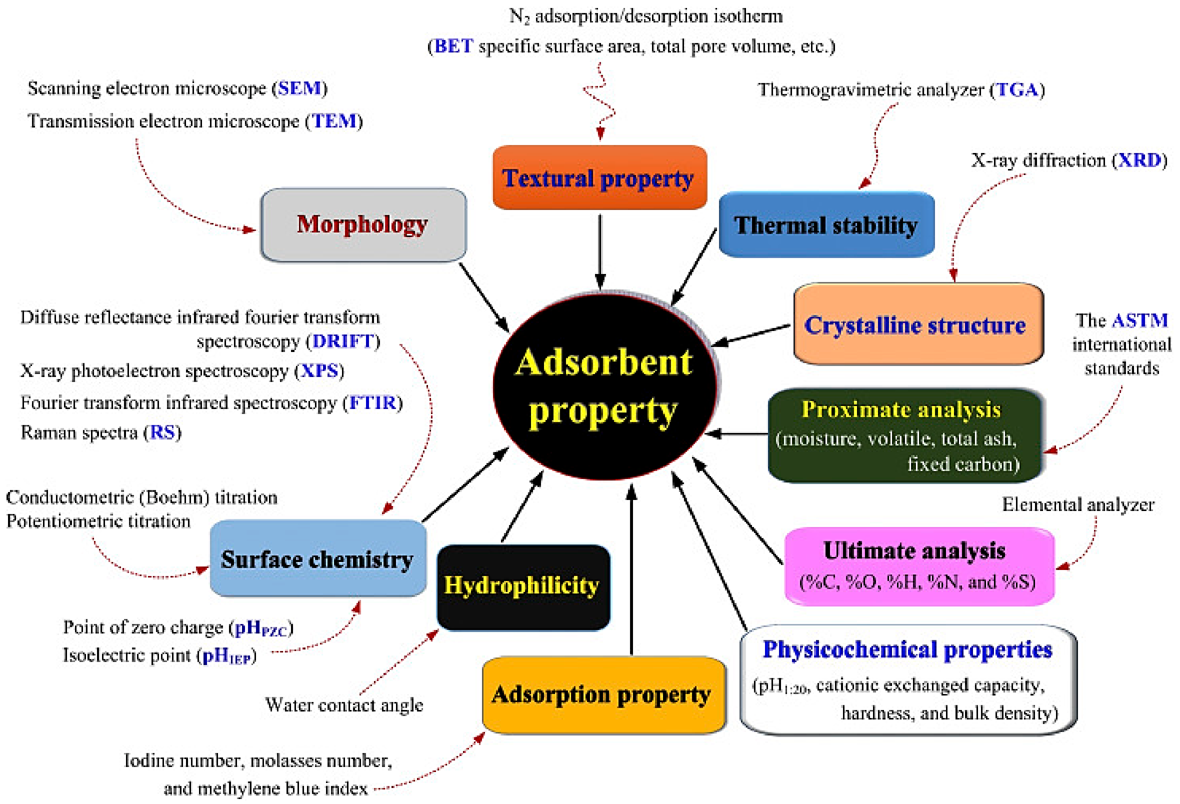

**Figure 1-5: Common adsorbent properties determined by various characterization techniques (Image adopted from [62].**

### 1.4.2 Adsorption using nanomaterials

Nanotechnology is the modification, manipulation design and application of materials and atoms that are below 100 nm ($10^{-9}$ m). Nanomaterials are used in cosmetics [66], medicine and pharmaceuticals [67], electronics [68] and water quality and treatment [69-70]. Nanomaterials possess decent mechanical, thermal, optical and physical properties; hence their use in environmental applications. An example of nano-sized matter is presented in Figure 1-6.

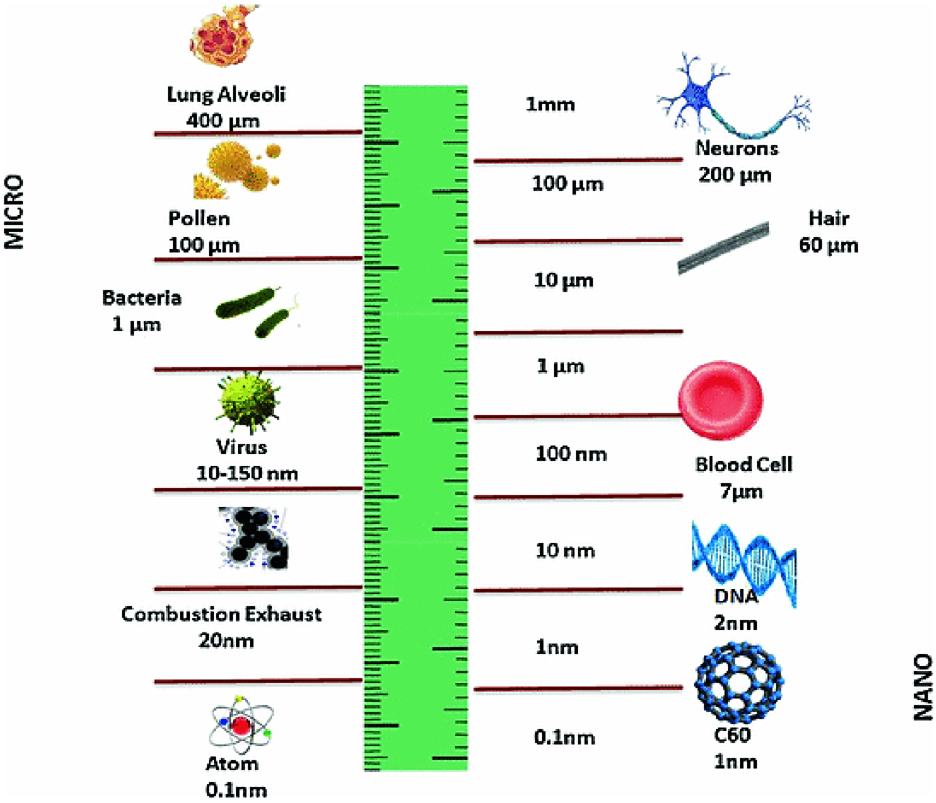

**Figure 1-6: A comparative diagram illustrating nano-sized objects with respect to micro-sized objects [65].**

There is a plethora of adsorbent materials being developed for water and wastewater treatment applications. This review focussed on magnetic nanomaterials and nanocomposites, as well as other nanocomposites. This review also focusses on the use of biomass-derived nanomaterials/nanocomposites for the removal of $Cu^{2+}$ in water. Magnetic nanoparticles have become increasingly popular in the engineering of nanomaterials. They are applicable in a number wide range of applications such as biotechnology [71], remediation technology [72-73], biomedicine [74] and sensor technology [75]. Generally, magnetic nanoparticles/nanomaterials can be classified as diamagnetic, paramagnetic, ferromagnetic, ferrimagnetic, and antiferromagnetic, depending on their magnetic dipole arrangements in the presence of an external magnetic field (Scheme 1-1). Magnetic dipoles are the repulsion/attraction forces between magnetic materials [76-77]. According to the magnetic family tree, magnetism is divided into diamagnetism and paramagnetism [76].

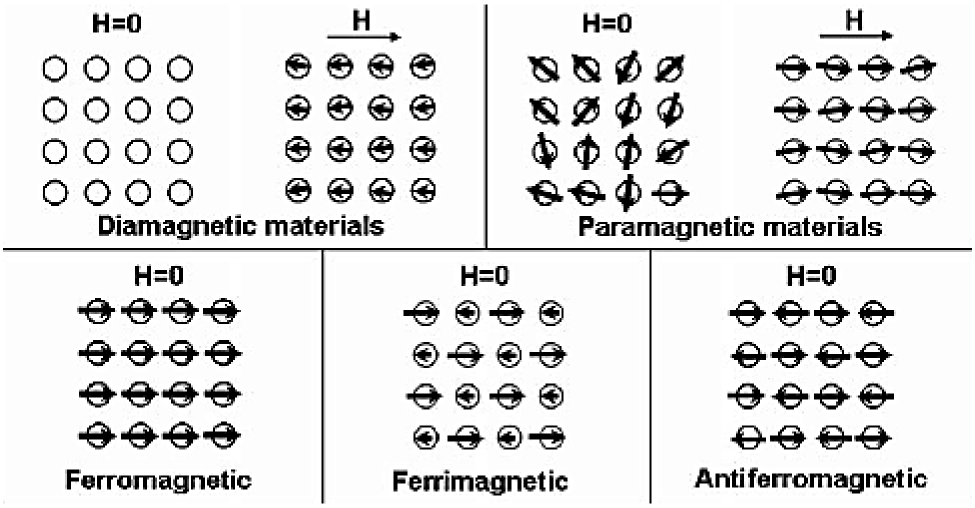

**Scheme 1-1: A schematic diagram demonstrating the arrangements of magnetic dipoles for the various types of materials with and without exposure to external magnetic field (H) [78].**

A high-level summary that is solely for the purpose of providing fundamental descriptions of the different types of magnetic materials is displayed in Table 1-4, which associates with Scheme 1-1.

**Table 1-4: Types of magnetism found in magnetic materials**

| Types of magnetism | Description | Ref |
|---|---|---|
| Diagmagnetic | Materials do not possess magnetic dipoles in the absence of an external field and have weak induced dipoles in the presence of an external magnetic field.<br>The external magnetic field and the response thereto, are in opposite directions.<br>The magnetic interactions are very weak. | [76, 79-80] |
| Paramagnetic | Materials have randomly oriented dipoles that can be aligned in an external field.<br>The external magnetic field and the response thereto, are in the same direction.<br>The magnetic interactions are very weak. | |
| Ferromagnetic | Materials always have magnetic dipoles, even in the absence of an external magnetic field.<br>Iron and magnetite are examples of such materials. | |
| Ferrimagnetic | Materials always have weaker magnetic dipoles that are aligned antiparallel to the adjacent, stronger dipoles in the absence of an external magnetic field. | |
| Antiferromagnetic | In these materials, the adjacent dipoles are antiparallel when there is no external magnetic field and they cancel each other. Thus they have zero overall magnetic moment. | |

The hysteresis loop (Figure 1-7) is used to characterise ferro- or ferromagnetic materials. Typically, the magnetic domains inside the material lead to the magnetization falling behind the applied magnetic field, thus forming the hysteresis loop [76]. The magnetic saturation ($M_s$), remeinance ($M_r$) or residual magnetization when there is no applied field can all be found from the magnetization curve [80].

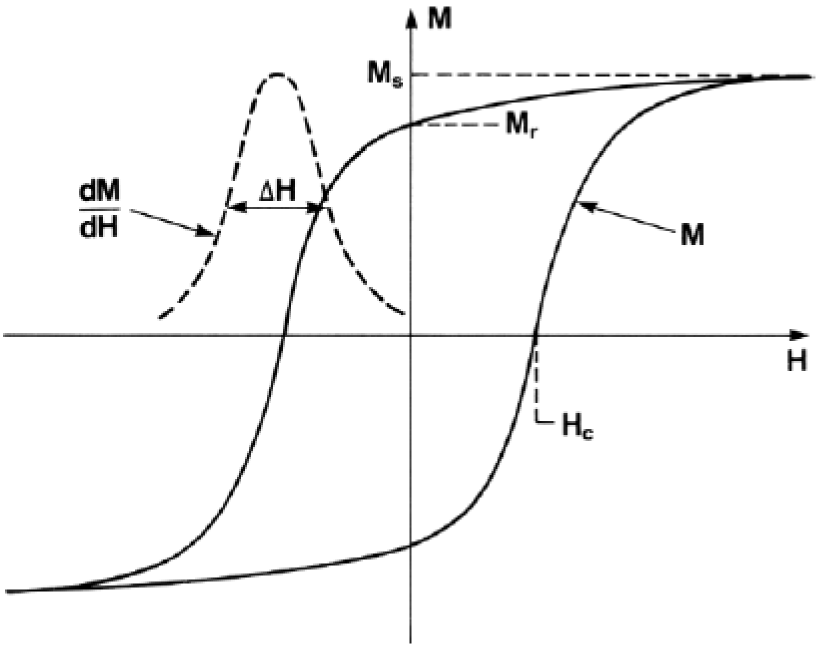

**Figure 1-7: A typical hysteresis loop or magnetization curve of a ferri- or ferromagnetic material [80].**

Magnetic nanoparticles are significantly active in their natural state; however they are prone to oxidation when exposed to air, thus losing their magnetism. Coating magnetic nanoparticles with polymeric materials such as polypyrrole, prevents particle aggregation, reduces the associated toxicity and prolongs the storage life of the nanoparticles. Furthermore, incorporating magnetic nanoparticles in the polymer matrix not only introduces magnetic properties to the polymer, but also introduces surface functionality for the magnetic nanoparticles [81-82]. Magnetic nanoparticles vary and are used in various applications. The most commonly used ones include magnetite/iron oxide ($Fe_3O_4$) [83-89], α-$Fe_2O_3$ [90-91], cobalt ferrite ($CoFe_2O_4$) [92-94], nickel ferrite ($NiFe_2O_4$) [95-97] and zinc ferrite (ZnFe2O4) [98-99]. Separation or the removal of spent adsorbents is an important aspect in water treatment processes. The use of magnetic nanocomposites in water treatment processes holds advantages that include relatively easy separation of spent treatment agents, the retrieval or separation time can possibly be reduced, thus deeming the process more economical [100]. A typical magnetic separation process would operate in a manner whereby the adsorbent is introduced to the contaminated water source and then post adsorption, a magnetic separator would be employed to remove the adsorbent [101] (Scheme 1-2).

Rahil *et al.* employed magnetic ion-imprinted polymer nanocomposites to preconcentrate silver and obtained a $Q_m$ of 62.5 mg/g [87]. Core-shell magnetic silicon dioxide ($Fe_3O_4@SiO_2$) microspheres were prepared, followed by titanium dioxide functionalisation 45 to form $Fe_3O_4@SiO_2@TiO_2$. Chitosan/polydopamine@C@magnetic fly ash (CPCMFA) beads were prepared as adsorbents for $Ag^+$ removal and had an adsorption capacity of 57 mg/g [102]. Magnetically modified clay mineral halloysites exhibited improved adsorption capacities (67.9 mg/g) compared to native halloysites (40.9 mg/g) [103]. Ma et al 2018, prepared amino-functionalized magnetic graphene oxide ($Fe_3O_4$/GO-$NH_2$) nanocomposites which had a maximum adsorption capacity detailing 114.90 $mg_{Ag}$/g [104].

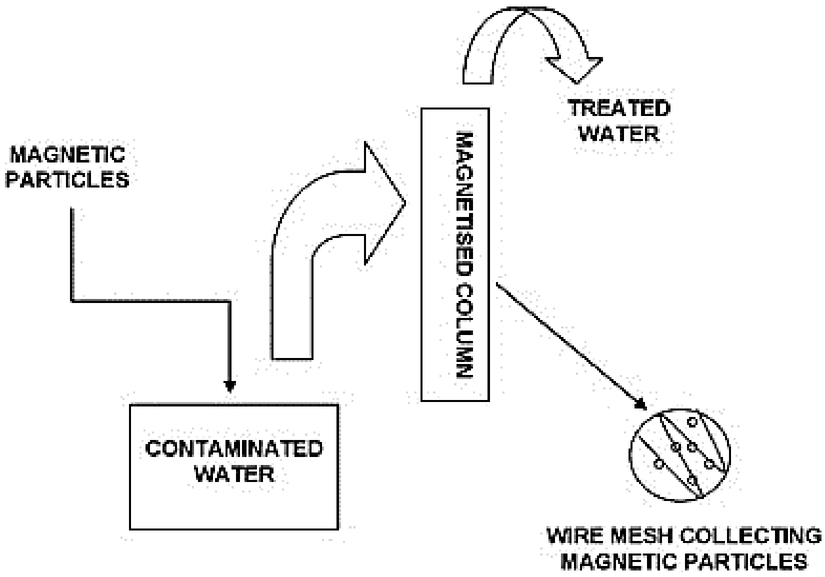

**Scheme 1-2: A schematic diagram illustrating a typical magnetic separation facility [101]**

### *1.4.2.1 Nano-metal oxides (NNMOs) as adsorbents*

The term metal oxide is usually applied to solid ionic compounds that contain the anion $O^{2-}$ and one, two or more metal cations [105]. Recently mixed nanosized metal oxides have emerged as promising adsorbents for water pollutants. They have outstanding physical and chemical properties owing to their small size and high charge density of edge surface sites namely particle size, electronic properties and the presence of coordinated atoms or O vacancies in oxide nanoparticles. Furthermore, they have occupied electronic states located above the valence band and as a result they have a rock salt crystal structure which increases their chemical activity [106,107,108]. As adsorbents, NNMOs offer many advantages including, large surface areas, high adsorption capacities, regenerability, good acidic and basic properties, fast kinetics, amenability to doping and the ability to mimic natural soil systems [106,107,108,109,110,114]. Typical metal oxides are alkaline, alkaline earth, rare earth and transition metal oxides like nanosized ferric, manganese, aluminum, titanium, magnesium, zinc, zirconium, lanthanum and cerium oxides [105,108,111].

Over the last ten years there has been much interest in the application of NNMOs especially in their mixed forms for removal of pollutants from water [108]. The binary Fe-Ti, Mn-Ce, Ce-Fe, Ce-Al, Al-Mg, Fe-Zr, Al-Fe and Mn-Al oxides [105,108,112,114] have been utilised for fluoride removal and more publications are still being released on the application of NNMOs. Tang and Zhang [114] synthesized Ce-Fe binary nano-metal oxides by a simple co-precipitation for the removal of fluoride ions by batch process. The NNMOs were reported to have a surface area was 164.9 $m^2/g$ and the adsorption capacity was 60.97 mg/g over a wide pH range of 2.9-11 in 40 minutes. The adsorption was well described by the Langmuir isotherm and the kinetics were pseudo-second-order modelled. For the effect of co-existing ions on fluoride adsorption, carbonate and hydrogen carbonate ions showed more interference, than sulphate, chloride and nitrate ions. The mechanism of adsorption was ion exchange between hydroxyl groups on the surface of the adsorbent and fluoride ions. In an effort to achieve a high surface area adsorbent, Wang et al. [112] prepared hollow Fe-Ce oxy hydrous metal micro cubes for fluoride removal by tuning the surface to afford a surface area of 242 $m^2/g$. The maximum adsorption capacity was 146.59 mg/g at pH 5 within 20 minutes. The adsorption was both Freundlich and Langmuir modelled. The pseudo-second-order model best described the kinetics where co-existing ions had very little effect on fluoride adsorption.

More recently, Dilhon et al. [113] synthesized Ce-Zn binary nano-metal oxides by a simple precipitation method followed by their application for the removal of fluoride ions from solution. The adsorbent showed a high adsorption capacity of 194 mg/g at a pH of 7. The adsorption process was Langmuir modelled and the pseudo-second-order model best describes the kinetics. The effect of co-existing ions was negligible with a mechanism of adsorption involving both ion exchange and electrostatic attractions between the surface hydroxyl groups of the nano-metal oxides and fluoride ions.

#### *1.4.2.2 Conducting polymer – polypyrrole*

Conducting polymers, also known as synthetic metals, are polymers that possess electronic properties whilst retaining traditional polymer properties. Such polymers get their electrical conductivity, low ionization potential and optical transitions from the π-electron backbone [114-119]. Significant attention has been focussed on conducting polymers and their derivatives such as polypyrrole (PPy), polyaniline (PANI), polythiophene (PTh), polyethelenamine (PEI). Their low toxicity, ease of synthesis, tunable morphology, porous structure, high stability in aqueous media, low cost and adaptable structures have led to numerous investigations and applications. Some applications include adsorption of heavy metals, dyes and emerging contaminants as well as applications in sensors, catalysis and energy storage [120-127]. PPy [116-118] is one of the most commonly used conducting polymers, possesses desirable attributes such as low toxicity, plausible environmental stability, ease of preparation and relatively inexpensive [118,128]. To improve the adsorption efficiency and selectivity towards target metal ions, considerable efforts have been made to introduce desirable functional properties to the adsorbent materials [121]. The chemical modification, with chelating substrates containing various functional groups (carboxylic acid, hydroxyl, amine, and thiol), is one of the superior ways to enhance the adsorption potential of the adsorbent materials for toxic metal ions removal from waterbodies [87,129].

Also, PPy has a low density and incorporating iron oxide ($Fe_3O_4$) nanoparticles in the polymer matrix will increase the density of the nanocomposites making the recovery of the spent adsorbent easier, as it would only require a magnetic field for separation [84]. PPy is synthesized in through chemical or electrochemical oxidative polymerization [121,130]. The standard mechanism of the formation of polypyrrole, via chemical oxidation polymerization of the pyrrole monomer, is shown in Scheme 1-3. The polymerization takes place in 3 steps: 1) oxidation of the pyrrole monomer takes place leading the generation of cations; 2) radical coupling then occurs, where a deprotonated bipyrrole is formed by the coupling of two radical cations; the bipyrrole becomes re-oxidated, leading to more radical couplings and thus leading to 3) chain propagation [118].

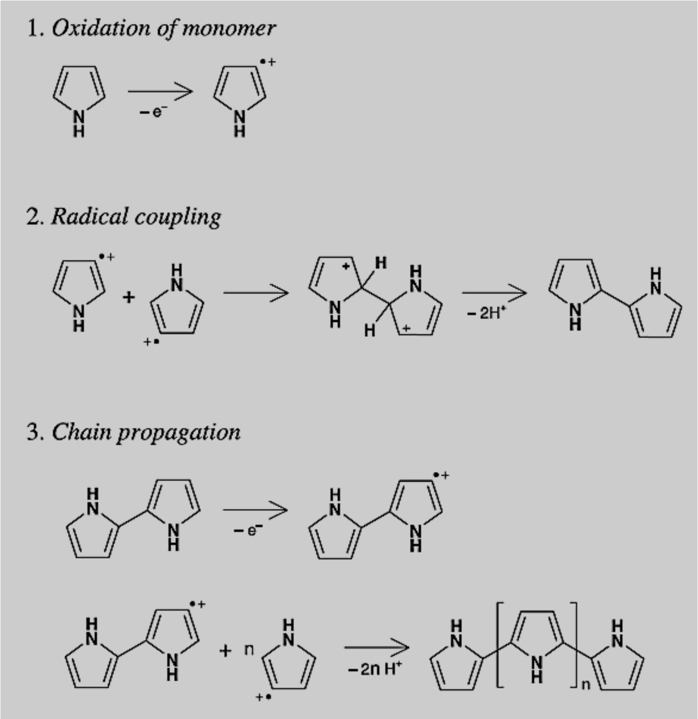

**Scheme 1-3: A schematic diagram of the oxidative polymerization process of pyrrole (Jang, 2006).**

### *1.4.2.3 Hollow Carbon Nano Spheres*

Hollow Carbon Nano Spheres (HCNS) can also be seen as alternate adsorbents in water remediation from heavy metals. This is because these HCNS offer advantages such as having a controllable permeability, surface functionality, excellent chemical and thermal stabilities, encapsulation ability as well as high surface-to-volume ratios [24]. By virtue of this study focusing on carbonaceous nanomaterials (HCNS) and their conducting polymer-based nanocomposites, polyaniline has been selected as the polymer of choice. This is because polyaniline belongs to the most effective class of chelating adsorbents as it chelates cationic adsorbates through electrostatic interactions and it can enrich as well as remove heavy metal contaminants from aqueous solution readily and effectively [25,33]. Polyaniline is also essential in this study by virtue of its ability to participate in acid/base interactions in the presence of basic gases such as ammonia which are able to deprotonate its amine groups in order to create a gas sensor response [34]. This makes polyaniline essential for the further application of these adsorbents in gas sensing applications. After the adsorption of the heavy metal contaminants onto the HCNS, it is important to avoid discarding the resultant metal-loaded adsorbents back into the environment by further applying them in gas sensing. The gas sensing application of these carbonaceous nanomaterials is important since their nitrogen-functionality, high surface area as well as being loaded with heavy metals such as cobalt and nickel will aid in the sensing and removal of toxic gases such as sulphur dioxide ($SO_2$), methane ($CH_4$), acetone ($C_3H_6O$), nitrogen dioxide ($NO_2$) and dihydrogen sulphide ($H_2S$). The sensing of these gases from the atmosphere is important because they have a harmful impact on the environment, vegetation as well as human life.

HCNS are attractive candidates in water remediation from heavy metals because they possess features which render them successful in this regard. Their cavities act as storage reservoirs which are capable of storing the adsorbed heavy metal ions. Their shells are permeable and will thus be able to allow guest species to diffuse through the mesopore channels between the core and the exterior of the shells. The mesopore channels in the shell layer are capable of incorporating, adsorbing as well as immobilizing guest substances and counts as an advantage with regard to the objective of this study [9]. Template synthesis is utilized in this study in order to obtain HCNS through the polymerization of a styrene monomer in order to obtain polystyrene spheres (PS) as templates. These resultant PS templates undergo sulfonation when treated with sulphuric acid in order to produce hydrophilic shells which possess sulfonic acid ($-SO_3H$) groups. These sulfonic acid groups aid in the adsorption of metal ions as well as the formation of a complex with polyaniline (PANI) [35]. Polyaniline is thus deposited on the surface of these sulfonated polystyrene (SPS) templates by chemical oxidative polymerization of an aniline monomer. By virtue of polyaniline possessing a large amount of amine and imine functional groups, it becomes an attractive material for the remediation of water from heavy metals since these functional groups render PANI with a strong affinity towards heavy metal ions as well as a high chemical flexibility [36, 37]. The carbonization of the resultant polystyrene@polyaniline spheres results in the formation of the HCNS which are rich in nitrogen-containing groups and possess a preselected morphology in the form of spheres [38]. The presence of the nitrogen heteroatoms will be beneficial by enhancing the properties of the HCNS such as chemical reactivity as well as electrical conductivity which will in turn be beneficial in gas sensing applications [42].

Nitrogen-containing carbons have been reported in the literature to exhibit excellent adsorption properties for polar or acidic gas molecules. Since the HCNS synthesized in this study are rich in nitrogen-containing functional groups, this will be advantageous in the sensing as well as adsorption of gases such as $H_2S$. The presence of nitrogen groups on the surface of these HCNS will enhance their surface basicity and this will favour the dissociation of $H_2S$, thus attracting HS- ions via electrostatic interactions. Literature has also shown that nitrogen-containing carbon has also been successful in the adsorption of gases such as $NO_2$, formaldehyde as well as $SO_2$ [39].

**Table 1-5: Adsorption capacities for various adsorbents studied for the removal of Ag from aqueous media.**

| Adsorbent | Adsorption capacity (mg/g) | pH | Temperature (ºC) | Ref |
|---|---|---|---|---|
| Sulfoethyl functionalized silica nanoparticle | 21.9 | 6 | 25 | [87] |
| Magnetic Photocatalytic Ion-Imprinted Polymer | 35.475 | 6 | 25 | [131] |
| Halloysite nanotubes | 109.79 | 6 | 20 | [132] |
| Cliptonolite (Zeolite) | 33.23 | 4 | 25 | [133] |
| Verdelodo clay | 55.55 | - | 20 | [53] |
| 4-vinyl pyridine -N,N-ethylene bisacrylamide | 75.64 | 6.5 | 25 | [134] |
| 1-vinyl imidazole-N,N-ethylene bisacrylamide | 74.18 | 6.5 | 25 | [134] |
| Carbon nanospheres | 152 | - | 25 | [135] |
| Poly (Styrene-Alternative-Maleic Anhydride) nanoparticles | 75 | 6 | 25 | [136] |
| Conducting polymers modified sawdust | 35 | 6 | 25 | [137] |
| Thiourea-grafted mesoporous polystyrene resin | 135 | 1.5 | 27 | [129] |
| Chitosan/polydopamine@C@magnetic fly ash (CPCMFA) adsorbent bead | 57.02 | 4 | 30 | [102] |
| amino-functionalized magnetic graphene oxide$Fe_3O_4$/GO-$NH_2$ | 114.90 | 5 | 25 | [104] |

### 1.4.3 Low cost adsorbent – biomass-derived activated carbon

The use of low-cost adsorbents, especially biomass-derived adsorbents, has shown to be invaluable for heavy metal removal [55]. Low-cost adsorbents include clays, zeolites, chitosan, agricultural and bio-waste [55]. These materials have gained a lot of interest however they exhibit low selectivity, which leads to reduced efficiencies and heavy metal adsorption capacities [57,138]. The modification and activation of these materials will aid in increasing specificity thus curbing the aforementioned limitations. Activated carbon (AC) is one of the oldest and popular adsorbents used in water and wastewater treatment, for the removal of inorganic and organic pollutants. Commercial AC is produced from coal; however, this kind of AC is expensive thus leading to its restrictive use [139]. AC can also be derived from various carbon-rich materials that are cheaper and abundantly available such as wood, coal, lignite, corn, bamboo and coconut shell. Surface modification of AC can lead to tailored properties which are specific to the targeted pollutants [54]. The highly porous and amorphous nature of AC has contributed to its relatively high efficiency in the removal of pollutants from water. Due to the expensive nature of commercial AC, there have been a lot of developments in deriving AC from low-cost and natural materials.

There are several methods used for the synthesising AC from biomass. Usually, the biomass is pre-treated, dried at temperatures around 100°C, and then crushed to obtain smaller particles. Thereafter, the biomass is carbonised between 300 and 800°C in order to remove contaminants and other volatile substances. Another process is hydrothermal activation and carbonisation, where the initial drying step is omitted; the biomass is mixed with water or desired reagent prior to the carbonisation step [140]. This process requires lower temperatures below 250°C. The use of acidic activating reagents is also common and presents less harsh conditions with regards to extremely high temperatures and high energy consumption [79,114]. Various combinations of conditions (temperature and reagents used) were reported on chemical activation in literature, as shown in Table 1-6.

**Table 1-6: Biomass-derived activated carbon for the removal of $Cu^{2+}$**

| Adsorbent | Activation or treatment type | Carbonisation Temp (°C) | pH | Adsorption capacity (mg/g) | Temp (°C) | Ref |
|---|---|---|---|---|---|---|
| Pine cone | NaOH |  | 5 | 30.2 | 17.8 | [142] |
| Mercapto-acetic acid modified orange peel | NaOH and ethanol | - | 5.3 | 70.67 | 25 | [143] |
| Sawdust | $H_2SO_4$ | 150 | 5.5 | 13.495 | 20 | [57] |
| Sawdust | $H_3PO_4$ | 800 | 6 | 11.5 | 25 | [144] |
| Chestnut shell | $ZnCl_2$ | 550 | 5 | 100 | 25 | [145] |
| Apricot stones | $H_2SO_4$ | 200 | 6 | 24.21 | 25(Kobya et al. , 2005) | [146] |
| grape bagasse | $H_3PO_4$ | 500 | 5 | 43.47 | 45 | [147] |
| Aspen wood | Citric acid | 130 | 5.1 | 7.9 | Not specified | [148] |
| hazelnut shell | $H_2SO_4$ | 200 | 6 | 58.27 | 49.8 | [149] |
| green vegetable waste | KOH | 400, 800 | 3.5 | 75.0 | 25 | [150] |
| Banana peel | KOH | 500 | 4 | 14.3 | 20 | [151] |
| *Ficus carica* plant fibres | Microwave assisted $H_3PO_4$ |  | 4 | 23.08 | 30 | [152] |

In a chemical activation process, usually activation and carbonisation are carried out simultaneously. It has also been reported that chemical activation of carbonised biomass has contributed towards increased adsorption capacities irrespective of the precursor materials [138,141]. Fluoride can similarly be adsorbed through using carbonaceous materials because of the high surface area, prevention of metal ion sintering in its porous internal framework and thus modifiable with appropriate metal ions to obtain improvised fluoride adsorption efficiency. Vences-Alvarez et al. developed lanthanum modified granular activated carbon (GAC-La0.05) as an adsorbent with fluoride adsorption capacity 9.98 mg/g which is five times higher than commercial GAC [153]. In another recent study, Velazquez-Jimenez et al. obtained a fluoride adsorption capacity of 7.40 mg/g by using Zr(IV) impregnated activated carbon (ZrOX-AC) as adsorbent where the size of Zr (IV) particles was controlled by using oxalic acid as a complexing ligand during the synthesis [154].

However, commercially available activated carbon is quite expensive, and its high cost makes the adsorption process less cost effective. Hence, Yu at al. derived carbon from an alternative cheaper and low-cost source, i.e. Sargassum species (Seaweed) and modified it with lanthanum to make lanthanum-modified carbon and applied the same as an adsorbent to obtain $F^-$ adsorption capacity of 94.34 mg/g at neutral pH condition [155]. Fluoride adsorption predominantly occurred via outer-sphere complex formation, along with electrostatic attraction and ion-exchange mechanism. Sivasankar et al. selected starch as the carbon source for the development of Ce dispersed in carbon (CeDC) and at pH 8.02 obtained a maximum $F^-$ uptake of 52 mg/g. However, the proper composite structure of CeDC could not be established which restricted its further scale up for real field study [156]. Lately, Ajisha and Rajagopal utilised Delonix regia pod to develop activated carbon without any chemical treatment and utilized the same for water defluoridation to obtain a maximum $F^-$ removal capacity of 33.4 mg/g in acidic pH range [157]. Regardless of demonstrating a significant fluoride adsorption capacity, adsorbent required lower pH conditions to operate optimally which makes it less feasible for real field groundwater treatment. Very recently, Singh et al. fabricated activated carbon from the shell of Aegle marmelos commonly known as Bael and employed the same as fluoride adsorbent to obtain maximum $F^-$ uptake of 1.07 mg/g and 2.4 mg/g for initial $F^-$ concentrations 4 mg/L and 8 mg/L, respectively [158].

Though quite a lot of research work has been done to develop surface modified carbonaceous materials, however, most of the studies are still in the preliminary stage at bench scale and lack information regarding their utilization in fixed bed continuous column systems for full scale real field water treatment application. Moreover, high quality activated carbons are of high cost with poor selectivity, regeneration issues, which renders their application impractical on a large scale.

### 1.4.4 Metal based adsorbents

Metal based adsorbents have attracted considerable attention in the field of water defluoridation due to their tendencies to acquire positive charge (by donating electrons) and hence electrostatically attract negatively charged fluoride ions. However, so far 15 different metal elements have been used for adsorbent development for various applications [159]. These adsorbents comprise of metal oxides, metal hydroxides also known as hydrous oxides or oxyhydroxides. Metal based adsorbents which have been utilized thus far as per the literature can be categorized as monometallic, bimetallic and trimetallic adsorbents based on the number of metal elements mixed to form oxides or hydrous oxides. Amongst them alkali metals such as Lithium and Sodium due to their low electronegativity predominately form covalent bond with fluoride and thus have not been reported as principal elements in fluoride adsorbents.

Calcium is an alkaline earth metal with great affinity to fluoride ions, low cost and biocompatibility with the human body, has attracted the considerable interest of researchers for fluoride removal studies. Islam and Patel conducted a fluoride removal study using quick lime (CaO) and concluded chemisorption along with precipitation as an underlying adsorption mechanism [160]. However, quick lime displayed a $F^-$ removal capacity of 16.67 mg/g for initial $F^-$ concentration 10 mg/L and could not effectively bring down the fluoride levels in the water below standard acceptable limits. Calcite ($CaCO_3$) as another calcium adsorbent was applied to remove fluoride from acid treated fluoride containing water [161]. On addition of calcite to acid treated fluoride contaminated water, a large number of $Ca^{2+}$ ions were produced which undergo chemical bond formation with fluoride ions to form $CaF_2$ precipitate and demonstrated a fluoride removal capacity of 7 mg/g. Gogoi and Dutta obtained a $F^-$ uptake capacity of 6.45 mg/g by using phosphoric acid modified limestone powder as adsorbent [162]. Sakhare et al. synthesized calcium aluminate (CA) as another highly porous fluoride adsorbent where $F^-$ ions were adsorbed chemically by calcium component and physically by aluminium component of CA, synergistically resulting in 85% $F^-$ removal for initial $F^-$ concentration 8.9 mg/L [163]. More recently, Chaudhary and Prasad carried out fluoride removal study using activated dolomite ($CaCO_3.MgCO_3$) which is a low-cost and readily available calcium mineral of geological origin mainly found in sedimentary rocks and composed of alternate layers of $CO_3^{2-}$, $Ca^{2+}$ and $Mg^{2+}$ ions. An excellent $F^-$ uptake capacity of 243.25 mg/g was observed for fluoride containing aqueous solution at neutral pH (~7.0) [164]

Another group of low-cost naturally occurring calcium mineral which has been widely employed as fluoride adsorbent is hydroxyapatite (HAP) with chemical formula $Ca_5(PO4)_3OH$. It involves the replacement of hydroxyl ions present in its apatite crystal structure by fluoride ions present in contaminated water to form thermodynamically more stable fluorapatite (FA) [165]. Gao et al. prepared synthetic HAP consisting particles of different sizes and comparatively evaluated its fluoride removal efficiency with that of HAP bulk synthesized using conventional solid state reactions [166]. It was observed that HAP with smaller particle size demonstrated higher $F^-$ uptake capacity and better effectiveness at lower pH. Recently, several studies have been carried out for surface modification of HAP either by coating or doping ions like alumina, magnesium and sulphate into the crystal structure of HAP. In the view of the same, Chen at al. fabricated sulphate doped hydroxyapatite hierarchical hollow microspheres and observed a significant enhancement in fluoride removal efficiency of HAP ($F^-$ removal capacity 28.3 mg/g) after sulphate doping because of the cooperative reinforcement effect between the surface hydroxyl groups and sulphate ions [167].

However, despite having high affinity towards fluoride ions, calcium based adsorbents still hold some limitations concerning reusability. Adsorption of fluoride ions onto the calcium based adsorbents occur via chemisorption (i.e. chemical bond formation) which makes desorption of adsorbed fluoride ions quite tricky during regeneration. The poor regeneration eventually results in drastic reduction in fluoride sorption capacity of calcium based adsorbents after successive adsorption-desorption cycles. Regarding other metals, transition elements such as zirconium, iron, titanium, cerium and manganese due to their multivalent behaviour and more active adsorption sites have gained greater attention in the field of water defluoridation as compared to alkali and alkaline earth elements. Transition elements being more electronegative show slightly weak electron transferring interactions with fluoride ions and hence do not tend to precipitate fluoride [168].

Dou et al. synthesized hydrous zirconium oxide (HZO) by a simple precipitation technique and used as an adsorbent for removal of fluoride. HZO demonstrated a reasonably high $F^-$ adsorption capacity of 68 mg/g, attributed to its plentiful surface OH groups (due to its hydrous nature) which actively adsorbed $F^-$ ions electrostatically as well as via ion exchange [169]. Moreover, Saha et al. in their work, conducted successful surface modification and functionalization of hydrous zirconium oxide using β-cyclodextrin (CY-HZO) which is a pretty well-documented inexpensive, non-toxic toroidal oligosaccharide [170]. As a consequence of the surface modification, the modified adsorbent (CY-HZO) incorporated more surface hydroxyl groups and displayed a reasonably higher $F^-$ uptake capacity (31.45 mg/g) than pristine HZO. Babaeivelni and Khodadoust explored fluoride removing properties of crystalline $TiO_2$ and reported optimum $F^-$ uptake in between pH range 2 to 5 [171]. Amongst the p-block elements only aluminium, tin and bismuth are evidenced to exhibit fluoride adsorbing properties. Other than tin and bismuth, aluminium has been explored hugely for fluoride removal in the form of alumina and alumina containing materials as discussed earlier. Hence, Srivastav et al. synthesized hydrous bismuth oxide (HBO) to evaluate its defluoridation potential and obtained a higher fluoride removal percentage (65%) as compared to commercial $Bi_2O_3$ (6%) [172]. However, there are several shortcomings associated with the use of mono metal based adsorbents such as slow removal, easy deactivation and tedious separation from aqueous solution. Considering these shortcomings, it became essential to try and develop novel and efficient binary metal oxides for water defluoridation. Hence, Dou et al. prepared a granular binary oxide of Zr and Fe (molar ratio 2.3:1), which exhibited $F^-$ adsorption capacity of 9.80 mg/g and exceptionally high mechanical strength and stability assuring better real field feasibility with minimal material loss [173].

Rare earth metal oxides of cerium (Ce) and lanthanum (La) are strongly basic with relatively small ionic potential and thus tend to hydrolyze their surface hydroxyl groups into $OH^-$ ions which are readily exchangeable with $F^-$ ions. However, the expensive nature of rare earth metal based materials makes them less viable as fluoride adsorbents for real field implementation in developing countries with poor economic status. Hence, Tang et al. in this study developed a hybrid binary metal oxide with hierarchical pore structure using Ce(IV) and a cheaper metal Fe(III) which has shown a significant affinity towards fluoride ions in the literature and obtained a $F^-$ adsorption capacity of 60.97 mg/g [174]. Quite recently, Yan et al. synthesized a composite adsorbent made up of La and $TiO_2$ ($TiO_2$-La), where $LaCO_3OH$ was properly oriented over the $TiO_2$ lattice, and the developed $TiO_2$-La composite removed fluoride optimally in a range of pH 3 to 9 with adsorption capacity 78.4 mg/g [175]. Nowadays, substantial work has been directed towards the development of trimetallic adsorbents in continuous efforts for developing highly competent and effective adsorbents for fluoride removal. In accordance, a trimetal composite comprising Mg/Fe/Al in molar ratio 25:1:4 was developed by Wang et al. and further calcined at 400°C [176]. The as-calcined Mg/Fe/La composite displayed a high $F^-$ removal capacity of 112.17 mg/g due to the addition of La (a rare earth element) which is well known to exhibit specific properties such as multivalence behaviour and high selectivity towards $F^-$ ions.  Besides, recently Mg-Al-Zr triple-metal composite was fabricated by Wang et al. which exhibited maximum fluoride uptake of 22.9 mg/g [177].

## 1.5 WATER DISINFECTION

Water disinfection has been part of water treatment routines since the beginning of the 20th century. In addition to the removal and eradication of pathogens, disinfectants are also used as oxidising agents for the elimination of taste and odour, enhancement of coagulation and flocculation, the prevention of algal growth, and so on [178].

### 1.5.1 Bacterial contaminants

In 2004 alone, 696 million cases of children in Africa, under the age of 5 years, were reported to be suffering from diarrhoea [179] (Figure 1.8). Waterborne diseases (cholera, typhoid, amoebic and bacillary dysentery and other diarrheal diseases) are mainly caused by the consumption of bacterially contaminated water, whereby faecal-oral transmission is the most common route of exposure to bacteria [179]. Bacteria are organisms that are single-celled, ranging from 0.1 to 10 µm in size. There are pathogenic and non-pathogenic strains of bacteria, with the following classifications and shapes: *Spirilla* are spiral, *Bacilli* are rod-shaped, *Cocci* are spherical and *Vibrios* are curved, rod-shaped bacteria [180]. The structural differences in bacteria are characterised by the thickness of the cell wall, where gram positive and gram negative bacteria have thin and thick cell walls, respectively [181]. The various bacterial strains that can be found in water sources are listed in Table 1-7. The ability for *E. coli* to survive outside the human body makes it a good indicator bacterium to test for faecal contamination. Although the majority of *E. coli* strains are non-pathogenic, there are serotypes that can cause severe illnesses in human beings [189].

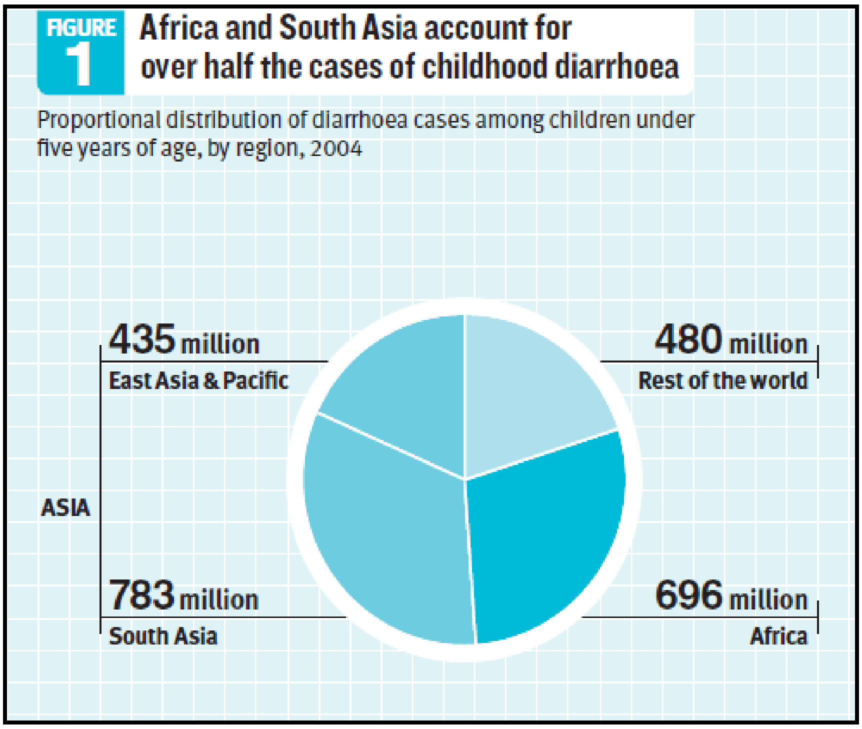

**Figure 1-8: Diagram illustrating the prevalence of diarrhoea in children under the age of 5 in developing countries [179].**

**Table 1-7: Types of bacteria that are found in water sources**

| **Bacterial strain** | **Characteristics** | **Associated disease** | **Ref** |
|---|---|---|---|
| *Escherichia coli* | Gram negative, rod-shaped | Acute diarrhoea, gastroenteritis, urinary tract infection, sepsis/meningitis | [182,183] |
| *Salmonella* | member of the family *Enterobacteriaceae*, Gram-negative ,motile, straight rods | Typhoid fever and other serious salmonellosis | [182,184] |
| *Legionella* | Gram negative, rod-shaped, motile | Legionnaires disease | [185-188] |
| *Vibrio cholerae* | small, curved-shaped Gram-negative rods, with a single polar flagellum | Cholera | [182,184] |
| *Shigella* | Gram-negative, non-sporeforming, non-motile, straight rod-like, member of the family *Enterobacteriaceae* | Bacillary dysentery or shigellosis. | [182,184] |
| *Campylobacter jejuni* | Gram negative, curved-spiral-rod-shaped, | Enteric diseases | [182,186] |

### 1.5.2 Conventional disinfection methods

Conventional disinfection processes currently used are chlorination [190], ultraviolet light (UV) [191], and membrane filtration [192]. The introduction of chlorine and its compounds as a disinfectant in water treatment processes is popular due to its high oxidising potential [190,193]. [193]Chlorination is regarded as an important step in water that is treated for public distribution, because chlorine remains in the water for as long as it is not used; thus preventing microbial recontamination in the distribution system [193]. UV radiation has been used for water treatment for many years, with over 7000 municipalities using UV disinfection systems in the world, since 2011. Current systems make use of low and medium-pressure mercury lamps. UV can also be used in combination with ozone and hydrogen peroxide for extended applications (merged) [194-195]. UV disinfection is an effective form of treatment; however, higher UV fluencies are needed for environmental water due to environmental microbial resistance [194-196]. Membrane technology has been used since World War II, thus making it well-known for water disinfection applications [197-198]. The formation of biofilms caused by microorganism reproduction has been a challenge because, it results in decreased membrane performance and membrane lifespan. It is also reported that biofouling is the most complex type of fouling; thus making membrane technology more complex as it causes additional fouling on the membranes [199].

Although these conventional processes are still widely used, they are reported to be stretched to their limits and are struggling to comply with the increasingly stringent water quality laws [200-201]. The need for new or improved disinfection technologies is also on the rise, due to the formation of harmful by-products by conventional chemical disinfectants. The use of free ozone, chlorine and chloramines for disinfection of drinking water is effective, but these react with various compounds in natural water, forming harmful disinfection by-products; of which, most of the disinfection by-products are carcinogenic [202]. Furthermore, elevated temperatures lead to re-colonization of microbes in water bodies, therefore presenting the need for hyperchlorination. Whilst this prolongs bacteria inactivation, the elevated chlorine concentrations accelerate corrosion in water pipes and increased concentrations of carcinogenic by-products [203-204]. The resistance of some pathogens leads to an increase in dosage of chemicals used for disinfection, thus increasing the formation of disinfection by-products [200]. Also, the lack in basic water treatment, leads to the contamination of natural water sources, mostly in developing countries [64].

### 1.5.3 Silver and copper-based disinfection agents

The challenge to disinfect water without forming unsafe disinfection by-products, has led to the exploration of alternative disinfection methods and technologies. An attractive alternative is antimicrobial surfaces, whereby water comes into contact with the surface rather than the disinfectant coming into contact with the water [205]. Such studies include incorporation of metals such as silver and copper nanoparticles in various supports or chemical modification of the supports using quaternary amine compounds, for bacteria inactivation [206]. Silver and copper have been used in different supports, either as single metals or in binary systems. The toxicity of heavy metals to bacteria is as follows: Ag >Hg >Cu >Cd >Cr >Pb >Co >Au >Zn >Fe >Mn >Mo >Sn [207]. The smaller size and high surface-to-volume ratio of nanoparticles induces antimicrobial activity through the enhancement of interaction between the microbes and nanoparticles. This, in turn, leads to broad-spectrum bactericidal properties and activity [208].

#### *1.5.3.1 Silver*

For centuries, silver has been in use as an antimicrobial agent for wound care and burns. Silver was also used for drinking water as early as 1000 B.C. [10]. Graphene oxide (GO) nanosheets have also been used as supports for silver nanoparticles (AgNPs) in water disinfection applications. Song *et al* 2016[209], synthesised GO-Ag nanocomposites by reducing $AgNO_3$ with ammonium formate ($HCOONH_4$) in a GO suspension, for the inactivation of *E. coli* and *S. aureus* in aqueous media. It was deduced that Ag ions were released from the AgNPs, thus being the main substance to inactivate the bacteria cells [210]. Sun *et al* 2015 [199], prepared GO-AgNPs via chemical and thermal reduction of $AgNO_3$ onto GO using the modified Turkevich method. Commercial membranes were then coated with the resultant GO-AgNPs composites. The presence of the nanocomposite enhanced the hydrophilicity of the membrane and 86% *E. coli* cells were inactivated 2 h of being in contact with the modified membrane. The membrane also reduced biofouling during the disinfection process [199]. AgNPs have also been affixed on polymer surfaces or matrices for water disinfection. Gangadharan *et al* 2010 [210], modified methacrylic acid copolymer resin beads with AgNPs via chemical reduction. Upon coating the resin beads with AgNPs, the beads showed antimicrobial activity towards gram-positive and gram-negative bacterial strains (*E. coli*, *P. aeruginosa*, *B. subtilis*, and *S. aureus*) [210]. The formation of biofilms was not observed, thus making them suitable for water disinfection. More recently, $Ag/Al_2O_3$ spheres were synthesised, whereby Ag was impregnated in commercially available γ-alumina spheres (Sasol, code 604130). The spheres were then calcined at 400°C. The spheres exhibited antimicrobial properties towards *E. coli* and *E. feacalis*, after being applied in semi-batch mode [211].

#### *1.5.3.2 Copper*

The use of copper in healthcare settings has gained attention in the past 7 years. Hospital trials have shown that copper did reduce the bacterial count [212]. Cu has been long been used as a bactericide, fungicide, algaecide and antiviral agent. Cu has also been used in water purification applications [190,213]. The ability of copper to change alternate the Cu(I) and Cu(II) oxidation states, makes it superior to other metals [214]. Studies of copper-based nanocomposites have been considerably less than those of silver-based nanocomposites. This is due to the minimal availability of knowledge concerning copper antimicrobial effects [215]. Polyanaline-copper (PANI-Cu) nanocomposites were prepared via oxidative polymerization in methanol. The CuNPs were formed *in situ*, during the formation of PANI, and where distributed throughout the polymer matrix. Copper chloride was used as the oxidant, thus the reduction took place *in situ*. The nanocomposites were used against *E.coli*, *S. aureus*, and *C. albicans* [214]. Cellulose-copper nanocomposites were prepared by the reduction of Cu onto cellulose fibres, using sodium borohydride and sodium hydroxide solutions, whilst sodium citrate was used as a stabilising agent. The prepared nanocomposites were successfully tested against *S. aureus* and *K. pneumoniae* [216]. Grace and colleagues 2009, prepared copper nanoparticles loaded alginate cotton cellulose (Cu-CACC) fibers. The cotton cellulose fibres were first functionalised with sodium alginate. Thereafter, they were subjected to a cuprous sulfate solution, which was further reduced to CuNPs using sodium borohydride. These nanocomposites showed antibacterial activity towards *E. coli*. [217].

An antimicrobial polymer hybrid nanocomposite, containing copper, was developed by Weickmann et al, 2005. Bentonite-supported CuNPs were prepared via the electroless copper plating process; using palladium (Pd) catalysed metallisation. Firstly, Pd-supported bentonite was prepared by through cation exchange, followed by reducing the Pd with hydrazinium hydrate. The bentonite-supported Pd was subjected to a poly-methyl methacrylate latex suspension, then further treated with an electroless plating bath containing distilled water, copper sulfate, potassium sodium tartrate and formaldehyde. The resultant PMMA/bentonite/copper nanocomposite exhibited antimicrobial properties against *S. aureus* [218]. CuNPs were supported by poly-l-lysine-modified reduced graphene oxide (PLL-rGO) for the inactivation of *E. coli* and *S. aureus* [219]. Copper nitrate was reduced to form CuNPs on PLL-rGO using hydrazine monohydrate at 85°C. The resultant material was proven to have antimicrobial properties and was able to keep the CuNPs stable.

### 1.5.4 Binary systems of silver and copper impregnation

Ruparelia and colleagues suggested that the use of copper/silver combined systems would be of great advantage towards complete bactericidal effects in a multi-bacterial strain sample; especially because of possible strain specificity of the two metals [220]. Aqueous solutions of copper and silver were also used as bactericidal agents in bandages. The bandages were submerged in solutions of $AgNO_3$ and $Cu_2SO_4$ (copper sulphate) and reduced to form NPs via heat treatment at 200°C (through ironing) [221]. Biswas and Bandyopadhaya 2017 [222], prepared Ag-AC and Cu-AC separately, and then (Biswas&Bandyopadhyaya, 2017) mixed the prepared materials together at a ratio of 50:50. The metallic NPs were prepared individually and then impregnated onto the plasma-treated AC. It was then reported that a synergistic approach yielded better performance than when Ag-AC and Cu-AC were applied individually [222]. Recently, Ag-NP decorated CuO nanowires, co-modified 3-D copper foam were developed for disinfection of *S. aureus* and *E. coli* through electroporation. CuO nanowires were grown on Cu foam in a mixture of sodium hydroxide and ammonium thiosulfate, and reduced at 180°C through the oxidation process. AgNPs were electroplated on the nanowires and further subjected to heat at 180°C [223]. Perdikaki and co-workers prepared metal ion and metal nanoparticle graphene hybrids with Ag and Cu. The metal-ion graphene hybrids were prepared by contacting graphene with metal ion (Cu and Ag) solutions and mixed under sonication for an hour. Metal-nanoparticle graphene hybrids were prepared for comparison purposes, whereby metal-ion solutions were mixed with graphene and further reduced using *N*,*N*-dimethylformamide for Ag (60°C) and potassium borohydride for Cu (100°C). The bi-metallic Ag/CuNP-graphene hybrids were successively prepared by mixing the two metal-nanoparticle hybrids. The bi-ionic and bi-metallic hybrids exhibited superior antimicrobial properties compared to the mono-ionic and mono-metallic graphene hybrids [224].

### 1.5.5 Fixed-bed column studies for water disinfection

The efficiency AgNP-coated polystyrene resin bead was also proven in continuous flow fixed-bed column studies by Mthombeni *et al* 2012 [225], where *E. coli* was inactivated in synthetic, river and groundwater [225]. In another study, a cation exchange resin ($R^-H^+$) was coated with AgNPs for the inactivation of *E. coli*, *Salmonella typhimurium*, *Shigella dysenteriae* and *Vibrio cholerae* in groundwater. The resin was first coated with a silver-amine complex to form $[R\text{-}Ag(NH_3)_2]$, followed by heating at 150°C to form $[R(Ag_2O)]^-H^+$ and subsequently reduced using sodium borohydride to form an AgNP-coated resin, $[R(Ag^0)]^-H^+$ [226]. Bharti *et al* 2019 [227] immobilised AgNPs on glass capillary tubes for *E. coli* disinfection in a continuous flow fixed bed reactor. AgNPs were prepared by the addition of $AgNO_3$ (dropwise) into a premixed trisodium citrate and sodium borohydride solution, at applied temperatures of 60 and 90°C. The glass capillary tubes were functionalised with amine groups, in a separate procedure [227], and incubated overnight in the AgNPs suspension [228]. Motshekga and Ray 2017,[229] supported Ag and zinc oxide (ZnO) NPs onto chitosan-bentonite composites for the inactivation of *E. coli* in synthetic and river water samples, using fixed-bed column studies. Acid-treated bentonite clay was mixed with $AgNO_3$ and heated in a microwave reactor at 500 W80°C, whilst ZnO NPs were calcined at 500°C. The resultant Ag-clay composite was then mixed with ZnO NPs in distilled water and heated in a microwave reactor at 500 W and 60°C. The chitosan solution was then added to the Ag/ZnO-clay nanoparticle suspension to form the Ag/ZnO-bentonite-chitosan nanocomposites [229].

Biswas and Bandyopadhyaya 2016 [230] synthesised AC-supported AgNPs. The AgNPs were synthesised using $AgNO_3$ as a precursor mixed with trisodium citrate under UV irradiation. Trisodium citrate was used as a reducing and capping agent. After the formation of AgNPs, plasma-treated AC was then submerged in the AgNP suspension and mixed overnight [230]. Bandyopadhaya *et al* 2008 [231] designed a water filtration system, whereby 50 L of tap water were filtered via gravity at 50 mL/min, daily. The filter was made of granulated activated carbon decorated with AgNPs (Ag-GAC). The nanocomposite was prepared by soaking granulated activated carbon (GAC) powder in a predetermined amount of $AgNO_3$, and thereafter, chemical reduction to form AgNPs was carried out using sodium borohydride [231].

The performance of various disinfection materials in continuous flow studies is expressed in Table 1-8.

**Table 1-8: Comparison of continuous flow microbial inactivation**

| Type of material/ support | Inactivated species | Species conc. (CFU/mL) | Flowrate (mL/min) | Bed mass (g) | water source/type | Breakthrough time (h) | Treated volume (L) | Reference |
|---|---|---|---|---|---|---|---|---|
| AgNPs-Resin | *E. coli* | $6 \times 10^3$ | 2 | 15 | Synthetic and groundwater | 60 | 7.2 | [225] |
| AgNPs-Capillary tubes | *E. coli* | $1 \times 10^3$ | 5 | 0.00124 (Ag loading) | Tap water | 251 | 75 | [227] |
| Ag-ZnO chitosan-bentonite (Cts-Bent) composite | *E. coli* | $5 \times 10^3$ | 5 | 15 | Synthetic and river | 19 | 5.7 | [229] |
| AgNPs-coated resin | *E. coli*,<br>*S. typhimurium*,<br>*S. dysenteriae* and<br>*V. cholerae* | $1 \times 10^3$ | 2 | 15 | Groundwater | 60 | 7.2 | [230] |
| AgNPs-AC | *E. coli* | $1 \times 10^4$ | 26.7* | - | Synthetic water | 6* | 9.8* | [230] |
| AgNPs-GAC | *E. coli* | $1 \times 10^3$ | 50 | 5 | Tap water | 192 | 350 | [231] |

* Calculated according to data received

The manner in which bacteria are inactivated during disinfection is still unclear [232-233], however there are a number of possible ways in which the bacteria are lysed by the heavy metal ions (Scheme 1-4) and are as follows:

- The positively charged ions interact with the negatively charged bacterial cell wall, which disintegrates the membrane. This leads of denaturation of proteins and eventually the cell dies [215,234].
- The metal ions are thiophilic, thus they bind to the sulfur groups on the iron-sulfur dehydratase enzymes. This process disrupts the metabolism of the bacteria [215,235].
- Metal ions activate the autolytic enzymes in the cell, thus leading to lesions which result in cell death [215,236].
- The metal ions inhibit the respiratory enzymes, which leads to the generation of oxygen reactive species (ROS) thereby damaging the cell itself [215,237].

### Proposed mechanism of disinfection

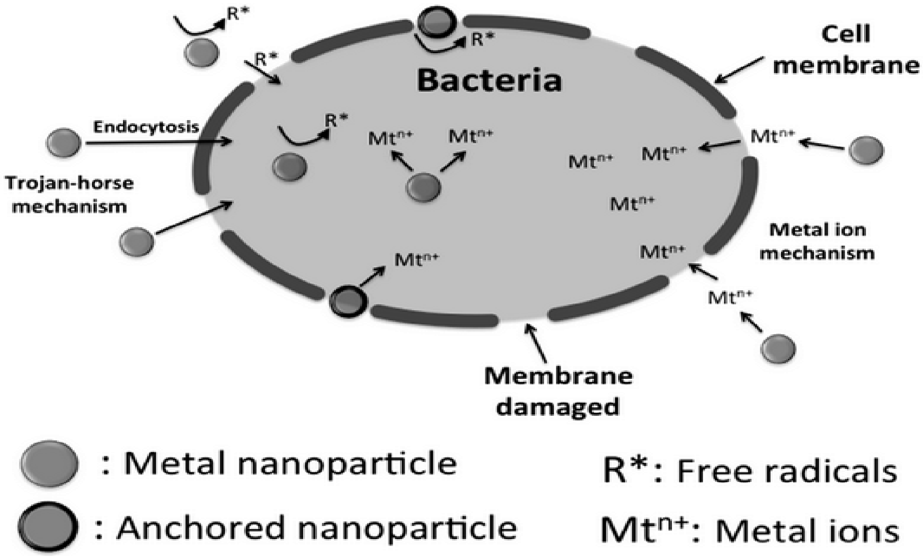

**Scheme 1-4: A schematic representation of possible mechanisms for antimicrobial activity due to free and supported metal ions and metal nanoparticles [215].**

## 1.6 SUMMARY

Anthropogenic activities have led to increased release of heavy metals to natural water resources. Amongst various technologies, adsorption has come out as the most desirable technique for heavy metal remediation. Very few literature reports on the use of adsorbents at a metal ion solutions natural pH, the pH is adjusted to fit the optimal adsorption conditions for the specific adsorbent materials.

In metallic nanomaterials, nanosized metal oxides have emerged as materials of great interest amongst researchers because of their superior fluoride uptake capacities along with faster adsorption kinetics. Nevertheless, some technical bottlenecks associated with the use of nanosized metal oxides need to be resolved, prior to their practical application in water defluoridation. For instance, NMOs are highly prone to agglomeration in aqueous solution and thus lose their activity resulting in lower adsorption capacity. Additionally, due to their fine particle size, they clog the filter pores and thus separation of spent NMOs from aqueous solution becomes one of the most gruelling tasks. Likewise, NMOs also generate excessive pressure drop when applied to column setups.

Also, the spent adsorbents contain enriched concentrations of heavy metals, thus requiring specialised disposal. The spent adsorbents that are regenerated require the use of more chemical reagents, leading to secondary waste generation. Until recently, very little work has been done to reuse and repurpose spent adsorbents. Also,   silver and copper are well-known metals for disinfection applications, thus making them attractive disinfectants in various applications. The incorporation or impregnation of silver and copper onto various supports was achieved by chemical and or thermal reduction of the precursor metal salts ($AgNO_3$ and $CuCl_2$). This entails the use of elevated temperatures, reducing agents and complex procedures which involve numerous washing steps. These processes would prove costly in terms of energy consumption and also time-consuming. Also, specialised reactors would be required for bulk manufacturing of these nanomaterials.  It was however, eminent that the antimicrobial activity of the reviewed nanocomposites and materials was indeed due to the incorporated metal ions (silver and copper).

Multi-functional systems or nanocomposites such as magnetic nanoparticles coated with functionalised shells can potentially provide more opportunities in ensuring that water security is achieved. Also, numerous studies have focussed on developing materials for pathogen removal and inactivation, whilst testing the materials using the disk diffusion method or batch method. However, very few continue to test the developed materials in water disinfection and real field applications. There are fewer commercially available copper nanoparticle-based products and this might provide an opportunity to instigate the commercialisation of copper nanoparticle-based products, starting with the development thereof.

## 1.7 REFERENCES

[1] South, African, National, Biodiversity, Institute, (SANBI), January 2014, 2014-last update, climate change and the water sector. Available: http://www.sanbi.org/sites/default/files/documents/documents/ltas-factsheetclimate-change-and-water-sector2013.pdf [20 JULY, 2016].

[2] S. De Gisi, G. Lofrano, M. Grassi, M. Notarnicola. Characteristics and adsorption capacities of low-cost sorbents for wastewater treatment: A review. Sustainable Mater. Technol. 9, 2016, 10-40.

[3] N.K. Srivastava, C.B. Majumder. Novel biofiltration methods for the treatment of heavy metals from industrial wastewater. J. Hazard. Mater. 151(1), 2008, 1-8.

[4] V. Masindi, K.L. Muedi. Environmental contamination by heavy metals. Heavy Metal. 2018, 10,115-32.

[5] M. Yadav, R. Gupta, R.K. Sharma. Green and sustainable pathways for wastewater purification. *Advances in Water Purification Techniques.* Elsevier, 2019, 355-383.

[6] W. H. O. 2011. Guidelines for Drinking-water Quality. *WHO chronicle,* **38**, pp. 104-108.

[7] US EPA, 28 FEBRUARY 2019, 2019-last update, Drinking Water Regulations and Contaminants | Regulation Development for Drinking Water Contaminants | US EPA. Available: 9. https://www.epa.gov/dwstandardsregulations/secondary-drinking-water-standards-guidance-nuisance-chemicals/ [October 2018, 2018].

[8] D. Michaud, 22 February 2016, 2016-last update, Chemistry Enrichment of Silver Deposits [Homepage of 911 Metallurgist], [Online]. Available: https://www.911metallurgist.com/blog/chemistry-enrichment-silver-deposits [July, 19, 2019].

[9] W. Nitayaphat, T. Jintakosol Removal of silver (I) from aqueous solutions by chitosan/bamboo charcoal composite beads. *J. Cleaner Production,* **87** 2015, 850-855.

[10] R.J. White, An historical overview of the use of silver in wound management. *British Journal of Nursing,* **10**(Sup4), 2001, S3-S8.

[11] A.D. Maynard, R.J. Aitken, T. Butz, V. Colvin, K. Donaldson, G. Oberdörster, M.A. Philbert, J. Ryan, A. Seaton, V. Stone, S.S. Tinkle. Safe handling of nanotechnology. Nature. 444(7117), 2006, 267-9.

[12] M.E. Vance, T. Kuiken, E.P. Vejerano, S.P. McGinnis, M.F. Hochella Jr, D. Rejeski, M.S. Hull. Nanotechnology in the real world: Redeveloping the nanomaterial consumer products inventory. Beilstein journal of nanotechnology. 6(1), 2015, 1769-80.

[13] D.A. Scheufele, E.A. Corley, S. Dunwoody, T.J. Shih, E. Hillback, D.H. Guston. Scientists worry about some risks more than the public. Nature nanotechnology. 2(12), 2007, 732-4.

[14] M.M. Shafer, J.T. Overdier, D.E. Armstrong. Removal, partitioning, and fate of silver and other metals in wastewater treatment plants and effluent-receiving streams. Environmental Toxicology and Chemistry: An International Journal. 17(4), 1998, 630-41.

[15] A.B. Lansdown. Silver in health care: antimicrobial effects and safety in use. In Biofunctional textiles and the skin 2006 (Vol. 33, pp. 17-34). Karger Publishers.

[16] N.S. Tomi, B. Kränke, W. Aberer. A silver man. The Lancet. 363, 2004 (9408), 532. *Lancet (London, England),* **363**(9408), pp. 532-6736(04)15540-2.

[17] S.H. Gulbranson, J.A. Hud, R.C. Hansen. Argyria following the use of dietary supplements containing colloidal silver protein. CUTIS-NEW YORK-. 66(5), 2000, 373-8.

[18] P.L. Drake, K.J. Hazelwood. Exposure-related health effects of silver and silver compounds: a review. The Annals of occupational hygiene. 49(7), 2005, 575-85.

[19] Wikipedia Contributors, 18 July 2019, 2019-last update, Copper [Homepage of Wikipedia, The Free Encyclopedia.], [Online]. Available: https://en.wikipedia.org/w/index.php?title=Copper&oldid=906787018 [August, 5, 2019].

[20] V. Aguirregabiria, A. Luengo. A microeconometric dynamic structural model of copper mining decisions. Unpublished manuscript, Department of Economics, University of Toronto. 2016 Mar 30.

[21] R. Schmuhl, H.M. Krieg, K. Keizer. Adsorption of Cu (II) and Cr (VI) ions by chitosan: Kinetics and equilibrium studies. Water Sa.; 27(1), 2001, 1-8.

[22] D.G. Barceloux, D. Barceloux. Copper. J. Toxicology: Clinical Toxicol. 37(2), 1999, 217-30.

[23] T. Theophanides, J. Anastassopoulou. Copper and carcinogenesis. Critical reviews in oncology/hematology. 42(1), 2002, 57-64.

[24] B. Halliwell, J.M. Gutteridge. [1] Role of free radicals and catalytic metal ions in human disease: an overview. InMethods in enzymology 1990 (Vol. 186, pp. 1-85). Academic Press.

[25] S.D. Aust, L.A. Morehouse, C.E. Thomas. Role of metals in oxygen radical reactions. Journal of free radicals in biology & medicine. 1(1), 1985, 3-25.

[26] Q. Wang, D. Kim, D. D. Dionysiou, G. A. Sorial, D. Timberlake. Sources and Remediation for Mercury Contamination in Aquatic Systems-a Literature Review. *Environ. Pollut. 131,* **2004**, 323-336.

[27] J. E. Jung, D. M. Geatches, K. Lee, S. Aboud, G. E. Brown Jr. J. Wilcox, First-principles investigation of mercury adsorption on the α-$Fe_2O_3$(1102) Surface. *J. Phys. Chem. C. 119*, **2015**, 26512-26518.

[28] G. Bayramoğlu, M. Y. Arica. Kinetics of Mercury ions removal from synthetic aqueous solutions using by novel magnetic p(GMA-MMA-EGDMA) Beads. *J. Hazard. Mater. 144*, **2007,** 449-457.

[29] V. Chandra, K. S. Kim. Highly selective adsorption of $Hg^{2+}$ by a Polypyrrole-reduced graphene oxide composite. *Chem. Commun.*, *47*, **2011,** 3942-3944.

[30] S. Jagtap, M.K. Yenkie, N. Labhsetwar, S. Rayalu, Fluoride in drinking water and defluoridation of water, Chem. Rev. 112 (2012) 2454-2466.

[31] M.G. García, L. Borgnino, CHAPTER 1. Fluoride in the Context of the Environment, in: n.d.: pp. 3-21.

[32] K. Yang, X. Liang, Fluoride in Drinking Water : Effect on Liver and Kidney Function, (2011) 769-775.

[33] F. Akbal, S. Camcı. Copper, chromium and nickel removal from metal plating wastewater by electrocoagulation. Desalination. 269(1-3), 2011, 214-22.

[34] F. Fu, Q. Wang. Removal of heavy metal ions from wastewaters: a review. Journal of environmental management. 92(3), 2011, 407-18.

[35] T.A. Kravchenko, L.L. Polyanskiy, V.A. Krysanov, E.S. Zelensky, A.I. Kalinitchev, W.H. Hoell. Chemical precipitation of copper from copper-zinc solutions onto selective sorbents. Hydrometallurgy. 95(1-2), 2009, 141-4.

[36] T.A. Kurniawan, G.Y. Chan, W.H. Lo, S. Babel. Physico-chemical treatment techniques for wastewater laden with heavy metals. Chemical engineering journal. 118(1-2), 2006, 83-98.

[37] O.B. Akpor, M. Muchie. Remediation of heavy metals in drinking water and wastewater treatment systems: Processes and applications. International Journal of Physical Sciences. 5(12), 2010, 1807-17.

[38] J.L. Huisman, G. Schouten, C. Schultz. Biologically produced sulphide for purification of process streams, effluent treatment and recovery of metals in the metal and mining industry. Hydrometallurgy. 83(1-4), 2006, 106-13.

[39] C.P. Gomes, M.F. Almeida, J.M. Loureiro. Gold recovery with ion exchange used resins. Separation Purification Technol. 24(1-2), 2001, 35-57.

[40] F.J. Desilva. The ion exchange deal. *Chem. Eng.* **101**(7), 86, 1994.

[41] S. Virolainen, M. Tyster, M. Haapalainen, T. Sainio. Ion exchange recovery of silver from concentrated base metal-chloride solutions. Hydrometallurgy. 152, 2015, 100-6.

[42] C. Cobzaru, V. Inglezakis. Ion exchange. In progress in filtration and separation 2015, (pp. 425-498). Academic Press.

[43] J. Mulwanda, C. Dorfling. Recovery of dissolved platinum group metals from copper sulphate leach solutions by precipitation. Minerals Eng. 80, 2015, 50-6.

[44] M.M. Benjamin, D.F. Lawler. Water quality engineering: Physical/chemical treatment processes. John Wiley & Sons, 2013 Jul 1.

[45] M. Graff. Disposal of metalworking fluids. *Metalworking Fluids (MWFs) for Cutting and Grinding.* Elsevier, 2012, 389-402.

[46] R.Y. Ning. Arsenic removal by reverse osmosis. Desalination. 143(3), 2002, 237-41.

[47] C.S. Slater, R.C. Ahlert, C.G. Uchrin. Applications of reverse osmosis to complex industrial wastewater treatment. Desalination. 48(2), 1983, 171-87.

[48] D.E. Speed. Environmental aspects of planarization processes. InAdvances in Chemical Mechanical Planarization (CMP) 2016, (pp. 229-269). Woodhead Publishing.

[49] R. Epsztein, O. Nir, O. Lahav, M. Green. Selective nitrate removal from groundwater using a hybrid nanofiltration-reverse osmosis filtration scheme. Chem. Eng. J. 279, 2015, 372-8.

[50] H. Koseoglu, M. Kitis. The recovery of silver from mining wastewaters using hybrid cyanidation and high-pressure membrane process. Minerals Engineering. 22(5), 2009, 440-4..

[51] E. Samper, M. Rodríguez, M.A.D. De la Rubia, Prats. Removal of metal ions at low concentration by micellar-enhanced ultrafiltration (MEUF) using sodium dodecyl sulfate (SDS) and linear alkylbenzene sulfonate (LAS). Separation and purification technology. 65(3), 2009, 337-42.

[52] J. Rouquerol, F. Rouquerol, P. Llewellyn, G. Maurin, K.S. Sing. Adsorption by powders and porous solids: principles, methodology and applications. Academic press; 2013 Sep 6.

[53] M.L. Cantuaria, A.F. de Almeida Neto, E.S. Nascimento, M.G. Vieira. Adsorption of silver from aqueous solution onto pre-treated bentonite clay: complete batch system evaluation. Journal of Cleaner Production. 2016, 112, 1112-21.

[54] Bhatnagar, W. Hogland, M. Marques, M. Sillanpää. An overview of the modification methods of activated carbon for its water treatment applications. Chemical Engineering Journal. 2013, 219, 499-511.

[55] Ali, M. Asim, T.A. Khan. Low cost adsorbents for the removal of organic pollutants from wastewater. Journal of environmental management. 113, 2012, 170-83.

[56] F. Fu, Q. Wang. Removal of heavy metal ions from wastewaters: a review. Journal of environmental management. 92(3), 2011, 407-18.

[57] F.N. Acar, Z. Eren. Removal of Cu (II) ions by activated poplar sawdust (Samsun Clone) from aqueous solutions. Journal of hazardous materials. 137(2): 2006, 909-14.

[58] A.F. Almeida Neto, M.G. Vieira, M.G. Silva. Cu (II) adsorption on modified bentonitic clays: different isotherm behaviors in static and dynamic systems. Materials Research. 15(1), 2012, 114-24.

[59] J. Kammerer, R. Carle, D.R. Kammerer. Adsorption and ion exchange: basic principles and their application in food processing. Journal of agricultural and food chemistry. 59(1), 2011, 22-42.

[60] C.C. Global. Institute, $CO_2$ Capture Technologies: Post combustion capture (PCC). Australia: Global CCS Institute; 2012.

[61] S.D. Faust, O.M. Aly. Adsorption processes for water treatment. Elsevier; 2013 Oct 22.

[62] H.N. Tran, S.J. You, A. Hosseini-Bandegharaei, H.P. Chao. Mistakes and inconsistencies regarding adsorption of contaminants from aqueous solutions: a critical review. Water research. 120, 2017, 88-116.

[63] E. Worch. Adsorption technology in water treatment: fundamentals, processes, and modeling. Walter de Gruyter, 2012 Aug 31.

[64] X. Qu, P.J. Alvarez, Q. Li. Applications of nanotechnology in water and wastewater treatment. Water research. 47(12), 2013, 3931-46.

[65] Dhasmana, S. Firdaus, K.P. Singh, S. Raza, Q.M. Jamal, K.K. Kesari, Q. Rahman, M. Lohani. Nanoparticles: Applications, toxicology and safety aspects. InPerspectives in Environmental Toxicology 2017 (pp. 47-70). Springer, Cham.

[66] N. Sharma, S. Singh, N. Kanojia, A.S. Grewal, S. Arora. Nanotechnology: a modern contraption in cosmetics and dermatology. Applied Clinical Research, Clinical Trials and Regulatory Affairs. 5(3), 2018, 147-58.

[67] S. Ali, S. Rasheed, I. Hassan, S. Rashid. Role of nanotechnology in medicine and cancer treatment.

[68] G. Pandey, D. Rawtani, Y.K. Agrawal. Aspects of nanoelectronics in materials development. InNanoelectronics and Materials Development 2016 Jul 27. IntechOpen.

[69] Street, R. Sustich, J. Duncan, N. Savage, editors. Nanotechnology applications for clean water: solutions for improving water quality. William Andrew; 2014 May 15.

[70] Ahsan, A.F. Ismail, editors. Nanotechnology in Water and Wastewater Treatment: Theory and Applications. Elsevier; 2018 Nov 15.

[71] M.I. Hussein, M.I. Shekfa, Y. Haik. Pathogen detection using single tunnel junction sensor (STJ) with magnetic nano particles. In2012 International Conference on Electromagnetics in Advanced Applications 2012 Sep 2 (pp. 83-86). IEEE.

[72] M. Zahid, N. Nadeem, M.A. Hanif, I.A. Bhatti, H.N. Bhatti, G. Mustafa. Metal ferrites and their graphene-based nanocomposites: synthesis, characterization, and applications in wastewater treatment. InMagnetic Nanostructures 2019 (pp. 181-212). Springer, Cham.

[73] S. Linley, T. Leshuk, F.X. Gu. Magnetically separable water treatment technologies and their role in future advanced water treatment: a patent review. Clean-Soil, Air, Water. 41(12), 2013, 1152-6.

[74] J. Singh, M. Srivastava, J. Dutta, P.K. Dutta. Preparation and properties of hybrid monodispersed magnetic α-$Fe_2O_3$ based chitosan nanocomposite film for industrial and biomedical applications. International Journal of Biological Macromolecules. 2011, 48(1), 170-6.

[75] S. Pal, E.C. Alocilja. Electrically active polyaniline coated magnetic (EAPM) nanoparticle as novel transducer in biosensor for detection of Bacillus anthracis spores in food samples. Biosensors and Bioelectronics. 24(5), 2009, 1437-44.

[76] J.M. Coey. *Magnetism and magnetic materials.* Cambridge University press 2010.

[77] R.C. O'handley. Modern magnetic materials: principles and applications. Wiley 2000.

[78] Jeong, A. Gutowska. Lessons from nature: stimuli-responsive polymers and their biomedical applications. TRENDS in Biotechnol. 20(7), 2002, 305-11.

[79] R.M. Cornell, U. Schwertmann. The iron oxides: structure, properties, reactions, occurrences and uses. John Wiley & Sons; 2003 Oct 17.

[80] U. Jeong, X. Teng, Y. Wang, H. Yang, Y. Xia. Superparamagnetic colloids: controlled synthesis and niche applications. Adv. Mater. 19(1), 2007, 33-60.

[81] H. Wang, X. Yuan, Y. Wu, X. Chen, L. Leng, H. Wang, H. Li, G. Zeng. Facile synthesis of polypyrrole decorated reduced graphene oxide-$Fe_3O_4$ magnetic composites and its application for the Cr (VI) removal. Chemical Engineering Journal. 262, 2015, 597-606.

[82] A.H. Lu, E.E. Salabas, F. Schüth. Magnetic nanoparticles: synthesis, protection, functionalization, and application. Angewandte Chemie International Edition. 46(8), 2007, 1222-44.

[83] E. Karaoğlu, A. Baykal, H. Deligöz, M. Şenel, H. Sözeri, M.S. Toprak. Synthesis and characteristics of poly (3-pyrrol-1-ylpropanoic acid)(PPyAA)-$Fe_3O_4$ nanocomposite. J. Alloys and compounds. 509(33), 2011, 8460-8468.

[84] J. Deng, Y. Peng, C. He, X. Long, P. Li, A.S. Chan. Magnetic and conducting $Fe_3O_4$-polypyrrole nanoparticles with core-shell structure. *Polym. Int.* **52**(7), 2003, 1182-1187.

[85] Maity, D.C. Agrawal. Synthesis of iron oxide nanoparticles under oxidizing environment and their stabilization in aqueous and non-aqueous media. Journal of Magnetism and Magnetic Materials. 308(1), 2007, 46-55.

[86] S. Santra, R. Tapec, N. Theodoropoulou, J. Dobson, A. Hebard, W. Tan. Synthesis and characterization of silica-coated iron oxide nanoparticles in microemulsion: the effect of nonionic surfactants. Langmuir. 17(10), 2001, 2900-6.

[87] L. Zhang, G. Zhang, S. Wang, J. Peng, W. Cui. Sulfoethyl functionalized silica nanoparticle as an adsorbent to selectively adsorb silver ions from aqueous solutions. Journal of the Taiwan Institute of Chemical Engineers. 71, 2017, 330-7.

[88] X. Zhang, J. Qian, B. Pan. Fabrication of novel magnetic nanoparticles of multifunctionality for water decontamination. Environ. Sci. Technol. 50(2), 2016, 881-889.

[89] F.Y. Cheng, C.H. Su, Y.S. Yang, C.S Yeh, C.Y. Tsai, C.L. Wu, M.T. Wu, D.B. Shieh. Characterization of aqueous dispersions of $Fe_3O_4$ nanoparticles and their biomedical applications. *Biomaterials,* **26**(7), 2005, 729-738.

[90] F.A. Harraz, A.A. Ismail, S.A. Al-Sayari, A. Al-Hajry. Novel α-$Fe_2O_3$/polypyrrole nanocomposite with enhanced photocatalytic performance. Journal of Photochemistry and Photobiology A: Chemistry. 299, 2015, 18-24.

[91] K.E. Greenstein, N.V. Myung, G.F. Parkin, D.M. Cwiertny. Performance comparison of hematite (α-$Fe_2O_3$)-polymer composite and core-shell nanofibers as point-of-use filtration platforms for metal sequestration. *Water research,* **148**, 2019, 492-503.

[92] Fan, K. Li, J. Li, D. Ying, Y. Wang, J. Jia. Comparative and competitive adsorption of Pb (II) and Cu (II) using tetraethylenepentamine modified chitosan/$CoFe_2O_4$ particles. J. Hazard. Mater. 326, 2017, 211-20.

[93] Y. Zhang, T. Yan, L. Yan, X. Guo, L. Cui, Q. Wei, B. Du. Preparation of novel cobalt ferrite/chitosan grafted with graphene composite as effective adsorbents for mercury ions. Journal of Molecular Liquids. 198, 2014, 381-7.

[94] S. Jauhar, J. Kaur, A. Goyal, S. Singhal. Tuning the properties of cobalt ferrite: a road towards diverse applications. RSC Adv. 6(100), 2016, 97694-719.

[95] M. Zahid, N. Nadeem, M.A. Hanif, I.A. Bhatti, H.N. Bhatti, G. Mustafa. Metal ferrites and their graphene-based nanocomposites: synthesis, characterization, and applications in wastewater treatment. InMagnetic Nanostructures 2019 (pp. 181-212). Springer, Cham.

[96] L.P. Lingamdinne, Y.L. Choi, I.S. Kim, J.K. Yang, J.R. Koduru, Y.Y. Chang. Preparation and characterization of porous reduced graphene oxide based inverse spinel nickel ferrite nanocomposite for adsorption removal of radionuclides. J. Hazard Mater. 326, 2017, 145-56.

[97] S. Agrawal, N.B. Singh. Removal of toxic hexavalent chromium from aqueous solution by nickel ferrite-polyaniline nanocomposite. Desalination and Water Treatment. 57(38), 2016, 17757-66.

[98] Sharma, Z.M. Siddiqi, D. Pathania. Adsorption of polyaromatic pollutants from water system using carbon/ZnFe2O4 nanocomposite: equilibrium, kinetic and thermodynamic mechanism. J. Molecular Liquids. 240, 2017, 361-71.

[99] Karamipour, N. Rasouli, M. Movahedi, H. Salavti. A kinetic study on adsorption of congo red from aqueous solution by ZnO-$ZnFe_2O_4$-polypyrrole magnetic nanocomposite. Phys. Chem. Res. 4(2), 2016, 291-301.

[100] D.H.K. Reddy, and S. Lee. Application of magnetic chitosan composites for the removal of toxic metal and dyes from aqueous solutions. Adv. colloid and Interface Sci. 201, 2013, 68-93.

[101] R.D. Ambashta, M. Sillanpaa. Water purification using magnetic assistance: a review. *J. Hazard. Mater.* **180**(1-3), 2010, 38-49.

[102] Mu, L. Zhang, X. Zhang, L. Zhong, Y. Li. Selective adsorption of Ag ( I ) from aqueous solutions using Chitosan/polydopamine@C@ magnetic fly ash adsorbent beads. Journal of hazardous materials. 381, 2020, 120943.

[103] Janacek, L. Kvitek, M. Karlikova, K. Pospiskova, I. Safarik. Removal of silver nanoparticles with native and magnetically modified halloysite. Applied Clay Science. 162, 2018, 10-4.

[104] Y. Ma, D. Xing, Y. Ruan, X. Du, P. La. Fabrication of amino-functionalized magnetic graphene oxide nanocomposites for adsorption of Ag (I) from aqueous solution. *Environ. Eng. Sci.* **35**(3), 2018, 219-230.

[105] J. Jeevanadam, K.J. Klabunde, Synthesis, Properties and applications of oxide nanoparticles adsorbents in J.A. Rodríguez, M Fernández-García, N.J. Whiley: (2007) chapter 14.

[106] J. Lu, D. Liu, J. Hao, G. Zhang, B. Lu, Phosphate removal from aqueous solutions by a nano-structured Fe-Ti bimetal oxide adsorbent, Chem. Eng. Res. Des. 93 (2015) 652-661.

[107] T. Basu, U.C. Gosh, Nano-structured iron (III)-cerium (IV) mixed oxide: synthesis, characterization and arsenic sorption kinetics in the presence of co-existing ions aiming to apply for high arsenic ground water treatment, Appl. Surf. Sci. 283 (2013) 471-481.

[108] M. Hua, S. Zhang, B. Pan, W. Zhang, L. Lv, Q. Zhang, Heavy metal removal from water/wastewater by nanosized metal oxides: a review, J. Hazard. Mater. 211 (2012) 317-331.

[109] A.A. Ismail, A.A. El-Midany, A.I. Ibrahim, H. Matsunaga, Heavy metal removal using $SiO_2$-$TiO_2$ binary oxide: experimental design approach, Adsorption 14 (2008) 21-29.

[110] R.G. Gohari, W.J. Lau, T. Matsuura, A.F. Ismail, Fabrication and characterization of novel PES/Fe-Mn binary oxide UF mixed matrix membrane for adsorptive removal of As(III) from contaminated water solution, Sep. Purif. Technol. 118 (2013) 64-72.

[111] K. Biswas, K. Gupta, A. Goswami, U.C. Ghosh, Fluoride removal efficiency from aqueous solution by synthetic iron(III)-aluminum(III)-chromium (III) ternary mixed oxide. Desalination 255 (2010) 44-51.

[112] X. Wang, G. Zhang, H. Lan, R. Liu, H. Liu, J. Qu, Preparation of hollow Fe-Al binary oxyhydroxide for efficient removal of fluoride ions, Colloids Surf. Physicochem. Eng. Asp.520 (2017) 580-589.

[113] Dilhon, S.K. Soni, D. Kumar, Enhanced fluoride removal performance by Ce-Zn binary metal oxide: Adsorption characteristics and mechanism, J. Fluorine Chem. 199 (2017) 67-76.

[114] Tang, Y. Shu, R. Zhang, X. Li, J. Song, B. Li, Y. Zhang, D. Ou. Comparison of the removal and adsorption mechanisms of cadmium and lead from aqueous solution by activated carbons prepared from Typha angustifolia and Salix matsudana. RSC Adv. 7(26), 2017, 16092-103.

[115] M. Gerard, A. Chaubey, B.D. Malhotra. Application of conducting polymers to biosensors. Biosensors and Bioelectronics. 17(5), 2002, 345-59.

[116] W. Chen, X. Li, G. Xue, Z. Wang, W. Zou. Magnetic and conducting particles: preparation of polypyrrole layer on $Fe_3O_4$ nanospheres. Appl. Surface Sci. 218(1-4), 2003, 216-22.

[117] Weidlich, K.M. Mangold, K. Jüttner. Conducting polymers as ion-exchangers for water purification. Electrochimica Acta. 47(5), 2001, 741-5.

[118] J. Jang. Conducting polymer nanomaterials and their applications. *Emissive Materials Nanomaterials.* Springer, 2006, 189-260.

[119] M. Choi, J. Jang. Heavy metal ion adsorption onto polypyrrole-impregnated porous carbon. Journal of colloid and interface science. 325(1), 2008, 287-9.

[120] Y. Huang, J. Li, X. Chen, X. Wang. Applications of conjugated polymer based composites in wastewater purification. *Rsc Adv.* **4**(107), 2014, 62160-62178.

[121] H.N. Muhammad Ekramul Mahmud, A.K. Huq. The removal of heavy metal ions from wastewater/aqueous solution using polypyrrole-based adsorbents: a review. *Rsc Adv.* **6**(18), 2016, 14778-14791.

[122] H. Eisazadeh. Removal of mercury from water using polypyrrole and its composites. Chinese J. Polym. Sci. 25(04), 2007, 393-97.

[123] H.B. Fredj, S. Helali, C. Esseghaier, L. Vonna, L. Vidal, A. Abdelghani. Labeled magnetic nanoparticles assembly on polypyrrole film for biosensor applications. Talanta. 75(3), 2008, 740-747.

[124] M. Hepel, Z. Xingmin, R. Stephenson, S. Perkins. Use of electrochemical quartz crystal microbalance technique to track electrochemically assisted removal of heavy metals from aqueous solutions by cation-exchange composite polypyrrole-modified electrodes. Microchemical J. 56(1), 1997, 79-92.

[125] E.N. Zare, A. Motahari, M. Sillanpää. Nanoadsorbents based on conducting polymer nanocomposites with main focus on polyaniline and its derivatives for removal of heavy metal ions/dyes: a review. Environ. Res. 162, 2018, 173-95.

[126] K. Dutta, S. De. Aromatic conjugated polymers for removal of heavy metal ions from wastewater: a short review. *Environ. Sci. Water Res. Technol.* **3**(5), 2017, 793-805.

[127] V.V. Tatyana, O.N. Efimov. Polypyrrole: a conducting polymer; its synthesis, properties and applications. *Russian Chem. Rev.* **66**(5), 1997, 443.

[128] Zhou, H. Zhu, Q. Wang, J. Wang, J. Cheng, Y. Guo, X. Zhou, R. Bai. Adsorption of mercury (ii) with an $Fe_3O_4$ magnetic polypyrrole-graphene oxide nanocomposite. *RSC Adv.* **7**(30), 2017, 18466-18479.

[129] P. Kumar, K.B. Ansari, A.C. Koli, V.G. Gaikar. Sorption behavior of thiourea-grafted polymeric resin toward silver ion, reduction to silver nanoparticles, and their antibacterial properties. *Industrial & Eng. Chem. Res.* **52**(19), 2013, 6438-6445.

[130] G. Cakmak, Z. Kucukyavuz, S. Kucukyavuz. Conductive copolymers of polyaniline, polypyrrole and poly (dimethylsiloxane). *Synth. Met.* **151**(1), 2005, 10-18.

[131] X. Yin, J. Long, Y. XI, X. Luo. Recovery of silver from wastewater using a new magnetic photocatalytic ion-imprinted polymer. *ACS Sustain. Chem. Eng.* **5**(3), 2017, 2090-2097.

[132] G. Kiani. High removal capacity of silver ions from aqueous solution onto halloysite nanotubes. *Appl. Clay Sci.* **90**, 2014, 159-164.

[133] M. Akgül, A. Karabakan, O. Acar, Y. Yürüm. Removal of silver (I) from aqueous solutions with clinoptilolite. *Microporous and Mesoporous Mater.* **94**(1), 2006, 99-104.

[134] M.E. Ahamed, X.Y. Mbianda, A.F. Mulaba-Bafubiandi, L. Ion imprinted polymers for the selective extraction of silver (I) ions in aqueous media: Kinetic modeling and isotherm studies. *Reactive and Functional Polym.* **73**(3), 2013, 474-483.

[135] X. Song, P. Gunawan, R. Jiang, S.S. Leong, K. Wang, R. Xu. Surface activated carbon nanospheres for fast adsorption of silver ions from aqueous solutions. *J. Hazard. Mater,* **194**, 2011, 162-168.

[136] R. Ansari, N. Samadi, B. Khodavirdilo. Synthesized Nano Particle Derivation of Poly (Styrene-Alternative-Maleic Anhydride) for the Removal of the Silver (I) Ions From Aqueous Solutions. *Iranian J. Analytical Chem.* **4**(2), 2017, 50-61.

[137] R. Ansari, A.F. Delavar. Sorption of silver ion from aqueous solutions using conducting electroactive polymers. *J. Iranian Chem. Soc.* **5**(4), 2008, 657-668.

[138] S. Wong, N. Ngadi, I.M. Inuwa, O. Hassan. Recent advances in applications of activated carbon from biowaste for wastewater treatment: a short review. J. Cleaner Production. 175, 2018, 361-75.

[139] S. Afroze, T. Sen, M. Ang. Agricultural solid wastes in aqueous phase dye adsorption: a review. *Agricultural wastes: Characteristics, types and management.* Nova Publishers, 2015, 169-213.

[140] M.A. Islam, M.J. Ahmed, W.A. Khanday, M. Asif, B.H. Hameed. Mesoporous activated carbon prepared from NaOH activation of rattan (Lacosperma secundiflorum) hydrochar for methylene blue removal. *Ecotoxicol. and Environ. Safety,* **138**, 2017, 279-285.

[141] Demirbaş. Adsorption of cobalt (II) ions from aqueous solution onto activated carbon prepared from hazelnut shells. *Adsorption Sci. Technol.* **21**(10), 2003, 951-963.

[142] A.E. Ofomaja, E.B. Naidoo, S.J. Modise. Removal of copper (II) from aqueous solution by pine and base modified pine cone powder as biosorbent. J. Hazard. Mater. 168(2-3), 2009, 909-17.

[143] L. Sha, G. Xueyi, F. Ningchuan, T. Qinghua. Adsorption of $Cu^{2+}$ and $Cd^{2+}$ from aqueous solution by mercapto-acetic acid modified orange peel. *Colloids and Surfaces B: Biointerfaces,* **73**(1), 2009, 10-14.

[144] X. Gao, L. Wu, Q. Xu, W. Tian, Z. Li, N. Kobayashi. Adsorption kinetics and mechanisms of copper ions on activated carbons derived from pinewood sawdust by fast $H_3PO_4$ activation. *Environ. Sci. Pollution Res.* **25**(8), 2018, 7907-7915.

[145] Özçimen, A. Ersoy-Meriçboyu. Removal of copper from aqueous solutions by adsorption onto chestnut shell and grapeseed activated carbons. J. Hazard. Mater. 168(2-3), 2009, 1118-25.

[146] M. Kobya, E. Demirbas, E. Senturk, M. Ince. Adsorption of heavy metal ions from aqueous solutions by activated carbon prepared from apricot stone. Bioresource Technol. 96(13), 2005, 1518-21.

[147] H. Demiral, C. Güngör. Adsorption of copper (II) from aqueous solutions on activated carbon prepared from grape bagasse. *J. Cleaner Production,* **124**, pp. 2016, 103-113.

[148] J.D. McSweeny, R.M. Rowell, S.H. Min. Effect of citric acid modification of aspen wood on sorption of copper ion. J. Nat. Fibers. **3**(1), 2006, 43-58.

[149] Demirbas, N. Dizge, M.T. Sulak, M. Kobya. Adsorption kinetics and equilibrium of copper from aqueous solutions using hazelnut shell activated carbon. Chem. Eng. J. 148(2-3), 2009, 480-7.

[150] M.I. Sabela, K. Kunene, S. Kanchi, N.M. Xhakaza, A. Bathinapatla, P. Mdluli, D. Sharma, K. Bisetty. Removal of copper (II) from wastewater using green vegetable waste derived activated carbon: An approach to equilibrium and kinetic study. Arabian J. Chem. 12(8), 2019, 4331-9.

[151] T. Van Thuan, B.T. Quynh, T.D. Nguyen, L.G. Bach. Response surface methodology approach for optimization of $Cu^{2+}$, $Ni^{2+}$ and $Pb^{2+}$ adsorption using KOH-activated carbon from banana peel. Surfaces and Interfaces. 6, 2017, 209-17.

[152] V.K. Gupta, D. Pathania, S. Sharma. Adsorptive remediation of Cu (II) and Ni (II) by microwave assisted $H_3PO_4$ activated carbon. Arabian J. Chem. 10, 2017, S2836-44.

[153] Vences-Alvarez, L.H. Velazquez-Jimenez, L.F. Chazaro-Ruiz, P.E. Diaz-Flores, J.R. Rangel-Mendez, Fluoride removal in water by a hybrid adsorbent lanthanum-carbon, J. Colloid Interface Sci. 455 (2015) 194-202.

[154] L.H. Velazquez-jimenez, R.H. Hurt, J. Matos, J.R. Rangel-mendez, Zirconium-Carbon hybrid sorbent for removal of fluoride from water : oxalic acid mediated Zr(IV) assembly and adsorption mechanism, Environ. Sci. Technol. 48 (2014) 1166-1174.

[155] Y. Yu, C. Wang, X. Guo, J. Paul Chen, Modification of carbon derived from Sargassum sp. by lanthanum for enhanced adsorption of fluoride, J. Colloid Interface Sci. 441 (2015) 113-120.

[156] V. Sivasankar, S. Murugesh, S. Rajkumar, A. Darchen, Cerium dispersed in carbon (CeDC) and its adsorption behavior: A first example of tailored adsorbent for fluoride removal from drinking water, Chem. Eng. J. 214 (2013) 45-54.

[157] M. Angelina Thanga Ajisha, K. Rajagopal, Fluoride removal study using pyrolyzed Delonix regia pod, an unconventional adsorbent, Int. J. Environ. Sci. Technol. 12 (2015) 223-236.

[158] K. Singh, D.H. Lataye, K.L. Wasewar, Removal of fl uoride from aqueous solution by using bael (Aegle marmelos ) shell activated carbon : Kinetic , equilibrium and thermodynamic study, J. Fluor. Chem. 194 (2017) 23-32.

[159] L.H. Velazquez-Jimenez, E. Vences-Alvarez, J.L. Flores-Arciniega, H. Flores-Zuñiga, J.R. Rangel-Mendez, Water defluoridation with special emphasis on adsorbents-containing metal oxides and/or hydroxides: A review, Sep. Purif. Technol. 150 (2015) 292-307.

[160] M. Islam, R.K. Patel, Evaluation of removal efficiency of fluoride from aqueous solution using quick lime, J. Hazard. Mater. 143 (2007) 303-310.

[161] M. Poonam, G. Suja, M. Dhiraj, Use of Calcite for Defluoridation of Drinking Water in Acidic medium, Res. J. Chem. Sci. 4 (2014) 62-65.

[162] S. Gogoi, R.K. Dutta, Fluoride removal by hydrothermally modified limestone powder using phosphoric acid, J. Environ. Chem. Eng. 4 (2016) 1040-1049.

[163] N. Sakhare, S. Lunge, S. Rayalu, S. Bakardjiva, J. Subrt, S. Devotta, N. Labhsetwar, Defluoridation of water using calcium aluminate material, Chem. Eng. J. 203 (2012) 406-414.

[164] V. Chaudhary, S. Prasad, Rapid removal of fluoride from aqueous media using activated dolomite, Anal. Methods. 7 (2015) 8304-8314.

[165] Dhillon, S. Prasad, D. Kumar, Recent advances and spectroscopic perspectives in fluoride removal, Appl. Spectrosc. Rev. 4928 (2016) 1-56.

[166] S. Gao, R. Sun, Z. Wei, H. Zhao, H. Li, F. Hu, Size-dependent defluoridation properties of synthetic hydroxyapatite, J. Fluor. Chem. 130 (2009) 550-556.

[167] L. Chen, K.S. Zhang, J.Y. He, W.H. Xu, X.J. Huang, J.H. Liu, Enhanced fluoride removal from water by sulfate-doped hydroxyapatite hierarchical hollow microspheres, Chem. Eng. J. 285 (2016) 616-624.

[168] L.H. Velazquez-Jimenez, E. Vences-Alvarez, J.L. Flores-Arciniega, H. Flores-Zuñiga, J.R. Rangel-Mendez, Water defluoridation with special emphasis on adsorbents-containing metal oxides and/or hydroxides: A review, Sep. Purif. Technol. 150 (2015) 292-307.

[169] X. Dou, D. Mohan, C.U. Pittman, S. Yang, Remediating fluoride from water using hydrous zirconium oxide, Chem. Eng. J. 198-199 (2012) 236-245.

[170] Saha, A. Ghosh, D. Nandi, K. Gupta, D. Chatterjee, U.C. Ghosh, β-Cyclodextrin modified hydrous zirconium oxide: Synthesis, characterization and defluoridation performance from aqueous solution, Chem. Eng. J. 263 (2015) 220-230.

[171] K. Babaeivelni, A.P. Khodadoust, Adsorption of fluoride onto crystalline titanium dioxide: Effect of pH, ionic strength, and co-existing ions, J. Colloid Interface Sci. 394 (2013) 419-427.

[172] A.L. Srivastav, P.K. Singh, V. Srivastava, Y.C. Sharma, Application of a new adsorbent for fluoride removal from aqueous solutions, J. Hazard. Mater. 263 (2013) 342-352.

[173] X. Dou, Y. Zhang, H. Wang, T. Wang, Y. Wang, Performance of granular zirconium-iron oxide in the removal of fluoride from drinking water, Water Res. 45 (2011) 3571-3578.

[174] Tang, G. Zhang, Efficient removal of fluoride by hierarchical Ce-Fe bimetal oxides adsorbent: Thermodynamics, kinetics and mechanism, Chem. Eng. J. 283 (2016) 721-729.

[175] L. Yan, H. Tu, T. Chan, C. Jing, Mechanistic study of simultaneous arsenic and fluoride removal using granular $TiO_2$-La adsorbent, Chem. Eng. J. 313 (2017) 983-992.

[176] J. Wang, D. Kang, X. Yu, M. Ge, Y. Chen, Synthesis and characterization of Mg-Fe-La trimetal composite as an adsorbent for fluoride removal, Chem. Eng. J. 264 (2015) 506-513.

[177] M. Wang, X. Yu, C. Yang, X. Yang, M. Lin, L. Guan, Removal of fluoride from aqueous solution by Mg-Al-Zr triple-metal composite, Chem. Eng. J. 322 (2017) 246-253.

[178] USEPA. Microbial and Disinfection Byproduct Rules. Simultaneous Compliance Guidance Manual, 1999.

[179] W. H. O. April 2013, 2011-last update, Water and Sanitation [Homepage of World Health Organisation], [Online]. Available: http://www.who.int/gho/mdg/environmental_sustainability/en/index.html [October, 2013].

[180] S.K. Jain, V.P. Singh. Water resources systems planning and management. Elsevier; 2003 Sep 12.

[181] L. Tamayo, M. Azócar, M. Kogan, A. Riveros, M. Páez. Copper-polymer nanocomposites: An excellent and cost-effective biocide for use on antibacterial surfaces. *Mater. Sci. Eng: C.* **69,** 2016, 1391-1409.

[182] P.K. Pandey, P.H. Kass, M.L. Soupir, S. Biswas, V.P. Singh. Contamination of water resources by pathogenic bacteria. *Amb Express,* **4**(1), 2014, 51.

[183] J.P. Nataro, J.B. Kaper. Diarrheagenic *Escherichia coli*. *Clinical Microbiol. Rev.* **11**(1), 1998, 142-201.

[184] J.P. Cabral. Water microbiology. Bacterial pathogens and water. *Int. J. Environ. Res. Public Health,* **7**(10), 2010, 3657-3703.

[185] P.H. Edelstein, L. Christian. Legionella. *Manual of Clinical Microbiol. Eleventh Ed.* A. Soc. Microbiol. 2015, 887-904.

[186] M.E. Woolhouse. Population biology of emerging and re-emerging pathogens. Trends in Microbiol. 10(10), 2002, 3-7.

[187] B.S. Fields, R.F. Benson, R.E. Besser. Legionella and Legionnaires' disease: 25 years of investigation. *Clinical Microbiol. Rev.* **15**(3), 2002, 506-526.

[188] L. Growth-promoting. Disinfection of water distribution systems for Legionella, *Seminars in Respiratory Infections.* 1998, 147-159.

[189] Z. Iqbal, E.P. Lai, T.J. Avis. Development of polymer-modified magnetic nanoparticles and quantum dots for *Escherichia coli* binding test. *Microchim Acta,* **176**, 2012, 193-200.

[190] M.J. Nieuwenhuijsen, M.B. Toledano, N.E. Eaton, J. Fawell, P. Elliott. Chlorination disinfection byproducts in water and their association with adverse reproductive outcomes: a review. *Occupational and Environ. Medicine,* **57**(2), 2000, 73-85.

[191] J.C. Chang, S.F. Ossoff, D.C. Lobe, M.H. Dorfman, C.M. Dumais, R.G. Qualls, J.D. Johnson. UV inactivation of pathogenic and indicator microorganisms. *Appl. Environ. Microbiol.* **49**(6), pp. 1985, 1361-1365.

[192] S. Madaeni. The application of membrane technology for water disinfection. *Water Res.* **33**(2), 1999, 301-308.

[193] K. Gopal, S.S. Tripathy, J.L. Bersillon, S.P. Dubey. Chlorination byproducts, their toxicodynamics and removal from drinking water. J. Hazard. Mater. 140(1-2), 2007, 1-6.

[194] K. Song, M. Mohseni, F. Taghipour. Application of ultraviolet light-emitting diodes (UV-LEDs) for water disinfection: A review. *Water Res.* **94**, pp. 2016, 341-349.

[195] W.A. Hijnen, E.F. Beerendonk, G.J. Medema. Inactivation credit of UV radiation for viruses, bacteria and protozoan (oo)cysts in water: a review. *Water Res.* **40**(1), 2006, 3-22.

[196] R.L. Wolfe. Ultraviolet disinfection of potable water. *Environ. Sci. Technol.* **24**(6), 1990, 768-773.

[197] M. Bodzek, K. Konieczny, M. Rajca. Membranes in water and wastewater disinfection. Archives of Environmental Protection. 45(1), 2019.

[198] A.B. Koltuniewicz, E. Drioli. Membranes in clean technologies-theory and practice-vol. 1. *Environ. Eng. Management J.* **7**(5), 2008, 649-650.

[199] X.F. Sun, J. Qin, P.F. Xia, B.B. Guo, C.M. Yang, C. Song, S.G. Wang. Graphene oxide-silver nanoparticle membrane for biofouling control and water purification. Chem. Eng. J. 281, 2015, 53-9.

[200] Q. Li, S. Mahendra, D.Y. Lyon, L. Brunet, M.V. Liga, D. Li, P.J. Alvarez. Antimicrobial nanomaterials for water disinfection and microbial control: potential applications and implications. *Water Res.* **42**(18), 2008, 4591-4602.

[201] S.W. Krasner, H.S. Weinberg, S.D. Richardson, S.J. Pastor, R. Chinn, M.J. Sclimenti, G.D. Onstad, A.D. Thruston. Occurrence of a new generation of disinfection byproducts. *Environ. Sci. Technol.* **40**(23), 2006, 7175-7185.

[202] A.S. Adeleye, J.R. Conway, K. Garner, Y Huang, Y. Su, A.A. Keller. Engineered nanomaterials for water treatment and remediation: Costs, benefits, and applicability. *Chem. Eng. J.* **286**, 2016, 640-662.

[203] R.L. Jolley, R.J. Bull, W.P. Davis, S. Katz, M.H. Roberts Jr, V.A. Jacobs. Water chlorination: chemistry, environmental impact and health effects. Volume 5. Oak Ridge National Lab., TN (USA); Washington Univ., Seattle (USA); 1985 Jan 1.

[204] P. Muraca, J.E. Stout, V.L. Yu. Comparative assessment of chlorine, heat, ozone, and UV light for killing Legionella pneumophila within a model plumbing system. *Appl. Environ. Microbiol.* **53**(2), 1987, 447-453.

[205] J. Lalley, D.D. Dionysiou, R.S. Varma, S. Shankara, D.J. Yang, M.N. Nadagouda. Silver-based antibacterial surfaces for drinking water disinfection—an overview. Curr. Opinion in Chem. Eng. 3: 2014, 25-29.

[206] Z. Li, D. Lee, X. Sheng, R.E. Cohen, M.F. Rubner. Two-level antibacterial coating with both release-killing and contact-killing capabilities. *Langmuir,* **22**(24), 2006, 9820-9823.

[207] T.J. Berger, J.A. Spadaro, S.E. Chapin, R.O. Becker. Electrically generated silver ions: quantitative effects on bacterial and mammalian cells. *Antimicrobial Agents and Chemotherapy,* **9**(2), 1976, 357-358.

[208] Ingle, A. Gade, S. Pierrat, C. Sonnichsen, M. Rai. Mycosynthesis of silver nanoparticles using the fungus Fusarium acuminatum and its activity against some human pathogenic bacteria. *Curr. Nanoscience,* **4**(2), 2008, 141-144.

[209] Song, C. Zhang, G. Zeng, J. Gong, Y. Chang, Y. Jiang. Antibacterial properties and mechanism of graphene oxide-silver nanocomposites as bactericidal agents for water disinfection. Archives Biochem. Biophysic. 604, 2016, 167-76.

[210] Gangadharan, K. Harshvardan, G. Gnanasekar, D. Dixit, K.M. Popat, P.S. Anand. Polymeric microspheres containing silver nanoparticles as a bactericidal agent for water disinfection. *Water Res.* **44**(18), 2010, 5481-5487.

[211] S.P. Theofilou, B.K. Constantinou, V.K. Chatziiona, N. Pantelidou, S. Plyastsov, K. Kapnisis, P.G. Savva, I. Meshkovsky, A. Anayiotos, C.N. Costa. New insights into the antimicrobial treatment of water on Ag-supported solids. *J. Chem. Technol. Biotechnol.* **94**(4), 2019, 1134-1143.

[212] Grass, C. Rensing, M. Solioz. Metallic copper as an antimicrobial surface. *Appl. Environ. Microbiol.* **77**(5), 2011, 1541-1547.

[213] Borkow, J. Gabbay. Copper as a biocidal tool. *Curr. medicinal Chem.* **12**(18), 2005, 2163-2175.

[214] U. Bogdanovic, V. Vodnik, M. Mitric, S. Dimitrijevic, S.D. Skapin, V. Zunic, M. Budimir, M. Stoiljkovic. Nanomaterial with High Antimicrobial Efficacy☐Copper/Polyaniline Nanocomposite. ACS Appl. Mater. Interfaces. 7(3), 2015, 1955-66.

[215] Palza. Antimicrobial polymers with metal nanoparticles. Int. J. Molec. Sci. 16(1), 2015, 2099-2116.

[216] R.J. Pinto, S. Daina, P. Sadocco, C.P. Neto, T. Trindade. Antibacterial activity of nanocomposites of copper and cellulose. BioMed Res. Int. 2013, 2013, 280512.

[217] M. Grace, Chand N, Bajpai SK. Copper alginate-cotton cellulose (CACC) fibers with excellent antibacterial properties. J. Engineered Fibers and Fabrics. 4(3), 2009, 155892500900400303.

[218] Weickmann, J.C. Tiller, R. Thomann, R. Mülhaupt. Metallized organoclays as new intermediates for aqueous nanohybrid dispersions, nanohybrid catalysts and antimicrobial polymer hybrid nanocomposites. Macromol. Mater. Eng. 290(9), 2005, 875-83.

[219] Y. Ouyang, X. Cai, Q. Shi, L. Liu, D. Wan, S. Tan, Y. Ouyang. Poly-l-lysine-modified reduced graphene oxide stabilizes the copper nanoparticles with higher water-solubility and long-term additively antibacterial activity. Colloids and surfaces B: Biointerfaces. 107, 2013, 107-14.

[220] J.P. Ruparelia, A.K. Chatterjee, S.P. Duttagupta, S. Mukherji. Strain specificity in antimicrobial activity of silver and copper nanoparticles. Acta biomaterialia. 4(3), 2008, 707-16.

[221] A.M. Eremenko, I.S. Petrik, N.P. Smirnova, A.V. Rudenko, Y.S. Marikvas. Antibacterial and antimycotic activity of cotton fabrics, impregnated with silver and binary silver/copper nanoparticles. Nanoscale Res. Lett. 11(1), 2016, 28.

[222] P. Biswas, R. Bandyopadhyaya. Synergistic antibacterial activity of a combination of silver and copper nanoparticle impregnated activated carbon for water disinfection. Environ. Sci. Nano. 4(12), 2017, 2405-17.

[223] L. Yue, S. Chen, S. Wang, C. Wang, X. Hao, Y.F. Cheng. Water disinfection using Ag nanoparticle-CuO nanowire co-modified 3D copper foam nanocomposites in high flow under low voltages. Environ. Sci.: Nano. 6(9), 2019, 2801-9.

[224] Perdikaki, A. Galeou, G. Pilatos, A. Prombona, G.N. Karanikolos. Ion-based metal/graphene antibacterial agents comprising mono-ionic and bi-ionic silver and copper species. Langmuir. 34(37), 2018, 11156-66.

[225] N.H. Mthombeni, L. Mpenyana-Monyatsi, M.S. Onyango, M.N. Momba. Breakthrough analysis for water disinfection using silver nanoparticles coated resin beads in fixed-bed column. J. Hazard. Mater. 217, 2012, 133-40.

[226] L. Mpenyana-Monyatsi, N.H. Mthombeni, M.S. Onyango, M.N. Momba. The effects of material loading and flow rate on the disinfection of pathogenic microorganisms using cation resin-silver nanoparticle filter system. Phys. Chem. Earth. Parts A/B/C. 2017, 100, 181-8.

[227] S. Bharti, S. Agnihotri, S. Mukherji, S. Mukherji. Effectiveness of immobilized silver nanoparticles in inactivation of pathogenic bacteria. *J Environ. Res. Dev.* **9**(3A), 2015, 849-856.

[228] S. Bharti, S. Mukherji, S. Mukherji. Water disinfection using fixed bed reactors packed with silver nanoparticle immobilized glass capillary tubes. Sci. Total Environ. 689, 2019, 991-1000.

[229] S.C. Motshekga, S.S. RAY. Highly efficient inactivation of bacteria found in drinking water using chitosan-bentonite composites: Modelling and breakthrough curve analysis. Water Res. 111, 2017, 213-223.

[230] P. Biswas, R. Bandyopadhyaya. Water disinfection using silver nanoparticle impregnated activated carbon: *Escherichia coli* cell-killing in batch and continuous packed column operation over a long duration. *Water Res.* **100**, 2016, 105-115.

[231] R. Bandyopadhyaya, M.V. Sivaiah, P. Shankar. Silver-embedded granular activated carbon as an antibacterial medium for water purification. *Journal of Chemical Technology & Biotechnology: International Research in Process, Environmental & Clean Technology,* **83**(8), 2008, 1177-1180.

[232] S. Liau, D. Read, W. Pugh, J. Furr, A. Russell. Interaction of silver nitrate with readily identifiable groups: relationship to the antibacterial action of silver ions. *Lett. Appl. Microbiol.* **25**(4), 1997, 279-283.

[233] J.A. Lemire, J.J. Harrison, R.J. Turner. Antimicrobial activity of metals: mechanisms, molecular targets and applications. *Nature Rev. Microbiol.* **11**(6), 2013, 371.

[234] Y.E. Lin, R.D. Vidic, J.E. Stout, L.Y. Victor. Individual and combined effects of copper and silver ions on inactivation of Legionella pneumophila. *Water Res.* **30**(8), (1996), 1905-1913.

[235] F.F. XU, J.A. Imlay. Silver(I), mercury(II), cadmium(II), and zinc(II) target exposed enzymic iron-sulfur clusters when they toxify *Escherichia coli*. *Appl. Environ. Microbiol.* **78**(10), (2012), 3614-3621.

[236] M. Qayyum, B. Ahmad, S. Nawazish-I-Hussain, J. Iqbal, A.H. Khan. The antimicrobial activity of different zinc salts Proc. SZPGMI. (1998),12, 8-12.

[237] Sondi, B Salopek-Sondi. Silver nanoparticles as antimicrobial agent: A case study on *E. coli* as a model for Gram-negative bacteria. *J. Colloid Interface Sci.* **275**(1), (2004), 177-182.

# CHAPTER 2: HYDROUS $ZrO_2$ DECORATED POLYANILINE NANOFIBRES: SYNTHESIS, CHARACTERIZATION AND APPLICATION AS AN EFFICIENT ADSORBENT FOR WATER DEFLUORIDATION

## 2.1 INTRODUCTION

Fluoride ($F^-$) being ubiquitously present in the earth's crust, enters into the environment both naturally through the dissolution of rock minerals, emissions of volcanoes, and marine aerosols and anthropogenically through various industrial processes like steel manufacturing, coal combustion and phosphate fertilizer production [1,2]. As one of the essential micronutrients in humans, $F^-$ levels up to a certain extent (1.0-1.5 mg/L) as endorsed by World Health Organization (WHO) has remarkable prophylactic influence over dental and bone health, above which it becomes detrimental and causes dental and skeletal fluorosis along with various non-skeletal manisfestations including neurological disorders [3,4]. Hence, as a prerequisite to mitigate or bring down the $F^-$ level to standard permissible limits stipulated by various health organizations, many water defluorination techniques have been developed so far like electrocoagulation, precipitation, ion exchange, membrane based processes and adsorption [5]. Among these techniques, adsorption due to its high efficiency, environment-friendly nature, simple design, and economic viability, has emerged as a most captivating and widely employed defluoridation technique for field implementation particularly in rural areas [6]. Consequently, various existing materials like activated alumina, activated carbon, mixed metal oxides, polymeric materials and their composites have been acknowledged as some of the promising defluoridating scavengers [6,7]. However, researchers are still concentrating on developing innovative and more efficient $F^-$ adsorbents to overcome the applicational drawbacks associated with the conventional adsorbents such as low adsorption capacity, poor mechanical stability and narrow working pH range, etc.

Polyaniline (PANI) is a conducting polymer that is cheap, easily synthesizable, environmentally stable with exciting redox and electrochemical properties and has thus gained the special attention of scientific communities in various fields of application [8]. Recently, one-dimensional (1-D) PANI nanostructures (nanorods/wires/fibers) have attracted much scientific interest over conventional bulk counterparts as they offer a possibility of improved performance as a result of a large interfacial area and possess the advantages of both low-dimensional systems and organic conductors [9,10]. In view of this, Bhaumik et al. have demonstrated the great potential of bare PANI nanofibres (PANI NFs) and its composite with nano-sized $Fe^0$ in the removal of As(V), Cr(VI) and dyes [11,12]. Though, it is widely accepted that the positively charged backbone of PANI (protonated amine groups) can act as excellent adsorption sites for anions, yet its $F^-$ removing properties were not fully explored. However, in this regard, an effort was also made by Karthikeyan et al. who successfully synthesized bare PANI and its composites with chitosan and alumina and obtained a defluoridation capacity of 0.78, 5.9 and 6.6 mg/g, respectively [13-15]. Hence, further modification of PANI with reactive materials having significant affinity towards $F^-$ ions would constitute a viable approach in developing highly efficient PANI-based $F^-$ adsorbents.

Among various polyvalent metal oxides, zirconium(IV) oxide ($ZrO_2$) is well-known to have a strong $F^-$ affinity through Lewis acid-base interaction and is insoluble over a wide pH range [16]. However, it is typically present as ultrafine particles which lead to the loss of activity due to agglomeration, difficulty in separation, and excessive pressure drop when applied to continuous flow through column systems [17]. To mitigate the above technical bottlenecks, various Zr(IV) based hybrid adsorbents have been reported recently, which synergistically blend, the strong $F^-$ uptake property of $ZrO_2$ with hydraulic properties of support materials and provide a much better applicability than pristine oxides [18]. Among the wide range of materials available, activated carbon, graphene and carbon nanotubes have been demonstrated as some of the most effective support matrices due to their porous structure, high surface area and the presence of various active surface functional groups [19]. Hence, the inherent property of nanostructured PANI NFs (presence of surface functional groups and large surface area), encouraged an investigation into its potential as a support material. It was anticipated that deposition of hydrous zirconium oxide ($HZrO_2$) on PANI NFs supporting matrices, would fabricate multifunctional 1D composite nanostructure with enhanced $F^-$ removal as well as reasonable hydraulic properties for the large scale real field application.

Hence, in this article, $HZrO_2$@PANI NFs as a novel adsorbent was fabricated via a two-step synthetic procedure where in the first step PANI NFs were developed via a rapid mixing polymerization technique, and in the following step, $HZrO_2$ was decorated on as-synthesized PANI NFs via a simple precipitation method. The as-developed $HZrO_2$@PANI NFs adsorbent was extensively characterized using various spectro-analytical techniques and effectively employed for removal of $F^-$ from aqueous solution. The effects of solution pH, contact time, initial concentration, temperature and co-existing ions were investigated on the $F^-$ sorption. The best fit adsorption kinetic and isotherm models were established using equilibrium adsorption experimental data. Furthermore, the underlying mechanism responsible for preferable $F^-$ adsorption onto $HZrO_2$@PANI NFs was investigated. Adsorption-desorption cycles were conducted along with a real field test, to evaluate the economic viability and real field applicability of $HZrO_2$@PANI NFs.

## 2.2 EXPERIMENTAL PROCEDURES

### 2.2.1 Reagents and chemicals

Aniline monomer (ANI, 99%), zirconium oxychloride ($ZrOCl_2.8H_2O$), iron (III) chloride ($FeCl_3$), anhydrous sodium fluoride (NaF), sodium hydroxide, hydrochloric acid, ammonia and all other chemicals of analytical reagent grade were purchased from Sigma-Aldrich, USA. Ultrapure deionized water (resistivity > 18.5 MΩ cm) was used for all the experiments.

### 2.2.2 Adsorbent synthesis

#### *2.2.2.1 Synthesis of polyaniline nanofibres (PANI NFs)*

PANI NFs were fabricated via a rapid mixing polymerization of ANI monomers at room temperature as reported by Bhaumik et al., wherein $FeCl_3$ was used as an oxidant to polymerize ANI monomers [20]. In brief, 6 g of $FeCl_3$ was dissolved in 80 mL of distilled water in a 250 mL conical flask and 0.8 mL of ANI monomer was syringed simultaneously into the oxidant solution under vigorous (600 rpm) stirring, to distribute the oxidant and monomer molecules evenly and to prevent the subsequent secondary growth of PANI. The reaction mixture was stirred for 4 min and thereafter the reaction mixture was kept for 48 h without stirring. The nanofibres obtained were filtered and washed with deionized water until the filtrate became colourless. Finally, the product was washed with acetone to remove oligomers and then dried at 60°C for 24 h.

### 2.2.3 Synthesis of hydrous $ZrO_2$ decorated polyaniline nanofibers ($HZrO_2$@PANI NFs)

$HZrO_2$@PANI NFs were synthesized using a simple technique in which $HZrO_2$ was precipitated onto the prepared PANI NFs using $ZrOCl_2.8H_2O$ as a precursor salt. To select an optimal wt. % of $HZrO_2$ decorated on PANI NFs, the varied amount of PANI NFs, i.e. 1 g, 0.75 g, 0.5 g and 0.25 g, were added to the fixed concentration of $ZrOCl_2.8H_2O$ solution and the resulting adsorbents were named as $HZrO_2$@PANI NFs-1, $HZrO_2$@PANI NFs-2, $HZrO_2$@PANI NFs-3 and $HZrO_2$@PANI NFs-4, respectively. Characteristically, 0.5 g of $ZrOCl_2.8H_2O$ was dissolved in 100 mL of 0.01 N HCl solutions and warmed up to ~ 40°C. 0.5 g PANI NFs were then added to the above solution and continuously stirred for 30 min to obtain a homogeneously well-dispersed mixture of nanofibers and metal ions. Then 0.1M $NH_4OH$ solution was added dropwise to the well-stirred mixture until the pH of solution rose up to ~ 7.0±0.1. The greyish black solid mass which was obtained was left undisturbed and aged with mother liquor for 48 h. Afterwards, the product ($HZrO_2$@PANI NFs) obtained was filtered, washed with deionized water and oven dried at 60°C for 24 h. The total weights of as-synthesized $HZrO_2$@PANI NFs obtained with different % $HZrO_2$ loadings are mentioned in Table 1.

### 2.2.4 Characterization

The Fourier transformed infrared (FTIR) spectra of adsorbents in the region of 4000-400 $cm^{-1}$ using the standard KBr pellet method, were obtained on a Perkin Elmer Spectrum FTIR spectrophotometer. The adsorbent crystal structure was analyzed using X-ray diffraction (XRD) spectra recorded on a PAN Analytical X'Pert PRO-diffractometer using Cu Kα radiation in the 2θ range of 10-80º. A Micrometrics ASAP 2020 gas adsorption apparatus (USA) was used to record BET (Brunauer-Emmet-Teller) surface area of the adsorbent using $N_2$ adsorption-desorption analysis. An Oxford energy dispersive X-ray spectrometer (EDS, Oxford, UK) and a high resolution scanning transmission electron microscope (HR-STEM, JEOL Japan) fitted with an EDS system were used to examine the morphology, microstructure and elemental composition of adsorbents. A zeta potential analyzer (Malvern Zeta Sizer Nano series, UK) was used to measure zeta potential of the adsorbents. A Kratos Axis Ultra device, with a focused monochromatized Al Kα radiation (hν = 1486.6 eV) was used to carry out X-ray photoelectron spectroscopic (XPS) analysis of adsorbents.

### 2.2.5 Adsorption experiments

The $F^-$ stock solution was prepared with NaF and deionized water, while working solutions of $F^-$ were prepared by appropriate dilution of the stock solution (1000 mg/L) and adsorption experiments were conducted in batch equilibrium technique. The effect of pH (2-11), adsorbent dosage (0.01- 0.15 g) and co-existing ions ($Cl^-$, $NO_3^-$, $SO_4^{2-}$, $HCO_3^-$, and $PO_4^{3-}$ ) were investigated with 50 mL of $F^-$ solution (10 mg/L) at 25°C. Adsorption isotherms were investigated at different pH values (3, 4, 5 and 6.5) as well as at different temperatures (15, 25, 35 and 45°C) using initial $F^-$ concentrations 10 to 120 mg/L. Adsorption kinetics were also investigated under different initial $F^-$ concentrations (5, 10, 15 and 20 mg/L) and different temperatures (15°C, 25°C, 35°C and 45°C). The residual $F^-$ concentration was determined by a fluoride ion selective electrode using a total ionic strength adjustment buffer TISAB II to avoid the interference by complexing ions. The % $F^-$ removal efficiency and adsorption capacity of the adsorbent at equilibrium ($q_e$) and at time *t* ($q_t$) in mg/g were calculated using equations (1), (2) and (3) respectively:

$$\%\ \text{removal} = \left(\frac{C_0-C_e}{C_0}\right) \times 100 \tag{1}$$

$$q_e = \left(\frac{C_0-C_e}{m}\right) \times V \tag{2}$$

$$q_t = \left(\frac{C_0-C_t}{m}\right) \times V \tag{3}$$

where $C_o$, $C_e$ and $C_t$ are $F^-$ concentrations (mg/L) at initial, equilibrium and at time $t$, respectively and $m$ and $V$ are mass of adsorbent (g) and volume of $F^-$ solution (L), respectively.

### 2.2.6 Adsorbent regeneration

Regeneration studies for the spent adsorbent, i.e. $F^-$ laden adsorbent were carried out in the form of adsorption-desorption batch experiments. Typically, 0.025 g of adsorbent was first loaded with $F^-$ by contacting it with 50 mL of 10 mg/L $F^-$ solution at pH 3, filtered, dried in air and shaken with 50 mL of 0.01, 0.025, 0.05, 0.075 and 0.1M NaOH solutions respectively, for 24 h to desorb the adsorbed $F^-$ ions. The % desorption efficiency was then calculated using equation (4):

$$\%\ desorption = \frac{C_{des}}{C_{ads}} \times 100 \tag{4}$$

where $C_{des}$ and $C_{ads}$ are the amounts of total $F^-$ desorbed and adsorbed (mg/L), respectively. The spent adsorbent was shaken with 50 mL of 2 M HCl for 5 h for regeneration and then further subjected to consecutive cycles of adsorption and desorption.

## 2.3 RESULTS AND DISCUSSIONS

### 2.3.1 Characterization

The FTIR spectra of PANI NFs and $HZrO_2$@PANI NFs before and after $F^-$ adsorption are shown in Fig. 1A(a-c). For pure PANI NFs (Fig. 1A(a)), the characteristic stretching bands for, N-H bond, quinonoid ring, benzenoid ring, secondary aromatic amine, aromatic C-H in-plane and out-of-plane deformations were obtained at 3434, 1584, 1487, 1293, 1122 and 787 $cm^{-1}$, respectively [14,15]. The FTIR spectrum of as-synthesized $HZrO_2$@PANI NFs (Fig. 2.1A(b)) displayed all the characteristic adsorption peaks of PANI NFs (as mentioned above in Fig. 2.1A(a)) at 1588, 1497, 1313, 1122 and 795 $cm^{-1}$. Furthermore, the broad adsorption peaks obtained at 3000-3600 $cm^{-1}$ in Fig. 2.1A(b) can be attributed to surface OH groups of $HZrO_2$ and N-H stretching band of PANI NFs [16]. Besides, the peaks present at 1638 and 1384 correspond to the characteristic bending vibrations of the H-O-H bond [21] and Zr-OH groups [22], respectively, thus confirming the hydrated nature of $ZrO_2$ deposited over PANI NFs in as-synthesized $HZrO_2$@PANI NFs.

Hence, the presence of functional groups of $HZrO_2$ as well as PANI NFs in Fig. 2.1A(b) indicate the successful fabrication of $HZrO_2$@PANI NFs. After $F^-$ treatment (Fig. 2.1A(c)), the intensity of broad absorption peaks lying in the region 3000-3600 $cm^{-1}$ was reduced significantly suggesting the interaction of both NH group of PANI NFs and surface OH groups of $HZrO_2$ with $F^-$ ions. The protonated NH groups of PANI NFs underwent a dopant exchange mechanism where $Cl^-$ ions doped in PANI backbone were exchanged with $F^-$ ions and surface OH groups contributed by $HZrO_2$ were replaced with $F^-$ ions [13,16]. Also, the adsorption peak present at 1638 $cm^{-1}$ in Fig. 2.1A(b) weakened in intensity after $F^-$ adsorption (Fig. 2.1A(c)), further demonstrating that $F^-$ has substituted a significant fraction of surface OH groups associated with Zr(IV). However, Zr-F absorption peaks were not detected in Fig. 2.1A(c), as they usually appear in a range of 200-400 $cm^{-1}$ and herein a mid-range (400-4000 $cm^{-1}$) spectrometer was used [16]. Hence, it can be concluded that $F^-$ ion adsorption on $HZrO_2$@PANI NFs, took place via ion exchange involving replacement of surface OH groups and doped $Cl^-$ ions with $F^-$ ions.

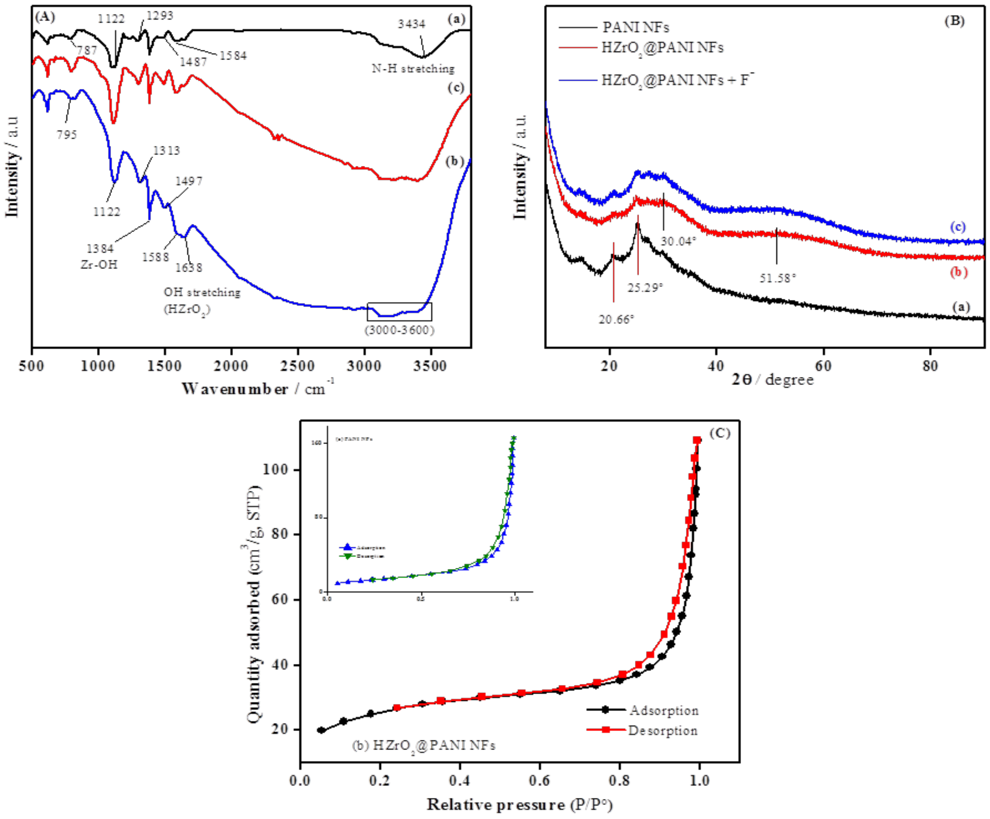

**Figure 2-1: (A) FTIR spectra of (a) PANI NFs, (b) $HZrO_2$@PANI NFs before and (c) after F-sorption; (B) XRD patterns of (a) PANI NFs, (b) $HZrO_2$@PANI NFs before and (c) after F-adsorption; (C) N2 adsorption-desorption curves of $HZrO_2$@PANI NFs and PANI NFs (inset graph).**

XRD patterns of PANI NFs and $HZrO_2$@PANI NFs before and after $F^-$ adsorption are presented in Fig 2.1B(a-c). Fig. 2.1B(a), displayed clear diffraction peaks at 20.66º and 25.29º due to the semi-crystalline nature of PANI NFs [8]. Though polymers are typically considered to be amorphous in nature, in this case, both conductive nature (repetition of benzenoid and quinonoid rings in PANI chains) and fibre structure of PANI NFs, are contributing towards its significant crystallinity [23]. However, the degree of crystallinity, as well as intensity, decreased after the deposition of hydrous $ZrO_2$ particles on PANI NFs (see Fig. 2.1B(b)), which might be attributed to the amorphous nature of $HZrO_2$. The broad diffraction peaks at 30.04° and 51.58° (Fig. 2.1B(b)) can be accredited to (101) and (211) diffraction planes of $ZrO_2$ (JCPDS File no. 81-1544) [16,21]. Conclusively the deposition of amorphous $HZrO_2$ particles on PANI NFs altered the crystallinity of PANI NFs and resulted in an amorphous $HZrO_2$@PANI NFs. On comparing the XRD patterns of $HZrO_2$@PANI NFs before (Fig. 2.1B(c)) and after $F^-$ treatment, no substantial change was observed which suggested that $F^-$ interaction with $HZrO_2$@PANI NFs did not alter its crystal structure. $N_2$ adsorption-desorption isotherms corresponding to PANI NFs and $HZrO_2$@PANI NFs are depicted in Fig. 2.1C (a) and (b), respectively. The distinct hysteresis loop present in the curves revealed the mesoporous nature of the adsorbent with pores in the diameter range of 2-50 nm [24]. The BET surface area obtained for PANI NFs was much higher (44.72 m$^2$/g) in comparison to conventional PANI (20.02 m$^2$/g) which might be due to the formation of 2.1-D nanostructured polyaniline nanofibres [11].

Moreover, the specific surface area of $HZrO_2$@PANI NFs (≈ 86.64 m$^2$/g) was found to be almost double the surface area of pure PANI NFs ( ≈ 44.72 m$^2$/g) which can be attributed to the fact that scattering of high surface area $HZrO_2$ particles (≈ 92.7 m$^2$/g) onto the matrix of PANI NFs, played a role as scaffold to mitigate the $\pi$- $\pi^*$ aggregation of the PANI chains, which eventually inhibited the agglomeration of PANI NFs and thus enhanced the surface area. In addition, $HZrO_2$@PANI NFs with average pore diameter ≈ 20.05 nm can easily accommodate small sized $F^-$ ions ≈ 0.24 nm.

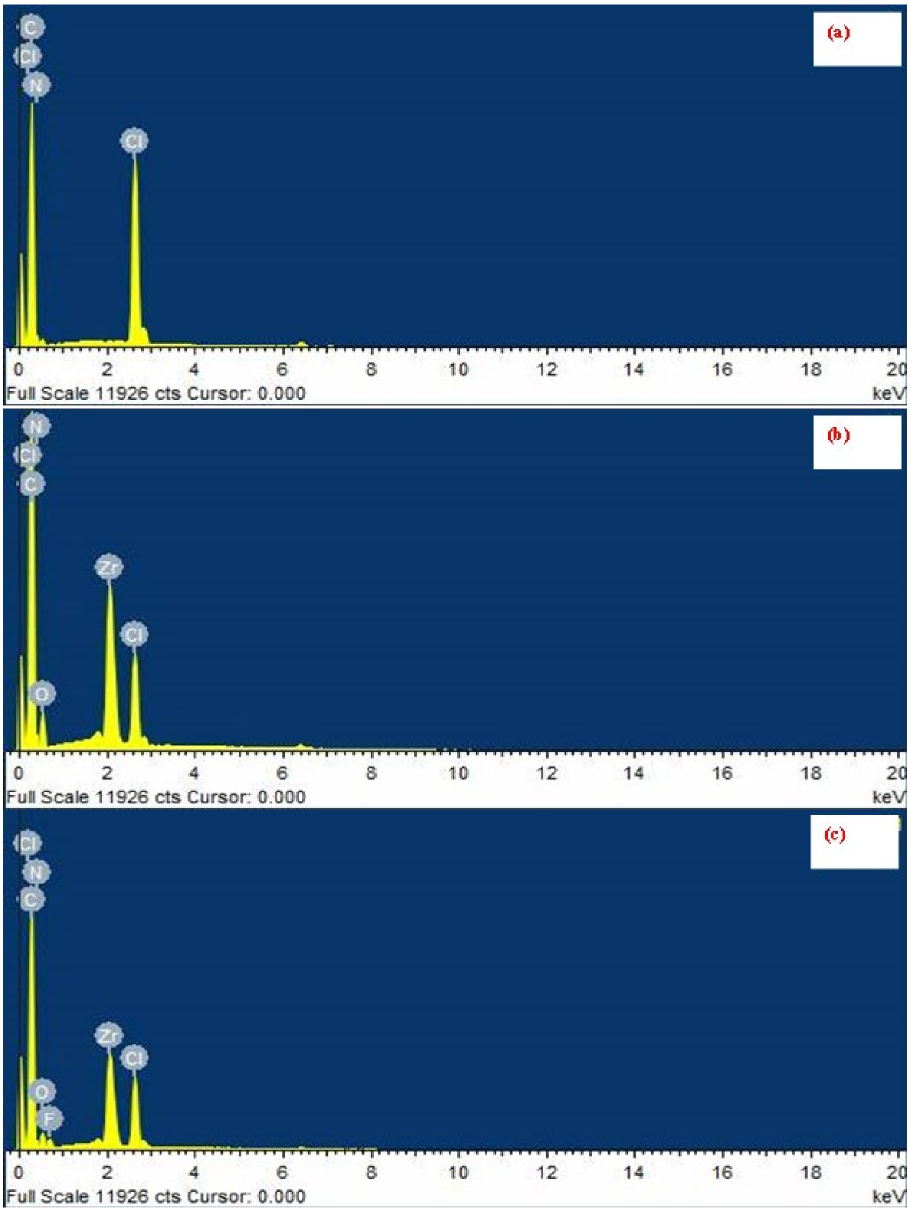

**Figure 2-2: EDX spectra of (a) PANI NFs and $HZrO_2$@PANI NFs (b) before and (c) after F- sorption.**

The qualitative EDX spectrum of the elemental composition of pure PANI NFs demonstrated peaks for C, N and Cl (Fig. 2.2(a)), whereas EDX spectrum of as-prepared $HZrO_2$@PANI NFs exhibited peaks of C, N, Cl, Zr and O as shown in Fig. 2.2(b). Besides, the $F^-$ sorption onto $HZrO_2$@PANI NFs was successfully confirmed by the presence of distinct F peak in after adsorption EDX spectra (Fig. 2.2(c)). In addition, Fig. 2.3 shows the elemental mapping image of $HZrO_2$@PANI NFs after $F^-$ sorption with an even distribution of C, N, O, Zr and F, which further validated the successful adsorption of $F^-$ on the surface of $HZrO_2$@PANI NFs.

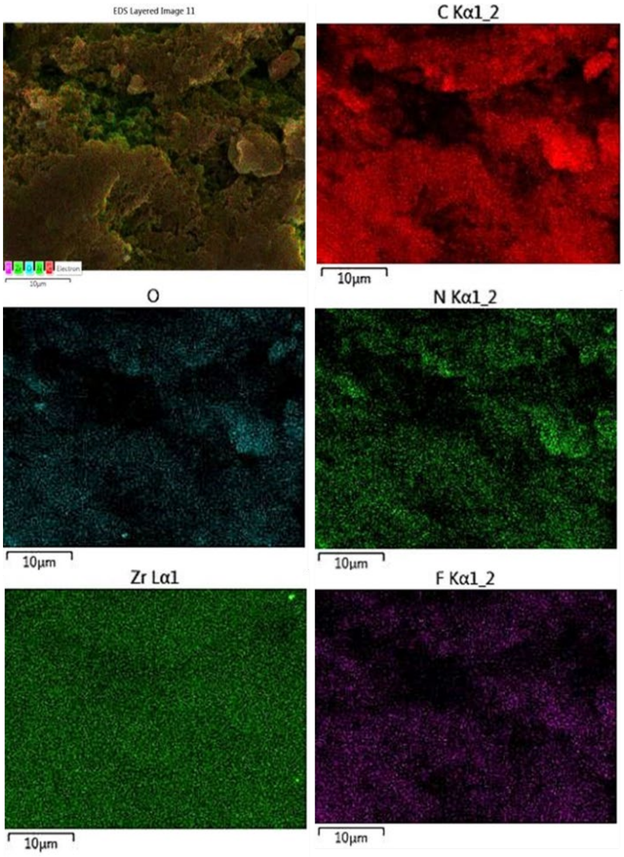

**Figure 2-3: Elemental mapping image of $HZrO_2$@PANI NFs after $F^-$ sorption showing the elemental distribution of Carbon (C), Nitrogen (N), Oxygen (O), Zirconium (Zr) and Fluorine (F).**

To confirm the interaction between Zr and F, the merged elemental distribution image was provided in Fig. 2.4. It was clearly noticed from Fig. 2.4 that there was interaction between Zr and F. This results confirmed the enhanced removal of $F^-$ by $HZrO_2$@PANI NFs compared to PANI NFs. The transmission electron microscopic analysis (Fig. 2.5(a)) showing a TEM micrograph of as-prepared $HZrO_2$@PANI NFs revealed nonfibrillar morphology which tended to conglomerate in an interconnected nanofibrous network with narrow diameter distribution. Fig. 2.5(a) indicated agglomerated hydrous zirconium oxide randomly deposited on the surface of PANI NFs matrix. STEM analysis (Fig. 2.5(b)) was also employed for better understanding of the distribution of $HZrO_2$ on the surface of PANI NFs. Fig. 2.5(c) depicts the distribution of carbon (contributed by PANI NFs) and Fig. 2.5(d) presents the random deposition of zirconium (contributed by $HZrO_2$), in as-synthesized $HZrO_2$@PANI NFs.

Fig. 2.6A depicts the zeta potentials of $HZrO_2$@PANI NFs as a function of solution pH to determine its point of zero charge, i.e. $pH_{pzc}$, which can be used to qualitatively evaluate the adsorbent's surface charge and demonstrate the protonation and deprotonation of its surface functional groups. The $pH_{pzc}$ for $HZrO_2$@PANI NFs is 9.8 (Fig. 2.6A), which is higher than bare PANI NFs ~7.9 as well as most of the literature reported $F^-$ adsorbents as well as most of the literature reported $F^-$ adsorbents [6,11]. This could be possibly due to the significantly higher specific surface area of $HZrO_2$@PANI NFs (~ 86.64 $m^2/g$) as compared to bare PANI NFs (~ 44.72 $m^2/g$), which apparently increased the number of accessible adsorption active surface functional groups by preventing the agglomeration of PANI chains due to $\pi$- $\pi^*$ aggregation, and hence eventually resulting in higher $pH_{pzc}$. At pH < $pH_{pzc}$ the superficial charge is positive, favouring anion adsorption via coulombic attraction and at pH > $pH_{pzc}$ the superficial charge is negative, favouring cation adsorption. Hence, in the present study high $pH_{pzc} \approx 9.8$ indicates that $HZrO_2$@PANI NFs is positively charged up to pH 9.8 and can efficiently adsorb negatively charged $F^-$ ions in the entire environmentally relevant pH range.

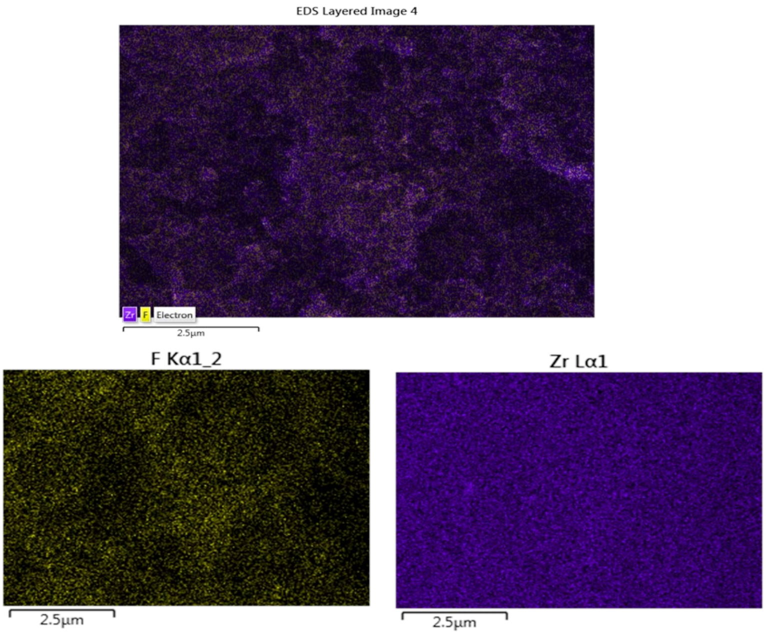

**Figure 2-4: Elemental mapping image of $HZrO_2$@PANI NFs after $F^-$ sorption showing the elemental distribution of Fluorine (F) and Zirconium (Zr).**

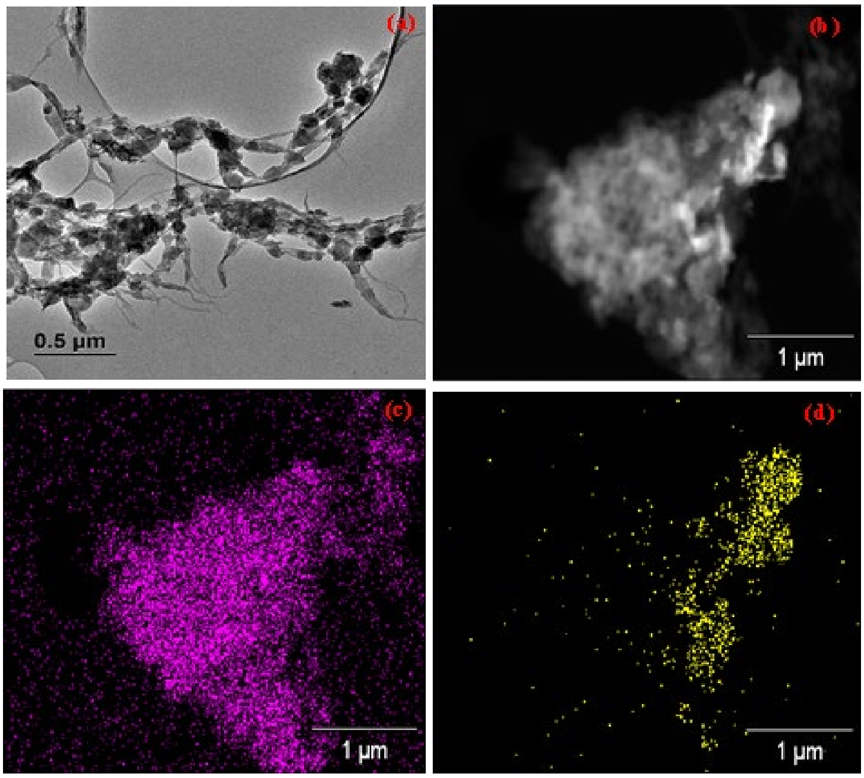

**Figure 2-5: (a) TEM image of $HZrO_2$@PANI NFs and (b) STEM images of $HZrO_2$@PANI NFs with (c) EDS mapping of Carbon and (d) Zirconium.**

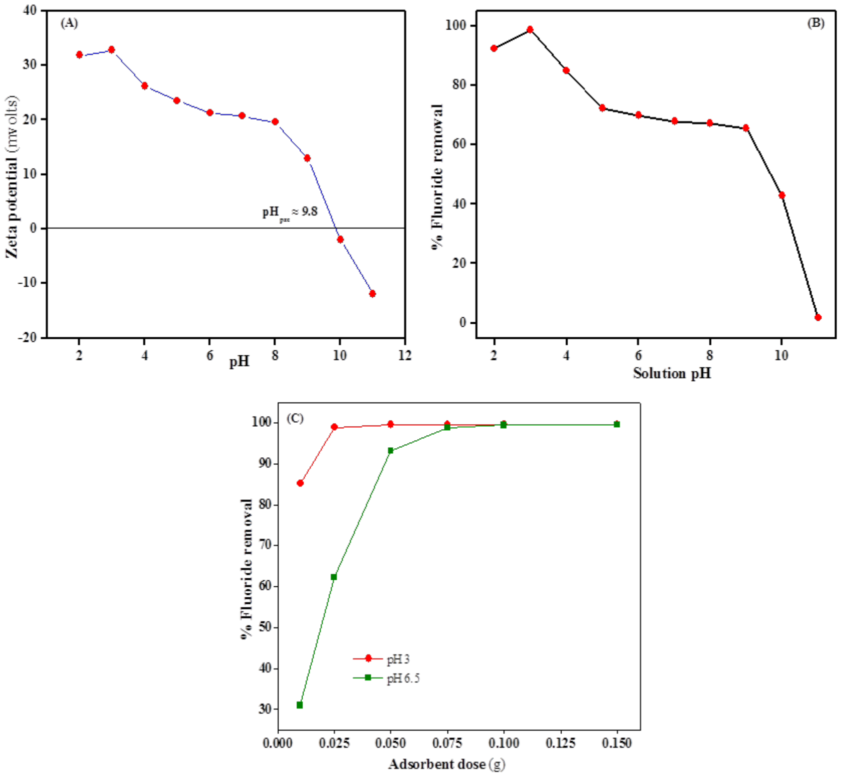

**Figure 2-6: (A) Zeta potential plot of $HZrO_2$@PANI NFs as a function of pH; (B) effect of solution pH and (C) effect of adsorbent dosages at pH 3 and 6.5 on % $F^-$ removal efficiency of $HZrO_2$@PANI NFs.**

### 2.3.2 Adsorption Characteristics

#### *2.3.2.1 Effect of % $ZrO_2$ content*

Effect of different % $HZrO_2$ loadings on $F^-$ removal efficiency of as-developed $HZrO_2$@PANI NFs was studied using 10 mg/L $F^-$ solution, an adsorbent dose of 0.025 g/50 mL at pH 6.5 ±0.1 and the results obtained are presented in Table 1.

**Table 2-1: Composition, yield and % $F^-$ removal obtained for different % loadings of $HZrO_2$ in as-synthesized adsorbents.**

| PANI NFs (g) | $ZrOCl_2.8H_2O$ (g) in 100 mL 0.01 N HCl | Yield (g) | % $ZrO_2$ deposited | Adsorbents symbol | % Fluoride removal |
|---|---|---|---|---|---|
| 0.25 | 0.5 | 0.4674 | 46.51 | $HZrO_2$ @PANI NFs-1 | 65.01 |
| 0.5 | 0.5 | 0.6604 | 24.29 | $HZrO_2$ @PANI NFs-2 | 69.37 |
| 0.75 | 0.5 | 0.8834 | 15.1 | $HZrO_2$ @PANI NFs-3 | 65.44 |
| 1 | 0.5 | 1.0894 | 8.21 | $HZrO_2$ @PANI NFs-4 | 60.86 |
| 1 | 0 | 1 | 0 | PANI NFs | 18.31 |

It was observed that pure PANI NFs demonstrated 18.31% $F^-$ removal which prominently increased to 69.37% with an increase in % $HZrO_2$ loading to 24.29 ($HZrO_2$@PANI NFs-3) and after that started decreasing. The highest $F^-$ removal efficiency (69.37%) displayed by $HZrO_2$@PANI NFs-3 with 24.29 wt. % $HZrO_2$ loading, might be attributed to its optimal structure with the maximum accessibility of active adsorption sites of both the counterparts (PANI NFs as well as $HZrO_2$) for the $F^-$ adsorption. Therefore, 24.29 wt. % $HZrO_2$ was chosen as an optimum wt. % $HZrO_2$ loading in as-synthesized $HZrO_2$@PANI NFs, to achieve the maximum $F^-$ removal efficiency.

#### *2.3.2.2 Effect of pH*

Solution pH as an imperative parameter, can meticulously affect the adsorption efficiency of an adsorbent via ionization of the surface functional groups, alteration of adsorbate speciation and the variation of the solution composition. The $F^-$ adsorption trend of $HZrO_2$@PANI NFs evaluated at different pH values (2 to 11) and depicted in Fig. 5B, reveals a relatively wide $F^-$ adsorption pH range from 3 to 9 with maximum $F^-$ removal (98%) achieved at pH 3, which slowly decreased to 42% at pH 10 and rapidly dropped to 1.7% at pH 11. This can be possibly ascribed to the change in the adsorbent's surface charges and high $pH_{pzc} \approx 9.8$ as shown in Fig 6A. The $F^-$ adsorption at $pH < pH_{pzc} \approx 9.8$, is a result of electrostatic attraction between positively charged surface of $HZrO_2$@PANI NFs (due to the protonation of the nitrogen atoms of the PANI matrix and hydroxyl groups of $HZrO_2$ in the presence of excess $H^+$ ions) and negatively charged $F^-$ ions [11,16]. At the same time, $Cl^-$ ions doped in PANI backbone and some unprotonated hydroxyl groups can still undergo ion exchange with anionic $F^-$ ions [13,21]. The release of $OH^-$ and $Cl^-$ ions in the solution was confirmed by increase of solution pH (Table 2) and appearance of white coloured precipitate of AgCl, upon addition of $AgNO_3$ to the filtrate (after adsorption), respectively.

**Table 2-2: Solution pH before and after $F^-$ adsorption.**

| Initial Ph | 2 | 3 | 4 | 5 | 6 | 7 | 8 | 9 | 10 | 11 |
|---|---|---|---|---|---|---|---|---|---|---|
| Final pH | 2.3 | 4.2 | 5 | 5.9 | 6.9 | 7.8 | 8.7 | 9.5 | 10.3 | 11.1 |

Whereas, at $pH = pH_{pzc} \sim 9.8$, when the adsorbent's surface turns neutral, the ion exchange mechanism was the predominant possible cause for the $F^-$ sorption. Hence, $F^-$ adsorption on $HZrO_2$@PANI NFs can be visualised as a concurrent outcome of both electrostatic attractions and ion-exchange mechanisms.

A decreased $F^-$ adsorption at $pH < 3$, can be attributed to the formation of electrically neutral hydrofluoric acid, which will reduce the coulombic forces between $F^-$ and adsorbent surface [25]. At higher pH values ( $pH > pH_{pzc} \sim 9.8$), $HZrO_2$@PANI NFs were negatively charged due to deprotonation of the nitrogen atoms of the PANI NFs and hydroxyl groups of $HZrO_2$, which tended to repel the anionic $F^-$ ions via columbic repulsion and decreased the $F^-$ adsorption [11,16]. Meanwhile, $OH^-$ ions present in aqueous solution are also more likely compete with $F^-$ ions for the same adsorption sites and thus further contribute to the decrease in $F^-$ removal at high alkaline pH [26]. Although $HZrO_2$@PANI NFs exhibited maximum $F^-$ removal at optimum pH 3, it was interesting to note that 65% $F^-$ removal was still maintained up to pH 9, and due to this wide range pH applicability, $HZrO_2$@PANI NFs as an adsorbent is anticipated to be beneficial for $F^-$ removal from real field natural water as well as industrial wastewater.

#### *2.3.2.3 Effect of adsorbent dosage*

The effect of adsorbent dosage variation on $F^-$ removal efficiency of $HZrO_2$@PANI NFs at pH 3 and pH 6.5 was evaluated and is depicted as a dose responsive curve in Fig. 5C. It can be seen that at pH 3, the % F$^-$ removal sharply increased from 85.13 to 98.90% with an increase in adsorbent dose from 0.01 to 0.025 g, whereas pH 6.5, demonstrated a gradual increase in % F$^-$ removal from 30.97 to 98.85% with an increase in adsorbent dose from 0.01 to 0.075 g. This increase in the % F$^-$ removal with increase in adsorbent dose might be speculated as a direct consequence of enrichment in the number of active sites available for F$^-$ ions adsorption from a fixed initial solute concentration [19]. However, a further increase in adsorbent dose beyond 0.025 and 0.075 g, showed no substantial quantitative effect on adsorption efficiency. This might be because after the adsorption of most of the F$^-$ ions, the lower equilibrium F$^-$ ion concentration per active site of adsorbent becomes a limiting factor for further F$^-$ adsorption [27]. Hence to maintain low cost and effectiveness, 0.025 g and 0.075 g were assessed as optimum dosages of $HZrO_2$@PANI NFs for F$^-$ removal at pH 3 and pH 6.5, respectively.

### *2.3.2.4 Adsorption kinetics*

The kinetic performance of an adsorbent is of great significance for its pilot application as it provides the adsorbate uptake rate, to determine the residence time required for completion of adsorption reaction [28]. Fig. 2.7A depicts the effect of contact time on the adsorption of F$^-$ ions by $HZrO_2$@PANI NFs at initial F$^-$ concentrations of 5, 10, 15 and 20 mg/L, respectively. It clearly manifested rapid initial F$^-$ uptake with nearly 80% removal in first 20 min, followed by a slower removal rate that gradually attained equilibrium in 30 min for F$^-$ concentration 5 mg/L and 180 min for F$^-$ concentration 20 mg/L. Fig. 7B illustrates temperature-dependent kinetics demonstrating the effect of contact time on F$^-$ sorption at different temperatures (15, 25, 35 and 45°C) and fixed initial F$^-$ concentration of 10 mg/L.

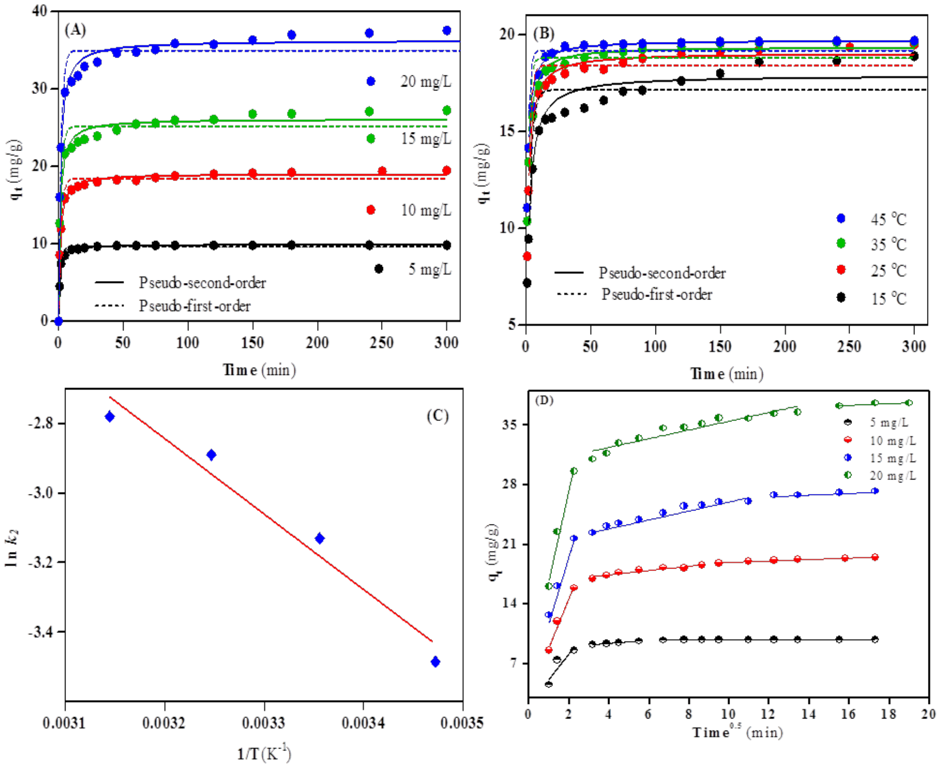

**Figure 2-7: (A) Effect of contact time and non-linear pseudo-second-order and pseudo-first-order model for different initial concentrations; (B) effect of contact time and non-linear pseudo-second-order and pseudo-first-order model for different temperatures; (C) Arrhenius plot and (D) intraparticle diffusion model for F$^-$ adsorption.**

To have a better understanding of adsorption reaction kinetics and F$^-$ adsorption rate on HZrO$_2$@PANI NFs, two most widely employed kinetic models, pseudo-second-order and pseudo-first-order, were applied to fit the experimental data obtained from concentration (Fig. 6A) as well as temperature dependent kinetics (Fig. 2.7B). The non-linear forms of the pseudo-first-order and pseudo-second-order kinetic models can be represented by equations (5) and (6), respectively:

$$q_t = q_e(1 - \exp(-k_1 t) \tag{5}$$

$$q_t = \frac{k_2 {q_e}^2 t}{1 + k_2 q_e t} \tag{6}$$

where $q_e$ and $q_t$ are adsorption capacities in mg/g at equilibrium and time $t$ (min), respectively; $k_1$ (1/min) and $k_2$ (g/mg/min) are the pseudo-first-order and pseudo-second-order rate constants, respectively.

Fig. 7A and 7B display the concentration and temperature dependent kinetic data fits for non-linear pseudo-second-order and pseudo-first-order kinetic equations (5-6), respectively. The linear fittings for concentration and temperature dependent kinetics were also obtained after applying linear pseudo-second-order and pseudo-first-order kinetic equations and the respective plots are depicted in Fig 2.8A, B, C and D, respectively. The corresponding kinetic parameters calculated from the non-linear and linear regression analysis of the Fig. 2.7A and 2.7B are tabulated in Table 2.3 and Table 2.4, respectively.

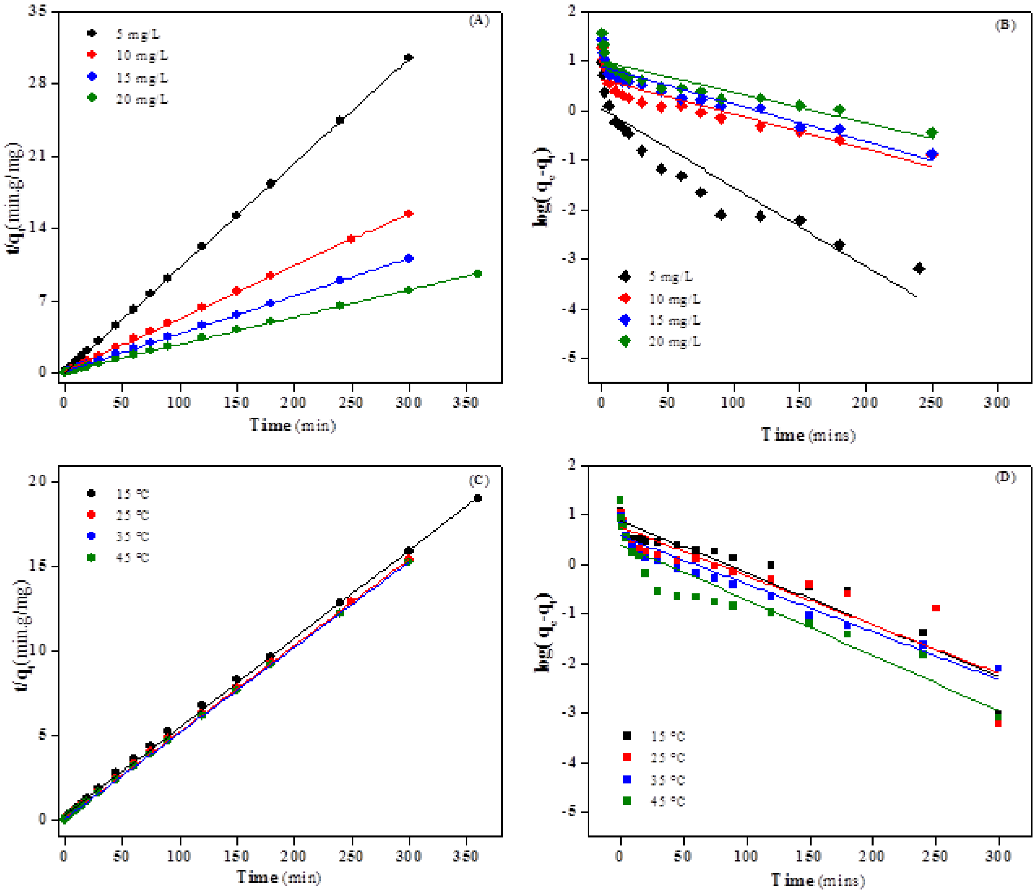

**Figure 2-8: Linear fit of (A) pseudo-second-order and (B) pseudo-first-order model for different initial F$^-$ concentrations and (C) pseudo-second-order and (D) pseudo-first-order model for different temperatures at initial F$^-$ concentration 10 mg/L.**

**Table 2-3: Kinetic parameters for $F^-$ adsorption by $HZrO_2$@PANI NFs.**

| Kinetic Models | Parameters | Initial Concentration (mg/L) | | | | Temperature (°C) | | | |
|---|---|---|---|---|---|---|---|---|---|
| | | 5 | 10 | 15 | 20 | 15 | 25 | 35 | 45 |
| Pseudo-second-order | Best fit values | | | | | | | | |
| | $k_2$ (g/mg/min) | 0.109 | 0.044 | 0.032 | 0.021 | 0.031 | 0.044 | 0.056 | 0.062 |
| | $q_e$ (mg/g) | 9.948 | 19.07 | 26.15 | 36.28 | 17.92 | 19.07 | 19.39 | 19.73 |
| | Std Error. | | | | | | | | |
| | $k_2$ | 0.009 | 0.002 | 0.003 | 0.002 | 0.003 | 0.002 | 0.002 | 0.002 |
| | $q_e$ | 0.074 | 0.097 | 0.263 | 0.300 | 0.223 | 0.097 | 0.085 | 0.065 |
| | Goodness of fit | | | | | | | | |
| | Degree of freedom | 15 | 15 | 15 | 16 | 16 | 15 | 15 | 15 |
| | $R^2$ | 0.992 | 0.996 | 0.986 | 0.990 | 0.98 | 0.996 | 0.997 | 0.998 |
| | Absolute sum of squares | 0.888 | 1.436 | 10.58 | 15.91 | 8.133 | 1.436 | 1.157 | 0.702 |
| | *Sy.x* | 0.243 | 0.309 | 0.839 | 0.996 | 0.713 | 0.309 | 0.277 | 0.215 |
| | Number of points analysed | 17 | 17 | 17 | 18 | 18 | 17 | 17 | 17 |
| Pseudo-first-order | Best fit values | | | | | | | | |
| | $k_1$(1/min) | 0.656 | 0.531 | 0.550 | 0.511 | 0.376 | 0.531 | 0.665 | 0.724 |
| | $q_e$ (mg/g) | 9.667 | 18.42 | 25.20 | 34.98 | 17.16 | 18.42 | 18.8 | 19.19 |
| | Std Error. | | | | | | | | |
| | $k_1$ | 0.039 | 0.047 | 0.071 | 0.061 | 0.056 | 0.053 | 0.067 | 0.065 |
| | $q_e$ | 0.078 | 0.222 | 0.442 | 0.552 | 0.349 | 0.222 | 0.254 | 0.228 |
| | Goodness of fit | | | | | | | | |
| | Degree of freedom | 15 | 15 | 15 | 16 | 16 | 15 | 15 | 15 |
| | $R^2$ | 0.988 | 0.975 | 0.949 | 0.955 | 0.935 | 0.976 | 0.966 | 0.974 |
| | Absolute sum of squares | 1.221 | 9.784 | 39.00 | 69.09 | 26.68 | 9.784 | 13.07 | 10.62 |
| | *Sy.x* | 0.285 | 0.807 | 1.613 | 2.078 | 1.291 | 1.452 | 0.933 | 0.841 |
| | Number of points analysed | 17 | 17 | 17 | 18 | 18 | 17 | 17 | 17 |

**Table 2-4: Kinetic parameters evaluated from pseudo-first-order and pseudo-second-order linear fit for $F^-$ sorption by $HZrO_2$@PANI NFs.**

| Kinetic Models | Parameters | Initial Concentration (mg/L) | | | | Temperature (°C) | | | |
|---|---|---|---|---|---|---|---|---|---|
| | | 5 | 10 | 15 | 20 | 15 | 25 | 35 | 45 |
| Pseudo-second-order | $k_2$ | 0.173 | 0.024 | 0.013 | 0.008 | 0.011 | 0.024 | 0.035 | 0.064 |
| | $q_e$ | 9.862 | 19.49 | 27.32 | 37.74 | 19.048 | 19.49 | 19.72 | 19.92 |
| | $R^2$ | 1 | 0.9998 | 0.9997 | 0.9997 | 0.9992 | 0.9998 | 1 | 1 |
| Pseudo-first-order | $k_1$ | 0.042 | 0.016 | 0.024 | 0.020 | 0.024 | 0.016 | 0.022 | 0.026 |
| | $q_e$ | 1.13 | 1.884 | 2.729 | 3.026 | 2.411 | 1.884 | 1.771 | 1.496 |
| | $R^2$ | 0.855 | 0.801 | 0.862 | 0.839 | 0.913 | 0.801 | 0.915 | 0.862 |

Units: $q_e$: (mg/g), $k_1$: (1/min), $k_2$: (g/mg/min)

The regression coefficients ($R^2$) values obtained for the pseudo-second-order model were higher than those obtained for the pseudo-first-order model for both concentration and temperature-dependent kinetics, thus indicating a better fit of experimental kinetic data to the pseudo-second-order model. Moreover, experimental $q_e$ values were also in good agreement with the calculated ones by the pseudo-second order model. Overall, the results demonstrated that the concentration as well as temperature dependent kinetics of $F^-$ adsorption onto $HZrO_2$@PANI NFs obeyed the pseudo-second-order kinetic model. It was observed in Fig. 2.9B, that $q_e$ values increased with increase in temperature which thereby manifested the endothermic nature of $F^-$ adsorption. Besides, pseudo-second-order rate constant $k_2$ rose from 0.031 to 0.062 g/mg/min with an increase in the temperature from 15°C to 45°C that might be accredited to the Arrhenius law of temperature dependence of reaction rates. Hence, to evaluate the apparent activation energy involved in $F^-$ adsorption onto $HZrO_2$@PANI NFs, pseudo-second-order rate constants, $k_2$ obtained from temperature dependent kinetics were applied to linear Arrhenius equation (7).

$$\ln k_2 = \ln A + \left(-\frac{E_a}{R}\right)\frac{1}{T} \tag{7}$$

where $A$ is the pre-exponential factor (g/mg/min), $E_a$ is adsorption activation energy (kJ/mol), $R$ is gas constant (0.008314 kJ/mol/K), and $T$ is the temperature (K). $E_a$ was evaluated from the slope of the plot of ln $k_2$ against $1/T$ (Fig. 2.7C) and came out to be 18.04 kJ/mol (< 40 kJ/mol) suggesting physical nature of $F^-$ sorption [29].

Furthermore, the rate determining step and mechanism involved in $F^-$ adsorption onto $HZrO_2$@PANI NFs was explored by the Weber-Morris intraparticle diffusion model as expressed in equation (8).

$$q_t = k_{int} t^{0.5} + C_i \tag{8}$$

where $k_{int}$ ($mg/g/min^{0.5}$) is the intraparticle diffusion rate constant, and $C_i$ (mg/g) is the thickness of boundary layer.

Fig. 2.7D depicts the intraparticle diffusion plots for four initial $F^-$ concentrations studied with multilinearity, which infers that the process involves more than one kinetic stage (or sorption rates) [30]. The first rapid region indicates initial boundary layer effect due to binding of $F^-$ ions to the adsorbent's surface, followed by second region involving gradual diffusion of $F^-$ ions inside the pores of adsorbent also known as intraparticle diffusion stage and the last region of curve is the equilibrium stage. The values of the intra-particle diffusion rate constants, $k_{int}$ and intercepts, $C_i$ were calculated from the slopes and intercepts of the first and second region, of the curve (Fig. 2.7D) and are presented in Table 5. From results (Table 2.1), it was observed that both regions fit well to the Weber-Morris model

($R^2$ > 0.900) and therefore, signify the intraparticle diffusion as a dominant rate-limiting step in $F^-$ adsorption on $HZrO_2$@PANI NFs.

**Table 2-5: Intraparticle diffusion model parameters for $F^-$ adsorption by $HZrO_2$@PANI NFs.**

| Initial concentration (mg/L) | First phase | | | Second phase | | |
|---|---|---|---|---|---|---|
| | $k_{int1}$ (mg/g.min$^{0.5}$) | $C_{i1}$ (mg/g) | $R_1^2$ | $k_{int2}$ (mg/g.min$^{0.5}$) | $C_{i\,2}$(mg/g) | $R_2^2$ |
| 5 | 2.994 | 2.206 | 0.818 | 0.192 | 8.625 | 0.998 |
| 10 | 5.764 | 3.204 | 0.980 | 0.256 | 16.42 | 0.907 |
| 15 | 7.184 | 5.703 | 0.997 | 0.487 | 21.26 | 0.950 |
| 20 | 10.627 | 6.238 | 0.975 | 0.512 | 30.36 | 0.917 |

#### *2.3.2.5 Adsorption isotherm*

An adsorption isotherm is a prerequisite to calculate the adsorption capacity of the sorbent and to design and operate and adsorption system proficiently [31]. Fig. 9A. shows the pH dependent isotherm illustrating the effect of pH (3-6.5) on $F^-$ adsorption by $HZrO_2$@PANI NFs at 25°C. Likewise, Fig. 2.9B presents the conventional temperature dependent adsorption isotherm depicting the effect of temperature (15, 25, 35 and 45°C) on $F^-$ adsorption at pH 3. Furthermore, $F^-$ adsorption equilibrium data obtained (Fig. 2.7A-B) was fitted with two eminent isotherm models, Langmuir and Freundlich to estimate the adsorption equilibrium characteristics. Langmuir model depicts monolayer adsorption on the structurally homogeneous surface of the adsorbent with identical binding sites and is expressed in non-linear form by equation (9) [32]:

$$q_e = \frac{b.q_m.C_e}{1+b.C_e} \tag{9}$$

where, $q_m$ (mg/g) and $b$ (L/mg) are Langmuir constants related to maximum adsorption capacity and binding energy of adsorption, respectively. Furthermore, the Langmuir constant, b, is used to calculate the feasibility of the adsorption process by means of a dimensionless constant, called separation factor ($R_L$). The mathematical expression of $R_L$ is expressed by equation (10):

$$R_L = \frac{1}{1+bC_0} \tag{10}$$

where $C_o$ (mg/L) is the initial concentration of $F^-$ ions. The value of separation factor ($R_L$) indicates the type of isotherm to be irreversible when $R_L = 0$, favorable when $0 < R_L < 1$, linear for $R_L = 1$or unfavorable for $R_L > 1$ [33].

The Freundlich model assumes multilayer adsorption on energetically heterogeneous surfaces and expressed in non-linear form by equation (11) [32]:

$$q_e = K_f.C_e{}^{1/n} \tag{11}$$

where, $K_f$ (mg/g) and $1/n$ are the symbolic Freundlich constants, which signify the adsorption capacity and adsorption intensity, respectively.

Fig 2.9A shows the non-linear fits for Langmuir and Freundlich model, for pH dependent isotherm data obtained at pH 3, 4, 5 and 6.5 respectively, while non-linear fits for Langmuir and Freundlich model, for temperature dependent isotherm data obtained at 15, 25, 35 and 45°C, respectively are depicted in Fig. 2.9B.

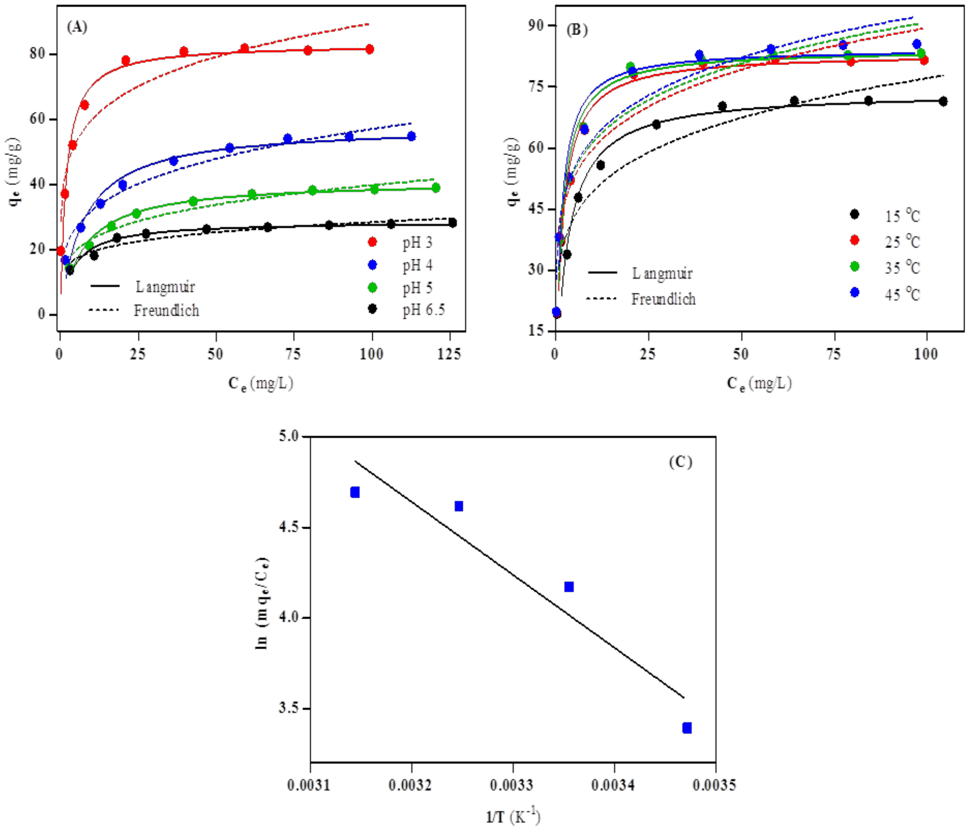

**Figure 2-9: Langmuir and Freundlich model fitting of adsorption isotherm data obtained at (A) different initial solution pH values (3, 4, 5 and 6.5), (B) different temperatures, i.e. 15, 25, 35 and 45°C and (C) Vant Hoff's plot.**

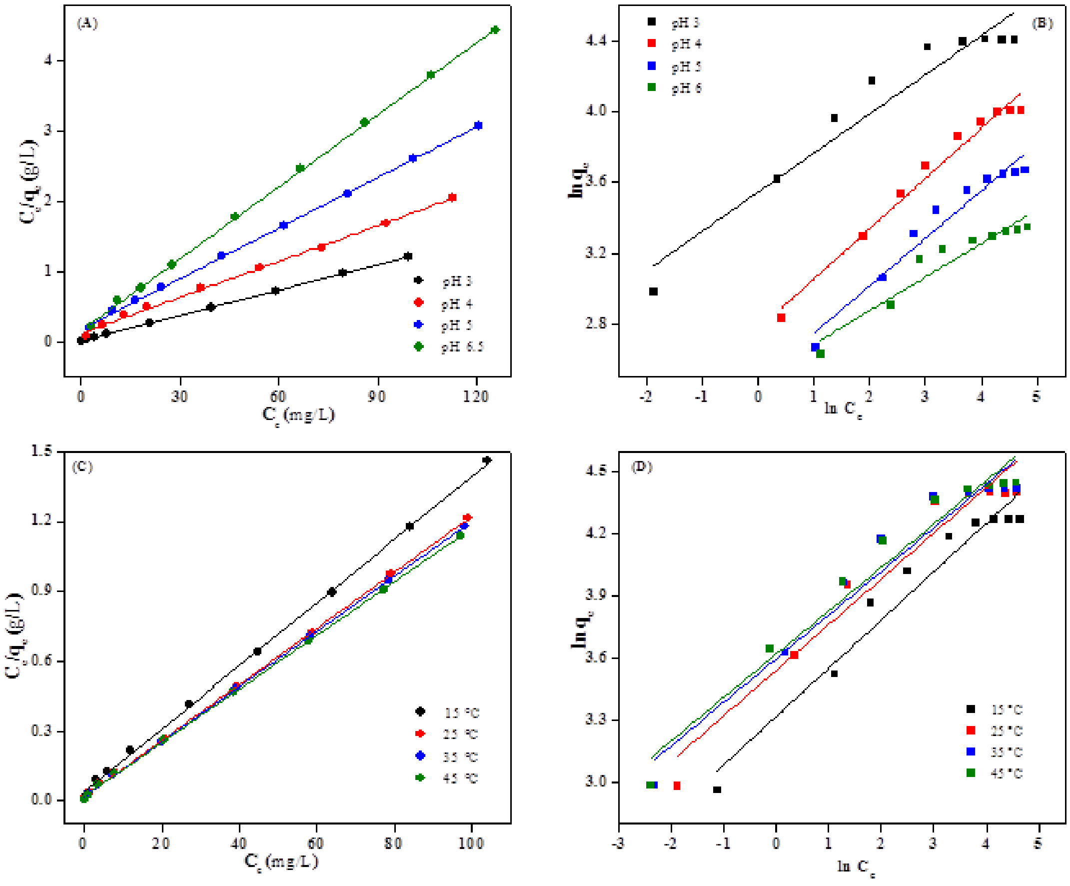

**Figure 2-10: (A) Langmuir and (B) Freundlich model linear fittings of pH-dependent adsorption isotherm obtained at differents pHs; (C) Langmuir and (D) Freundlich model linear fittings of temperature dependent isotherm data obtained at different temperatures.**

Langmuir and Freundlich model linear fits were also obtained after applying linear Langmuir and Freundlich equations (S3-S4) (Appendix) to both pH and temperature dependent isotherms and are presented in Fig 2.10(A-B) and 2.10C-D) (supplementary figures), respectively. The related isotherm parameters were also calculated for non-linear and linear fittings, and are indicated in Table 2.6 and Table 2.7, respectively. The relatively higher $R^2$ (correlation coefficient) values obtained for Langmuir model (non-linear as well as linear) suggested Langmuir model as a more appropriate and better fit for $F^-$ sorption onto $HZrO_2$@PANI NFs as compared to Freundlich model for all pHs (3, 4, 5 and 6.5) and temperatures (15, 25, 35 and 45°C) studied. The maximum adsorption capacities $q_m$, as calculated from non-linear Langmuir fit of pH dependent isotherms were 83.23, 58.10, 41.26 and 28.77 mg/g at pH 3, 4, 5 and 6.5, respectively. Moreover, the maximum adsorption capacities $q_m$, evaluated from non-linear Langmuir fit of temperature dependent isotherms, increased from 73.81 to 84.45 mg/g with an increase in the temperature from 15 to 45°C, signifying the endothermic nature of adsorption process. The values of $R_L$ were found to be less than unity thereby confirming the favourable nature of $F^-$ adsorption on $HZrO_2$@PANI NFs over the range of temperature studied.

**Table 2-6: Langmuir and Freundlich isotherm parameters for $F^-$ sorption by $HZrO_2$@PANI NFs**

| Isotherm models | Parameters | pH variation at 25°C | | | | Temperature variation (°C) at pH 3 | | | |
|---|---|---|---|---|---|---|---|---|---|
| | | 3 | 4 | 5 | 6.5 | 15 | 25 | 35 | 45 |
| Langmuir | Best fit values | | | | | | | | |
| | $q_{max}$ (mg/g) | 83.23 | 58.1 | 41.26 | 28.77 | 73.81 | 83.23 | 84.25 | 84.45 |
| | *b* (L/mg) | 0.545 | 0.134 | 0.134 | 0.239 | 0.317 | 0.545 | 0.599 | 0.701 |
| | Std Error. | | | | | | | | |
| | $q_{max}$ | 2.84 | 2.156 | 0.984 | 0.644 | 2.793 | 2.84 | 3.215 | 3.568 |
| | *b* | 0.119 | 0.024 | 0.016 | 0.036 | 0.071 | 0.118 | 0.15 | 0.207 |
| | Goodness of fit | | | | | | | | |
| | Degree of freedom | 7 | 7 | 7 | 7 | 7 | 7 | 7 | 7 |
| | $R^2$ | 0.95 | 0.956 | 0.976 | 0.951 | 0.941 | 0.949 | 0.937 | 0.921 |
| | Absolute sum of squares | 212.6 | 66.4 | 14.92 | 9.651 | 172.4 | 212.6 | 279.1 | 364.4 |
| | *Sy.x* | 5.511 | 3.08 | 1.46 | 1.174 | 4.963 | 5.511 | 6.314 | 7.215 |
| | Number of points analysed | 9 | 9 | 9 | 9 | 9 | 9 | 9 | 9 |
| Freundlich | Best fit values | | | | | | | | |
| | $k_f$ (mg/g) | 39.98 | 17.9 | 13.6 | 13.23 | 31.56 | 39.98 | 41.58 | 41.86 |
| | *1/n* | 0.175 | 0.252 | 0.2335 | 0.167 | 0.194 | 0.175 | 0.17 | 0.173 |
| | Std Error. | | | | | | | | |
| | $k_f$ | 3.851 | 1.54 | 1.382 | 1.244 | 2.984 | 3.851 | 3.69 | 3.034 |
| | *1/n* | 0.026 | 0.021 | 0.025 | 0.023 | | | | |
| | Goodness of fit | | | | | | | | |
| | Degree of freedom | 7 | 7 | 7 | 7 | 7 | 7 | 7 | 7 |

| | | | | | | | | | |
|---|---|---|---|---|---|---|---|---|---|
| | $R^2$ | 0.912 | 0.965 | 0.944 | 0.902 | 0.931 | 0.912 | 0.92 | 0.948 |
| | Absolute sum of squares | 372.9 | 50.95 | 34.21 | 19.4 | 199.4 | 372.9 | 347.6 | 236.9 |
| | *Sy.x* | 7.299 | 2.698 | 2.211 | 1.665 | 5.337 | 7.299 | 7.047 | 5.818 |
| | Number of points analysed | 9 | 9 | 9 | 9 | 9 | 9 | 9 | 9 |

**Table 2-7: Isotherm parameters evaluated from Langmuir and Freundlich linear fit for $F^-$ sorption by $HZrO_2$@PANI NFs.**

| Isotherm models | Parameters | pH variation at 25°C | | | | Temperature variation (°C) at pH 3 | | | |
|---|---|---|---|---|---|---|---|---|---|
| | | 3 | 4 | 5 | 6.5 | 15 | 25 | 35 | 45 |
| Langmuir | $q_{max}$ (mg/g) | 83.33 | 58.82 | 41.66 | 29.24 | 74.07 | 83.33 | 84.75 | 85.96 |
| | *b* (L/mg) | 0.658 | 0.133 | 0.13 | 0.205 | 0.357 | 0.658 | 0.694 | 0.593 |
| | $R_L$ | 0.132 | 0.428 | 0.435 | 0.328 | 0.219 | 0.132 | 0.126 | 0.143 |
| | $R^2$ | 0.9997 | 0.9981 | 0.9993 | 0.9996 | 0.9994 | 0.9997 | 0.9998 | 0.9996 |
| Freundlich | $k_f$ (mg/g) | 34.67 | 16.03 | 11.98 | 12.18 | 27.71 | 34.67 | 36.66 | 37.47 |
| | *1/n* | 0.22 | 0.282 | 0.267 | 0.189 | 0.233 | 0.22 | 0.21 | 0.209 |
| | $R^2$ | 0.9361 | 0.9772 | 0.9529 | 0.912 | 0.9503 | 0.9361 | 0.9466 | 0.9598 |

**Table 2-8: Atomic % of O, Cl and F elements.**

| | Atomic % of | | |
|---|---|---|---|
| Materials | O | Cl | F |
| $HZrO_2$@PANI NFs before $F^-$ adsorption | 20.7 | 1.4 | - |
| $HZrO_2$@PANI NFs after $F^-$ adsorption | 11.6 | 0.4 | 3.5 |

Furthermore, a comparative assessment of maximum adsorption capacity and working pH of $HZrO_2$@PANI NFs with various zirconium and polyaniline based composites for $F^-$ removal reported in the literature is presented in Table 2.5 [13-15,21,22,25,34-41]. It can be seen that $HZrO_2$@PANI NFs provided better adsorption capacity than most of the adsorbents, at pH 3 as well as drinking water pH

~ 6.5. Moreover, the adsorption capacity of $HZrO_2$@PANI NFs (at pH ~ 6.5) is nearly 36 times higher than that of bare PANI (at pH 7). Therefore $HZrO_2$@PANI NFs as a promising adsorbent can be applied to defluoridation of groundwater as well as industrial wastewater due to its high adsorption capacity and relatively wider working pH range.

**Table 2-9: A comparative assessment of the defluoridation capacity of $HZrO_2$@PANI NFs with other adsorbents.**

| Adsorbents | $Q_{max}$ (mg/g) | pH | References |
|---|---|---|---|
| Zr(IV) entrapped chitosan polymeric matrix | 4.85 | 7 | 34 |
| Zr(IV) impregnated dithiocarbamate modified chitosan beads | 4.58 | 7 | 35 |
| Chitosan-montmorillonite-$ZrO_2$ NC | 23 | 4 | 36 |
| Polyacryamide-Zr complex | 9.6 | 3 | 22 |
| Zirconium alginate beads | 32.797 | 2 | 37 |
| Polyacryamide-Zr magnetic nanocomposite | 124.5 | 3 | 25 |
| Zirconium-Modified-Na-attapulgite | 24.55 | 4.13 ± 0.02 | 38 |
| Beta-cyclodextrin modified hydrous zirconium oxide | 31.45 | 5.5 | 21 |
| $ZrO_2$ impregnated chitosan beads | 22.1 | 5 | 39 |
| Granular zirconium iron oxide | 9.8 | 7 | 40 |
| Polyaniline | 0.78 | 7 | 13 |
| Polyaniline-Chitosan composite | 5.9 | 7 | 14 |
| Polyaniline-alumina composite | 6.6 | 7 | 15 |
| Chitosan-polyaniline/zirconium biopolymeric complex | 8.713 | 7 | 41 |
| $HZrO_2$@PANI NFs | 83.23 | 3 | Present work |
| $HZrO_2$@PANI NFs | 28.77 | 6.5 | Present work |

### *2.3.2.6 Adsorption thermodynamics*

Thermodynamic parameters such as $\Delta G^o$ (Gibb's free energy change), $\Delta H^o$ (enthalpy change) and $\Delta S^o$ (entropy change) for $F^-$ adsorption onto $HZrO_2$@PANI NFs can be calculated from temperature dependent isotherm data, to ascertain the thermodynamic spontaneity and feasibility of the adsorption process. Hence, temperature dependent isotherm data (*section 3.2.5*) was employed to the well-known thermodynamic relations, i.e. Gibbs isotherm equation (12) and Vant Hoff equation (13):

$$\Delta G^\circ = -RT\ln K_c = -RT\ln(m\frac{q_e}{C_e}) \tag{12}$$

$$\ln K_c = \ln(m\frac{q_e}{C_e}) = \frac{-\Delta H^\circ}{RT} + \frac{\Delta S^\circ}{R} \tag{13}$$

where, $R$ (0.008314 kJ/mol/K) is the gas constant, $T$ is the temperature in Kelvin, and $K_c$ is the thermodynamic equilibrium constant, $m$ is the adsorbent dose (g/L), and the ratio $mq_e/C_e$ is the adsorption affinity. The values of $\Delta H^o$ and $\Delta S^o$ were computed from the slope and intercept of the classic Vant Hoff plot of ln $mq_e/C_e$ against 1/T (Fig. 2.9C) and the results are listed in Table 2.10. The increasingly negative $\Delta G^o$ values (Table 2.10) with increase in temperature suggested the increase in degree of spontaneity and feasibility of $F^-$ adsorption. The positive value of $\Delta H^o$ confirmed the endothermic nature of adsorption process [42]. Furthermore, the positive value of $\Delta S^o$ signifies the increased randomness at the solid-liquid interface due to displacement of the coordinated water molecules during $F^-$ adsorption [43].

**Table 2-10: Thermodynamic parameters for adsorption of $F^-$ onto $HZrO_2$@PANI NFs.**

| Temperature (K) | $\Delta H^\circ$ (kJ/mol) | $\Delta S^\circ$ (kJ/mol/K) | $\Delta G^\circ$ (kJ/mol) |
|---|---|---|---|
| 15 | 33.44 | 0.145 | -8.128 |
| 25 | | | -10.33 |
| 35 | | | -11.83 |
| 45 | | | -12.41 |

### *2.3.2.7 Effect of co-existing anions*

Anions such as chloride ($Cl^-$), nitrate ($NO_3^-$), bicarbonate ($HCO_3^-$), sulfate ($SO_4^{2-}$) and phosphate ($PO_4^{3-}$) are some of the most commonly present coexisting anions in natural water environments, which can possibly compete with $F^-$ ions for adsorption sites. Therefore, the impact of these coexisting anions on $F^-$ adsorption onto $HZrO_2$@PANI NFs was investigated as a function of initial concentration of $Cl^-$, $NO_3^-$, $SO_4^{2-}$, $HCO_3^-$ and $PO_4^{3-}$ (0-40 mg/L) at optimum pH 3 and drinking water pH 6.5 ±0.1, and depicted in Fig 2.8A and 2.8B, respectively. It was observed that at pH 3 (Fig. 2.8A) $Cl^-$, $NO_3^-$ and $SO_4^{2-}$ ions have no significant effect on $F^-$ removal, while $PO_4^{3-}$ ions at its concentration 40 mg/L, decreased the $F^-$ removal by 6%. Similarly, at pH 6.5 ±0.1, $Cl^-$ and $NO_3^-$ exhibited no noteworthy effect on $F^-$ removal, but $SO_4^{2-}$, $HCO_3^-$ $PO_4^{3-}$ displayed obvious interference in following the order: $PO_4^{3-} > HCO_3^- > SO_4^{2-}$. Herein, $Cl^-$ and $NO_3^-$ being low-affinity ligands involve weaker bonds via outer-sphere complex formation and thus did not interfere with the $F^-$ removal while $SO_4^{2-}$ forms both outer and inner-sphere surface complexes and hence considerably affected the $F^-$ removal [44]. Besides, $HCO_3^-$ hydrolyzed and raised the solution pH by producing more hydroxyl ions to compete with $F^-$ ions for the adsorption sites and thus hindered the $F^-$ adsorption [45]. However, $PO_4^{3-}$ ions demonstrated the major negative impact on $F^-$ removal because like $F^-$, $PO_4^{3-}$ also forms inner-sphere surface complex and can compete with $F^-$ ions for same adsorption sites [46]. Typically, $SO_4^{2-}$ and $PO_4^{3-}$ are present in very low concentrations in natural waters and hence does not exhibit strong interferences in real field conditions [47]. Conclusively, the developed adsorbent demonstrated much more selective uptake of $F^-$ ions at pH 3 than drinking water pH 6.5 ±0.1.

### **2.3.3 Real field study**

The real field applicability of $HZrO_2$@PANI NFs was established using real water samples collected from a borehole in northwest province, South Africa. Some chemical characteristics of groundwater sample were assessed as pH (7.7), electrical conductivity (680 μS/cm), $F^-$ (1.4 mg/L), $Cl^-$ (20.27 mg/L), $NO_3^-$ (2.32 mg/L), $SO_4^{2-}$ (16.28 mg/L) and $PO_4^{3-}$ (1.07 mg/L). The groundwater was spiked with known amount of fluoride to increase its $F^-$ concentration to 5.48 mg/L and effect of adsorbent dosages were studied at optimum pH 3 (adjusted using 0.1-1M HCl) and pH 8.9 (pH of spiked fluoride groundwater) as shown in Fig. 2.11A and 2.11B, respectively, It was noticed that at pH 3, 0.025 g of $HZrO_2$@PANI NFs demonstrated 92.95% $F^-$ removal and effectively reduced the $F^-$ concentration to 0.39 mg/L which is much below the WHO recommended limit of $F^-$ in drinking water (<1.5 mg/L), whereas at pH 8.9, 0.15 g of $HZrO_2$@PANI NFs was needed to bring down the $F^-$ concentration to 1.29 mg/L (< 1.5 mg/L).

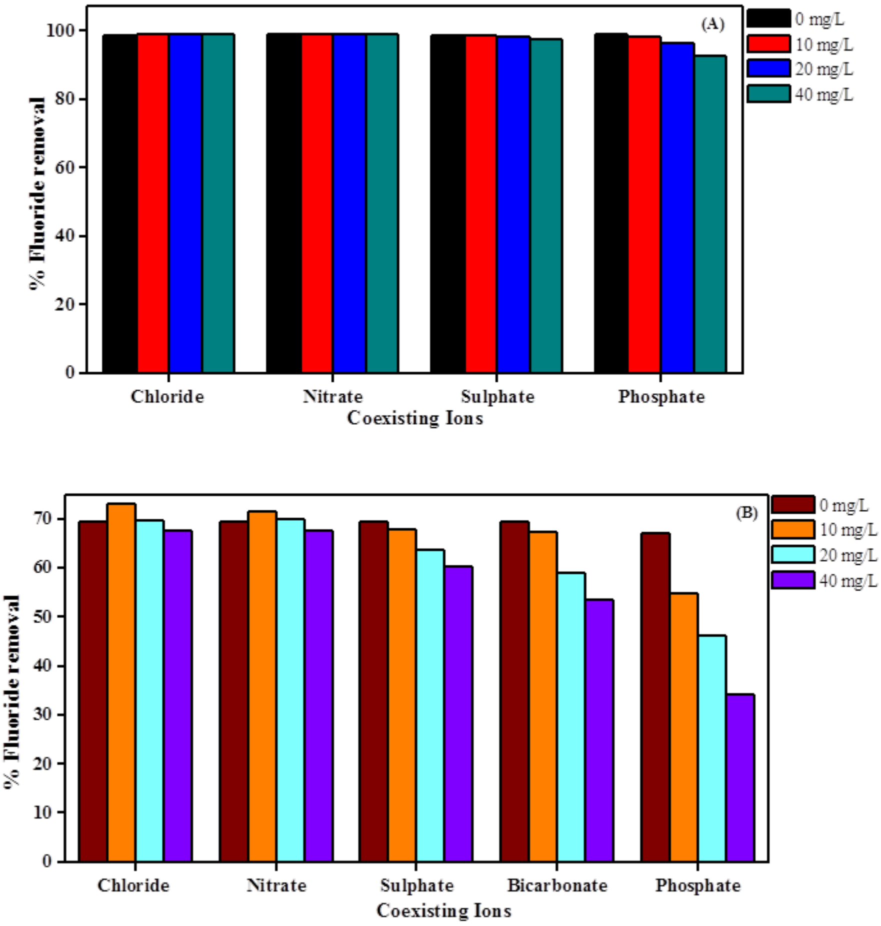

**Figure 2-11: Effect of coexisting anions on the $F^-$ removal efficiency of $HZrO_2$@PANI NFs at (A) pH 3 and (B) pH 6.5 ±0.1.**

### 2.3.4 Desorption/regeneration studies

The regeneration of an adsorbent is a crucial step in adsorption study, which makes the process more cost effective for real field application. The result of pH effect on $F^-$ adsorption by $HZrO_2$@PANI NFs (Fig. 2.12B), showed that % $F^-$ removal decreased gradually with increase in pH and only 1.7% $F^-$ removal was obtained at highly alkaline condition ( pH ~ 11). Hence, in the view of the same, the desorption experiments were carried out using NaOH solutions of different concentrations (0.01-0.1 M), where maximum $F^-$ desorption efficiency (~87.25%) was achieved with 0.1M NaOH as shown in Fig. 13. The exhausted adsorbent was treated with 50 mL of 2 M HCl for regeneration and four such consecutive adsorption-desorption cycles were performed as shown in Fig. 9C. During the regeneration process, $F^-$ ions were desorbed and exchanged with new hydroxyl groups (NaOH as desorbing agent), which being inactive enough to further contribute in $F^-$ sorption, ultimately resulted in lower $F^-$ adsorption efficiency over successive adsorption-desorption cycles and thus, $F^-$ removal efficiency of $HZrO_2$@PANI NFs came down to 78% after four cycles [48].

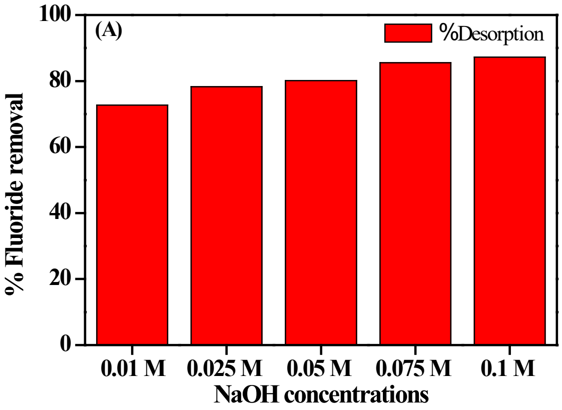

**Figure 2-12: % $F^-$ desorption obtained using various molar concentrations of NaOH as a desorbing agent.**

### 2.3.5 Adsorption mechanisms

The mechanistic facet of $F^-$ adsorption is important for a better understanding of adsorbent characteristics and designing its future applications. Hence, the mechanism of $F^-$ sorption onto $HZrO_2$@PANI NFs was established by FTIR, XPS and zeta potential analysis. As per the FTIR spectral findings (section *3.1*, Fig. 3.1A), the $F^-$ adsorption by $HZrO_2$@NFs primarily occurred due to the replacement of surface OH groups of $HZrO_2$ and $Cl^-$ ions doped at protonated NH groups of PANI NFs with negatively charged $F^-$ ions as a result of ion exchange.

However, for an in-depth analysis of $F^-$ adsorption mechanism, XPS analysis of $HZrO_2$@PANI NFs was carried out. The complete XPS survey scans of $HZrO_2$@PANI NFs before and after $F^-$ adsorption as shown in Fig. 2.13A displayed characteristic peaks of C 1s, N 1s, O 1s, Cl 2p and Zr 3d at binding energies of 284.9, 398.8, 532.2, 197.7 and 183.4 eV, respectively. After $F^-$ adsorption, the presence of a new additional photoemission signal attributed to F 1s at a binding energy of 684.1 eV (Fig. 2.13A) indicated the effective uptake of $F^-$ by $HZrO_2$@PANI NFs. The XPS spectrum of Zr 3d before $F^-$ adsorption (Fig. 2.13B) was deconvoluted into two different peaks at 182.5 and 184.8 eV corresponding to Zr $3d_{5/2}$ and Zr $3d_{3/2}$, respectively [16]. After $F^-$ adsorption (Fig. 2.13C), the Zr $3d_{5/2}$ and Zr $3d_{3/2}$ peaks broadened and shifted to higher binding energies 183.1 and 185.5, respectively, which might be due to the participation of hydroxyl groups bonded to Zr (IV) in $F^-$ adsorption, leading to the formation of new zirconium species (Zr-oxyfluorides or $ZrF_4$) [16]. Characteristically, Zr on binding with highly electronegative fluorine, was subjected to greater electron withdrawal, that eventually led to the loss of electron density at Zr and resulted in higher $3d_{5/2}$ and $3d_{3/2}$ binding energies [49]. Moreover, the XPS spectrum of O 1s before $F^-$ adsorption (Fig. 2.13D) was deconvoluted into three components at 530, 532.1 and 533 eV which can be ascribed to bulk oxide ($O^{2-}$), surface hydroxyl groups bound to Zr (IV) (Zr-OH) and adsorbed water in the adsorbent ($H_2O$), respectively [50,51]. However, after $F^-$ adsorption the intensity of O 1s peaks (Fig. 2.13E) showed apparent changes, where the relative peak area of surface hydroxyl groups, i.e M-OH decreased from 65.38% to 50.03%, which further designates the imperative role of the surface hydroxyl groups in the $F^-$ adsorption by $HZrO_2$@PANI NFs.

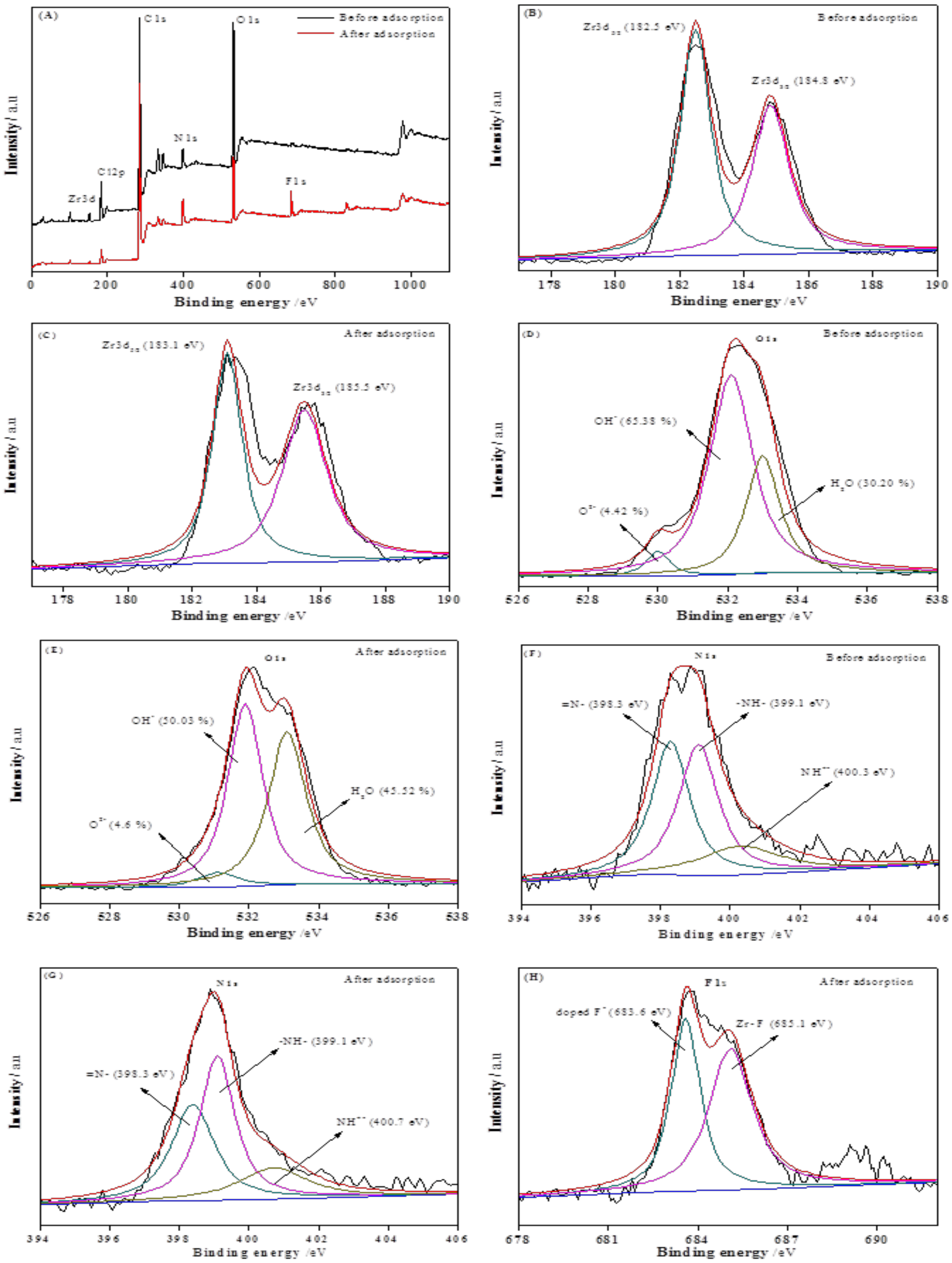

**Figure 2-13: (A) XPS spectra of HZrO$_2$@PANI NFs before and after F$^-$ adsorption; high resolution Zr 3d spectrum (B) before and (C) after F$^-$ sorption; O 1s spectrum (D) before and (E) after F$^-$ sorption; N 1s spectrum (F) before and (G) after F$^-$ sorption and (H) F 1s spectrum after F$^-$ sorption.**

The high-resolution spectrum of N 1s (Fig. 2.13F) consists of a broad peak, suggesting the presence of several oxidation states of nitrogen in PANI NFs. The deconvoluted peaks of N 1s as shown in Fig. 2.13F were centered at 398.3, 399.1 and 400.3 eV and can be allocated to quinonoid imine (=N-), benzenoid amine (-NH-) and positively charged doped imine (NH$^{+\cdot}$-) respectively [52]. However, after F$^-$ adsorption (Fig. 2.13G), the binding energy of peak assigned to positively charged doped imine

($NH^{+\cdot}$-) increased by about 0.4 eV. This might be due to the replacement of $Cl^-$ ions present as a dopant in PANI chain, with highly electronegative $F^-$ ions during the adsorption, which was in agreement with the reduction in peak intensity of Cl 2p in wide scan XPS spectra of $HZrO_2$@PANI NFs after $F^-$ adsorption as shown in Fig. 2.13A. This was further confirmed by F 1s spectrum shown in Fig. 2.13H, which on deconvolution showed peaks at 683.6 and 685.1 eV due to doped $F^-$ ions and zirconium associated F (Zr-F), respectively [16]. Hence, $F^-$ was possibly adsorbed onto $HZrO_2$@PANI NFs via ion-exchange between $F^-$ ions present in solution with surface hydroxyl groups and doped $Cl^-$ ions of adsorbent. This phenomenon could be explained by atomic % of O, Cl and F of $HZrO_2$@PANI NFs before and after $F^-$ adsorption as shown in Table 2.8. From Table 2.8, it was observed that the atomic % of O and Cl in the $HZrO_2$@PANI NFs before $F^-$ adsorption were 20.7 and 1.4 which reduced to 11.6 and 0.4 after $F^-$ adsorption, respectively. It was also noticed that the atomic % of $F^-$ is 3.5 in the $HZrO_2$@PANI NFs after $F^-$ adsorption.

Moreover, on comparing the results of zeta potential (section *3.1*, Fig. 2.6A) and effect of pH (Fig. 2.6B), it was noticed that highly positive zeta potentials obtained at lower pH (Fig. 6A), resulted in higher $F^-$ removal (Fig 2.6B) whereas at pH 10 and above, the negative zeta potentials (Fig. 2.6A), caused reduction in $F^-$ removal (Fig. 2.6B) due to increased coulombic repulsion between negatively charged adsorbent's surface and anionic $F^-$ ions. This suggests that electrostatic attraction has also substantially contributed in the adsorption of $F^-$ by $HZrO_2$@PANI NFs. Since $pH_{pzc}$ of $HZrO_2$@PANI NFs is 9.8, nitrogen groups of PANI NFs and some of the hydroxyl groups of $HZrO_2$ are protonated below pH 9.8, and hence might adsorb negatively charged $F^-$ ions via electrostatic attraction. Moreover, along with electrostatic attraction, involvement of ion exchange mechanism was also justified by increase in solution pH after $F^-$ adsorption as shown in Table 2.2 and appearance of white colour precipitate of AgCl in $AgNO_3$ test as discussed in detail in section *3.2.2* (effect of pH). Nevertheless, at pH > $pH_{pzc} \approx$ 9.8, where adsorbent's surface is negatively charged, coulombic repulsion comes into play and ion exchange remains as an only possible mechanism for $F^-$ adsorption at and above $pH_{pzc} \approx$ 9.8, and thus the $F^-$ removal decreases sharply above $pH_{pzc}$. Hence, conclusively both ion exchange and electrostatic attraction play a significant role in the adsorption of $F^-$ ions onto $HZrO_2$@PANI NFs.

## 2.4 SUMMARY

In this chapter, we have demonstrated a novel approach to develop $HZrO_2$@PANI NFs as an adsorbent by growing hydrous zirconium oxide particles onto the support of polyaniline nanofibres via a simple precipitation method and applied the same for the remediation of $F^-$ from drinking water. Various spectro-analytical techniques (FTIR, XRD, BET, SEM, EDS, TEM, STEM, Zeta potential analysis and XPS) confirmed the formation of $HZrO_2$@PANI NFs adsorbent, with a strong affinity toward $F^-$ ions. The as-synthesized $HZrO_2$@PANI NFs demonstrated optimum $F^-$ removal over a wide pH range (3-9), indicating its applicability in the removal of $F^-$ from real field ground water as well as industrial wastewater. The adsorption kinetics fitted well with pseudo-second-order model and equilibrium was attained in 30 min. The adsorption isotherm was fitted well with Langmuir model and the maximum $F^-$ adsorption capacity obtained was 83.23 mg/g and 28.77 mg/g, at pH 3 and 6.5, respectively. The thermodynamic parameters indicated the endothermic and spontaneous nature of adsorption process. At pH 3, no other co-existing anion except $PO_4^{3-}$evidently inhibited the $F^-$ removal, whereas at pH 6.5 ±0.1 both $HCO_3^-$ and $PO_4^{3-}$ showed a significant effect over $F^-$ removal efficiency of as-prepared $HZrO_2$@PANI NFs. Desorption studies indicated the recyclability of $HZrO_2$@PANI NFs up to four cycles without much loss of its $F^-$ removal efficiency. XPS and FTIR spectral analysis proved that $F^-$ sorption onto $HZrO_2$@PANI NFs occurred by ion-exchange mechanism, while involvement of electrostatic attraction was supported by the zeta potential results. Thus, the empirical results obtained herein, envision the potential utility of $HZrO_2$@PANI NFs as an adsorbent in the field of water defluoridation.

## 2.5 REFERENCES

[1] S. Jagtap, M.K. Yenkie, N. Labhsetwar, S. Rayalu, Fluoride in drinking water and defluoridation of water, Chem. Rev. 112 (2012) 2454-2466.

[2] A. Lewandowska, L. Falkowska, J. Jóźwik, Factors determining the fluctuation of fluoride concentrations in PM10 aerosols in the urbanized coastal area of the Baltic Sea (Gdynia, Poland), Environ. Sci. Pollut. Res. 20 (2013) 6109-6118.

[3] S. Ayoob, A.K. Gupta, Fluoride in Drinking Water: A Review on the Status and Stress Effects, Crit. Rev. Environ. Sci. Technol. 36 (2006) 433-487.

[4] Z. Mandinic, M. Curcic, B. Antonijevic, M. Carevic, J. Mandic, D. Djukic-Cosic, et al., Fluoride in drinking water and dental fluorosis, Sci. Total Environ. 408 (2010) 3507-3512.

[5] S. Ayoob, A.K. Gupta, V.T. Bhat, A conceptual overview on sustainable technologies for the defluoridation of drinking water, Crit. Rev. Env. Sci. Technol. 38 (2008) 401-470.

[6] A. Bhatnagar, E. Kumar, M. Sillanpää, Fluoride removal from water by adsorption-A review, Chem. Eng. J. 171 (2011) 811-840.

[7] S.P. Suriyaraj, R. Selvakumar, Advances in nanomaterial based approaches for enhanced fluoride and nitrate removal from contaminated water, RSC Adv. 6 (2016) 10565-10583.

[8] V.K. T, S.L. Belagali, Characterization of Polyaniline for Optical and Electrical Properties, IOSR J. Appl. Chem. Ver. II. 8 (2015) 53-56.

[9] J. Huang, R.B. Kaner, A General Chemical Route to Polyaniline Nanofibers, J. Am. Chem. Soc. 126 (2004) 851-855.

[10] J. Huang, S. Virji, B.H. Weiller, R.B. Kaner, Polyaniline nanofibers: Facile synthesis and chemical sensors, J. Am. Chem. Soc. 125 (2003) 314-315.

[11] M. Bhaumik, R.I. McCrindle, A. Maity, S. Agarwal, V.K. Gupta, Polyaniline nanofibers as highly effective re-usable adsorbent for removal of reactive black 5 from aqueous solutions, J. Colloid Interface Sci. 466 (2016) 442-451.

[12] M. Bhaumik, H.J. Choi, R.I. McCrindle, A. Maity, Composite nanofibers prepared from metallic iron nanoparticles and polyaniline: High performance for water treatment applications, J. Colloid Interface Sci. 425 (2014) 75-82.

[13] M. Karthikeyan, K.K. Satheeshkumar, K.P. Elango, Defluoridation of water via doping of polyanilines, J. Hazard. Mater. 163 (2009) 1026-1032.

[14] M. Karthikeyan, K.K.S. Kumar, K.P. Elango, Batch sorption studies on the removal of fluoride

ions from water using eco-friendly conducting polymer/bio-polymer composites, Desalination. 267 (2011) 49-56.

[15] M. Karthikeyan, K.K. Satheesh Kumar, K.P. Elango, Conducting polymer/alumina composites as viable adsorbents for the removal of fluoride ions from aqueous solution, J. Fluor. Chem. 130 (2009) 894-901.

[16] X. Dou, D. Mohan, C.U. Pittman, S. Yang, Remediating fluoride from water using hydrous zirconium oxide, Chem. Eng. J. 198-199 (2012) 236-245.

[17] B. Pan, J. Xu, B. Wu, Z. Li, X. Liu, Enhanced removal of fluoride by polystyrene anion exchanger supported hydrous zirconium oxide nanoparticles, Environ. Sci. Technol. 47 (2013) 9347-9354.

[18] L.H. Velazquez-Jimenez, E. Vences-Alvarez, J.L. Flores-Arciniega, H. Flores-Zuñiga, J.R. Rangel-Mendez, Water defluoridation with special emphasis on adsorbents-containing metal oxides and/or hydroxides: A review, Sep. Purif. Technol. 150 (2015) 292-307.

[19] C. Xu, J. Li, F. He, Y. Cui, C. Huang, H. Jin, et al., Al2O3-$Fe_3O_4$-expanded graphite nano-sandwich structure for fluoride removal from aqueous solution, RSC Adv. 6 (2016) 97376-97384.

[20] M. Bhaumik, C. Noubactep, V.K. Gupta, R.I. McCrindle, A. Maity, Polyaniline/Fe0 composite nanofibers: An excellent adsorbent for the removal of arsenic from aqueous solutions, Chem. Eng. J. 271 (2015) 135-146.

[21] I. Saha, A. Ghosh, D. Nandi, K. Gupta, D. Chatterjee, U.C. Ghosh, β-Cyclodextrin modified hydrous zirconium oxide: Synthesis, characterization and defluoridation performance from aqueous solution, Chem. Eng. J. 263 (2015) 220-230.

[22] S. Muthu Prabhu, S. Meenakshi, Chemistry of defluoridation by one-pot synthesized dicarboxylic acids mediated polyacrylamide-zirconium complex, Chem. Eng. J. 262 (2015) 224-234.

[23] B. Kavitha, K. Siva Kumar, N. Narsimlu, Synthesis and characterization of polyaniline nano-fibers, Indian J. Pure Appl. Phys. 51 (2013) 207-209.

[24] S. Wu, K. Zhang, J. He, X. Cai, K. Chen, Y. Li, et al., High efficient removal of fluoride from aqueous solution by a novel hydroxyl aluminum oxalate adsorbent, J. Colloid Interface Sci. 464 (2016) 238-245.

[25] N. Thakur, S.A. Kumar, H. Parab, A.K. Pandey, P. Bhatt, S.D. Kumar, et al., A fluoride ion selective Zr(IV)-poly(acrylamide) magnetic composite, RSC Adv. 4 (2014) 10350.

[26] L. Chai, Y. Wang, N. Zhao, W. Yang, X. You, Sulfate-doped $Fe_3O_4$/$Al_2O_3$ nanoparticles as a novel adsorbent for fluoride removal from drinking water, Water Res. 47 (2013) 4040-4049.

[27] D. Thakre, S. Jagtap, N. Sakhare, N. Labhsetwar, S. Meshram, S. Rayalu, Chitosan based mesoporous Ti-Al binary metal oxide supported beads for defluoridation of water, Chem. Eng. J. 158 (2010) 315-324.

[28] H. Qiu, L. Lv, B. Pan, Q. Zhang, W. Zhang, Q. Zhang, Critical review in adsorption kinetic models, J. Zhejiang Univ. Sci. A. 10 (2009) 716-724.

[29] Y. Cantu, A. Remes, A. Reyna, D. Martinez, J. Villarreal, H. Ramos, et al., Thermodynamics, kinetics, and activation energy studies of the sorption of chromium(III) and chromium(VI) to a $Mn_3O_4$ nanomaterial, Chem. Eng. J. 254 (2014) 374-383.

[30] M.H. Dehghani, G.A. Haghighat, K. Yetilmezsoy, G. McKay, B. Heibati, I. Tyagi, et al., Adsorptive removal of fluoride from aqueous solution using single and multi-walled carbon nanotubes, J. Mol. Liq. 216 (2016) 401-410.

[31] K.Y. Foo, B.H. Hameed, Insights into the modeling of adsorption isotherm systems, Chem. Eng. J. 156 (2010) 2-10.

[32] S.R. Mishra, R. Chandra, J. Kaila A., S. Darshi B., Kinetics and Isotherm studies for the adsorption of metal ions onto two soil types, Environ. Technol. Innov. 7 (2016) 87-101.

[33] K. Li, Y. Wang, M. Huang, H. Yan, H. Yang, S. Xiao, et al., Preparation of chitosan-graft-polyacrylamide magnetic composite microspheres for enhanced selective removal of mercury ions from water, J. Colloid Interface Sci. 455 (2015) 261-270.

[34] N. Viswanathan, S. Meenakshi, Synthesis of Zr(IV) entrapped chitosan polymeric matrix for selective fluoride sorption, Colloids Surfaces B Biointerfaces. 72 (2009) 88-93.

[35] B. Liu, D. Wang, G. Yu, X. Meng, Removal of $F^-$ from aqueous solution using Zr(IV) impregnated dithiocarbamate modified chitosan beads, Chem. Eng. J. 228 (2013) 224-231.

[36] A. Teimouri, S. Ghanavati Nasab, S. Habibollahi, M. Fazel-Najafabadi, A.N. Chermahini, Synthesis and characterization of a chitosan/montmorillonite/$ZrO_2$ nanocomposite and its application as an adsorbent for removal of fluoride, RSC Adv. 5 (2015) 6771-6781.

[37] Z. Qiusheng, L. Xiaoyan, Q. Jin, W. Jing, L. Xuegang, Porous zirconium alginate beads adsorbent for fluoride adsorption from aqueous solutions, RSC Adv. 5 (2015) 2100-2112.

[38] G. Zhang, Z. He, W. Xu, A low-cost and high efficient zirconium-modified-Na-attapulgite adsorbent for fluoride removal from aqueous solutions, Chem. Eng. J. 183 (2012) 315-324.

[39] D.W. Cho, B.H. Jeon, Y. Jeong, I.H. Nam, U.K. Choi, R. Kumar, et al., Synthesis of hydrous zirconium oxide-impregnated chitosan beads and their application for removal of fluoride and lead, Appl. Surf. Sci. 372 (2016) 13-19.

[40] X. Dou, Y. Zhang, H. Wang, T. Wang, Y. Wang, Performance of granular zirconium-iron oxide in the removal of fluoride from drinking water, Water Res. 45 (2011) 3571-3578.

[41] S. Muthu Prabhu, S. Meenakshi, Defluoridation of water using dicarboxylic acids mediated chitosan-polyaniline/zirconium biopolymeric complex, Int. J. Biol. Macromol. 85 (2016) 16-22.

[42] P. Saha, S. Chowdhury, Insight into adsorption thermodynamics, Thermodyn. Tech. (2011).

[43] M. Mohapatra, D. Hariprasad, L. Mohapatra, S. Anand, B.K. Mishra, Mg-doped nano ferrihydrite-A new adsorbent for fluoride removal from aqueous solutions, Appl. Surf. Sci. 258 (2012) 4228-4236.

[44] Y.H. Huang, Y.J. Shih, C.C. Chang, Adsorption of fluoride by waste iron oxide: The effects of solution pH, major coexisting anions, and adsorbent calcination temperature, J. Hazard. Mater. 186 (2011) 1355-1359.

[45] K. Zhang, S. Wu, J. He, L. Chen, X. Cai, K. Chen, et al., Development of a nanosphere adsorbent for the removal of fluoride from water, J. Colloid Interface Sci. 475 (2016) 17-25.

[46] M. Bhaumik, T.Y. Leswifi, A. Maity, V. V. Srinivasu, M.S. Onyango, Removal of fluoride from aqueous solution by polypyrrole/$Fe_3O_4$ magnetic nanocomposite, J. Hazard. Mater. 186 (2011) 150-159.

[47] Z. Wan, W. Chen, C. Liu, Y. Liu, C. Dong, Preparation and characterization of γ-AlOOH @CS magnetic nanoparticle as a novel adsorbent for removing fluoride from drinking water, J. Colloid Interface Sci. 443 (2015) 115-124.

[48] L. Chen, S. He, B.Y. He, T.J. Wang, C.L. Su, C. Zhang, et al., Synthesis of iron-doped titanium oxide nanoadsorbent and its adsorption characteristics for fluoride in drinking water, Ind. Eng. Chem. Res. 51 (2012) 13150-13156.

[49] H. Cai, L. Xu, G. Chen, C. Peng, F. Ke, Z. Liu, et al., Removal of fluoride from drinking water using modified ultrafine tea powder processed using a ball-mill, Appl. Surf. Sci. 375 (2016) 74-84.

[50] J. He, K. Zhang, S. Wu, X. Cai, K. Chen, Y. Li, et al., Performance of novel hydroxyapatite nanowires in treatment of fluoride contaminated water., J. Hazard. Mater. 303 (2016) 119-30.

[51] J. Wang, D. Kang, X. Yu, M. Ge, Y. Chen, Synthesis and characterization of Mg-Fe-La trimetal composite as an adsorbent for fluoride removal, Chem. Eng. J. 264 (2015) 506-513.

[52] M. Bhaumik, R.I. McCrindle, A. Maity, Enhanced adsorptive degradation of Congo red in aqueous solutions using polyaniline/$Fe^0$ composite nanofibers, Chem. Eng. J. 260 (2015) 716-729.

## 2.6 APPENDIX

**Kinetic model equations:**

Pseudo-second-order model linear equation (S1):

$$\frac{t}{q_t} = \frac{1}{k_2 {q_e}^2} + \frac{t}{q_e} \qquad \text{(S1)}$$

Pseudo-first-order model linear equation (S2):

$$\log(q_e - q_t) = \log q_e - \frac{k_1}{2.303} t \qquad \text{(S2)}$$

where $k_1$ (1/min) and $k_2$ (g/mg.min) are the pseudo-first order and the pseudo-second order rate constants, respectively; $q_t$ and $q_e$ are the adsorption capacity (mg/g) at any time $t$ and equilibrium.

**Isotherm model equations**

Langmuir isotherm model linear equation (S3):

$$\frac{C_e}{q_e} = \frac{1}{q_m b} + \frac{C_e}{q_m} \qquad \text{(S3)}$$

Freundlich isotherm model linear equation (S4):

$$\ln q_e = \ln K_f + \frac{1}{\mathrm{n}} \ln C_e \qquad \text{(S4)}$$

where $q_m$ and $b$ are Langmuir constants related to maximum adsorption capacity and binding energy of adsorption, respectively. $K_f$ (mg/g) and $1/n$ are the characteristic Freundlich constants, which signify the adsorption capacity and adsorption intensity, respectively.

# CHAPTER 3: SYNTHESIS, CHARACTERIZATION AND APPLICATION OF THIOL-FUNCTIONALIZED POLYPYRROLE (PPY/MAA) COMPOSITES

## 3.1 INTRODUCTION

With the rapid expansion of industries and technology, environmental pollution has become a serious problem because of the negative impact on human health and other life systems [1,2]. Global pollution is expanding as a result of variations in natural and anthropogenic activities that lead to adulteration of terrestrial as well as aquatic ecosystem with heavy metals, non-metals and metalloids. Untreated discharge of waste, sewage disposal, use of fertilizers and use of agricultural pesticides are some of the major contributors. In that regard, existing freshwater resources are progressively becoming polluted and unavailable. A recent study on the global threats to human water security and river biodiversity revealed that 80% of the world's population is exposed to high levels of threat to water security [3]. Hence, various technologies have been designed and developed for the purpose to purify and remove water pollutants that may lead to human health and ecosystem damages. The main focus of the current report is on the removal of fluoride ($F^-$) and heavy metals (Hg and Ag).

Heavy metals are widely used in innovative research areas such as catalysis, electronic devices, energy sources and chemical industry. Water pollution with highly toxic heavy metal ions like Hg, Ag, Cr and Pb ions has become a major environmental issue for several decades [4,5]. Mercury (Hg) is recognised as one of the most hazardous metal pollutant. Burning of petrochemical oil and coal, discharge of waste effluents from mining plant, printing industries, cement processing and batteries manufacturing are the main sources of mercury pollution in waterway. Mercury exists in several physical and chemical forms: elemental mercury ($Hg^0$), divalent mercury ($Hg^{2+}$) and monomethyl mercury cation ($CH_3Hg^+$) [6]. Divalent inorganic mercury ($Hg^{2+}$) has been found to be a serious contaminant due to its high solubility and stability. It is reported that divalent mercury ($Hg^{2+}$) may be easily transferred into higher toxic organometallic forms via biological methylation [7]. Alkylmercury ($CH_3Hg^+$) has received considerable attention because of its low biodegradability and greater toxicity to biological system than other chemical forms [8]. Trace amounts of mercury can affect the central nervous system and also cause serious damage to kidney and lung tissues [9]. Based on the best available science to prevent potential health problems, the United States Environmental Protection Agency (EPA) has set 0.002 mg/L (2 ppb) as the maximum allowable limit for mercury in drinking water [10]. Silver, on the other hand, is one of the most important and precious noble metals because of its versatile property in various applications such as electronics [11,12], laminations [13], catalysts [14,15], antimicrobial activity [16,17] and sensing materials [18]. In spite of its beneficial use in daily life, high concentration of silver ions ($Ag^+$) in drinking water can reach toxic levels in the human body. The concentration of silver in drinking water beyond the permissible limit (0.1 mg/L) causes serious diseases (skin, liver and kidneys) and disorders (blood) in human body [19]. According to a recent study, Ag concentration in sewage sludge ranged from 2 to 195 $mg.kg^{-1}$ and was found to be harmful towards environment [20]. Silver concentration in sewage sludge mostly depends upon the sources and differs from various parts of world. It is of serious concern that large volumes of industrial effluents containing silver ions are being discarded into rivers, lakes and ponds without suitable treatment. Therefore, the effective removal and recycling of heavy metal ions from wastewater has received significant attention [21,22].

Several techniques have been developed to reduce the levels of fluoride and heavy metals in contaminated industrial effluents, and these include chemical precipitation [23], ion exchange [24], solvent extraction [25], membrane filtration [26], coagulation [27], adsorption [28-30] and chemical reduction [31,32]. Of all these techniques, adsorption is regarded as a superior for the wastewater purification because of the following reasons: simple to design, wide range of adsorbents available, high efficiency and cost-effectiveness. Adsorption is a mass transfer technique that involves accumulation of substances (adsorbate) at the surface provided by solid materials (adsorbent) through physical or sometime weak chemical forces. Polypyrrole (PPy) and Polyaniline (PANI) are considered as the most effective adsorbent materials due to outstanding properties such as high conductivity, high stability, easy preparation, low cost and biocompatibility [33,34,35]. However, while polypyrrole has already been applied on a large scale to the adsorption of metal ions and dyes from aqueous solutions, the benefits of introducing suitable chelating agents into the polymeric chain has recently drawn great attention [36]. The adsorption capacity for specific metal ions increases many fold, with selective accumulation of the complexing agent onto the surface of the adsorbent. Chelating agents with electronegative donor atoms like sulphur, nitrogen, oxygen are most effective for the selective adsorption of heavy metal ions through strong metal-binding capacity. Remarkably, nanomaterials have also been widely deployed as sustainable nanocatalysts, antimicrobial agents or gas sensing.

Several aspects of sustainable development including waste minimization and reuses of waste-derived nanomaterials are keys to green chemistry [37-39]. There has been a significant interest in silver nanoparticles owing to their diverse application in antimicrobial and catalysis research fields [40-42]. For example, Baruah and co-workers reported the synthesis of AgNP as an effective catalyst for the reduction of 4-nitrophenol to 4-aminophenol in the presence of $NaBH_4$. The reduction followed a pseudo-first-order reaction with a rate constant of $5.50 \times 10^{-3}$ $s^{-1}$ and an activity parameter of 1375 $s^{-1}$ $g^{-1}$. Hg, on the other hand, was used in the form of mercury(II) trifluoromethanesulfonate ,$Hg(OTf)_2$, for the transformation of $CH_4$ to MeOH [43]. Likewise, hydration of alkynes and cyclization of propargyl **tert**-butyl carbonates were achieved using $Hg(OTf)_2$. Metal nanoparticles have also been incorporated into gas sensors to increase the sensitivity, selectivity and response time to the experimental gases tested [44-45]. Ragachev *et al* reported the preparation of PANI-based materials for ammonia gas sensing applications. The incorporation of AgNPs was found to enhance the sensing properties at low frequency region of impedance spectra. Silver is also known to exhibit significant anti-microbial activity upon fungi, bacteria and viruses [46-47]. Graphene oxide nanocomposites modified with AgNPs, for example, showed excellent antimicrobial activity towards *Escherichia coli* (*E. coli*) and *Staphylococcus epidermidis* (*S. epidermidis*). In the current study, after adsorption of metals from the aqueous solution, metal-laden adsorbents were to be screened for their potential application in catalysis, gas sensing and/or bacteria growth inhibition. The main aim of this investigation was to remove heavy metal ions (Hg and Ag) from aqueous media using modified-polymer nanocomposites. Subsequently, the metal-laden nanocomposites were screened for potential catalytic, gas sensing and/or antimicrobial activities.

## 3.2 EXPERIMENTAL

### 3.2.1 Materials

Pyrrole monomer (Py, 99%, Sigma-Aldrich, USA) was purified by vacuum distillation and stored at 4°C prior to use. Mercury(II) nitrate ($Hg(NO_3)_2$), ammonium persulfate (APS) and mercaptoacetic acid (Thioglycolic acid), sodium hydroxide, hydrochloric acid, ammonia, silver nitrate, sodium borohydride, p-nitrophenol, sodium bicarbonate and dichloromethane were purchased from Sigma-Aldrich (USA). All the chemicals used in this study were of analytical grade unless otherwise stated. Ultrapure deionized water (resistivity > 18.5 MΩ cm) was used for all the experiments.

### 3.2.2 Characterization techniques

The surface morphologies and elemental composition of PPy/MAA and silver adsorbed PPy/MAA were determined by a Field Emission-Scanning Electron Microscope (Auriga FE-SEM, Carl Zeiss, Germany) with an Oxford energy dispersive X-ray spectrometer (EDS, Oxford, UK). A JEOL JEM 2100 High Resolution-(Scanning) Transmission Electron Microscope (HR-STEM, JEOL Japan) fitted with an EDS system (Thermo Scientific, USA) was also used to characterise samples. A Spectrum 100 Attenuated Total Reflectance-Fourier Transform Infrared (ATR-FTIR, Perkin-Elmer, USA) was employed to record the infrared spectra of PPy/MAA before and after adsorption of silver in the scanning range of 600-4000 cm$^{-1}$ at a resolution of 4 cm$^{-1}$/s. The powder X-ray Diffraction (XRD) patterns of adsorbent before and after adsorption were performed by using PANalytical X'Pert PRO-diffractometer with Cu Kα radiation (wavelength, $\lambda = 1.5406$ Å), and angular variation of 5-90° operated at a generator voltage and current of 40 kV and 40 mA respectively. Oxidation states of the elements of the composite were obtained using high-resolution X-ray photoelectron spectroscopy (XPS) on a Kratos Axis Ultra device, with a focused monochromatized Al Kα radiation (hv = 1486.6 eV). The $N_2$ adsorption-desorption isotherm was analysed by Quatachrome Autosorb-1C surface analyzer (USA). The specific surface areas of PPy and PPy/MAA composite were calculated according to the Brunauer-Emmett-Teller (BET) method. The pore size distribution was achieved by desorption branch of the isotherm with the Barrett-Joyner-Halenda (BJH) method. Zeta potential of the composite was measured using Zetasizer NanoS (Malvern, UK).

The concentration of $Ag^+$ ion in the filtrate was determined using an inductively Coupled Plasma Mass Spectroscopy (ICP-MS) (Thermo Fisher Scientific, USA). UV-vis spectrophotometer (Perkin-Elmer, Lambda 35) has been used to measure the concentration of 4-Nitrophenol in reaction medium during catalytic performance. GC analyses were recorded with Agilent 7890A gas chromatograph using SBP- 20 column (GC method: Oven program: 80°C for 3 min then 10°C/min to 250°C for 10 min, Run time: 25 min). An Agilent VNMRS Premium Shield 600MHz spectrometer was used to record NMR spectra of the pure compound (acetophenone) and chemical shifts (δ) were reported in parts per million (ppm) using TMS as reference signal. Aluminium plates coated with Kieselgel 60 F-254 silica gel were used for thin layer chromatography (TLC), and visualization was done under UV light. The pure product was isolated through column chromatography, performed over 100-200 mesh silica gel using ethyl acetate/hexane solvent mixtures as the eluent. The data of NMR splitting patterns were presented as singlet (s) and multiplet (m).

### 3.2.3 Synthesis of mercaptoacetic acid containing polypyrrole (PPy/MAA) composite

The PPy/MAA composite was synthesized via chemical oxidative polymerization at room temperature [48]. In the typical oxidative polymerization process, 1.6 mL (23 mmol) mercaptoacetic acid was initially dissolved slowly in 60 mL of ultrapure water in a 250 mL conical flask. The solution was stirred magnetically at 400 rpm for 30 min. Afterwards, 0.8 mL (11.4 mmol) of pyrrole monomer was syringed into the mercaptoacetic acid solution, and stirred for another 30 min to form a completely homogeneous reaction mixture. In another beaker, 6.8 g (~ 30 mmol) of oxidant ammonium persulfate was dissolved in 20 mL of ultrapure water, and the resultant ammonium persulfate solution was added dropwise to the aqueous reaction mixture of mercaptoacetic acid and pyrrole. The polymerization reaction started upon the addition of oxidant to the reaction mixture, which gradually developed into a black coloured composite. Then the polymerization reaction was allowed to continue for 6h at ambient temperature. The final product was filtered and washed with ultrapure water followed by acetone, and then dried overnight under vacuum at 60°C.

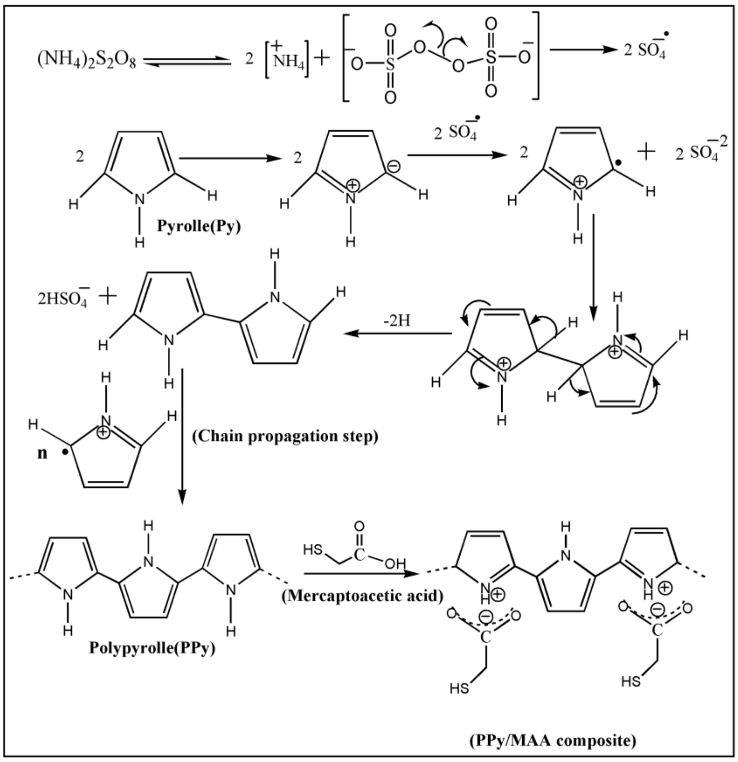

**Scheme 3-1: Plausible Schematic Representation for the Synthesis of PPy/MAA Composite.**

A plausible explanation for polymerization of Py monomer is based on the well-established oxidative mechanism indicating that ammonium persulfate (APS) generates free radical sites on pyrrole backbone [48]. These free radical sites react with another monomer to generate polymer (polypyrrole) as shown in Scheme 1. During polymerization of Py monomer, PPy carries positive charge on the hetero atoms at the time of propagation stage in polymerization reaction medium [48, 49]. Due to charge neutrality of N atoms, negative charge mercaptoacetic acid dopants are introduced into polypyrrole networks through electrostatic interaction.

### 3.2.4 Adsorption procedure

#### *3.2.4.1 Hg(II)*

Batch adsorption technique was applied to investigate the adsorption behaviours of Hg(II) from aqueous solution using PPy/MAA composite within the range of pH 2 to 8 at 25°C. Mercury nitrate was used to prepare an aqueous stock solution of 1000 ppm Hg(II) in the presence of 0.2 (M) $HNO_3$. The desired Hg(II) concentration for the adsorption studies was obtained by diluting the stock solution using water. To explore the adsorption behaviour, 20 mg of as-prepared PPy/MAA composite were loaded into 100 mL capped glass bottles with 50 mL of the target concentration of metal solutions started from 100 to 800 mg/L. The mixture in the glass bottles was agitated on a thermostatic incubator shaker (Separation Scientific, South Africa) at 200 rpm for 24 h. The adsorption temperature was maintained constant at 25 ± 0.2°C, and the pH of the adsorption medium was adjusted and maintained at the target levels during the course of experiment using 0.1 (M) $HNO_3$ or NaOH.

After 24 h, aliquots were withdrawn from the adsorption medium, filtered immediately through 0.45 µm membrane filters and the remaining concentration of metal ions in the adsorption medium was determined using ICP-OES. The amount of adsorbed mercury on the polymer composite was determined by subtracting the residual Hg(II) concentration in the medium from its initial concentration. The adsorption capacity $q_e$ was calculated with eq. 1. Four different initial metal ions concentrations (25, 50, 100 and 200 mg/L) has been selected for kinetics study of Hg(II) adsorption. An amount of 0.4 g of adsorbent was placed into 1L of experimental Hg(II) solution at optimize adsorption condition (200 rpm, 25°C and pH=5.5). At a certain time intervals 10 mL aliquots were sampled from the adsorption medium and filtered through 0.45 µm membrane filters. The quantity of Hg(II) present in PPy/MAA composite per unit mass at time t ($q_t$) was analysed using eq. 2.

#### *3.2.4.2 Ag(I)*

Batch adsorption experiments were investigated using a thermostatic orbital shaker (Separation Scientific, South Africa) with a shaking speed of 200 rpm. A stock solution of 1000 ppm of $Ag^+$ was prepared by dissolving silver nitrate in ultrapure water as the source of $Ag^+$ metal ion. To evaluate the efficiency of the PPy/MAA composite for $Ag^+$ adsorption in aqueous medium, a series of solutions of metal ion ($Ag^+$) with different initial concentrations (50, 100, 150, 200, 250, 300, 400, 500 and 600 mg/L) were prepared from stock solution (1000 mg/L) to measure the equilibrium adsorption. For each experiment, required amount (20 mg) of adsorbent (PPy/MAA) was added to 100 mL glass bottles containing 50 mL of silver ions solution with a solution pH of 5.4. After 24 h of adsorption under shaking, a 10 mL sample solution was withdrawn from the batch and filtered through 0.45 µm membrane filters and analysed for the residual concentration of $Ag^+$ ion in solution. Inductively Coupled Plasma Mass Spectroscopy (ICP-MS) (Thermo Fisher Scientific) was used to measure the concentration of metal ion ($Ag^+$) in the remaining solution at equilibrium condition. The adsorbed amount of silver on the PPy/MAA composite was calculated on the basis eq. 1.

Kinetic adsorption measurements were performed using aqueous solution of silver ions with different initial concentration ranges from 25 to 100 mg/L. In total, 0.4 g adsorbent were contacted with 1L of experimental silver solution at optimize adsorption condition (200 rpm, 25°C and pH = 5.4). At definite time intervals 5 mL of aliquot was withdrawn and measured the silver ion concentration left in the experimental solution. The amount of adsorbed silver ions per unit mass of the adsorbent at time t, ($q_t$), was determined by eq. 2. The adsorption isotherm experiment was conducted at different initial concentration of silver solution (ranges from 50-600 mg/L) in solution pH (pH =5.4) at three different temperatures (i.e. 25, 35 and 45°C) to determine the maximum adsorption capacity of PPy/MAA composite.

### 3.2.5 Catalytic reduction of 4-nitrophenol by Ag-loaded PPy/MAA

The percentage of Ag loading in the composite material was calculated according to the remaining concentration of $Ag^+$ in the adsorption medium and the amount of silver present onto catalyst was 11.14 wt%. In a 25 mL round bottom flux, 4-nitrophenol (1 mmol, 0.1391 g), AgNC (5 mol%, 0.025 g), and $H_2O$ (10 mL) were stirred at room temperature (RT) under normal atmosphere. Sodium borohydride (10 mmol, 0.379 g) was added in portion wise to the stirred suspension over a period of 5 min at RT. The resulting reaction mixture was stirred at 25°C for 2 h. The reaction was monitored by TLC and then, quenched with saturated $NH_4Cl$ solution (10 mL). The aqueous layer was extracted with EtOAc (3 x 20 mL). The combined organic extract was washed with $H_2O$ (20 mL), brine (20 mL), and dried over anhydrous $MgSO_4$. The solvent was removed under reduced pressure to afford the pure 4-aminophenol as pure white solid (0.1025 g, 94% yield). The product was confirmed by $^1H$ and $^{13}C$ NMR spectra (See appendix).

### 3.2.6 Catalytic activity of Ag-loaded PPY/MAA for catalytic reduction of 4-nitrophenol

To test the catalytic activity, PPy/MAA composite was treated with 100 ppm aqueous solution of silver ion as mentioned earlier (in adsorption studies), and the silver adsorbed material was washed with double distilled water for 10 times and dried for 12 h under vacuum at room temperature. The percentage of Ag loading in the composite material was calculated according to the remaining concentration of $Ag^+$ in the adsorption medium and the amount of silver present onto catalyst was 19.75 wt%. In a typical reaction, 4-nitrophenol (1 mmol, 0.1391 g), PPy/MAA/Ag catalyst (5 mol%, 0.031g), and $H_2O$ (10 mL) were added to a 25 mL round bottom flux under $N_2$ atmosphere. Then, sodium borohydride solution (10 mmol, 0.379 g) was added portion wise to the reaction mixture for the period of 2 min. The resulting mixture was stirred at 30°C for 70 min. Afterwards, the mixture was diluted with saturated solution of $NH_4Cl$ (10 mL). The aqueous phase was extracted with ethyl acetate (3 x 20 mL) and the combined organic layer was washed with brine (20 mL) and dried over anhydrous $MgSO_4$. The solvent was removed under reduced pressure to give the isolated 4-aminophenol as a white solid (0.0898 g, 82% yield). The isolated product was confirmed by $^1H$ NMR spectroscopy as well as UV-visible spectroscopy.

### 3.2.7 $NO_2$ sensing ability of Ag-loaded PPy/MAA

The sensing responses of neat adsorbent (PPy/MAA) as well as silver adsorbed PPy/MAA (PPy/MAA/Ag) devices were measured using a gas sensing station KSGAS6S (KENOSISTEC, Italy) at 25°C. The sensing device was prepared by the drop casting method. The materials were ultrasonically dispersed in ethanol for 5 minutes and drop cast on the interdigitate electrode side of an alumina sensing strip, and dried at 60°C for 1 h. The resistive response of the device to the various concentrations of $NO_2$ gas was measured using a Keithley 6487 pico-ammeter/voltage source meter. The various concentration of $NO_2$ gas in the sensing chamber was achieved by controlling the flow rate of synthetic air and $NO_2$ gas. The synthetic air was used to dilute the $NO_2$ gas. The total flow rate of 500 sccm was maintained during the measurements. The response and recovery of the sensors were measured for 5 and 10 minute for each concentration, respectively.

### 3.2.8 Antimicrobial activity test with PPy/MAA/Ag on cell cultures of *Escherichia coli (E. coli)*

To test for the antimicrobial potential of Ag adsorbed PPy/MAA waste material (PPy/MAA/Ag), a set of 4 samples was tested against *E. coli*. The samples consisted of the neat material (PPy/MAA) and silver adsorbed PPy/MAA with different percentage of silver loading (11, 32 and 42%). The samples were labelled S0, S1, S2 and S3 containing 0, 11, 32 and 42% silver loading, respectively. Each material (50 mg) was weighed into a 50 mL centrifuge tube containing 20 mL of sterile distilled water. Tubes were prepared in triplicate for each test material. Each tube was then inoculated with an overnight culture of *E. coli* (American Type Culture Collection; ATCC® 25922) to obtain a final concentration of ~ $10^7$ colony forming units (CFU)/mL. A fifth set of 3 tubes containing distilled water and the bacteria but no antimicrobial material, was used as a control. Following inoculation, samples were immediately extracted (Time Zero) and plated on nutrient agar using the drop plate technique. Each tube was then sampled every ten minutes for 60 minutes. Plates were incubated at 37±0.2°C for 24 h, after which they were examined for growth and *E. coli* counts were recorded as CFU/mL.

## 3.3 RESULTS AND DISCUSSION

### 3.3.1 Synthesis, characterization and application of thiol-functionalized polypyrrole (PPy/MAA) composites for Hg(II)

Fig. 3.1a and b depict the FE-SEM images of surface morphology of PPy/MAA composite and after Hg(II) adsorption. As shown in Fig. 3.1a, the surface morphology of MAA modified PPy composite was relatively smooth with a homogeneous granular size of approximately 200 nm diameter. In contrast, the surface morphology of used adsorbent appeared rougher, possibly revealing the accumulation of mercury on its surface (Fig. 3.1b). EDX confirmed the presence of carbon, nitrogen, oxygen, and sulphur in PPy/MAA as expected (Fig. 3.2a) and an additional mercury peak in adsorbed material (Fig. 3.2b). Table 3.1 describes the surface elemental compositions (Wt.%) of adsorbent (PPy/MAA) before and after Hg(II) adsorption.

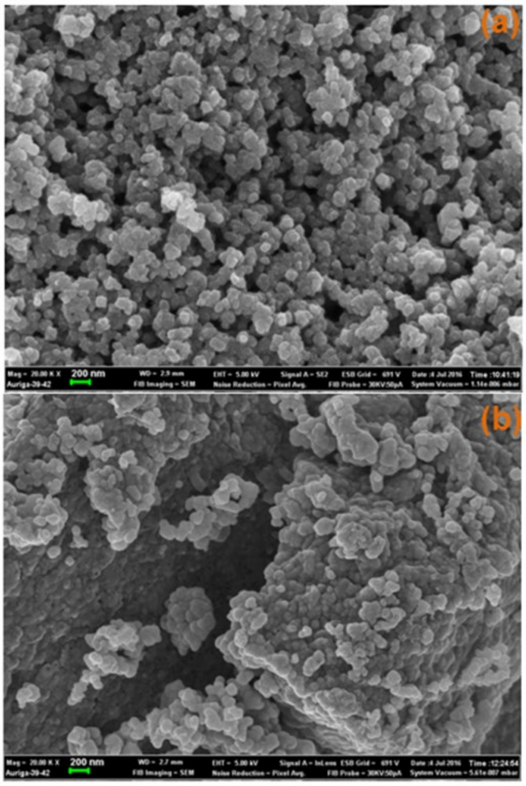

Figure 3-1: FE-SEM image of PPy/MAA (a) before, (b) after adsorption of Hg(II).

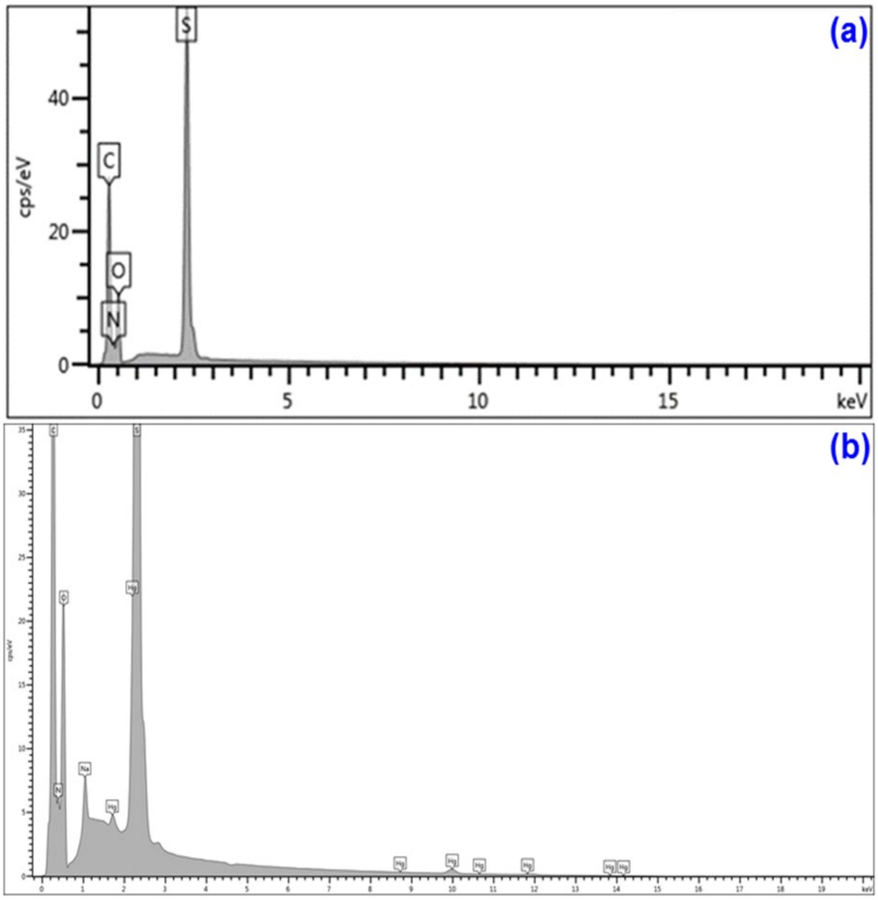

Figure 3-2: EDX spectra of PPy/MAA (a) before and (b) after Hg(II) adsorption.

**Table 3-1: Elemental composition before and after Hg(II) adsorption on PPy/MAA composite from EDX and XPS analysis results.**

| Composites | Elemental wt.% from EDX | | | | | Atomic % from XPS analysis | | | | |
|---|---|---|---|---|---|---|---|---|---|---|
| | C | N | O | S | Hg | C1s | N1s | O1s | S2p | Hg4f |
| PPy/MAA | 58.1 | 7.7 | 13.5 | 20.7 | - | 70.7 | 5.6 | 18.1 | 5.6 | - |
| PPy-MAA/Hg(II) | 37.3 | 2.6 | 7.9 | 26.9 | 25.3 | 67.1 | 4.7 | 13.2 | 6.1 | 8.9 |

The nanostructure of pure adsorbent and Hg(II)-adsorbed composite was further examined using HR-TEM. As shown in Fig. 3.3a, the pure adsorbent had a regular, spherical shape with diameter of 150-200 nm. However, the surface of Hg(II) adsorbed material appeared to be large agglomerates structure (Fig. 3.3b) with higher diameter (250-400 nm). Aggregation of water solvated Hg(II) ions around the adsorbent surface makes size differences of the post adsorbed material due to formation of bigger clumps at the time of adsorption process. Elemental mapping in STEM (Fig. 3.3c & e) revealed the homogeneous distribution of sulphur on the PPy/MAA composite before (Fig. 3.3d) and after Hg(II) adsorption (Fig. 3.3f). The distribution of mercury in adsorbed material can clearly be seen in Fig. 3g, and jointly with sulphur in Fig. 3.3h.

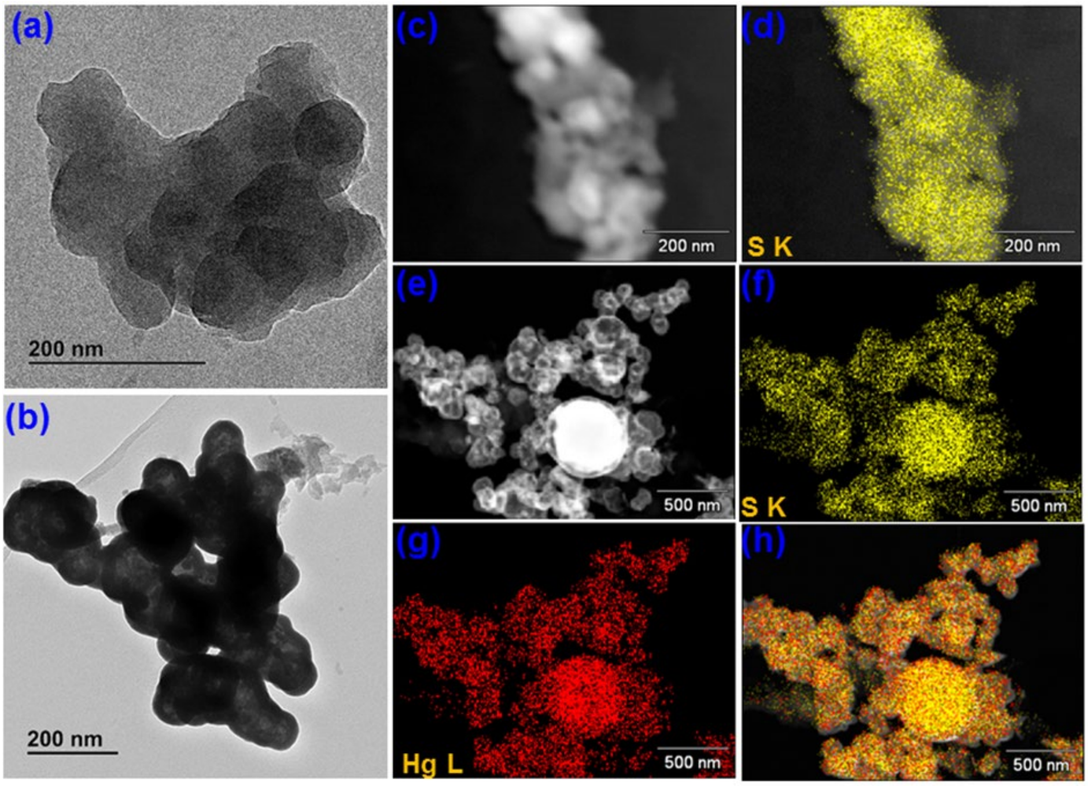

**Figure 3-3: HR-TEM image of PPy/MAA (a) before and (b) after adsorption; STEM image of PPy/MAA (c) before and (e) after adsorption of Hg(II); Homogeneous distribution of 'S' atom in PPy/MAA (d) before and (f) after adsorption, (g) distribution of adsorbed Hg(II), (h) combine distribution of 'S' and Hg(II) in the adsorbent.**

To investigate functional group present in PPy/MAA composite and the change of surface functionality of PPy/MAA composite after Hg(II) adsorption, FT-IR spectra in between 4000-600 cm$^{-1}$ wavenumbers were recorded. Fig. 3.4 shows the vibrational peaks at 3220, 2913, and 1696 cm$^{-1}$ of pure PPy/MAA characteristic of O-H stretching, C-H stretching, and vibration of the carbonyl group of mercaptoacetic acid, respectively. Infrared spectra described the symmetrical and asymmetrical PPy ring-stretching modes at 1544 and 1480 cm$^{-1}$, respectively [50, 51] as shown in Fig. 3.4. The stretching band at 2636 cm$^{-1}$ is identified as a S-H vibration which provides strong evidence supporting the presence of mercaptan groups in the polymer composite [52, 53]. In addition, the peak at 1255 cm$^{-1}$ was assigned to the C-O stretching frequency of MAA, and peaks at 1370 and 930 cm$^{-1}$ to C-N stretching and C-H deformation vibrations, respectively. These features indicated that MAA had been successfully incorporated into the PPy polymer matrix. The IR spectrum (Fig. 3.4) of post adsorbed material (PPy-MAA/Hg(II)) was also studied to explain the adsorption mechanisms with the help of functionality change after Hg(II) adsorption. PPy-MAA/Hg(II) material showed two major characteristic changes in FT-IR spectrum. It was found that the O-H stretching region almost disappeared, and a broad, less intense peak was observed in the infrared region at 3274-3115 cm$^{-1}$. Similarly, the strong, sharp peak of S-H vibrations at 2636 cm$^{-1}$ disappeared, and a new absorption band was observed in the 2636-2456 cm$^{-1}$ range. The IR peak shift to lower regions and the significant decrease in the intensity of peaks is indicative of the strong binding of Hg(II) with thiol and acid functionality of the PPy/MAA composite. It is proposed that the changes observed in FT-IR spectra arise from the fact that mercury is a soft metal, with a strong tendency to bind the soft bases like thiol.

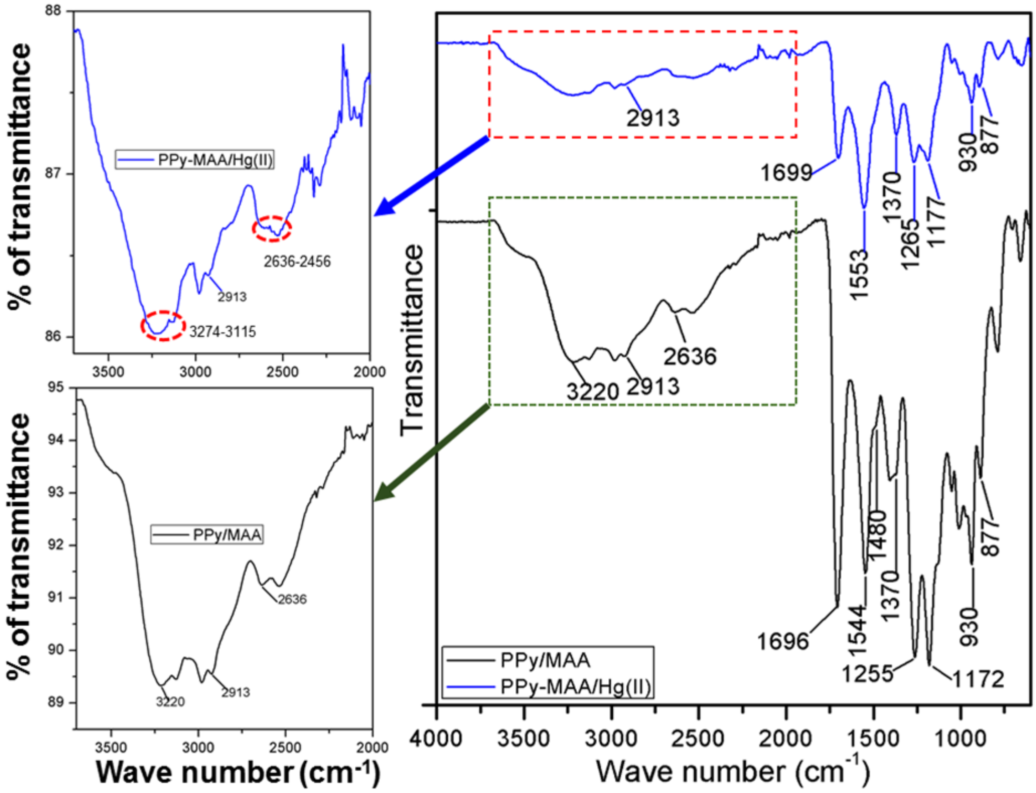

**Figure 3-4: FTIR spectra of PPy/MAA and PPy-MAA/Hg(II).**

Presence of thiol functional groups in the PPy/MAA composite was further investigated by Raman spectroscopy. The Raman spectra within 200-3000 cm$^{-1}$ for PPy/MAA composite and Hg adsorbed PPy/MAA are shown in Fig. 3.5. The Raman spectra in Fig. 3.5 show the Raman band at 1376 cm$^{-1}$ for C-N stretching vibration of polypyrrole ring [54]. The peaks at 1591 cm$^{-1}$ of PPy/MAA and 1596 cm$^{-1}$ of (PPy-MAA/Hg(II)) are assigned to C=C stretching vibration [54]. Before adsorption, PPy/MAA exhibits a Raman peak at 2532 cm$^{-1}$ due to -S-H stretching [55]. However, after Hg adsorption, the composite exhibits a band in the 2520-2665 cm$^{-1}$ region for Hg adsorbed thiol group (-SH stretching frequency). The -SH peak broadening indicates the interaction between thiol group and adsorbed Hg(II) ions.

Fig. 3.6 depicts XRD spectra from the PPy/MAA composite before and after (PPy-MAA/Hg(II)) adsorption. The lattice pattern of PPy/MAA composite exhibited a broad diffraction peak at 2θ = 20.5° (Fig. 3.6) due to the scattering from polypyrrole chain at the interplanar spacing. The corresponding XRD pattern of pure PPy/MAA (Fig. 3.6) illustrates the amorphous state of the synthesized composite material. In Fig.3.6 the Hg(II)-adsorbed PPy/MAA composite displays a broad peak near within 2θ = 31-35°. The XRD peak observed at 2θ = 32.4 matches closely the (011) plane of HgO [56]. It is possible that at the time of Hg(II) adsorption, the formation of a surface Hg-O complex with -COOH groups present in the composite material are responsible for the broadening of the peak observed at 2θ = 32.4°.

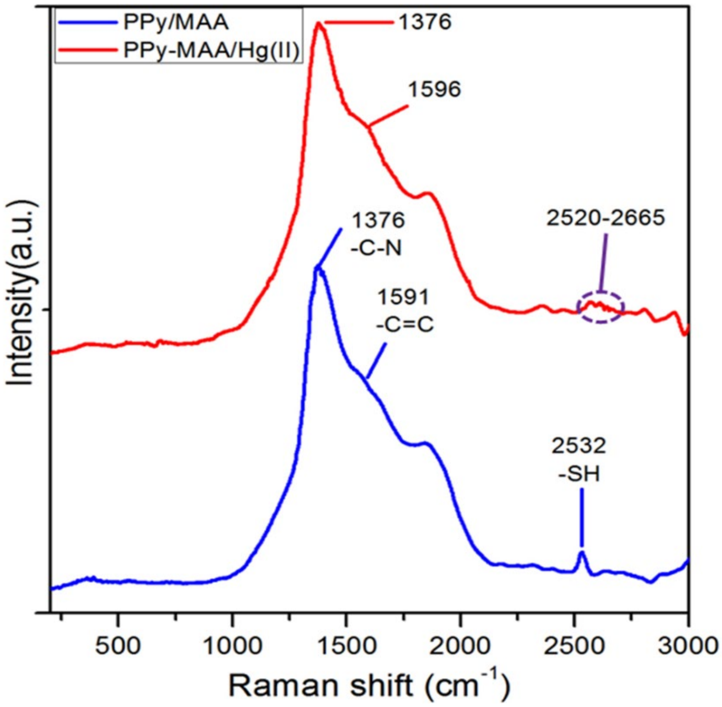

Figure 3-5: Raman spectra of PPy/MAA and PPy-MAA/Hg(II).

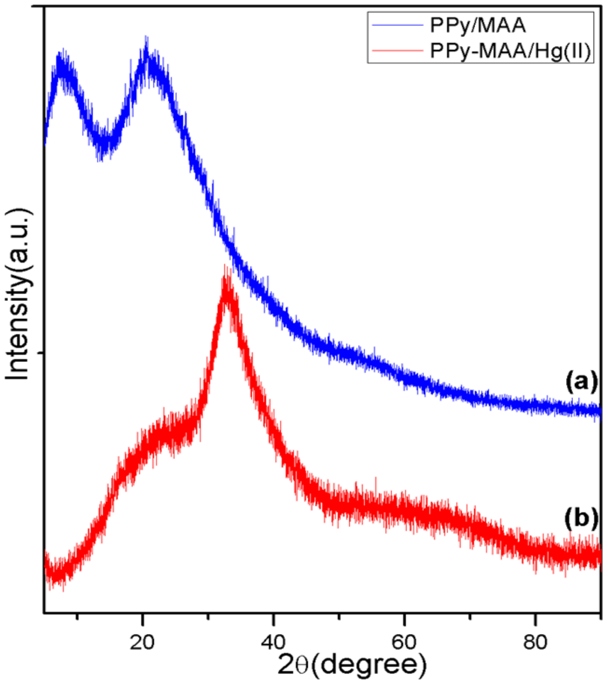

Figure 3-6: XRD patterns of PPy/MAA (a) before and (b) after adsorption of Hg(II).

Nitrogen adsorption experiments were performed to determine the surface areas (m$^2$/g), pore diameter (nm) and pore volume (cm$^3$/g) of the neat PPy and its composite (PPy/MAA) (Fig. 3.7). BET results showed that the surface area of as-prepared PPy/MAA composite calculated from the $N_2$ adsorption isotherm was 12.86 m$^2$/g, higher than pure PPy (7.91 m$^2$/g) [57]. Pore diameter was calculated with the help of BJH method, and the cumulative pore dimeter of PPy/MAA (40.83 nm) was almost twice than that of pure PPy (20.75 nm). The pore volume of PPy/MAA composite also increased from 0.0187 to 0.0849 cm$^3$/g relative to PPy.

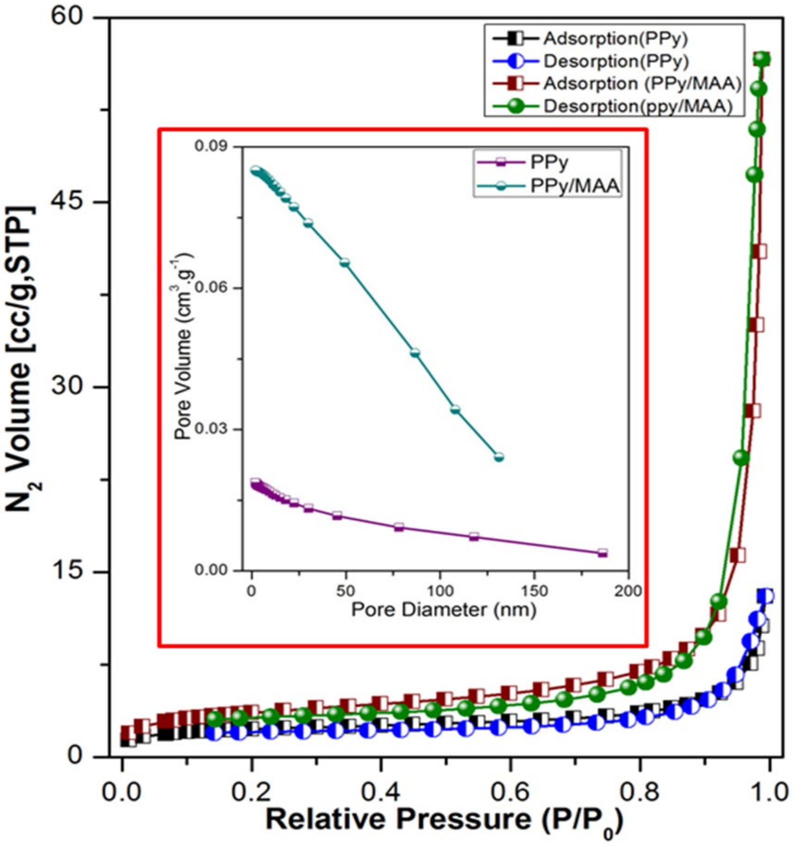

**Figure 3-7: Nitrogen adsorption and desorption isotherms of PPy/MAA composite with the corresponding pore-size distributions (inset).**

### 3.3.2 Adsorption of Hg(II)

#### *3.3.2.1 Influence of pH*

The pH of the adsorption medium plays an important role during metal ion removal. It not only affects the dominant form of metal ion in the adsorption medium but also changes the surface functional properties of the adsorbents. Fig. 3.8 summarizes the adsorption behaviour of the PPy/MAA composite at different pH values.

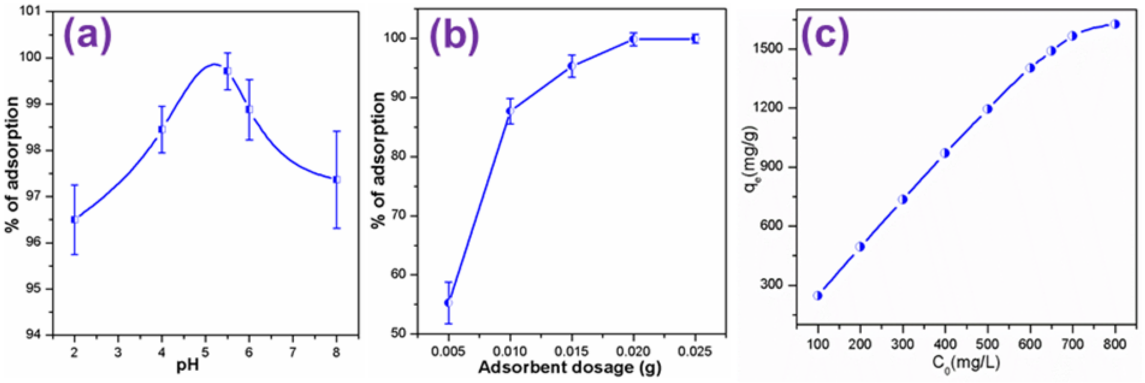

**Figure 3-8: Influence of (a) pH, (b) adsorbent dosage and (c) initial Hg(II) concentration of adsorption of Hg(II) onto PPy/MAA.**

The results reveal that adsorption efficiency rises from 96.5 to 99.4% with increasing pH from 2.0 to 6.0. Mercury ions exist in different Hg aqueous species [58, 59] such as $Hg^{2+}$, $HgOH^{+}$ and $Hg(OH)_2$ depending upon the pH values of the medium. At pH < 4, mercury ions exist predominantly as $Hg^{2+}$ in solution, whereas $HgOH^{+}$ and $Hg(OH)_2$ dominate at pH 4-6, and $Hg(OH)_2$ at pH > 6. Zeta potential values at various pH gave us a clear idea about the surface charge of the adsorbent. As seen in Fig. 3.8, increasing pH from 2.0 to 10.0 significantly decreases the zeta potential of PPy/MAA from -6.5 to -22.9 mV. From the results (Fig. 3.9), the observed low removal efficiency of PPy/MAA at very low and high pH is perhaps due to (i) competition in the exchange of $Hg^{2+}$, $H^{+}$ or $H_3O^{+}$ ions from the solution to the adsorbent surface; (ii) electrostatic repulsion between positively charged $Hg^{2+}$ ions in solution with protonated surface functional groups in the adsorbent.

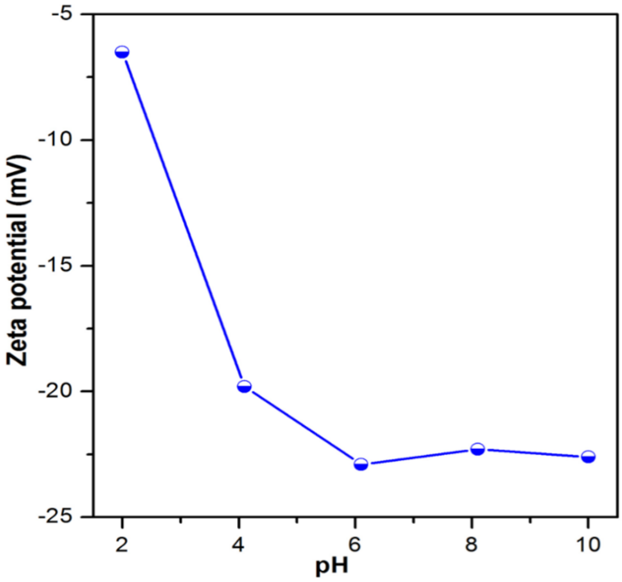

**Figure 3-9: Effect of pH on zeta potential of PPy/MAA composite.**

Moreover, it was found that at moderately acidic pH (4.0-6.0) not only deprotonated surface functional groups of adsorbent would be free for binding the metal ions but also PPy/MAA composite carried maximum negative zeta potential value (Fig. 3.9). Therefore, these two combine factors make the adsorbent PPy/MAA able to achieve maximum percentage (99.4%) of Hg(II) removal at pH 5.5. However, at higher initial pH (> 6), the quantity of Hg(II) adsorbed declines due of formation of insoluble $Hg(OH)_2$ as the dominant species in solution. It was expected that the binding strength would be reduced due to electrostatic interaction between the active groups in the adsorbent and neutral mercury species. However, neither precipitation of the metal hydroxide nor protonation of the functional group is expected at pH 5.5 and is therefore considered as an optimum pH for Hg(II) removal.

#### 3.3.2.2 *Effect of adsorbent dosage for Hg(II) removal*

To determine the optimum quantity of PPy/MAA material for maximum removal of Hg(II) from solution, the amount of composite used was varied from 5 to 25 mg in 50 mL of adsorption medium with $C_0$ = 200 mg/L at pH 5.5. The percentage of Hg(II) adsorbed increased proportionally with adsorbent mass and these results are shown in Fig. 3.8b. Surface area and active adsorption site, the two main factors on which the percentage adsorption of Hg(II) depends upon, significantly increase by the addition of more adsorbent onto the adsorption medium. Whereas, after reaching equilibrium, percentage adsorption of Hg(II) not sufficiently affected by increasing the sorbent dosage over 20 mg. Therefore, this dosage value (0.02 g for 50 mL metal solution) was employed for further adsorption experiments.

#### 3.3.2.3 *Influence of initial Hg(II) concentration and static adsorption capacity*

Initial concentration of Hg(II) in the adsorption medium also affects the removal percentage. The effect of mercury concentration on adsorption study was investigated with a wide range of Hg(II) solution from 100-800 mg/L under the optimized conditions of temperature (25°C) and pH (5.5). From Fig. 3.8c it is obvious that the amount of Hg(II) adsorption increases with Hg(II) concentration reaching equilibrium at higher Hg(II) concentration. Initial Hg(II) concentration has a key role to enhancement the movement of metal ions from solution to solid adsorbent surface. As a result with increasing the initial concentration of metal ions, the interaction between adsorbate and adsorbent also enhanced. Every adsorbent has a characteristic capacity to adsorb a fixed amount (maximum adsorption capacity) of particular ions at equilibrium [60-62]. Langmuir [63] and Freundlich [64], the two most popular adsorption models, were tested in an isotherm study to estimate the binding affinity of thiol functionalized PPy/MAA to Hg(II) at concentrations ranging from 100 to 800 mg/L. The above two isotherm equations are expressed as follows:

$$\frac{C_e}{q_e} = \frac{1}{bq_m} + \frac{C_e}{q_m} \tag{1}$$

$$\ln q_e = \ln k_F + \frac{1}{n} \ln C_e \tag{2}$$

where $q_e$ (mg/g) represents the equilibrium quantity of Hg(II) adsorbed by PPy/MAA, $C_e$ is equilibrium adsorbate concentration (mg/L) in solution, $q_m$ is the maximum binding capacity (mg/g), b is the Langmuir constant for monolayer adsorption (L/mg), $k_F$ is the Freundlich coefficient characteristic reflecting the adsorption capacity (mg/g) and n signifies linearity index related to adsorption intensity.

The adsorption data obtained from batch experimental results were correlated with a linearized form of Langmuir and Freundlich isotherm equations, and the curves are shown in the inset of Fig. 3.10. As shown in Table 3.2, the correlation coefficient ($R^2$) of Langmuir model (0.9988) was higher and thus better suited than that of Freundlich isotherm model (0.9046). Based on the Langmuir model, maximum Hg(II) adsorption capacity was 1736.8 mg/g at 25°C. Excess number of available -SH chelating groups are responsible for the accumulation of large amount of Hg(II) on the PPy/MAA surface. On the basis of the results (Table 3.2), it is obvious that the Langmuir isotherm appeared to be closer to the experimentally observed values than the Freundlich model. A comparison between synthesized PPy/MAA with that of other recently reported adsorbents reveals that our composite has significantly higher adsorption capacity towards Hg(II) (Table 3.3) [65-70] making it an ideal candidate to remove Hg(II) from aqueous media.

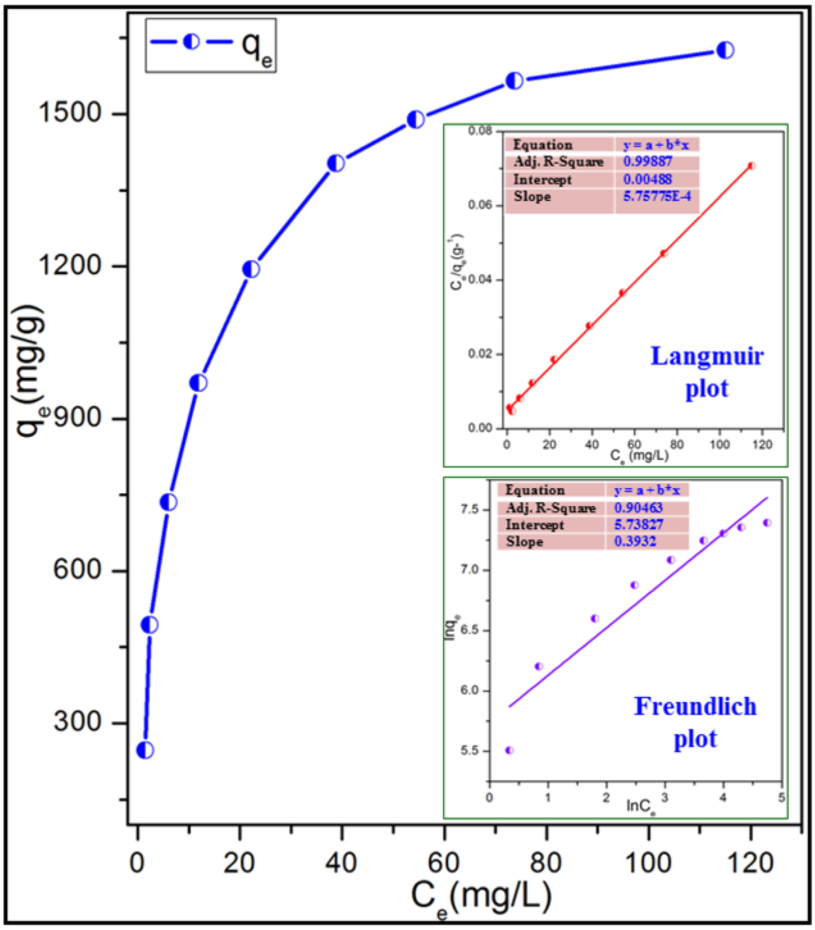

**Figure 3-10: Adsorption isotherm of Hg(II) on the PPy/MAA with different metal ion concentrations; (inset) best fitting of Langmuir and Freundlich isotherm model.**

**Table 3-2: Langmuir and Freundlich isotherm constants for adsorption of Hg(II).**

| Langmuir model | | Freundlich model | |
|---|---|---|---|
| $q_m$ (mg/g) | 1736.8 | $k_F$ (mg/g ) | 310.52 |
| b (L/mg) | 0.118 | n | 2.54 |
| $R^2$ | 0.9988 | $R^2$ | 0.9046 |

**Table 3-3: Comparison of maximum adsorption capacity against with other adsorbents for removal of Hg(II) ion.**

| **Adsorbent materials** | **Adsorption Time** | **pH** | **Adsorption capacity ($mg.g^{-1}$)** | **References** |
|---|---|---|---|---|
| Polypyrrole (PPy) multilayer-laminated cellulose | 60 min | 6.0 | 31.68 | 65 |
| graphene oxide-L-cystine | ------ | 5.5-7.0 | 79.36 | 66 |
| Graphene oxide-iron magnetic nanoparticles | 180 min | 5.0 | 16.6 | 67 |
| Thiol modified $Fe_3O_4$@$SiO_2$ | 10 min | 4.0 | 74 | 68 |

| Adsorbent materials | Adsorption Time | pH | Adsorption capacity ($mg.g^{-1}$) | References |
|---|---|---|---|---|
| $Fe_3O_4$ nanoparticles capped with 3,4-dihydroxyphenethylcarbamodithioate | ------ | 7.0 | 52.1 | 69 |
| Sulfur-Functionalized Silica Microspheres | 2 days | 7.5 | 62.3 | 70 |
| Polypyrrole/mercaptoacetic acid (PPy/MAA) | 24h | 5.5 | 1736.8 | Present study |

### *3.3.2.4 Adsorption kinetics for Hg ions*

Batch adsorption kinetics were studied to determine the optimal contact time for Hg(II) removal. The rate of Hg(II) adsorption was determined by employing the following experimental conditions: 0.4 g adsorbent in 1 L solution containing Hg(II) concentration ranging between 25 to 200 mg/L, at pH 5.5 and 25°C. Fig. 3.11a shows that the rate of Hg(II) adsorption was rapid in the first 20 minutes of adsorption study, and then slowed down with time until equilibrium was reached. Such rapid initial adsorption may have been due to the availability of active sites for metal binding on the adsorbent. As the number of vacant active adsorption sites decreases over time, so does the rate of adsorption. Although active sites are still available at equilibrium, further adsorption is prevented by repulsion forces between occupied sites on the adsorbent and incoming metal ions in the medium. To find out the mechanism of adsorption kinetics two well-known rate equations, pseudo-first-order [71] and pseudo-second-order [72] were applied.

**Pseudo-First-Order Kinetics**.

The linearized from of pseudo-first-order equation proposed by Lagergren [71] is mathematically described as follow:

$$\log(q_e - q_t) = \log q_e - \frac{k_1}{2.303}t \qquad (3)$$

where $q_e$ (mg/g) and $q_t$ (mg/g) are quantity of adsorbate at equilibrium and time t (min), respectively, $k_1$ (1/min) is rate constant. The kinetics data were fitted to eq. 3 and calculated results were depicted in Fig. 3.11 from the plot of $\log(q_e\text{-}q_t)$ versus t for Hg(II) ions.

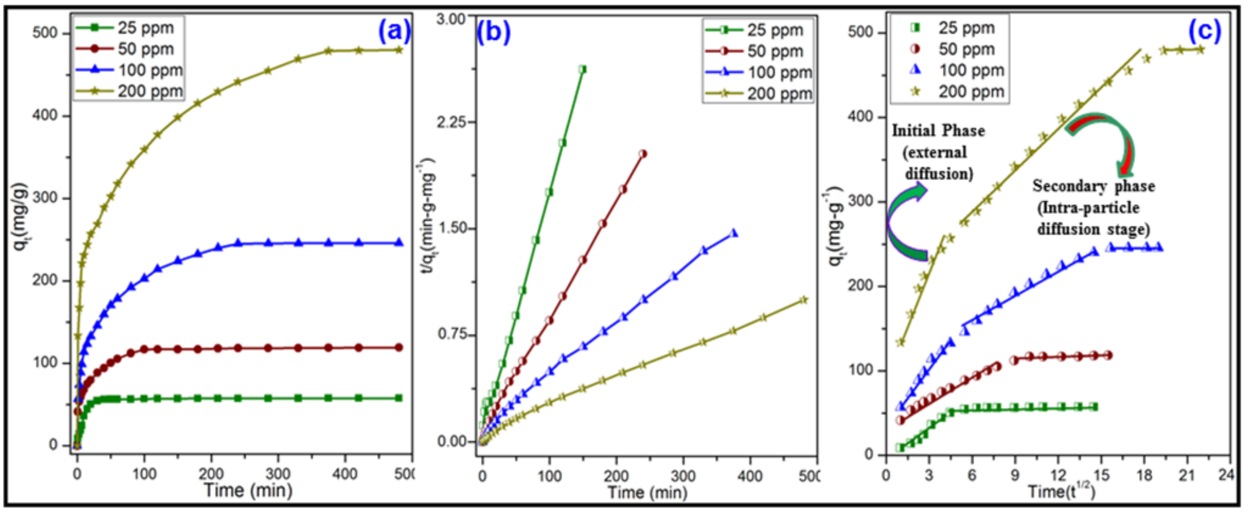

**Figure 3-11: (a) Adsorption kinetics of Hg(II) at 25°C with metal ion concentrations of 25, 50, 100 and 200 mg/L; (b) pseudo-second-order and (c) intraparticle diffusion model of Hg(II) ions adsorption onto PPy/MAA composite.**

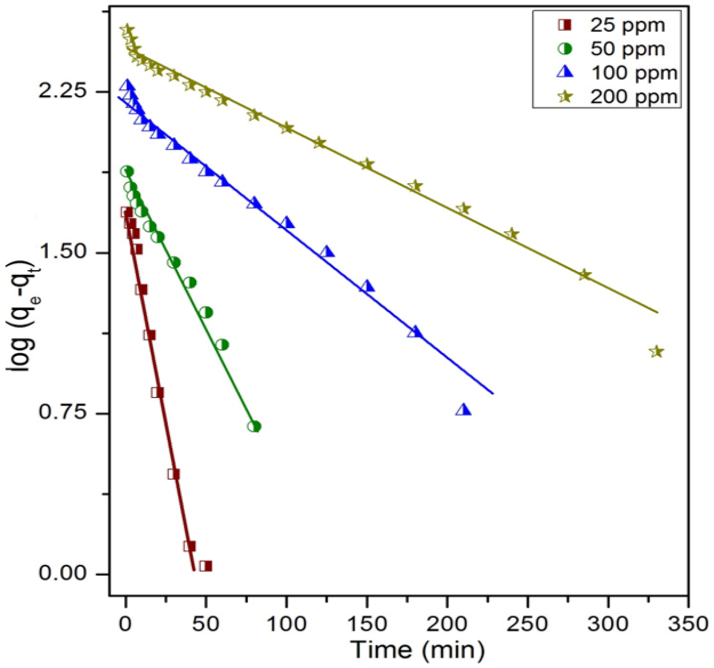

**Figure 3-12: Pseudo-first-order kinetics for Hg(II) adsorption on PPy/MAA composite.**

Table 3.4 summarises the kinetic constant and correlation coefficient ($R^2$) values. The calculated adsorption parameters not well matched with the experimental values. The correlation coefficient ($R^2$) values (0.9075-0.9888) also showed lack of linearity. It is clear from Table 3.4 that the calculated adsorption data were not suitable to define the kinetics profile of Hg(II) adsorption with linear fitting of pseudo-first-order model.

**Table 3-4: Kinetics parameters for adsorption of Hg(II) from aqueous medium.**

| Initial metal concentration ($C_0$)(mg/L) | Pseudo-first-order kinetic model | | | Pseudo-second-order kinetics model | | |
| --- | --- | --- | --- | --- | --- | --- |
| | $k_1$(1/min) | $q_e$(mg/g) | $R^2$ | $k_2$(mg/g.min) | $q_e$(mg/g) | $R^2$ |
| 25 | $8.5 \times 10^{-2}$ | 51.06 | 0.9761 | $32.8\times10^{-4}$ | 59.2 | 0.9982 |
| 50 | $3.1 \times 10^{-2}$ | 71.25 | 0.9888 | $12.1\times10^{-4}$ | 121.9 | 0.9983 |
| 100 | $1.4 \times 10^{-2}$ | 165.69 | 0.9852 | $2.4\times10^{-4}$ | 256.4 | 0.9956 |
| 200 | $1.1 \times 10^{-2}$ | 331.89 | 0.9075 | $0.9\times10^{-4}$ | 500 | 0.9935 |
| | Weber-Morris model (Intraparticle diffusion model) | | | | | |
| | Initial phase | | | Secondary phase | | |
| $C_0$(mg/L) | $K_{ip1}$ | $C_1$ | $R_1^2$ | $K_{ip2}$ | $C_2$ | $R_2^2$ |
| 25 | 12.93 | 5.17 | 0.9736 | 0.156 | 55.23 | 0.9143 |
| 50 | 17.01 | 37.92 | 0.9858 | 0.25 | 74.3 | 0.9254 |
| 100 | 22.38 | 73.35 | 0.9798 | 10.28 | 96.38 | 0.9842 |
| 200 | 35.38 | 109.53 | 0.9459 | 15.73 | 196.86 | 0.9865 |

**Pseudo-Second-Order Kinetics**.

The pseudo-second-order kinetic model of Ho and McKay [73] has been applied to investigate the adsorption kinetics.

$$\frac{t}{q_t} = \frac{1}{k_2 {q_e}^2} + \frac{t}{q_e} \tag{4}$$

where $k_2$ (g/mg.min) is pseudo-second-order rate constant. Kinetics parameters of this model were calculated from the linear plot of $t/q_t$ vs t (Fig. 3.11b). The correlation coefficients ($R^2$) shown in Table 4 indicate a strong relationship between metal ion uptake with contact time for the removal of Hg(II) ions by PPy/MAA. In addition, the theoretically calculated $q_e$ values were similar to the experimentally-determined $q_{e(exp.)}$ values. Therefore, comparing the two kinetic equations above reveals that the pseudo-second-order is the most appropriate model for the above adsorption system.

**Intraparticle diffusion**

The Weber and Morris [74] model for intraparticle diffusion was applied to determine the influence of diffusion in the adsorption process, and can be expressed mathematically using eq. 5.

$$q_t = k_{id} t^{1/2} + C \tag{5}$$

where, $k_{id}$ (mg/g.min$^{1/2}$) is a measure of diffusion constant and *C* is directly proportional to boundary layer thickness. A plot of the quantity of adsorbate ($q_t$) against the square root of the time ($t^{1/2}$) gives the rate constant (slope of the plot) and boundary layer thickness (intercept of linear plot). Fig. 3.12c displays the $q_t$ vs $t^{1/2}$ plot for various initial concentration of Hg(II) solution and it shows a multi-step adsorption process. The initial sharp linear section implies an external diffusion, i.e. mass transfer from solution to solute phase. The second linear section represents the intraparticle diffusion of adsorbate molecule within the micropores of the adsorbent networks. In the third phase, diffusion remains almost constant due to the exhaustion of pore volume in the adsorbent [75]. Intraparticle diffusion parameters ($k_{id}$ and C) at different step (1st phase

& 2nd phase) are presented in Table 3.4. The rate parameters ($k_{id}$) shifted to higher values with increasing initial concentration of Hg(II) ions. This may be attributed that at high metal ions concentration, the ionic mobility of adsorbate is faster from solution to solute phase. From the results (Table 3.4) it is obvious that adsorption data fit well the Weber-Morris equation with higher correlation coefficient value ($R^2 > 0.96$). Therefore, the observed results indicate that not only external mass transfer but also intraparticle diffusion play as a vital role for Hg(II) adsorption from aqueous media.

#### *3.3.2.5 Effect of ionic strength on Hg(II) adsorption*

The presence of dissolved salts has an effect on the Hg(II) adsorption capacity. Therefore, it is important to figure out the performance of PPy/MAA as a function of adsorbent in two different conditions from normal adsorption system to electrolyte present in the adsorption medium. To evaluate the ionic strength effect on Hg(II) adsorption, different $KNO_3$ solutions with concentrations ranging from 0.01 to 1.0M were introduced into the adsorption medium. There was no visible effect of salt concentration on the adsorption of Hg(II) (Fig. 3.13). Therefore, it can be concluded that the attraction between sulphur containing adsorbent (PPy/MAA) and Hg(II) ions is very effective as well as specific and unaffected by other significant effects of salt screening or attraction in adsorption medium.

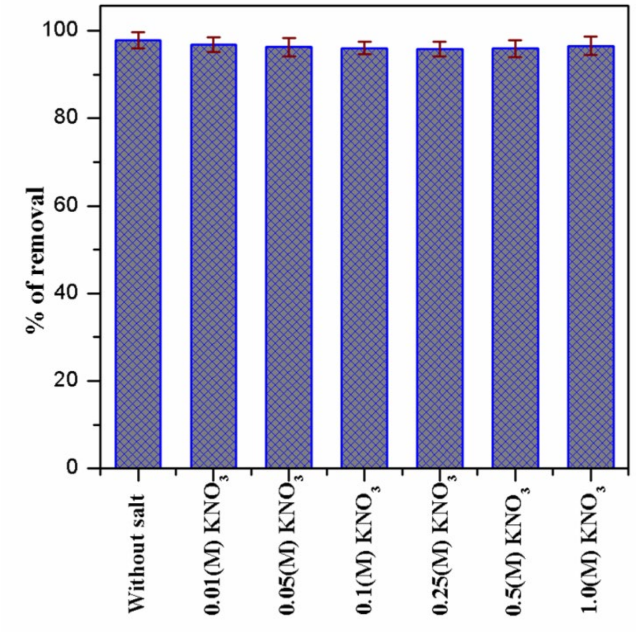

**Figure 3-13: Effect of ionic strength on adsorption of Hg(II) onto PPy/MAA composite.**

#### *3.3.2.6 Mechanism of Hg(II) removal*

There are several plausible mechanisms for metal ions adsorption using functionalized adsorbent including electrostatic interaction, surface precipitation and ion exchange processes [76-77]. Physico-chemical characterization techniques like FE-SEM, EDX, FTIR, STEM and XPS were used to explore the mechanisms involved in the removal of Hg(II) by PPy/MAA. It can be assumed that the mercapto functionalized PPy adsorbent, containing electron-rich sulphur and oxygen atoms in -SH and -COOH groups, has a strong ability to bind Hg(II). Based on Pearson's concept, Hg(II) forms a compatible metal chelate-complex through the coordination with sulphur, oxygen atom. Therefore, electron donor functionality of mercaptoacetic acids like thiol (-SH), carboxylic acid (-COOH) groups, contribute their lone pair of electrons to Hg(II) for strong soft acid-base interaction shown in Scheme 3.2.

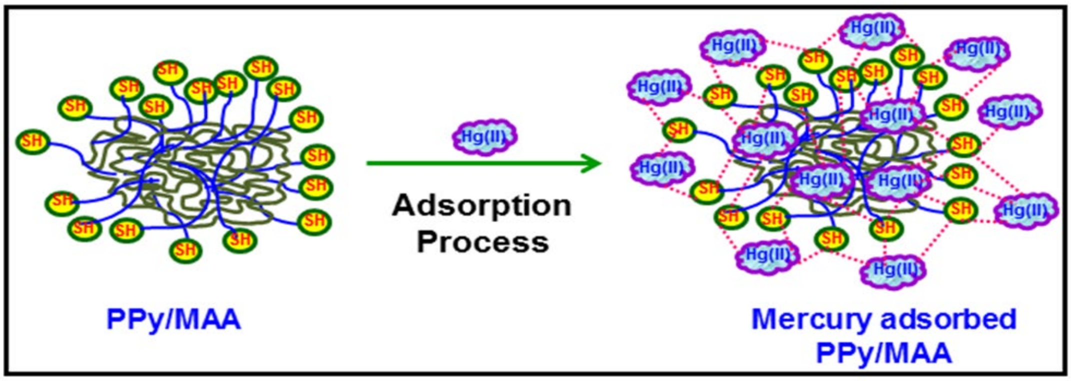

**Scheme 3-2: Schematic representation of possible adsorption mechanism of Hg(II) ions onto the PPy/MAA composite.**

A comparison of FTIR spectra of adsorbents with different functionalities (Fig. 3.17) revealed peak shifts after adsorption. One noteworthy change involved the peak corresponding to the stretching vibration band of S-H group of the adsorbent, which shifted from 2636 cm$^{-1}$ to a broad infrared region of 2456-2636 cm$^{-1}$. The peak broadening of S-H stretching frequency suggests that the sulphur atom in the thiol functional group was involved in the Hg(II) adsorption process. Another one major change was observed in the -OH stretching frequency of the -COOH group of the adsorbent. In pure adsorbent (Fig. 3.17), the strong stretching vibration band of O-H groups at approximately 3220 cm$^{-1}$ almost disappeared after adsorption of Hg(II) to exhibit a broad and weak band in the infrared region of 3115-3274 cm$^{-1}$. This characteristic spectral phenomenon further indicates that electrostatic interaction was involved between the positive metal ions (Hg(II)) and acid groups (-COOH) of adsorbent. HR-TEM and FE-SEM studies figure out the characteristics change happened into the post-adsorbed adsorbent. The different structural aspects between pure adsorbent and post-adsorbed materials help a lot to find out Hg(II) adsorption phenomenon.

To provide evidence for the adsorption mechanism, binding energies of surface compositions of the PPy/MAA and PPy-MAA/Hg(II) were measured using XPS over the range of 0-1350 eV (Fig. 3.14a). Spectra reveal the presence of Hg 4f signals after adsorption, which provides further evidence of the adsorption of Hg(II) onto PPy/MAA. Deconvolutions of Hg 4f signal (Fig. 3.14b) shows two peaks, with binding energies at 100.05 and 104.04 eV, corresponding to Hg 4f$^{7/2}$ and 4f$^{5/2}$ signals, respectively [65, 66, 78]. The binding energy of Hg4f$^{7/2}$ at 100.05 eV indicates an absence of Hg(0) (binding energy of Hg(0) 4f$^{7/2}$ between 99.2 to 99.8 eV) [75]. The adsorbed Hg exists on the surface of the adsorbent as either Hg(I) or Hg(II) species. Fig. 3.14c exhibits the deconvolution of C 1s spectra of the adsorbent (PPy/MAA) and post-adsorbed material (PPy-MAA/Hg(II)). High-resolution spectra clearly indicate that the C 1s could be divided into four major peaks due to four different bonding (C-C, C-N, C-S and C-O) environment. Fig. 3.14c indicates no major change in intensity, as well as binding energies of the C1s peaks for PPy/MAA and PPy-MAA/Hg(II). In Contrast, high-resolution S 2p spectra of PPy/MAA display remarkable change during Hg(II) removal (Fig. 15d).

Deconvolution of S 2p shows two peaks at 162.45 eV for S $2p^{3/2}$ and at 163.4 eV for S $2p^{1/2}$. For post-adsorbed material, the peak intensity of S atoms diminishes significantly, shifting towards higher binding energies (Fig. 3.14d). This phenomenon indicates the development of strong interactions between sulphur and mercury. Deconvolution of the O 1s shows peak at 531.89 eV attributed to the -COOH moiety of mercaptoacetic acid (Fig. 3.14e). Peak intensity decreases markedly after adsorption, and binding energy value (530.91 eV) also shifts towards lower energy indicating the interaction between oxygen atom of acid group and mercury ions. Based on the FTIR and XPS results, it is clear that Hg(II) adsorption likely takes place by the strong interaction with sulphur and oxygen atoms of PPy/MAA.

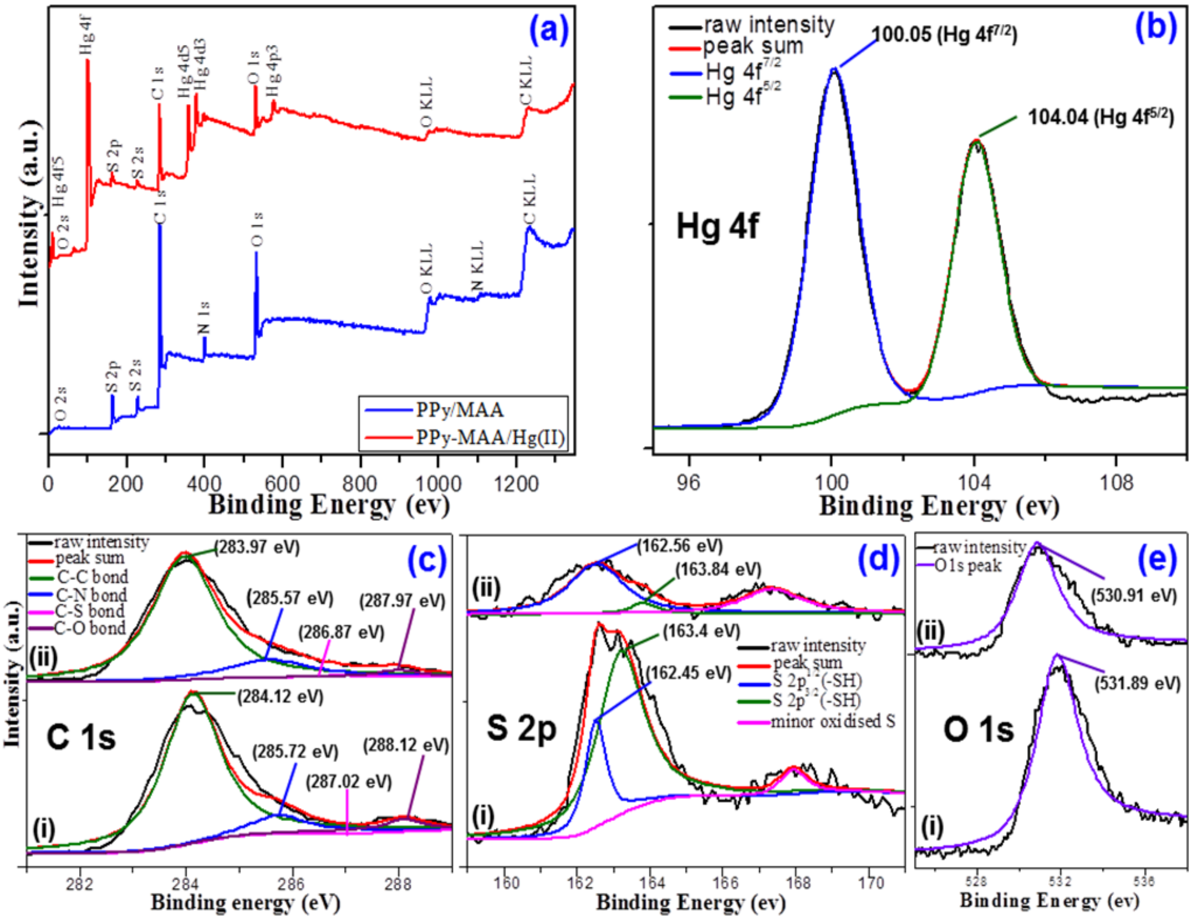

**Figure 3-14: (a) Full survey XPS spectra; (b) high resolution Hg 4f (c) C 1s (d) S 2p and (e) O1s spectra of PPy/MAA (i) before and (ii) after Hg(II) adsorption.**

### 3.3.3 Synthesis, characterization and application of thiol-functionalized polypyrrole (PPy/MAA) composites for Ag(I)

#### *3.3.3.1 Characterization*

The morphologies of the as-prepared PPy/MAA composite before and after adsorption of silver ion were investigated by FE-SEM and HR-TEM analysis. As can be seen in Fig. 3.15a, the typical FE-SEM image shows that the PPy/MAA composite possesses a uniform distribution of granular/spherical structure with relatively uniform diameters of around 150-200 nm. Fig. 3.15b shows the FE-SEM images of PPy/MAA composite after adsorption of silver ion. The results appear markedly different from neat PPy/MAA composite (Fig. 3.15a). The presence of metallic crystal-like structures on the surface of PPy/MAA composite suggests the accumulation of metal ion (silver) on the adsorbent surface. In addition, an even distribution of Ag adsorbed onto the composite surface is further confirmed with the EDS (Fig. 3.15e and f) and elemental mapping image (Fig. 3.15c and d) of C, N, O, S, Ag for PPy/MAA and silver adsorbed PPy/MAA. The existing of prominent silver peak in EDS spectra (Fig. 3.15f) and well distribution of silver onto the composite surface (Fig. 3.15d) confirmed the successive adsorption of silver particles into the adsorbent surface.

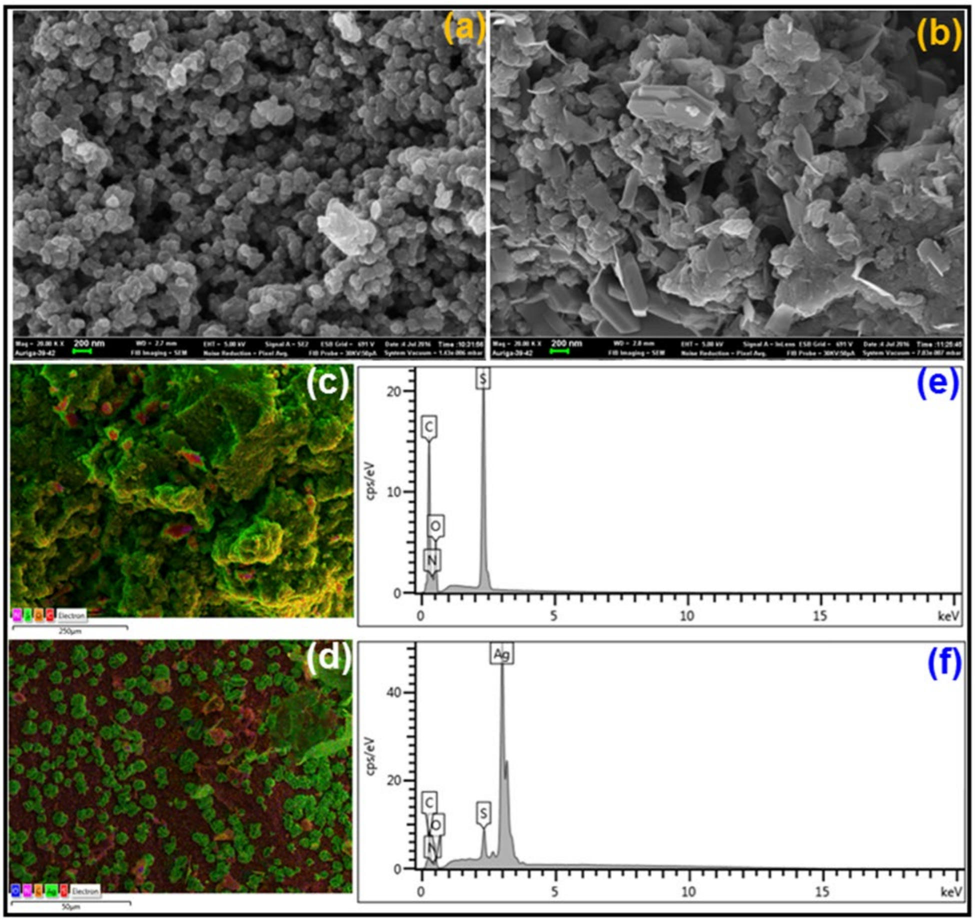

**Figure 3-15: Morphology and element composition of PPy/MAA: FE-SEM image of PPy/MAA (a) before, (b) after adsorption of silver; Elemental mapping image of PPy/MAA (c) before and (d) after adsorption; EDS element composition analysis of PPy/MAA (f) before and (g) after silver adsorption.**

HR-TEM analysis (Fig. 3.16a) showed PPy/MAA composite revealed spherical particles with an average diameter of ~200 nm. Fig. 3.17b showed silver nanoparticles Ag NPs randomly dispersed on the surface of the PPy/MAA matrix. The inset of Fig. 3.16b shows that the size distribution of Ag NPs on the composite matrix is broad, ranging from 10 to 50 nm. The interplanar spacing (d-spacing) of Ag crystallites was clearly observed in well-defined lattice fringes of the Ag NPs in Fig. 3.16c. The d-spacing of Ag crystallites was measured as 0.230 nm (inset of Fig. 3.16c) which is consistent with the reported value of the (111) crystallographic plane of cubic Ag [79, 80]. This result indicates that silver ions in the aqueous solution are adsorbed on the adsorbent surface and subsequently reduced to silver nanoparticles through electron reach groups of the polymer based composite. To better understand the distribution of silver nanoparticles on the adsorbent surface, STEM analysis was executed. Fig. 3.16e & g display the distribution of sulphur on the adsorbent before and after adsorption. Similarly, Fig. 3.16h presents the dispersion of Ag throughout the adsorbent surface after adsorption. Fig. 3.16i represents the STEM image where red spots indicate silver distribution and yellow spots for sulphur. Therefore, from HRTEM as well as STEM analysis, it is evident that the silver particles are randomly distributed throughout the composite matrix after adsorption.

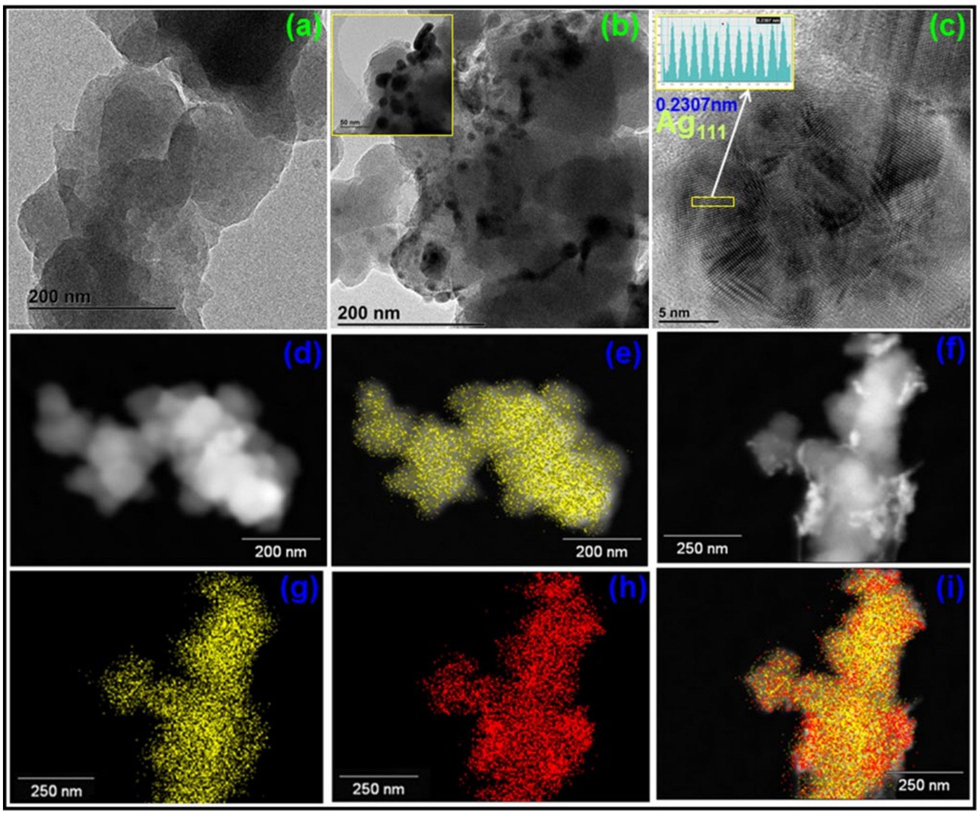

**Figure 3-16: HR-TEM image of PPy/MAA (a) before and (b) after adsorption (c) lattice fringes of the adsorbed Ag of silver at different magnification; STEM images of PPy/MAA (d) before and (f) after adsorption of silver; Homogeneous distribution of S atom in PPy/MAA (e) before and (g) after adsorption, (h) distribution of adsorbed Ag atom (i) composite map showing 'S' and 'Ag' on the adsorbent.**

The structural property of the functional group of PPy/MAA and PPy/MAA/Ag composite was further explored using FT-IR spectrometry, and results are shown in Fig. 3.17a and b. Additional structural information of pure and silver ions trapped PPy/MAA surface was obtained by wide angle powder X-ray diffraction (XRD) analyses. Fig. 3.18a presents the XRD pattern of the neat PPy/MAA composite before $Ag^+$ adsorption. The spectrum (Fig. 3.18a) only exhibits only a broad band at around 20.5° which can be assigned to the amorphous phase of the polymer matrix. It can be seen from Fig. 3.18b that PPy/MAA composite after silver ion sorption (PPy/MAA/Ag) showed five distinguishable sharp diffraction peaks at Bragg angles of 38.12, 44.30, 64.44, 77.40 and 81.7°, which exactly accord with the (111), (200), (220), (311) and (222) crystal planes of silver, respectively [81-83]. From the XRD spectra, it is apparent that adsorbed $Ag^+$ ions were reduced to metallic silver in the PPy/MAA composite. The above results provide direct evidence for the generation of metallic silver nanoparticle ($Ag^+$ ions to $Ag^0$) through reduction by the electron rich surface functionality of conducting polypyrrole networks based composite.

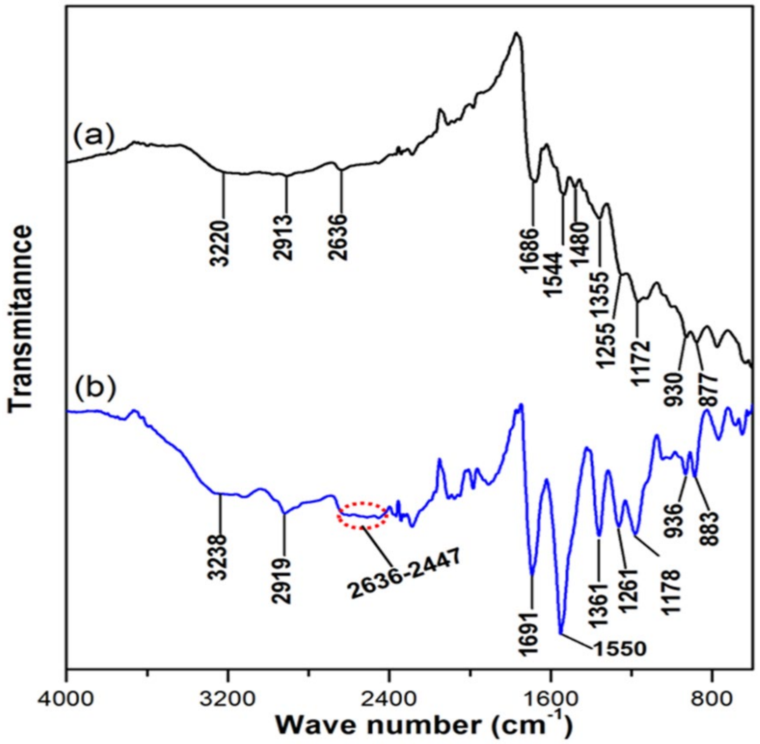

**Figure 3-17: FTIR spectra of PPy/MAA (a) before, (b) after adsorption of silver.**

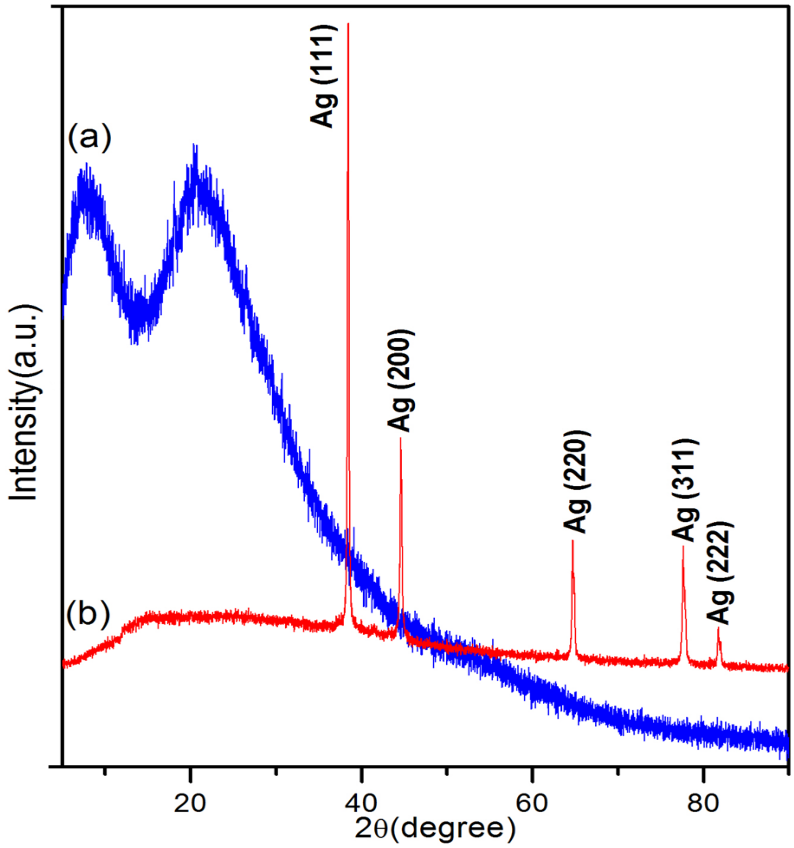

**Figure 3-18: XRD patterns of PPy/MAA (a) before and (b) after adsorption of silver.**

To analyse the surface area, pore volume, and pore diameter, the $N_2$ adsorption-desorption measurements were carried out for PPy and PPy/MAA composite and are shown in Fig. 3.19. Based on the BJH theory, the BET specific surface area, average pore diameter and pore volume of the corresponding materials are summarized in Table 3.5. Following polymerization with MAA, the surface area of PPy/MAA composite increased from 7.9 to 12.8 $m^2/g$. The corresponding pore size distributions calculated from the desorption branch of nitrogen isotherms by the BJH method are presented in the inset of Fig. 3.19. The cumulative pore volume of PPy is increased from 0.0187 to 0.0849 $cm^3/g$, and the average pore diameter doubled from 20.75 to 40.83 nm after polymerization with MAA.

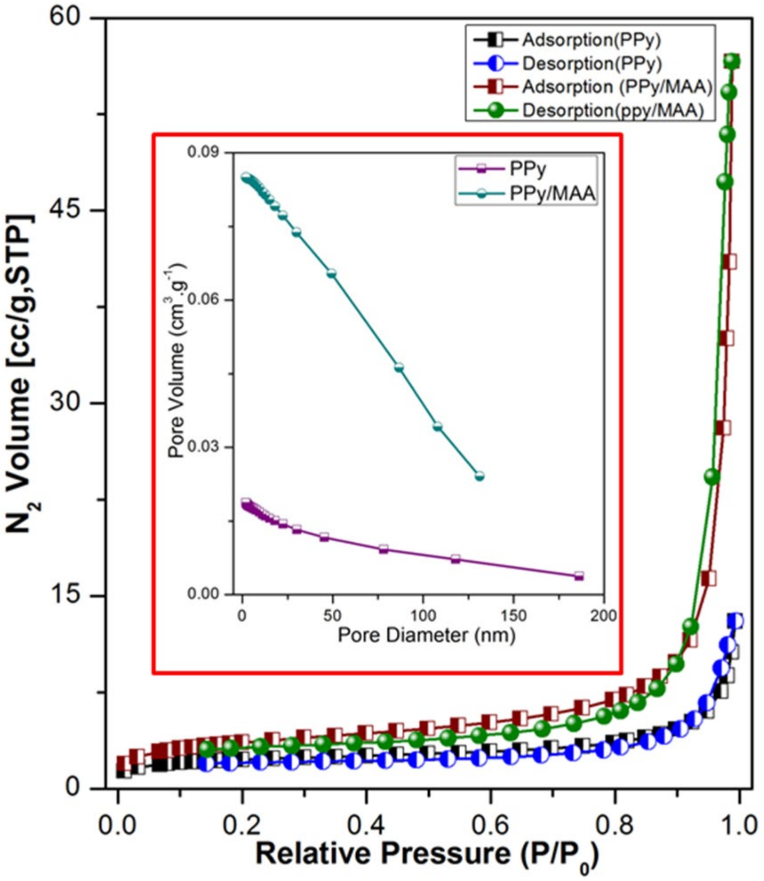

**Figure 3-19: Nitrogen adsorption and desorption isotherms of PPy/MAA composite with the corresponding pore-size distributions (inset).**

**Table 3-5: BET Analysis Result of PPy and PPy/MAA Composite.**

| Sample | Surface area (m$^2$/g) | Pore Volume (cm$^3$/g) | Pore diameter (nm) |
|---|---|---|---|
| **PPy** | 7.918 | 0.0187 | 20.75 |
| **PPy/MAA** | 12.864 | 0.0849 | 40.83 |

### 3.3.4 Silver ion adsorption property of the PPy/MAA composite

#### *3.3.4.1 Effect of the solution pH*

The pH of a solution plays an important role in metal ion adsorption, because it affects not only the protonation of the functional groups of adsorbent, but also the adsorptivity of the metal ions in solution. The percentage of adsorption of silver ions was investigated at a pH range between 1 and 6, but not above as silver ions precipitate above this value. As shown in Fig. 3.20a, the adsorption capacity increased steadily above pH 1 reaching a maximum [82, 84, 85] value at pH 5, decreasing at pH 6. It is likely that at higher pH, the deprotonation of mercaptoacetic acid takes place and hence the adsorption capacity of Ag$^+$ ions was enhanced by the strong ionic interaction between the adsorbent and Ag⁺. The pH of the silver nitrate solution (200mg/L) solution was 5.4, and this value was chosen as the working pH value for remainder of the study.

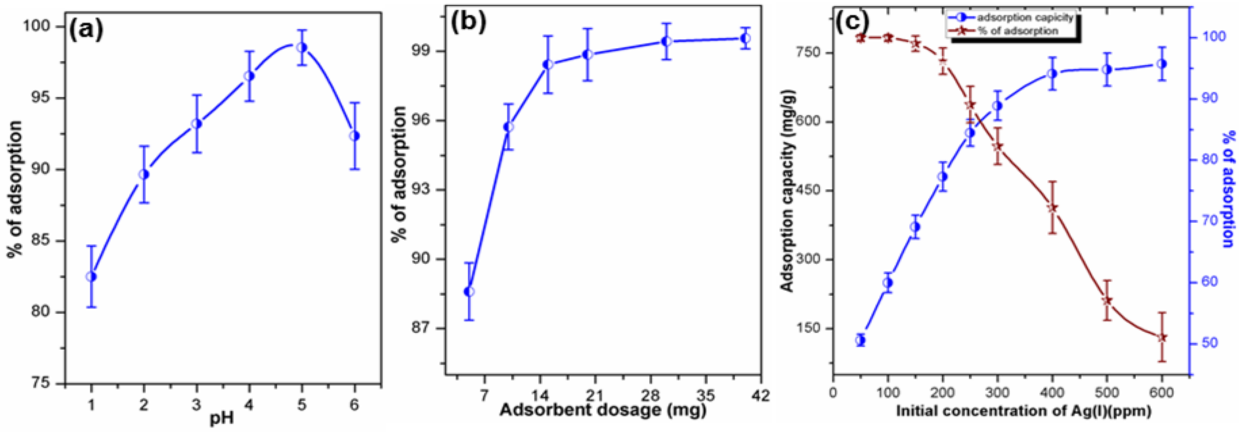

**Figure 3-20: Effect of (a) pH, (b) adsorbent dosage and (c) initial metal ions concentration on the adsorption of Ag(I) ions onto PPy/MAA composite.**

### *3.3.4.2 Effect of adsorbent dosage*

The effect of adsorbent dosage on the uptake of silver ions from the aqueous solution is shown in Fig. 3.20b. It is clear that the adsorption efficiency increases with an increase of adsorbent (PPy/MAA) from 5 to 40 mg in 50 mL of 100 mg/L $AgNO_3$ solution. At very low (5, 10 mg) adsorbent dosage, the percentage adsorption of Ag⁺ is very low. This is due to the lack of availability of the active sites on the adsorbent surface for silver adsorption. At 20 mg adsorbent dosage the efficiency of silver adoption was ~ 98.8% which is considered to be an equilibrium point. Further increase of adsorbent dosages did not yield any appreciable rise in adsorption efficiency due to the equilibrium of the adsorbent sites.

### *3.3.4.3 Effect of initial silver ion concentration*

The adsorption capacity of PPy/MAA composite to different initial concentrations of silver solution is shown in Fig. 3.20c. From the experimental results, it is evident that concurrent with an increase in the initial concentration of silver ion from 50 to 400 mg/L, the adsorption capacity of PPy/MAA composite increases from 125 to 706 mg/g, respectively. This trend may be explained by the fact that a higher initial silver concentration provides a correspondingly higher driving force attracting metal ions from the solution to the surface of adsorbent [86]. On the other hand, the adsorption capacity of silver solutions between 400 and 600 mg/L remained almost constant at approximately 720 mg/g. This may be because of the system reached equilibrium, with the available adsorption sites saturated with fixed Ag⁺.

### *3.3.4.4 Adsorption kinetics*

The rate of metal ion adsorption depends on the contact time between solid and liquid, and on the diffusion processes. The effect of the contact time on the adsorption of silver ions by PPy/MAA, and the metal ion concentration-dependent kinetics, are evident in Fig. 3.21, whereas Fig. 3.21b illustrates temperature dependent kinetics. Overall, both kinetic studies show that the silver ion adsorption efficiency was more rapid at initial stage and also it increased rapidly with increasing metal ion concentration and higher temperatures, before reaching equilibrium. In the case of 25 mg/L silver solution, adsorption reached saturation after 15 min whereas the 100 mg/L solution required 240 min before coming equilibrium point. Fig. 3.21b shows that equilibrium is reached faster at higher temperatures of the adsorption medium.

To get a better understanding of the adsorption rate and rate-controlling step of $Ag^+$ adsorption onto the PPy/MAA composite, two well-known adsorption models, pseudo-first- order [71] (eq. 6) and pseudo-second-order [72] (eq. 2.2) are used to fit experimental data.

$$\log(q_e - q_t) = \log q_e - \frac{k_1}{2.303} t \qquad (6)$$

$$\frac{t}{q_t} = \frac{1}{k_2 {q_e}^2} + \frac{t}{q_e} \qquad (7)$$

where $q_t$ and $q_e$ (mg/g) are the adsorption capacity at time t and equilibrium time, respectively, and $k_1$ ($min^{-1}$) and $k_2$ ($g\cdot mg^{-1}/min$) are the pseudo-first-order and the pseudo-second order model rate constants, respectively.

In order to investigate the mechanism for $Ag^+$ adsorption onto the PPy/MAA composite Weber-Morris intraparticle diffusion model [74] (eq. 8) can be introduced.

$$q_t = k_{id} t^{1/2} + C \qquad (8)$$

where $k_{id}$ ($mg.g^{-1}/min^{1/2}$) is an intraparticle diffusion rate constant and *C* is the the thickness of boundary layer. The plot of $q_t$ versus $t^{1/2}$ is presented in Fig. 3.21d.

It is evident that the experimental data are multilinear, including at least two linear segments. The first sharp phase represents the diffusion of adsorbate due to mass transfer from metal solution to the interface space of the adsorbent, and likely due to external diffusion [87, 88]. The second portion indicates a gradual adsorption step, corresponding with the diffusion of adsorbate molecules inside the pore of the adsorbent. This second step is also known as intra-particle diffusion stage. The constants of the intra-particle model are listed in Table 3.6. From these results, it was observed that both phases fit well to the Weber-Morris model ($R^2 > 0.96$). Therefore, intraparticle diffusion was the dominant rate-limiting process in silver ions adsorption on the PPy/MAA composite.

The linear-fitting result of pseudo-second-order kinetic plot t/qt versus t is shown in the inset of Fig. 3.21c and the pseudo-first-order kinetic plot is presented in Fig. 3.22. The correlation coefficient ($R^2$) value for pseudo-first-order model was 0.8697-0.9554 at different concentration of silver solution (from 25 to

100 mg/L) and calculated $q_e$ value was significantly lower than experimental value. Such low correlation coefficient and $q_e$ value suggested the poor agreement of pseudo-first-order model with the experimental data. The experimental data fitted well into the pseudo-second-order equation with correlation coefficients ($R^2$) from 0.9995 to 1, at different silver solution (from 25 to 100 mg/L) and the calculated value of $q_e$ was very close to the experimental result. The results show that the adsorption rates of $Ag^+$ onto the PPy/MAA can be considered as a pseudo-second-order adsorption process. The corresponding kinetic adsorption parameters calculated from the above two kinetic models are listed in Table 3.6.

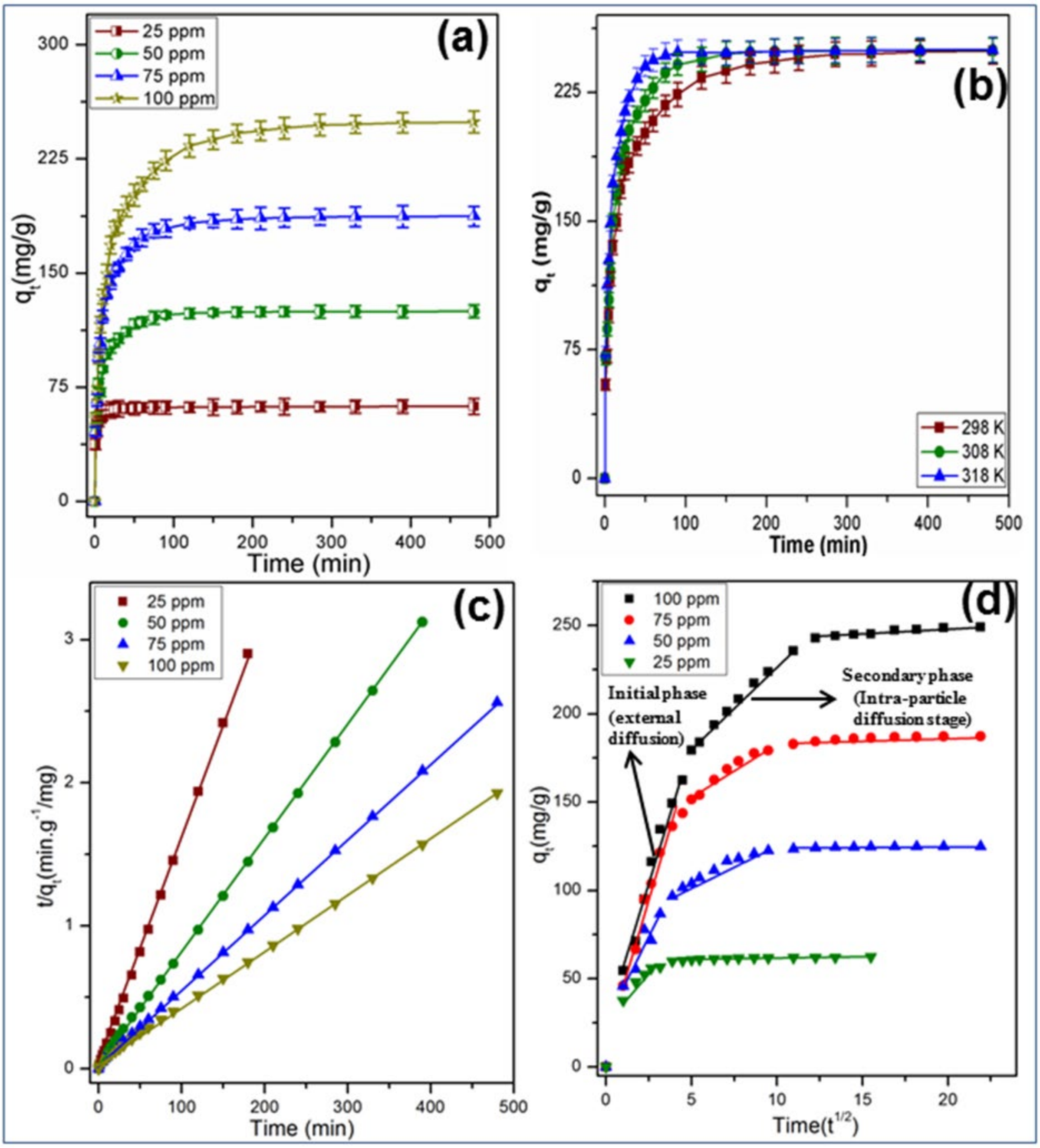

**Figure 3-21: Effect of contact time at (a) different initial concentration, (b) various temperature and kinetic curves of (c) pseudo-second-order, (d) intraparticle diffusion model of silver ions adsorption onto PPy/MAA composite.**

**Table 3.6: Concentration Dependent Kinetics Parameters for Adsorption of Silver Ions from Aqueous Medium.**

| Initial metal concentration ($C_0$)(mg/L) | Pseudo-first-order kinetic model | | | Pseudo-second-order kinetics model | | |
|---|---|---|---|---|---|---|
| | $k_1$($min^{-1}$) | $q_e$(mg/g) | $R^2$ | $k_2$($mg.g^{-1}/min$) | $q_e$(mg/g) | $R^2$ |
| 25 | $11.8 \times 10^{-2}$ | 22.66 | 0.8697 | $211.5\times10^{-4}$ | 62.5 | 1 |
| 50 | $3.5 \times 10^{-2}$ | 62.20 | 0.9554 | $21.5\times10^{-4}$ | 126.5 | 0.9999 |
| 75 | $2.4 \times 10^{-2}$ | 88.41 | 0.9380 | $10.48\times10^{-4}$ | 188.6 | 0.9999 |
| 100 | $1.5 \times 10^{-2}$ | 130.49 | 0.9731 | $4.12\times10^{-4}$ | 256.4 | 0.9995 |
| | Weber-Morris model (Intraparticle diffusion model) | | | | | |
| | Initial phase | | | Secondary phase | | |
| $C_0$(mg/L) | $K_{ip1}$ | $C_1$ | $R^2_1$ | $K_{ip2}$ | $C_2$ | $R^2_2$ |
| 25 | 8.94 | 30.86 | 0.9764 | 0.185 | 59.79 | 0.9754 |
| 50 | 18.96 | 26.59 | 0.9687 | 4.63 | 81.09 | 0.9808 |
| 75 | 32.64 | 11.07 | 0.9702 | 6.58 | 119.96 | 0.9854 |
| 100 | 32.86 | 22.11 | 0.9716 | 9.6 | 132.52 | 0.9943 |

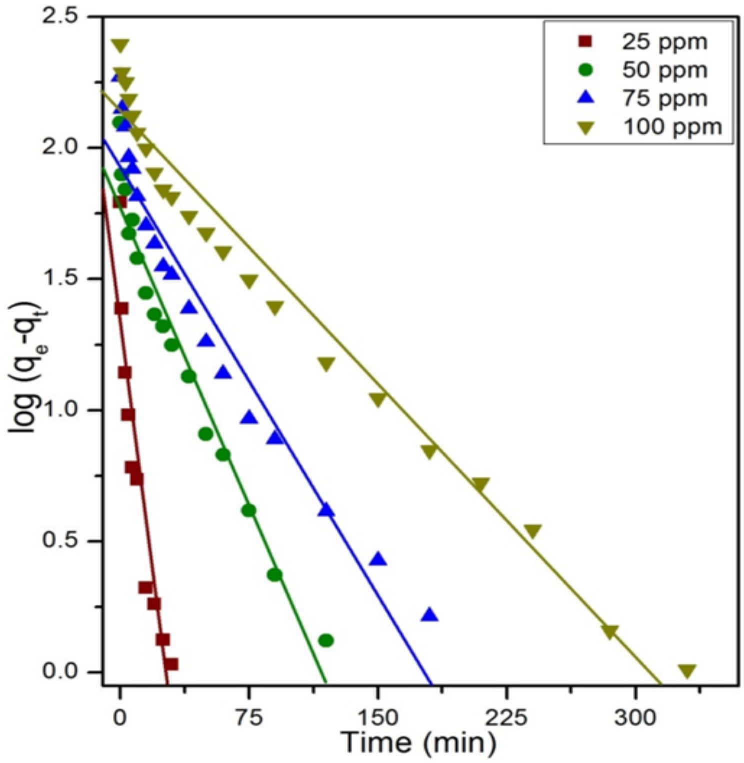

**Figure 3-22: Effect of contact time on adsorption capacity: the pseudo-first order model.**

### 3.3.4.5 Adsorption isotherms

The adsorption equilibrium isotherm represents the mathematical relation of the amount of adsorbed target per gram of adsorbent to the equilibrium solution concentration at fixed temperature. Fig. 3.23a shows the equilibrium isotherms for the adsorption of silver ions. The equilibrium adsorption data have been fitted into two well-known adsorption isotherm equations, Langmuir and Freundlich to discuss the equilibrium characteristics of the adsorption process. The linear form of the Langmuir [63] and Freundlich [64] isotherms is depicted by eq. 9 and eq. 10, respectively.

$$\frac{C_e}{q_e} = \frac{1}{bq_m} + \frac{C_e}{q_m} \tag{9}$$

$$\ln q_e = \ln k_F + \frac{1}{n} \ln C_e \tag{10}$$

where $q_e$ (mg/g) is the equilibrium adsorption capacity of the $Ag^+$ adsorbed onto the PPy/MAA, $C_e$ is the concentration of adsorbate at equilibrium (mg/L) and $q_m$ and b are Langmuir constants related to maximum adsorption capacity and binding energy of adsorption, respectively. $k_F$ (mg/g) and 1/n are the characteristic Freundlich constants which signify the adsorption capacity and adsorption intensity, respectively. The isotherms of the above two models are displayed in Fig. 3.23b & Fig. 3.24.

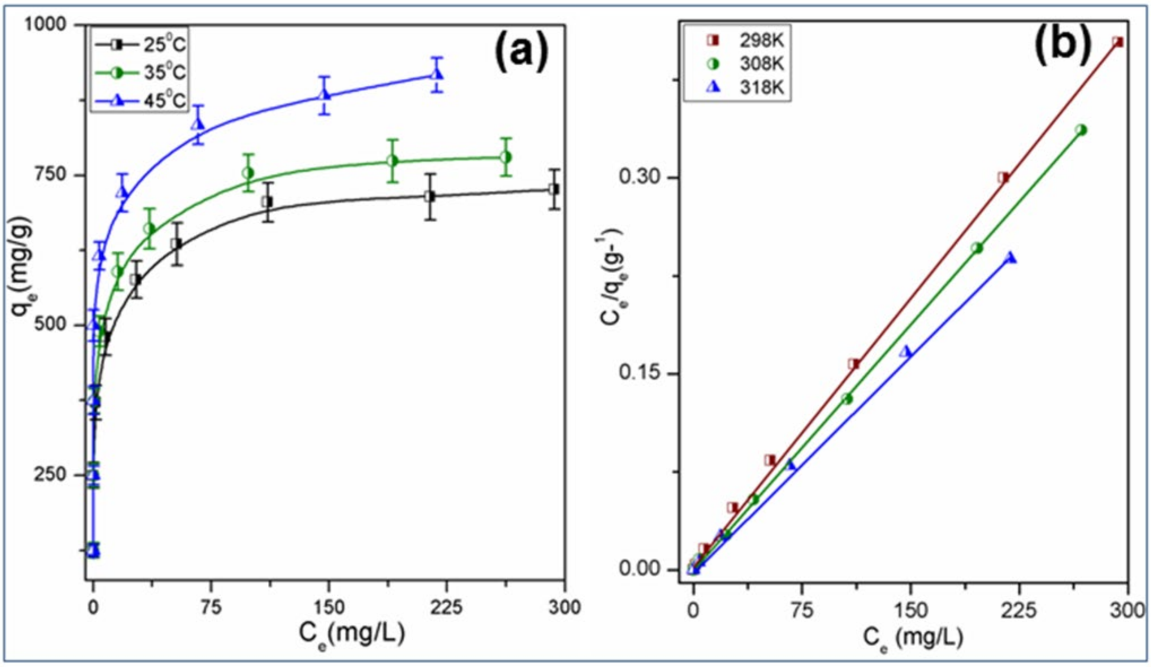

**Figure 3-23: (a) Adsorption isotherm of $Ag^+$ ions onto the PPy/MAA composite, (b) Langmuir adsorption isotherm plots.**

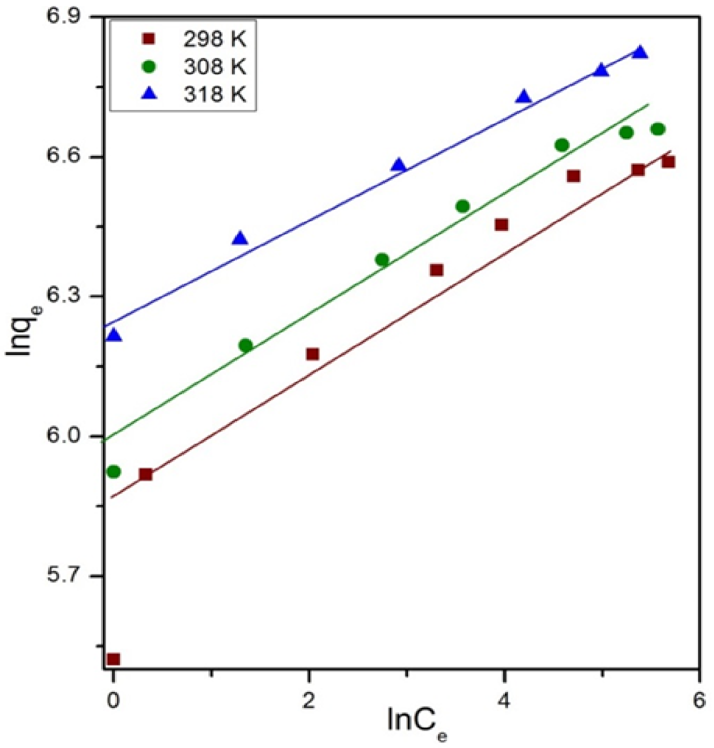

**Figure 3-24: Freundlich adsorption isotherm model of Ag(I) adsorption onto PPy/MAA.**

The related equilibrium parameters were determined from the corresponding linear fitting, and the results are listed in Table 3.7. It is evident that the adsorption isotherms become higher in consecutive order of 298, 308 and 318 K. From the experimental results, it can be seen that the higher temperature favours the adsorption process and the process is an endothermic in nature.

**Table 3-6: Langmuir and Freundlich Constants for Adsorption of Silver Ions.**

| Temp. | Langmuir model | | | | Freundlich model | | |
|---|---|---|---|---|---|---|---|
| (K) | $q_m$ (mg/g) | b (L/mg) | $R_L$ | $R^2$ | $k_F$ (mg/g ) | n | $R^2$ |
| 298 | 714.28 | 0.311 | 0.06 | 0.9993 | 311.99 | 6.05 | 0.9073 |
| 308 | 769.23 | 0.345 | 0.05 | 0.9998 | 397.30 | 7.60 | 0.9724 |
| 318 | 909.09 | 0.579 | 0.03 | 0.9988 | 517.13 | 9.11 | 0.9788 |

The Langmuir isotherm model was established on the basis of the assumptions that the adsorption occurs onto the structurally homogeneous surface of adsorbent with identical binding sites by monolayer adsorption without interaction between adsorbed molecules [89, 90]. As shown in Fig 3.23b, the experimental data is fitted well with the Langmuir isotherm model and the value of $q_m$ changes from 714.28 to 909.09 (mg/g) with an increase of the temperature from 298 K to 318 K. The correlation coefficient values ($R^2 = 0.999$) show good fitting of the Langmuir isotherm to the experimental data at three different temperatures. Furthermore, the Langmuir constant ‘b’ is used to calculate the feasibility of the adsorption process by mean of the dimensionless constant, called separation factor ($R_L$). The mathematical expression of '$R_L$' is repressed by the following equation (eq. 11) [91].

$$R_L = \frac{1}{1+bC_0} \tag{11}$$

where $C_0$ (mg/L) is the initial concentration of $Ag^+$ ions. Depending upon the value of separation factor ($R_L$), there are four possibilities of the adsorption process. The values of separation factor ($R_L$) within the range $0 < R_L < 1$ indicate favourable process, for unfavourable $R_L > 1$, for linear $R_L = 1$, and irreversible adsorption process $R_L = 0$. As shown in Table 3.7, the $R_L$ values were 0.06 to 0.03 for three different temperatures, which indicates that the silver adsorption on the PPy/MAA composite was favourable process.

The Freundlich model is based on the assumption of adsorption at multilayer and on energetically heterogeneous surfaces [64]. The $k_F$ (mg/g) and 'n' are the characteristic Freundlich constants which signify the adsorption efficiency and favourability of the adsorbent and adsorbate system. The values of $k_F$ and n obtained from the slope and intercept of the linear plots of the experimental data $\ln q_e$ versus $\ln C_e$ at different temperatures (Fig. 3.24) are also listed in Table 3.7. The values of 'n' were in the range of 1 to 10 (6.05 to 9.11), which provided evidence of a favourable adsorption process. According to the obtained results, the adsorption data of the metal ion on the PPy/MAA composite were fitted well with the Langmuir model compared to Freundlich model, as designated by the very high values of the correlation coefficient ($R^2$). In addition, the adsorption capacity of the Langmuir model ($q_m = 714.28$ mg/g at 25°C) were higher than that of the result obtained from the Freundlich model ($k_F = 311.9$ mg/g). So, the Langmuir model is more appropriate and a good fit for silver ions adsorption onto the PPy/MAA composite. The theoretical saturated capacity ($q_m$) obtained from the Langmuir isotherm model (714.28 mg/g at 25°C) was very much closer with the experimental saturated capacity.

### *3.3.4.6 Adsorption thermodynamics*

In order to investigate the spontaneity of the adsorption of silver ion and the effect of temperature, adsorption experiments were performed at 298, 308 and 318 K using 200 mg/L silver ions solution. As evident from the above isotherm results (Fig. 3.23a &Table 3.7), the adsorption process is endothermic since the increase in temperature leads to an increase in the adsorption capacities. Thermodynamic parameters can be evaluated using some well-known equations. The thermodynamic parameters for $Ag^+$ adsorption onto PPy/MAA composite are listed in Table 3.8, including the changes in Gibbs free energy ($\Delta G$, kJ/mol), enthalpy ($\Delta H$, kJ/mol), and entropy ($\Delta S$, kJ.mol$^{-1}$/K). All the $\Delta G$ values in Table 3.8 were negative which indicates that the adsorption process is thermodynamically feasible and spontaneous. Moreover, the $\Delta G$ values decreased with an increase in temperature, indicating an increased trend in the degree of spontaneity and feasibility of adsorption of $Ag^+$ onto PPy/MMA composite. The positive value of $\Delta H$ (Table 3.8) confirmed that the adsorption process is endothermic in nature. Furthermore, the positive value of $\Delta S$ reveals that the increase of disorderness and randomness at the solid solution interface during the fixation of silver ion on adsorbent surface.

**Table 3-7: Thermodynamic Parameters for the Adsorption of Silver Ions.**

| Temperature (K) | $\Delta G^0$ (kJ/mol) | $\Delta H^0$ (kJ/mol) | $\Delta S^0$ (kJ. mol$^{-1}$/K) | $R^2$ |
|---|---|---|---|---|
| 298 | -6.15 | 44.52 | 0.17 | 0.9990 |
| 308 | -7.99 | | | |
| 318 | -9.68 | | | |

### *3.3.4.7 Adsorption mechanism*

According to evidence from XRD, HR-TEM, FE-SEM, EDS and FTIR, the strong adsorption of $Ag^+$ by PPy/MAA composite can be explained by two different kinds of adsorption mechanisms: physical surface adsorption and redox adsorption [92]. In physical adsorption, porous adsorbent surface traditionally adsorbed the heavy metal ion through weak Van der Waals forces between adsorbents and adsorbates molecules [93]. On the other hand, the redox adsorption mainly occurs when adsorbents contain functional groups such as $-NH_2$, -SH, $-SO_3H$, -OH and -COOH. Heavy metal ions ($Ag^+$) with high standard reduction potential have a strong chelating ability with the above functional groups, which can be responsible for the reduction of initial adsorbed silver ions to the metallic silver nanoparticles during the sorption process [94, 95] ( Scheme 3.3).

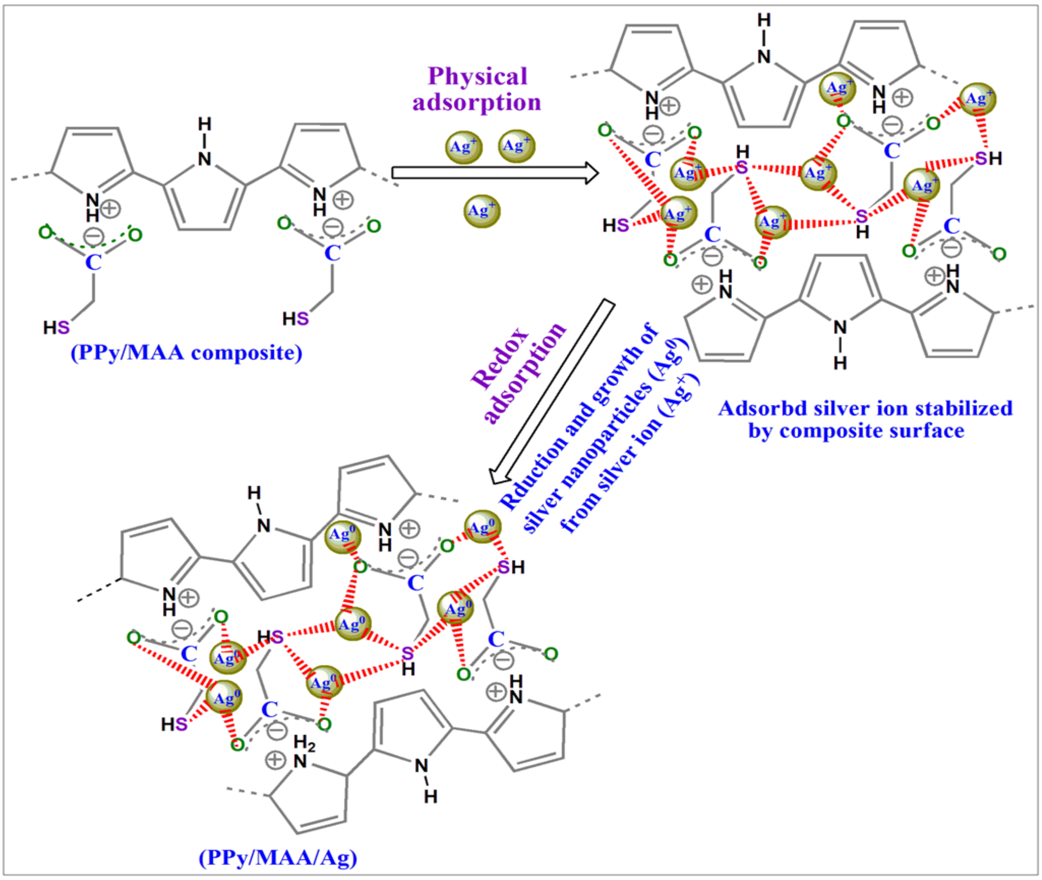

**Scheme 3-3: Schematic representation of possible adsorption mechanism of Silver Ions onto the Ppy/MAA composite.**

The redox adsorption mechanism and the form of adsorbed silver on the PPy/MAA surface could be verified by XRD analysis (Fig. 3.18). The XRD spectrum (Fig. 3.18b) exhibited five additional stronger peaks in compare to pure PPy/MAA composite for metallic $Ag^0$ crystals, supporting the likely reduction of adsorbed $Ag^+$ in the adsorbent surface by redox adsorption mechanism. The HR-TEM image (Fig. 3.16b & c) revealed the existence of a large amount of Ag nanoparticles on the surface of adsorbent. The presence of silver particles the adsorbent surface were also confirmed by FE-SEM (Fig. 3.16b) image and EDS (Fig. 3.16f). The occurrence of redox sorption can be further confirmed by FTIR spectra of PPy/MAA before and after adsorption of silver ion ($Ag^+$) (Fig. 3.17). It was seen from Fig. 3.17 that the intensity of the vibration band of S-H group (2636 $cm^{-1}$) became weak and broad after adsorption of silver ion which suggests the chelating interaction between -SH group and adsorbate molecules.

In order to further explore the adsorption mechanism and investigation the interaction between adsorbate and adsorbent molecule, XPS analysis of PPy/MAA composite was carried out before and after adsorption of silver. The complete XPS survey scans over the range of 0-1350 eV of PPy/MAA composite before and after adsorption of silver ions are shown in Fig. 3.25a. In addition, the characteristic peaks of C1s (Fig. 3.25c), S2p (Fig. 3.25d) and O1s (Fig. 3.25e) are detected at 284, 163, and 531 eV, respectively in PPy/MAA composite before and after adsorption of silver ions. The presence of photoemission signals of $Ag3d^{3/2}$ and $Ag3d^{5/2}$ in the full scans survey indicate significant amount of Ag has been adsorbed into the PPy/MAA composite surface. The spectrum of Ag 3d (Fig. 3.25b) displays that the two photoemission bands are located at 373.37 and 367.38 eV for Ag $3d^{3/2}$ and Ag $3d^{5/2}$, respectively. The XPS spectrum of C1s of PPy/MAA before adsorption of $Ag^+$ ions was deconvoluted into different signals and shown in Fig. 3.25c(i). The peak at 284.12 eV was attributed to C-C bond and the peak at 285.72 eV corresponded to C-N bond. The two photoemission peaks at 287.02 and 288.12 eV exhibited for C-S and C-O bond respectively. Fig. 3.25c(ii) clearly shows that there is no major change in intensity or binding energies of the C1s peaks after adsorption of $Ag^+$ ions.

The characteristic photoemission spectrum of S 2p shows a spin-orbital doublet (S $2p^{1/2}$ and S $2p^{3/2}$) [96, 97]. The peak deconvolution of S 2p in Fig. 3.25d(i) implies the two S chemical states: the first one at 162.45 eV for S $2p^{3/2}$ and the second one producing for S $2p^{1/2}$ at 163.4. It can be observed that the binding energy of the two chemical state of the S 2p increased from 162.45 to 162.65 and 163.40 to 163.76 eV (Fig. 3.25d(ii)) after adsorption of silver. This indicates that strong interaction between mercapto group (-SH) of the composite and uptake silver ions. Thus, the XPS analysis reveals that the adsorption mechanism (Scheme 3.3) of silver ions onto PPy/MAA composite surface is mainly through chelation of mercapto group (-SH) with $Ag^+$. Deconvolution of the O 1s shows (Fig. 3.25e(i)) peak at 531.89 eV attributed to the -COOH moiety of mercaptoacetic acid. The peak intensity decreases significantly after adsorption and binding energy values also shift towards lower energy (Fig. 3.25e(ii)) indicating the interaction between oxygen atom of acid group and silver ions. From the zeta potential analysis Fig. 3.26, it can be seen that the PPy/MAA composite carries negative charge at a wide range of pH. Since the composite contains acid group with increasing pH deprotonation takes place which results increasingly negative zeta values. Negative zeta values also suggest a strong ability of the adsorbent material for the chelation with positive metal ions.

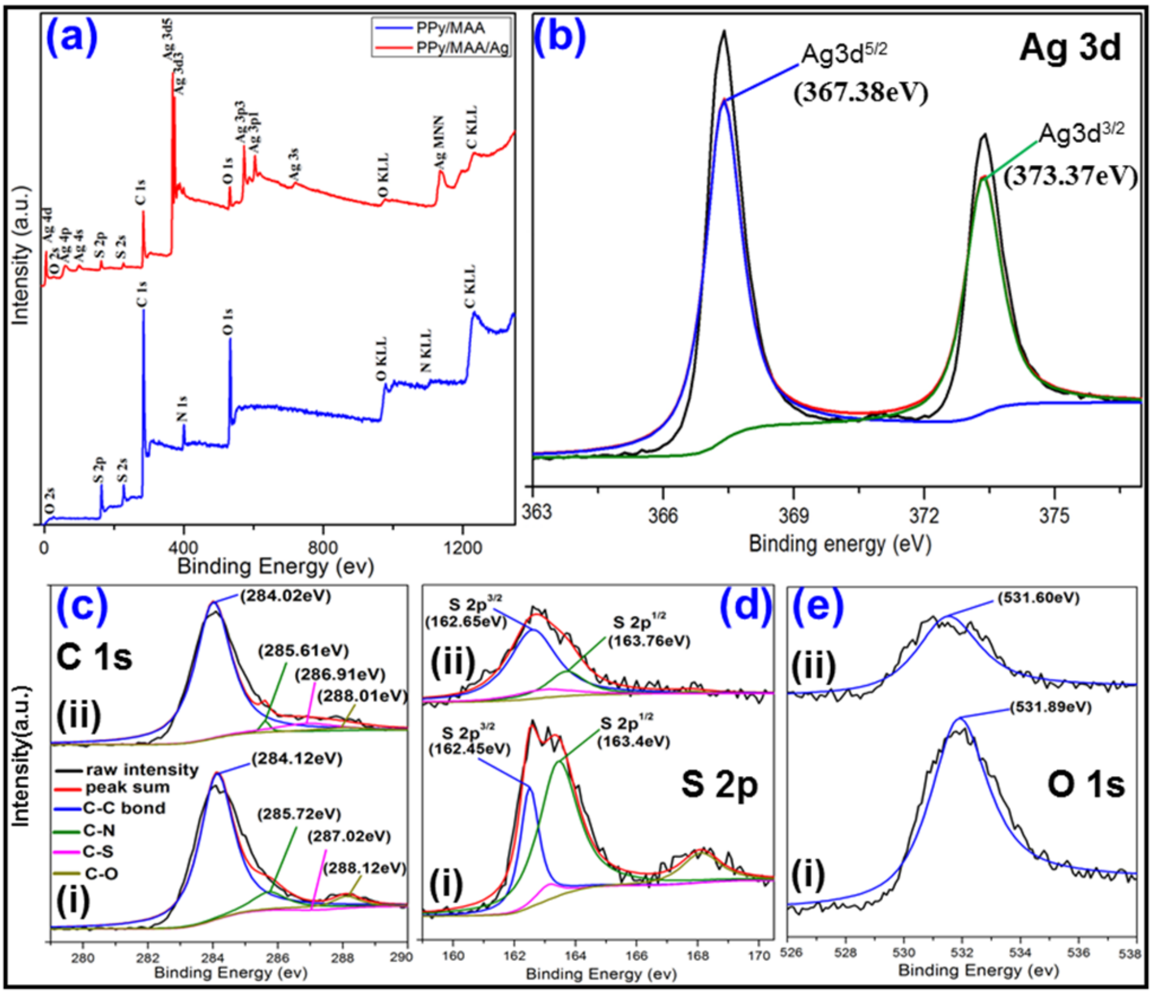

**Figure 3-25: (a) Full scans XPS spectra of PPy/MAA before and after adsorption of silver ions; high resolution (b) Ag 3d (c) C 1s (d) S 2p and (e) O 1s spectra of PPy/MAA before and after Ag adsorption**

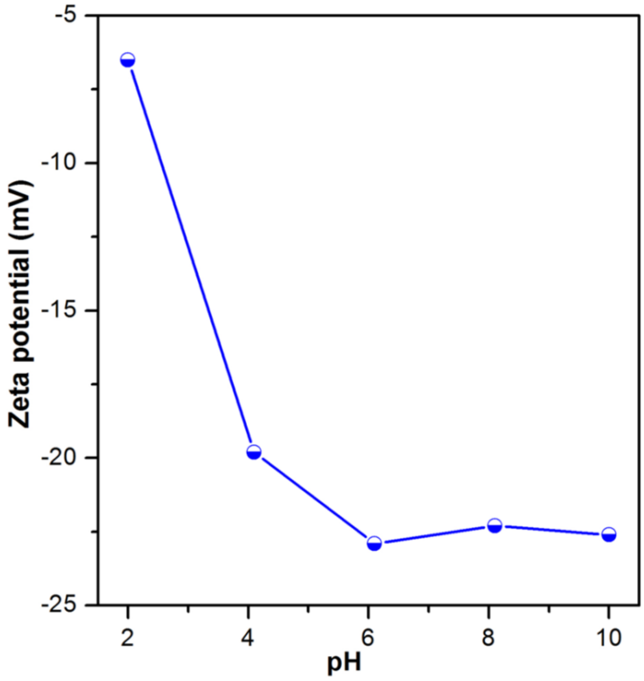

**Figure 3-26: Effect of pH on zeta potential of PPy/MAA composite**

### 3.3.5 Applications of post adsorbed secondary waste Hg(II)- and Ag-loaded PPy/MAA

#### *3.3.5.1 Hg(II)-loaded PPy/MAA as catalyst for the transformation of phenylacetylene*

This aspect of the study explored the potential of using Hg(II)-adsorbed composite (PPy-MAA/Hg(II)) in organic synthesis as a catalytic alternative, specifically for the transformation of phenyl acetylene to acetophenone (Scheme 3.4). Re-using PPy-MAA/Hg(II) would thus reduce the amount of waste generated from the remediation process [98].

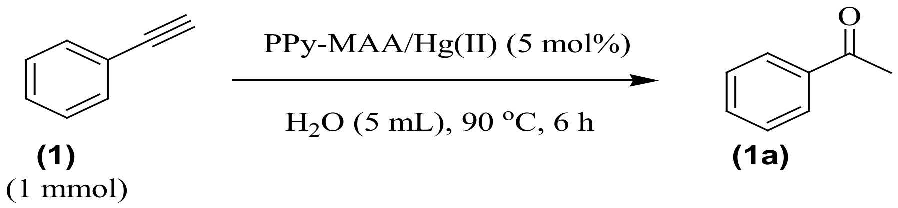

**Scheme 3-4: Catalytic transformation of phenylacetylene to acetophenone**

**Table 3-8: Optimization of the reaction conditions with PPy-MAA/Hg(II)[a]**

| Entry | Catalyst | 6 (N) HCl (mL) | Yield (%)[b] |
|---|---|---|---|
| 1 | PPy-MAA/Hg(II)-5[c] | - | 55 |
| 2 | PPy-MAA/Hg(II)-4[c] | - | 54 |
| 3 | PPy-MAA/Hg(II)-3[c] | - | 51 |
| 4 | PPy-MAA/Hg(II)-2[c] | - | 48 |
| 5 | PPy-MAA/Hg(II)-1[c] | - | 44 |
| 6 | PPy-MAA/Hg(II)-5[c] | 1 | 65 |
| 7 | No catalyst | 1 | - |
| 8 | PPy-MAA (50 mg) | 1 | - |

[a]Reaction conditions: **1** (1 mmol), catalyst (5 mol%), $H_2O$ (5 mL), 90°C, 6 h. [b]Isolated yields of **1a**. [c]PPy-MAA/Hg(II) composites-1, -2, -3, -4 and -5 with 10.87%, 19.71%, 33.2%, 49.21%, and 49.21 wt% Hg, respectively

Treatment of **1** (Scheme 3.4) in the presence of 5 mol% PPy-MAA/Hg(II)-5 yielded 55% acetophenone (**1a**) in $H_2O$ as solvent at 90°C for 6 h. Furthermore, we have checked the catalytic activity of various Hg-loaded materials [PPy-MAA/Hg(II)-1, -2, -3, -4 and -5 with 10.87, 19.71, 33.2, 42.34 and 49.21 wt% of Hg respectively] under similar conditions, affording the desired product in 44, 48, 51, 54 and 55% yields, respectively. Screening of the catalysts indicated that PPy-MAA/Hg(II)-5 catalyst was proved to be the best choice among others to give the desired product in 55% yield. The reaction mixture was charged with 1 mL 6 (N) HCl to improve the conversion of the desired product under identical reaction conditions with a variety of catalysts (PPy-MAA/Hg(II)-1, -2, -3, -4 and -5). Satisfyingly, PPy-MAA/Hg(II)-5 catalyst was found to be efficient to furnish the product **1a** in 65% yield (Table 3.9, entry 6). However, leaching test of the liquid phase that was done after the reaction using ICP-OES revealed 0.02, 0.03, 1.58, 5.16 and 5.19 ppm of mercury had drifted to the solution from PPy-MAA/Hg(II)-1, -2, -3, -4 and -5 catalyst, respectively. These results confirmed that leaching of mercury in water media enhances its catalytic activity; the aqueous part of the reaction was not discarded without further processing). However, no desired product was obtained in absence of PPy-MAA/Hg(II) catalyst (Table 3.9, entry 7). In addition, the reaction was performed with PPy/MAA (50 mg) composite and no trace of product was found (Table 3.9, entry 8). These experiments confirmed a definite role of Hg (II) for this transformation. However, optimization, substrates scopes and general applicability of this method are needed to be explored further. The product (**1a**) was confirmed by $^{1}H$ and $^{13}C$ NMR spectroscopy.

### *3.3.5.2 Reusability of the catalyst*

To check the reusability of the catalyst, the catalyst was subjected to five consecutive runs under the similar conditions previously described (Table 10). The catalyst (PPy-MAA/Hg(II)-3) was separated from the reaction mixture through simple filtration technique using 0.45 µm cellulose filter paper. After washing sequentially with deionized water (20 mL) and acetone (25 mL), the residue was dried under vacuum for 30 min at RT. The recovered material thus obtained was employed for the next catalytic experiments, affording the desired product in 41-57% yields in five consecutive runs, as summarized in Table 3.10. Additionally, a leaching test of the liquid phase of the reaction mixture was performed by ICP-OES analysis as given in Table 3.10. These results indicated that PPy-MAA/Hg(II)-3 was relatively unstable under these reaction conditions. Modest deactivation of the catalyst was observed over catalytic cycles due to the leaching of mercury ions into the reaction medium.

**Table 3-9: Reusability of PPy-MAA/Hg(II)-3 catalyst**[a]

| Entry | Leaching (ppm) | Yield (%)[b] |
|---|---|---|
| 1st run | 1.27 | 57 |
| 2nd run | 0.7 | 55 |
| 3rd run | 0.45 | 50 |
| 4th run | 0.39 | 48 |
| 5th run | 0.35 | 41 |

[a]Reaction conditions: **1** (1 mmol), PPy-MAA-Hg(II)-3 (5 mol%), 6 (N) HCl (1 mL), $H_2O$ (5 mL), 90°C, 6 h. [b]Isolated yields of **1a**

### 3.3.6 Silver adsorbed waste material Applications

#### *3.3.6.1 Ag(I)-loaded PPy/MAA as catalyst for the reduction of 4-nitrophenol*

4-Aminophenol (AP) has shown potential application in pharmaceuticals, whereas 4-nitrophenol (4-NP) is one of the most common and toxic pollutant dyes found in industrial wastewater. In past years, the catalytic reduction of 4-NP has been extensively studied using metal nanoparticles with an excess amount of $NaBH_4$ in aqueous solution [99, 97]. Herein, we demonstrated the reduction of 4-NP in the presence of PPy/MAA/Ag waste material as catalyst and evaluated the efficiency. Initially, the reaction was performed by reducing 4-NP with a 10-fold excess of $NaBH_4$ and monitored by UV-visible spectrophotometry as depicted in Fig. 3.27.

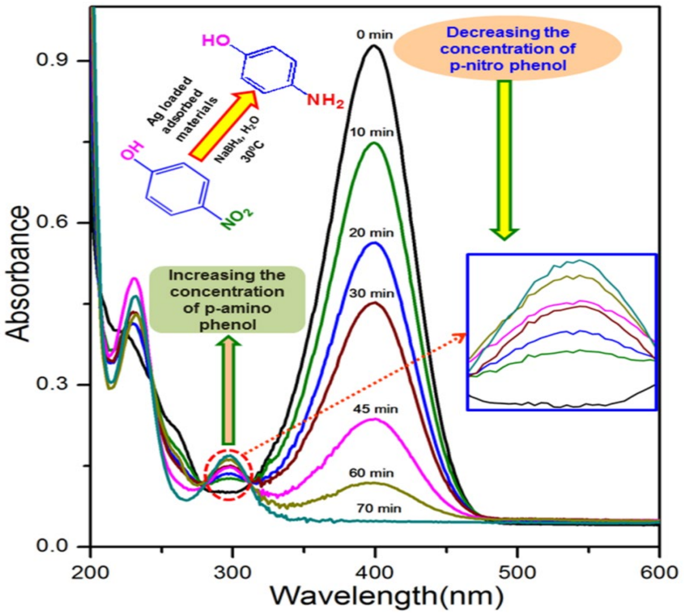

**Figure 3-27: Typical time-resolved UV-vis spectra of the catalytic reduction of 4-nitro phenol (4-NP) in presence of Ag-loaded adsorbent in aqueous medium.**

After addition of $NaBH_4$, the colour of the 4-NP solution immediately changed from light-yellow to bright-yellow and the $\lambda_{max}$ showed an absorbance peak at 400 nm due to the formation of 4-nitrophenolate ion. However, incorporation of PPy/MAA/Ag to the stirred reaction mixture led a reduced intensity of this peak, as shown in Fig. 3.27. In contrast, the peak absorption intensity did not change markedly in the absence of PPy/MAA/Ag, even after 24 h. This suggests that the PPy/MAA/Ag catalyst displayed a definite catalytic role for the reduction of 4-NP under reaction conditions. Furthermore, the full conversion of product was obtained after 70 min, as confirmed by the UV-visible spectrum (Fig. 3.27). The colour of the reaction mixture transformed from bright yellow to a completely faded colour and a slow increase of the peak of 4-aminophenol (4-AP) at 300 nm was observed. In addition, aliquots of the reaction mixture were monitored by Gas chromatography (GC) and the full conversion of product was obtained after 70 min Fig. 3.28. The product was further confirmed by $^1$H NMR spectroscopic study.

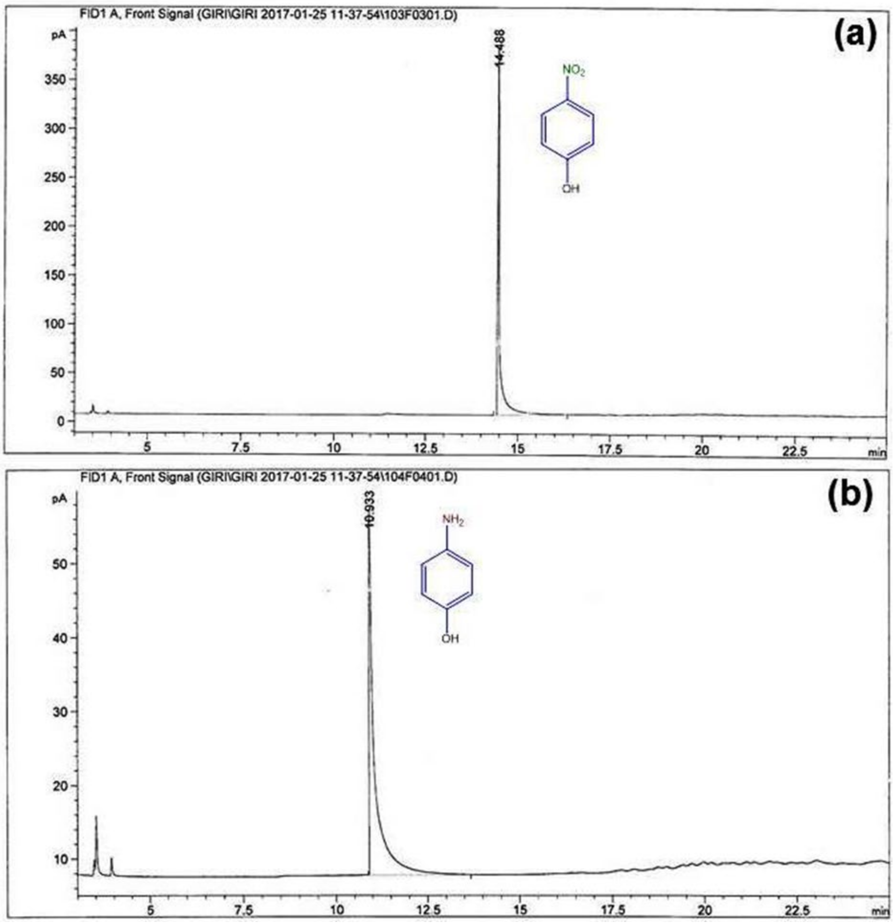

**Figure 3-28: GC analyses of (a) 4-NP and (b) reaction mixture after 70 min.**

The mechanism for the catalytic reduction of 4-NP is predicted to follow according to the reported literatures [100, 101] as shown in Scheme 3.5. Initially, the hydrogen ($H_2$) gas is liberated upon addition of $NaBH_4$ into the aqueous suspension of 4-NP in the presence of Ag NPs. Then, adsorption of hydrogen on the surface of the silver nanoparticles generates the silver hydride complex. Due to the presence of electron-rich conductive PPy-MAA matrix, electron-deficient 4-nitrophenolate ions attach to the catalyst surface of AgNPs. Thus, the intermediates are in close proximity to the hydride species, which reduces the nitro group of 4-nitrophenolate ion to nitroso species, followed by further stepwise reduction to hydroxylamine intermediates and lastly 4-amino derivative. Finally, the catalyst surface is regenerated through desorption of 4-AP and it can be reused for the next catalytic cycle.

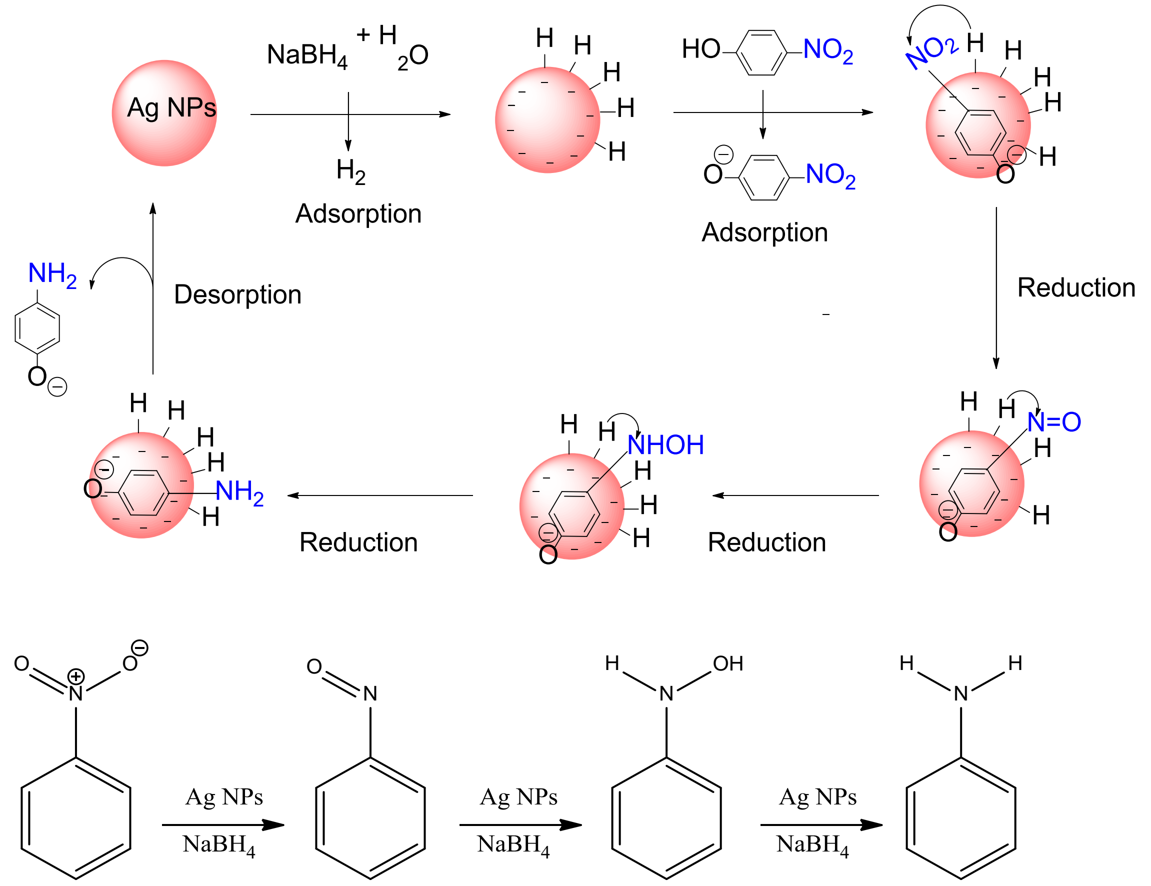

**Scheme 3-5: Plausible mechanism for the reduction of 4-NP using waste-based Ag NPs**

### *3.3.6.2 Antimicrobial activity of silver adsorbed waste material*

The antimicrobial activity of various silver adsorbed PPy/MAA composite was investigated using *E. coli* (Gram-negative) bacteria following 60 min incubation time. The killing kinetics of assays was determined by the amount of viable cells remaining after treatment with the PPy/MAA/Ag composite. Antimicrobial assay results of each of the four samples (neat PPy/MAA and 11, 32 and 42% of Ag loaded in PPy/ MAA) are shown in Fig 3.29. The bacterial inhibition growth curve suggests that the bacterial growth was delayed with increasing the concentration of silver into the PPy/MAA composite.

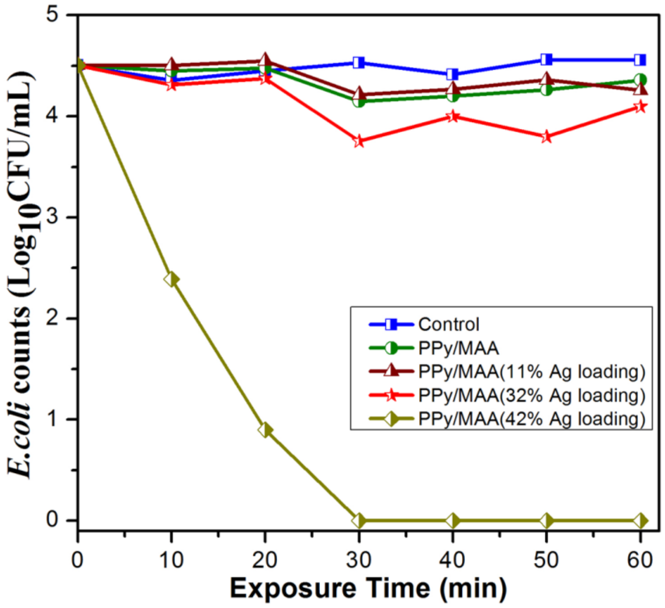

**Figure 3-29: Killing kinetics of PPy/MAA and Ag-loaded PPy/MAA against *Escherichia coli* bacteria.**

The growth of *E. coli* was completely inhibited by the PPy/MAA/Ag composite after 30 min exposure time at Ag of 42%. Although the sample containing 32% Ag showed some effect, this was very minimal as up to $10^4$ CFU/mL could still be counted on the agar plates after 60 min exposure. Neat PPy/MAA composite and 11% loading did not show any effect on *E. coli* bacteria. These antimicrobial assay results confirmed that the higher concentrations tested of Ag loaded-PPy/MAA composite possessed enhanced antimicrobial activity compared to pure PPy/MAA.

### *3.3.6.3 $NO_2$ gas sensing behaviour of the PPy/MAA/Ag*

In order to investigate the effect of Ag adsorbed PPy/MAA composite upon $NO_2$ gas detection, a systematic gas sensing experiment was carried out with different concentrations (20-100 ppm) of $NO_2$ gas at room temperature. Fig. 3.30 shows that the incorporation of Ag in the PPy/MAA composite enhances the response of the device. An increase in the current upon exposure to oxidising gas reveals a typical *p*-type semiconducting behaviour of the materials. The baseline current of the polymer was found to decrease after absorption of Ag, due to the recombination of holes the majority charge carrier from PPy/MAA composite and the free electron from the Ag particles. The response ($R_{res}$) was calculated as $R_{res} = I_g/I_a$, where $I_g$ and $I_a$ are current in presence and absence of $NO_2$, respectively. Fig. 31b shows the responses obtained with and without Ag the incorporation of the PPy/MAA composite. The increase in Ag percentage from 0 to 11 and 32 in the composite (PPy/MAA) enhances the sensor response from 1.4, 4.2 to 7.2, respectively. Hence, the Ag particles enhance the activity of PPy/MAA by increasing the number of sites available for the $NO_2$ adsorption and subsequent dissociation. In general, the surface defective site adsorbs the oxygen from the atmosphere. The physisorbed oxygen is further ionized to $O_2^-$ at room temperature by obtaining an electron from the valance band and hence increases the hole concentration in the conduction band. However, $NO_2$ has no or negligible affinity for ionized oxygen, so it interacts directly with the polymer. The physisorbed $NO_2$ takes the electron from the valance band, or shares it with ionized oxygen as follows [102]:

$$NO_2(gas) + e^- \leftrightharpoons NO_2^-(Surf.adsorbed) \tag{12}$$

The chemisorbed $NO_2^-$ releases the NO in the atmosphere by leaving behind an adsorbed $O^-$ on the surface, hence increasing the hole concentration for conduction to occur. Accordingly, the presence of Ag increases the surface area available for the physisorption of $NO_2$, particularly in the presence of pre-adsorbed oxygen ions, facilitating the reduction of $NO_2$ to NO gas at the interface between the Ag and polymer, and leading to the high response observed.

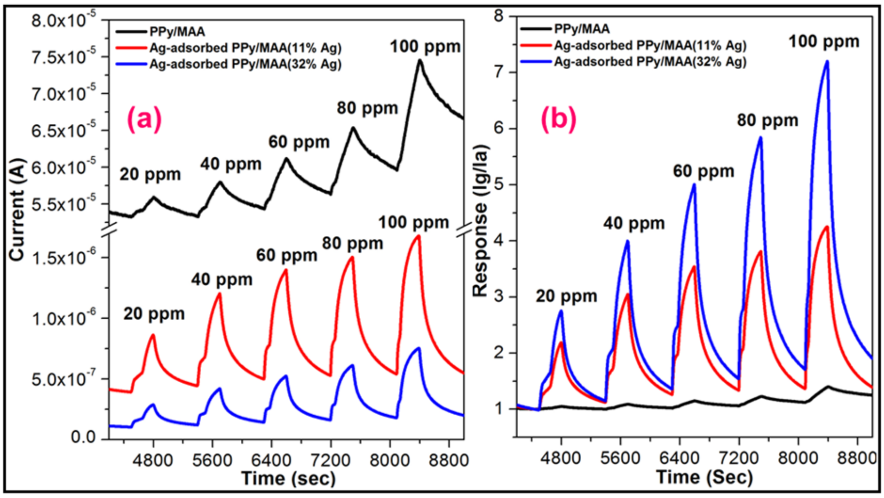

**Figure 3-30: (a) Current variation (b) dynamic sensing performance of pure adsorbent (PPy/MAA) and different percentage of silver loaded adsorbent towards $NO_2$ gas at concentrations ranging from 20 to 100 ppm under the operation temperature of 120°C.**

## 3.4 SUMMARY

In this chapter, PPy composite containing thiol functionalized chelating group, was developed and tested for the remediation of toxic metal ion Hg(II) and Ag(I). Results revealed that the mercaptoacetic acid containing thiol functionality played important role for the removal of mercury due to strong binding ability between soft acid mercury with soft base thiol. Adsorption data obeyed a pseudo-second-order rate equation, and a maximum adsorption capacity of PPy/MAA was calculated 1736.8 mg/g at 25°C using the Langmuir adsorption isotherm. In addition, post-adsorbed waste material containing considerable amount of mercury played a vital catalytic role for organic transformation reaction. The catalytic performance of waste-derived mercury material for the transformation of phenylacetylene to acetophenone as an alternative route was encouraging, although further studies are required. With regard to silver ions uptake, the equilibrium adsorption capacity of on PPy/MAA reached up to 714.28 mg/g at 25°C in the solution at 5.4 pH. The experimental adsorption results correlated well with pseudo-second-order kinetics model, and the adsorption equilibrium followed the Langmuir isotherm model when compared to the Freundlich isotherm model. Negative Δ*G* and positive Δ*H* values for adsorption thermodynamic analysis revealed that the adsorption of $Ag^+$ on the PPy/MAA composite is a spontaneous and endothermic process. Furthermore, the PPy/MAA composite not only effectively adsorbed $Ag^+$ from aqueous solutions but also converted the adsorbed $Ag^+$ to metallic silver nanoparticles ($Ag^0$) by chemical reduction. The newly formed nanoparticles might be stabilized by the chelation with electron reach functionality (-SH, $-COO^-$) of the composite matrix. The post-adsorption material containing large amount of silver inhibited *Escherichia coli* (*E. coli*) bacterial growth, and thus the waste silver adsorbed material could be used as an antimicrobial agent in various applications. Moreover, Ag-containing waste material played a vital catalytic role for the reduction of 4-nitrophenol under standard reaction condition and the full conversion of product was obtained within 70 min of the reaction. This Ag adsorbed waste material also exhibited good sensitivity and response towards $NO_2$ gas detection. Thus the empirical results suggest that PPy/MAA composite can be used as a promising adsorbent for removal of toxic metal ions from contaminated water and their remarkable environmental applications can further be explored. The synthesized nanostructured materials, their characterizations, their metal ion adsorption properties as well as the reusability of their metal laden wastes in environmental applications have since been published (See List of publications).

## 3.5 REFERENCES

[1] M. R. Huang, S. Li, X. Li, G. Longan Shell as Novel Biomacromolecular Sorbent for Highly Selective Removal of Lead and Mercury Ions. *J. Phys. Chem. B* **2010**, *114*, 3534-3542.

[2] S. E. Bailey, T. J. Olin, R. M. Bricka, D. D. Adrian. A Review of Potentially Low-cost Sorbents for Heavy Metals. *Water Res.* **1999**, *33*, 2469-2479.

[3] C. J. Vörösmarty, P. B. McIntyre, M. O. Gessner, D. Dudgeon, A. Prusevich, P. Green, S. Glidden, S. E. Bunn, C. A. Sullivan, C. Reidy Liermann, Davies, P. M. Global threats to human water security and river biodiversity. *Nature* **2010**, *467*, 555-561.

[4] B. Wang, B. Luo, M. H. Liang, A. L. Wang, J. Wang, Y. Fang, Y. Chang, L Zhi. Chemical Amination of Graphene Oxides and Their Extraordinary Properties in the Detection of Lead Ions. Nanoscale **2011**, 3, 5059-5066.

[5] L. Liu, L. Ding, X. Wu, F. Deng, R. Kang, Luo, X. Enhancing the Hg(II) removal efficiency from real wastewater by novel Thymine-Grafted reduced graphene oxide complexes. Ind. Eng. Chem. Res. **2016**, 55, 6845-6853.

[6] F. Luo, J. L. Chen, L. D. Dang, W. N. Zhou, H. L. Lin, J. Q. Li, S. J. Liu, M. B. Luo. High-Performance $Hg^{2+}$ Removal from Ultra-low concentration aqueous solution using both acrylamide-and hydroxyl-functionalized metal-organic framework. J. Mater. Chem. A. **2015**, 3, 9616-9620.

[7] Q. Wang, D. Kim, D. D. Dionysiou, G. A. Sorial, D. Timberlake. Sources and remediation for mercury contamination in aquatic systems-a literature review. Environ. Pollut. **2004**, 131, 323-336.

[8] J. E. Jung, D. Geatches, K. Lee, S. Aboud, Jr. G. E. Brown, J. Wilcox. First-principles investigation of mercury adsorption on the α-$Fe_2O_3$(1102) surface. J. Phys. Chem. C. **2015**, 119, 26512-26518.

[9] G. Bayramoğlu, M. Y. Arica. Kinetics of mercury Ions removal from synthetic aqueous solutions using by novel magnetic p(GMA-MMA-EGDMA) Beads. *J. Hazard. Mater.* **2007**, *144*, 449-457.

[10] V. Chandra, K. S. Kim. Highly selective Adsorption of $Hg^{2+}$ by a polypyrrole-reduced graphene oxide composite. *Chem. Commun*. **2011**, *47*, 3942-3944.

[11] D. K. Ferry. Nanowires in Nanoelectronics. *Science* **2008**, *319*, 579-580. H. Alshehri, M. Jakubowska, A. Młożniak, M. Horaczek, D. Rudka, C. Free, Carey, J. D. Enhanced electrical conductivity of silver nanoparticles for high frequency electronic applications. *ACS Appl. Mater. Interfaces* **2012**, *4(12)*, 7007-7010.

[12] T. Lasanta, M. E. Olmos, A. Laguna, J. M. López-de-Luzuriaga, P. Naumov. Making the golden connection: reversible mechanochemical and vapochemical switching of luminescence from bimetallic gold-silver clusters associated through aurophilic interactions. *J. Am. Chem. Soc.* **2011**, *133*, 16358-16361.

[13] B. Baruah, G. J. Gabriel, M. J. Akbashev, M. E. Booher. Facile synthesis of silver nanoparticles stabilized by cationic polynorbornenes and their catalytic activity in 4-nitrophenol reduction. *Langmuir* **2013**, *29*, 4225-4234.

[14] H. Hu, J. H. Xin, H. Hu. PAM/graphene/Ag ternary hydrogel: synthesis, characterization and catalytic application. *J. Mater. Chem. A* **2014**, *2*, 11319-11333.

[15] J. Jain, S. Arora, J. M. Rajwade, P. Omray, S. Khandelwal, K. M. Paknikar. Silver nanoparticles in therapeutics: development of an antimicrobial gel formulation for topical use. *Mol. Pharmaceutics* **2009**, *6*, 1388-1401.

[16] K. A. Rieger, H. J. Cho, H. F. Yeung, W. Fan, J. D. Schiffman. Antimicrobial activity of silver ions released from zeolites immobilized on cellulose nanofiber mats. *ACS Appl. Mater. Interfaces* **2016**, *8*, 3032-3040.

[17] W. Bai, F. Nie, J. Zheng, Q. Sheng. Novel silver nanoparticle manganese oxyhydroxide graphen oxide nanocomposite prepared by modified silver mirror reaction and its application for electrochemical sensing. *ACS Appl. Mater. Interfaces* **2014**, *6*, 5439-5449.

[18] P. L. Drake, K. J. Hazelwood, Exposure-related health effects of silver and silver compounds: A review. Ann. Occup. Hyg. **2005**, *49*, 575-585.

[19] P. Wang, N. W. Menzies, P.G. Dennis, J. Guo, C. Forstner, R. Sekine, E. Lomb, P. Kappen, P. M. Bertsch, P. M. Kopittke. Silver nanoparticles entering soils via the wastewater-sludge-soil pathway pose low risk to plants but elevated Cl concentrations increase Ag bioavailability. *Environ. Sci. Technol.* **2016**, *50*, 8274-8281.

[20] P. Kumar, K. B. Ansari, A. C. Koli, V. G. Gaikar. Sorption behavior of thiourea-grafted polymeric resin toward silver ion, reduction to silver nanoparticles, and their antibacterial properties. *Ind. Eng. Chem. Res.* **2013**, *52*, 6438-6445.

[21] Z. W. He, Q. F. Lü, J. Y. Zhang. Facile preparation of hierarchical polyaniline-lignin composite with a reactive silver-ion adsorbability. *ACS Appl. Mater. Interfaces* **2012**, *4*, 369-374.

A. U. Skyllberg, A. Drott. Competition between disordered iron sulfide and natural organic matter associated thiols for mercury(II)-an EXAFS study. Environ. Sci. Technol. **2010**, 44, 1254-1259. Oehmen, D. Vergel, J. Fradinho, M. A. M. Reis, J. G. Crespo, S. Velizarov. Mercury removal from water streams through the ion exchange membrane bioreactor concept. J. Hazard. Mater. **2014**, 264, 65-70.

[22] S. A. Idris, S. R. Harvey, L. T. Gibson. Selective extraction of mercury(II) from water samples using Mercapto functionalised-MCM-41 and regeneration of the sorbent using microwave digestion. J. Hazard. Mater. **2011**, 193, 171-176.

[23] K. Chakrabarty, P. Saha, A. K. Ghoshal. Separation of mercury from its aqueous solution through supported liquid membrane using environmentally benign diluent. J. Membr. Sci. **2010**, 350, 395-401.

[24] Y. K. Henneberry, T. E. C. Kraus, J. A. Fleck, D. P. Krabbenhoft, P. M. Bachand, W. R. Horwath. Removal of inorganic mercury and methylmercury from surface waters following coagulation of Dissolved Organic Matter with Metal-Based Salts. Sci. Total Environ. **2011**, 409, 631-637.

[25] N. Li, R. Bai, C. Liu. Enhanced and selective adsorption of mercury ions on chitosan beads grafted with polyacrylamide via surface-initiated atom transfer radical polymerization. Langmuir **2005**, 21, 11780-11787.

[26] Y. L. Xu, Q. Zhong, X. Y. Liu. Elemental mercury oxidation and adsorption on magnesite powder modified by Mn at low temperature. J. Hazard. Mater. **2015**, 283, 252-259.

[27] P. Huttenloch, K. E. Roehl, K. Czurda. Use of copper shavings to remove mercury from contaminated groundwater of wastewater by amalgamation. Environ. Sci. Technol. **2003**, 37, 4269-4273.

[28] R. Stolle, H. Koeser, H. Gutberlet. Oxidation and reduction of mercury by SCR De $NO_x$ catalysts under flue gas conditions in coal fired power plants. Appl. Catal. B. **2014**, 144, 486-497.

   A. M. Berkovic, S. G. Bertolotti, L. S. Villata, M. C. Gonzalez,; R. Pis Diez, D. O. Mártire. Photoinduced reduction of divalent mercury by quinones in the presence of formic acid under anaerobic conditions. Chemosphere **2012**, 89, 1189-1194.

   B. Yan, B. Li, F. Kunecke, Z. Gu, L. Guo. Polypyrrole-based implantable electroactive pump for controlled drug microinjection. ACS Appl. Mater. Interfaces **2015**, 7, 14563-14568.

[29] H. Wang, X. Yuan, Y. Wu, X. Chen, L. Leng, H. Wang, H. Li, G. Zeng. Facile synthesis of polypyrrole decorated reduced graphene oxide-$Fe_3O_4$ magnetic composites and its application for the Cr(VI) removal. J. Chem. Eng. **2015**, 262, 597-606.

[30] K. T. Vadiraj, S. L. Belagali, Characterization of polyaniline for optical and electrical properties. IOSR J. Appl. Chem. Ver. II. **2015**, 8, 53-56.

[31] H. N. M. E. Mahmud, A. K. O. Huq, R. B. Yahya. The removal of heavy metal ions from wastewater/aqueous solution using polypyrrole-based adsorbents: A Review. RSC Adv. **2016**, 6, 14778-14791.

[32] R. A. Sheldon. Fundamentals of green chemistry: efficiency in reaction design. Chem. Soc. Rev. **2012**, 41, 1437-1451.

[33] S. L. Y. Tang, R. L. Smith, M. Poliakoff. Principles of green chemistry: productively. Green Chem. **2005**, 7, 761-762.

[34] G. Centi, S. Perathoner. Catalysis and sustainable (green) chemistry. Catal. Today **2003**, 77, 287-297.

[35] C. Kästner, A. F. Thünemann. Catalytic reduction of 4-Nitrophenol using silver nanoparticles with adjustable activity. Langmuir **2016**, 32, 7383-7391.

[36] M. Kaloti, A. Kumar, N. K. Navani. Synthesis of glucose-mediated Ag-γ-$Fe_2O_3$ multifunctional nanocomposites in aqueous medium-a kinetic analysis of their catalytic activity for 4-Nitrophenol reduction. Green Chem. **2015**, 17, 4786-4799.

[37] X. Yuan, H. Wang, Y. Wu, G. Zeng, X. Chen, L. Leng, Z. Wu, H. Li. One-pot self-assembly and photoreduction synthesis of silver nanoparticle-decorated reduced graphene oxide/MIL-125(Ti) photocatalyst with improved visible light photocatalytic activity. Appl. Organometal. Chem. **2016**, 30, 289-296.

   A. Leyva-perez, A. Corma. Similarities and differences between the “Relativistic” triad gold, platinum, and mercury in catalysis. Angew. Chem. Int. Ed. **2012**, 51, 614-635.

   B. A. Ragachev, M. A. Yarmolenko, J. Xiaohong, R. Shen, A.P. Luchnikov. A. V. Rogachev. Molecular structure, optical, electrical and sensing properties of PANI-Based coatings with silver nanoparticles deposited from the active gas phase. Appl. Surf. Sci. **2015**, 351, 811-818.

[38] X. Li, Y. Gao, J. Gong, L. Zhang, L. Qu. Polyaniline/Ag composite nanotubes prepared through UV rays irradiation via fiber template approach and their $NH_3$ gas sensitivity. J. Phys. Chem. C **2009**, 113, 69-73.

[39] W. Shao, X. Liu, H. Min, G. Dong, Q. Feng, S. Zuo. Preparation, characterization, and antibacterial activity of silver nanoparticle-decorated graphene oxide nanocomposite. ACS Appl. Mater. Interfaces **2015**, 7(12), 6966-6973.

[40] K. Chauhan, R. Sharma, R. Dharela, G. S. Chauhan, R. K. Singhal. Chitosan-thiomer stabilized silver nano-composites for antimicrobial and antioxidant applications. RSC Adv. **2016**, 6, 75453-75464.

[41] M. Bhaumik, T. Y. Leswifi, A. Maity, V. V. Srinivasu, M. S. Onyango. Removal of fluoride from aqueous solution by Ploypyrrole/$Fe_3O_4$ magnetic nanocomposite. J. Hazard. Mater. **2011**, 186, 150-159.

[42] S. Machida, S. Miyata. Chemical synthesis of highly electrically conductive, polypyrrole. Synth. Met. **1989**, 31, 311-318.

[43] X. Zhang, J. Zhang, W. Song, Z. Liu. Controllable synthesis of conducting polypyrrole nanostructures. J. Phys. Chem. B **2006**, 110, 1158-1165.

[44] G. Cho, B. M. Fung, D. T. Glatzhofer, J. S. Lee, Y. G. Shul. Preparation and Characterization of polypyrrole-coated nanosized novel ceramics. Langmuir **2001**, 17, 456-461.

[45] F. He, W. Wang, J. W. Moon, J. Howe, E. M. Pierce, L. Liang. Rapid removal of Hg(II) from aqueous solutions using thiol-functionalized Zn-doped biomagnetite particles. ACS Appl. Mater. Interfaces **2012**, 4, 4373-4379.

[46] S. T. Song, N. Saman, K. Johari, H. Mat. Removal of Hg(II) from aqueous solution by adsorption using raw and chemically modified rice Straw as novel adsorbents. Ind. Eng. Chem. Res. **2013**, 52, 13092-13101.

[47] H. Du, Y. Xie, C. Xia, W. Wang, F. Tiana. Electrochemical capacitance of polypyrrole-titanium nitride and polypyrrole-titania nanotube hybrids. New J. Chem. **2014**, 38, 1284-1293.

[48] S. J. L. Billinge, E. J. McKimmy, M. Shatnawi, H. J. Kim, V. Petkov, D. Wermeille, T. J. Pinnavaia. Mercury Binding Sites in Thiol-Functionalized Mesostructured Silica. J. Am. Chem. Soc. **2005**, 127, 8492-8498.

[49] K. P. Lisha, S. M. Maliyekkal, T. Pradeep. Manganese dioxide nanowhiskers: A potential adsorbent for the removal of Hg(II) from water. Chem. Eng. J. **2010**, 160, 432-439.

[50] R. Das, S. Giri, A. L. K. Abia, B. Dhonge, A. Maity. Removal of noble metal ions (Ag+) by mercapto group-containing polypyrrole matrix and reusability of its waste material in environmental applications. ACS Sustainable Chem. Eng. **2017**, 5, 2711-2724.

[51] F. S. Zhang, J. O. Nriagu, H. Itoh. Mercury removal from water using activated carbons derived from organic sewage Sludge. Water Res. **2005**, 39, 389-395.

[52] M. Puanngam, F. Unob. Preparation and use of chemically modified MCM-41 and silica gel as selective adsorbents for Hg(II) Ions. J. Hazard. Mater. **2008**, 154, 578-567.

[53] F. Qin, H. Zhao, G. Li, H. Yang, J. Li, R. Wang, Y. Liu, J. Hu, H. Sun, R. Chen. Size-tunable fabrication of multifunctional $Bi_2O_3$ porous nanospheres for photocatalysis, bacteria inactivation and template-synthesis. Nanoscale **2014**, 6, 5402-5409.

[54] F. Qin, G. Li, R. Wang, J. Wu, H. Sun, R. Chen. Template-Free Fabrication of $Bi_2O_3$ and $(BiO)_2CO_3$ Nanotubes and Their Application in Water Treatment. Chem. Eur. J. **2012**, 18, 16491-16497.

[55] E. Liu, H. Zhao, H. Li, G. Li, Y. Liu. Chen, R. Hydrothermal synthesis of porous a-$Fe_2O_3$ nanostructures for highly efficient Cr(VI) removal. New J. Chem. **2014**, 38, 2911-2916.

[56] Langmuir. The Constitution and fundamental properties of solids and liquids. J. Am. Chem. Soc. **1916**, 38, 2221-2295.

[57] H.M.F. Freundlich. Uber Die Adsorption in Losungen. Z. Phys. Chem. **1906**, 57, 385-470.

[58] Z. Hanif, S. Lee, G. H. Qasim, I. Ardiningsih, J. A. Kim, J. Seon, S. Han, S. Hong, M. H. Yoon. Polypyrrole multilayer-laminated cellulose for large-scale repeatable mercury ion removal. J. Mater. Chem. A **2016**, 4, 12425-12433.

    A. S. K. Kumar, S. J. Jiang. Preparation and characterization of exfoliated graphene oxide-L-cystine as an effective adsorbent of Hg(II) adsorption. RSC Adv. **2015**, 5, 6294-6304.

[59] P. N. Diagboya, B. I. Olu-Owolabi, K. O. Adebowale. Synthesis of covalently bonded graphene oxide-iron magnetic nanoparticles and the kinetics of mercury removal. RSC Adv. **2015**, 5, 2536-2542.

[60] K. Mandel, F. Hutter, C. Gellermann, G. Sextl. Modified superparamagnetic nanocomposite microparticles for highly selective HgII or CuII separation and recovery from aqueous solutions. ACS Appl. Mater. Interfaces **2012**, 4, 5633-5642.

[61] S. Venkateswarlu, M. Yoon. Surfactant-free green synthesis of $Fe_3O_4$ nanoparticles capped with 3,4-dihydroxyphenethylcarbamodithioate: stable recyclable magnetic nanoparticles for the rapid and efficient removal of Hg(II) ions from water. Dalton Trans. **2015**, 44, 18427-18437.

[62] N. Saman, K. Johari, H. Mat. Adsorption characteristics of sulfur-functionalized silica Microspheres with respect to the removal of Hg(II) from aqueous solutions. Ind. Eng. Chem. Res. **2014**, 53, 1225-1233.

[63] S. Legergren, K. Svenska. About the theory of so-called adsorption of soluble substances. *Vetenskapsakad. Handl*. **1898**, *24*, 1-39.

[64] Y. S. Ho, G. McKay. Pseudo-second order model for sorption processes. *Process Biochem.* **1999**, *34*, 451-465.

[65] Y. S. Ho, G. McKay. Sorption of dye from aqueous solution by peat. *Chem. Eng. J.* **1998**, *70*, 115-124.

[66] W. J. Weber, J. C. Morris. Kinetics of adsorption on carbon from solution. *J. Sanit. Eng. Div. ASCE* **1963**, *89(SA2)*, 31-59.

    A. E. Ofomaja. Intraparticle diffusion process for Lead(II) biosorption onto mansonia wood sawdust. *Bioresour. Technol*. **2010**, *101*, 5868-5876.

[67] F. Qin, G. Li, H. Xiao, Z.nLu, H. Sun, R. Chen. Large-scale synthesis of bismuth hollow nanospheres for highly efficient Cr(VI) removal. *Dalton Trans.* **2012**, *41*, 11263-11266.

[68] G. Li, F. Qin, H. Yang, Z. Lu, H. Sun, R. Chen. Facile microwave synthesis of 3D flowerlike BiOBr nanostructures and their excellent $Cr^{VI}$ removal capacity. *Eur. J. Inorg. Chem.* **2012**, 2508-2513.

[69] P. Behra, P. B. Gissinger, M. Alnot, R. Revel, J. J. Ehrhardt. XPS and XAS study of the sorption of Hg(II) onto pyrite. *Langmuir* **2001**, *17*, 3970-3979.

[70] X. Ding, G. Briggs, W. Zhou, Q. Chen, L. M. Peng. In situ growth and characterization of Ag and Cu nanowires. *Nanotechnology* **2006**, *17*, S376-S380.

[71] X. Yan, S. Li, J. Bao, N. Zhang, B. Fan, R. Li, X. Liu, Y. X. Pan. Immobilization of highly dispersed Ag nanoparticles on carbon nanotubes using electron-assisted reduction for antibacterial performance. *ACS Appl. Mater. Interfaces* **2016**, *8*, 17060-17067.

[72] S. Bhattarai, J. S. Kim, Y. S. Yun, Y. S. Lee. Preparation of polyaniline-coated Polystyrene nanoparticles for the sorption of silver ions. *React. Funct. Polym.* **2016**, *105*, 52-59.

[73] Q. F. Lu, Luo, J. J; Lin, T. T.; Zhang, Y. Z. Novel Lignin-Poly(N-methylaniline) Composite Sorbent for Silver Ion Removal and Recovery. *ACS Sustainable Chem. Eng.* **2014**, *2*, 465-471.

[74] Y. Yao, B. Gao, F. Wu, C. Zhang, L. Yang. Engineered biochar from biofuel residue: characterization and its silver removal potential. *ACS Appl. Mater. Interfaces* **2015**, *7*, 10634-10640.

[75] H. Hou, D. Yu, G. Hu. Preparation and properties of ion-imprinted hollow particles for the selective adsorption of silver ions. *Langmuir* **2015**, *31*, 1376-1384.

[76] X. Song, C. Li, R. Xu, K. Wang. Molecular-ion-imprinted chitosan hydrogels for the selective adsorption of silver(I) in aqueous solution. *Ind. Eng. Chem. Res.* **2012**, *51*, 11261-11265.

    A. S. Shen, Y. Shen, Y. Z. Wen, H. Y. Wang, W. P. Liu. Fast and highly efficient removal of dyes under alkaline conditions using magnetic chitosan-Fe(III) Hydrogel. *Water Res.* **2011**, *45*, 5200-5210.

[77] Q. Liu, L. B. Zhong, Q. B. Zhao, C. Frear, Y. M. Zheng. Synthesis of $Fe_3O_4$/polyacrylonitrile composite electrospun nanofiber mat for effective adsorption of tetracycline. *ACS Appl. Mater. Interfaces* **2015**, *7,* 14573-14583.

[78] S. He, F. Zhang, S. Cheng, W. Wang. Synthesis of sodium acrylate and acrylamide copolymer/GO hydrogels and their effective adsorption for $Pb^{2+}$ and $Cd^{2+}$. *ACS Sustainable Chem. Eng.* **2016**, *4*, 3948-3959.

[79] Langmuir. The adsorption of gases on plane surfaces of glass, mica and platinum. *J. Am. Chem. Soc*. **1918**, *40*, 1361-1403.

[80] O. Redlich, D. L. Peterson. A useful adsorption isotherm. *J. Phys. Chem*. **1959**, *63*, 1024-1029.

[81] K. R. Hall, L. C. Eagleton, A. Acrivos, T. Vermeulen. Pore and solid-diffusion kinetics in fixed-bed adsorption under constant-pattern conditions. *Ind. Eng. Chem. Fundam*. **1966**, *5*, 212-223.

[82] X. Song, P. Gunawan, R. Jiang, S. S. J. Leong, K. Wang, R. Xu. Surface activated carbon nanospheres for fast Adsorption of silver ions from aqueous solutions. *J. Hazard. Mater.* **2011**, *194*, 162-168.

[83] X. G. Li, H. Feng, M .R. Huang. Strong Adsorbability of mercury ions on aniline/sulfoanisidine copolymer nanosorbents. *Chem. Eur. J.* **2009**, *15,* 4573-4581.

[84] X. G. Li, X. L. Ma, J. Sun, M. R. Huang. Powerful reactive sorption of silver(I) and mercury(II) onto poly(*o*-phenylenediamine) microparticles. *Langmuir* **2009**, *25,* 1675-1684.

[85] X. G. Li, H. Feng, M .R. Huang. Redox sorption and recovery of silver Ions as silver nanocrystals on poly(aniline-co-5-sulfo-2-anisidine) nanosorbents. *Chem. Eur. J*. **2010**, *16*, 10113-10123.

[86] R. Vitaliano, I. Fratoddi, I. Venditti, G. Roviello, C. Battocchio, G. Polzonetti, M. V. Russo. Self-Assembled monolayers based on Pd-containing organometallic thiols: preparation and structural characterization. *J. Phys. Chem. A* **2009**, *113,* 14730-14740.

    A. Zubrägel, C. Deuper, F. Schneider, M. Neumann, M. Grunze, A. Schertel, C. Wöll,. The presence of two different sulfur species in self-assembled films of n-Alkanethiols on Au and Ag surfaces. *Chem. Phys. Lett.* **1995**, *238*, 308-312.

[87] M. Balakrishnan, V. S. Batra, J. S. J. Hargreaves, I. D. Pulford. Waste materials-catalytic opportunities: an overview of the application of large-scale waste materials as resources for catalytic applications, *Green Chemistry* **2011**, *13*, 16-24.

[88] R. Eising, W.C. Elias, B. L. Albuquerque, S. Fort, J. B. Domingos. Synthesis of silver glyconanoparticles from new sugar-based amphiphiles and their catalytic application. *Langmuir* **2014**, *30*, 6011-6020.

[89] J. Xia, G. He, L. Zhang, X. Sun, X. Wang. Hydrogenation of nitrophenols catalyzed by carbon black-supported nickel nanoparticles under mild conditions. *Appl. Catal. B*. **2016**, *180*, 408-415.

[90] P. Zhao, X.X. Feng, D. Huang, G. Yang, D. Astruc. Basic concepts and recent advances in nitrophenol reduction by gold-and other transition metal nanoparticles. *Coord. Chem. Rev.* **2015**, *287*, 114-136.

[91] B. Ruhland, T. Becker, G. Müller. Gas-kinetic interactions of nitrous oxides with $SnO_2$ surfaces. *Sens. Actuators, B* **1998**, *50*, 85-94.

# CHAPTER 4: SYNTHESIS OF FE$_3$O$_4$@PPY-MAA NANOCOMPOSITE FOR AG+ REMOVAL AND SUBSEQUENT USE AS AN ANTIMICROBIAL AND CATALYST

## 4.1 INTRODUCTION

As the modern industries have grown by leaps and bounds over the past few decades, environmental pollution is becoming a global and serious concern to humans' well-being. Among various types of environmental pollution, water body contamination due to discharge of untreated water-containing inorganic and organic species has attracted a lot of consideration in recent years [1, 2]. Global pollution is expanding as a result of variations in natural and anthropogenic activities that lead to adulteration of terrestrial as well as aquatic ecosystem with heavy metals, non-metals and metalloids. Untreated discharge of waste, sewage disposal, use of fertilizers and use of agricultural pesticides are some of the major contributors. In that regard, existing freshwater resources are progressively becoming polluted and unavailable. A recent study on the global threats to human water security and river biodiversity revealed that 80% of the world's population is exposed to high levels of threat to water security[3]. Hence, various technologies have been designed and developed for the purpose to purify and remove water pollutants that may lead to human health and ecosystem damages. The main focus of the current report is on the removal of silver (Ag) and fluoride (F) and other subsequent applications of the spent adsorbent.

Silver (Ag) is a natural constituent of the earth's crust and it is an attractive metal because of its malleability, photosensitivity and excellent thermal properties [3]. Ag is currently added in consumer products such as home appliances, textiles, food supplements and personal care products because of its bactericidal properties [4,5]. The escalating use of Ag in basic consumer products, has led to an increase in its release into the environment, particularly water sources [6]. Also, Silver is usually found in industrial effluent from electroplating, printing and photo processing industries [7]. Due to the toxicity associated with the excessive consumption of Ag [8], the United States Environmental Protection Agency has set the maximum contaminant level of Ag to 0.1 mg/L for drinking water [9]. It is thus, important to ensure that the amount of Ag released to the environment is within the allowable limit.

Adsorption is a mass transfer technique that involves accumulation of substances (adsorbate) at the surface provided by solid materials (adsorbent) through physical or sometime weak chemical forces. Polypyrrole (PPy) and Polyaniline (PANI) are considered as the most effective adsorbent materials due to outstanding properties such as high conductivity, high stability, easy preparation, low cost and biocompatibility [10,11,12]. However, while polypyrrole has already been applied on a large scale to the adsorption of metal ions and dyes from aqueous solutions, the benefits of introducing suitable chelating agents into the polymeric chain has recently drawn great attention [13]. Thus, there is still a rising interest in the use of polymer-based nanomaterials/nanocomposites for the removal of ions from aqueous media. The adsorption capacity for specific metal ions increases many fold, with selective accumulation of the complexing agent onto the surface of the adsorbent. Chelating agents with electronegative donor atoms like sulphur, nitrogen, oxygen are most effective for the selective adsorption of heavy metal ions through strong metal-binding capacity. PPy has a low density and incorporating iron oxide ($Fe_3O_4$) nanoparticles in the polymer matrix will increase the density of the nanocomposites making the recovery of the spent adsorbent easier, as it would only require a magnetic field for separation [14].

Recently, one-dimensional (1-D) PANI nanostructures (nanorods/wires/fibers) have attracted much scientific interest over conventional bulk counterparts as they offer a possibility of improved performance as a result of a large interfacial area and possess the advantages of both low-dimensional systems and organic conductors [15,16]. In view of this, Bhaumik *et al*. have demonstrated the great potential of bare PANI nanofibres (PANI NFs) and its composite with nano-sized $Fe^0$ in the removal of As(V), Cr(VI) and dyes [17,18]. Though, it is widely accepted that the positively charged backbone of PANI (protonated amine groups) can act as excellent adsorption sites for anions, yet its $F^-$ removing properties were not fully explored. However, in this regard, an effort was also made by Karthikeyan *et al*. who successfully synthesized bare PANI and its composites with chitosan and alumina and obtained a defluoridation capacity of 0.78, 5.9 and 6.6 mg/g, respectively [19-21]. Hence, further modification of PANI with reactive materials having significant affinity towards $F^-$ ions would constitute a viable approach in developing highly efficient PANI-based $F^-$ adsorbents. Most reported adsorbents were not re-used beyond regeneration upon and Ag adsorption, which could mean the spent adsorbents were discarded after use.Remarkably, nanomaterials have also been widely deployed as sustainable nanocatalysts, antimicrobial agents or gas sensing; thus leaving great opportunity to explore spent adsorbents for the latter.

Several aspects of sustainable development including waste minimization and reuses of waste-derived nanomaterials are keys to green chemistry [22-24]. There has been a significant interest in silver nanoparticles owing to their diverse application in antimicrobial and catalysis research fields [25-27]. For example, Baruah and co-workers reported the synthesis of AgNP as an effective catalyst for the reduction of 4-nitrophenol to 4-aminophenol in the presence of $NaBH_4$. The reduction followed a pseudo-first-order reaction with a rate constant of $5.50 \times 10^{-3}$ $s^{-1}$ and an activity parameter of 1375 $s^{-1}$ $g^{-1}$. Hg, on the other hand, was used in the form of mercury(II) trifluoromethanesulfonate, $Hg(OTf)_2$, for the transformation of $CH_4$ to MeOH [28]. Likewise, hydration of alkynes and cyclization of propargyl **tert**-butyl carbonates were achieved using $Hg(OTf)_2$. Metal nanoparticles have also been incorporated into gas sensors to increase the sensitivity, selectivity and response time to the experimental gases tested [29,30]. Ragachev *et al* reported the preparation of PANI-based materials for ammonia gas sensing applications. The incorporation of AgNPs was found to enhance the sensing properties at low frequency region of impedance spectra. Silver is also known to exhibit significant anti-microbial activity upon fungi, bacteria and viruses [31,32]. Graphene oxide nanocomposites modified with AgNPs, for example, showed excellent antimicrobial activity towards *Escherichia coli* (*E. coli*) and *Salmonella.* In this study, after adsorption of $Ag^+$ from the aqueous solution, metal-laden adsorbents were to be screened for their potential application in catalysis, gas sensing and/or bacteria growth inhibition.

## 4.2 EXPERIMENTAL

### 4.2.1 Materials

Pyrrole (Py, $C_4H_5N$), ammonium persulfate (APS, $(NH_4)_2S_2O_8$), 3-mercapto acetic acid (MAA, $HSCH_2CO_2H$), silver nitrate ($AgNO_3$), iron oxide nanoparticles ($Fe_3O_4$ NPs), 4-nitrophenol (4-NP), methyl orange (MO), methylene blue (MB), sodium bicarbonate, dichloromethane, magnesium nitrate ($Mg(NO_3)_3 \cdot 6H_2O$), sodium hydroxide (NaOH), hydrogen chloride (HCl) and sodium fluoride (NaF) were purchased and acetone were purchased from Sigma Aldrich (USA), South Africa. 65% Nitric acid ($HNO_3$) analytical grade was purchased from PerkinElmer, South Africa. The Py was distilled and stored at 4°C before use. 0.1M NaOH (> 99.9% grade) and 0.1M HCl/$HNO_3$ aqueous solutions were used to adjust the pH. Nutrient agar and nutrient broth were purchased from Merck Millipore, South Africa, and all the microbial strains were obtained from the Microbiology Laboratory of the Natural Resource and the Environment research group at the Council of Industrial and Scientific Research (CSIR), South Africa. All other reagents were purchased and used as received unless otherwise stated.

### 4.2.2 Characterisation techniques

The surface morphologies and elemental composition of the prepared composites and nanocomposites were determined by a Field Emission-Scanning Electron Microscope (Auriga FE-SEM, Carl Zeiss, Germany) with an Oxford energy dispersive X-ray spectrometer (EDS, Oxford, UK). A JEOL JEM 2100 High Resolution-(Scanning) Transmission Electron Microscope (HR-STEM, JEOL Japan) fitted with an EDS system (Thermo Scientific, USA) was also used to characterise samples. A Spectrum 100 Attenuated Total Reflectance-Fourier Transform Infrared (ATR-FTIR, Perkin-Elmer, USA) was employed to record the infrared spectra of the composites/nanocomposites before and after adsorption of the adsorbate in the scanning range of 600-4000 $cm^{-1}$ at a resolution of 4 $cm^{-1}/s$. The powder X-ray Diffraction (XRD) patterns of adsorbent before and after adsorption were performed by using PANalytical X'Pert PRO-diffractometer with Cu Kα radiation (wavelength, $\lambda = 1.5406$ Å), and angular variation of 5-90° operated at a generator voltage and current of 40 kV and 40 mA respectively. Oxidation states of the elements of the composite were obtained using high-resolution X-ray photoelectron spectroscopy (XPS) on a Kratos Axis Ultra device, with a focused monochromatized Al Kα radiation (hv = 1486.6 eV).

The $N_2$ adsorption-desorption isotherm was analysed by Quatachrome Autosorb-1C surface analyzer (USA). The specific surface areas of the composites/ nanocomposites were calculated according to the Brunauer-Emmett-Teller (BET) method. The pore size distribution was achieved by desorption branch of the isotherm with the Barrett-Joyner-Halenda (BJH) method. Zeta potential of the composite was measured using Zetasizer NanoS (Malvern, UK). The concentration of $Ag^+$ ion in the filtrate was determined using an inductively Coupled Plasma Mass Spectroscopy (ICP-MS) (Thermo Fisher Scientific, USA). UV-vis spectrophotometer (Perkin-Elmer, Lambda 35) has been used to measure the concentration of 4-Nitrophenol, methyl blue and methyl orange, in reaction medium during catalytic performance. GC analyses were recorded with Agilent 7890A gas chromatograph using SBP- 20 column (GC method: Oven program: 80°C for 3 min then 10°C/min to 250°C for 10 min, Run time: 25 min). An Agilent VNMRS Premium Shield 600MHz spectrometer was used to record NMR spectra of the pure compound (acetophenone) and chemical shifts ($\delta$) were reported in parts per million (ppm) using TMS as reference signal. Aluminium plates coated with Kieselgel 60 F-254 silica gel were used for thin layer chromatography (TLC), and visualization was done under UV light. The pure product was isolated through column chromatography, performed over 100-200 mesh silica gel using ethyl acetate/hexane solvent mixtures as the eluent. The data of NMR splitting patterns were presented as singlet (s) and multiplet (m).

A Waters® Synapt G2 high definition mass spectrometry (HDMS) system (Waters Inc., Milford, Massachusetts, USA) was used for compound detection and analysis. The system consists of a Waters Acquity Ultra Performance Liquid Chromatography (UPLC®) for the separation of the compounds hyphenated to the quadrupole-time-of-flight (QTOF) instrument. A Kinetex® 1.7 µm EVO C18 100 Å (2.1 mm ID x 100 mm length) column was used. The mobile phase consisted of solvent A: water with 0.1% formic acid and solvent B: acetonitrile with 0.1% formic acid). The gradient elution was optimized as follows: 3% B (0-0.1 min), 3% B (0.1-7.5 min), 100% B (7.5-9.0 min), 3% B (9.0-10.0 min). The flow rate was 0.4 mL/min, column temperature kept constant at 40°C for the entire run, with a total run time of 10 min and the injection volume was 5µL. The instrument was calibrated by direct infusion of 5 nM sodium formate solution at a flow rate of 10µL/min over a mass range of 50-1200 Da. The following MS source parameter were set for both positive and negative mode: Source temperature 100°C, sampling cone 15 V, extraction cone 4.0 V, desolvation temperature 400°C, cone gas flow 10.0 L/h, desolvation gas flow 700 L/h, capillary 2.0 kV. The positive and negative ion mass spectra were collected in separate chromatographic runs (employing the same separation conditions). Compounds were identified based on their accurate mass generated from MassLynx V 4.1, iFit value, MS/MS fragmentations (product ions).

### 4.2.3 Synthesis of thiol-modified magnetic polypyrrole nanocomposite ($Fe_3O_4$@PPy-MAA)

Polymerisation of Py occurred via *in situ* chemical oxidation [33]. Briefly, 0.2 g of $Fe_3O_4$ NPs was ultrasonically dispersed in 80 mL ultrapure deionised water for 15 min. Then, 1.6 mL of MAA was added to the $Fe_3O_4$ dispersion, followed by 0.8 mL of the Py at 25°C. After that, 6.8 g of the oxidising agent (APS) was dissolved in ultrapure deionised water and added dropwise to the suspension. Polymerisation continued for 6 h. The resultant $Fe_3O_4$@PPy-MAA NC was retrieved through vacuum filtration and washed thoroughly with deionised water and acetone. The NC was dried at 60°C under vacuum for 24 h. PPy-MAA was prepared in the same manner as the $Fe_3O_4$@PPy-MAA NC, but without $Fe_3O_4$, and used as a control for comparison purposes.

### 4.2.4 Ag Adsorption procedure

The adsorption performance of the $Fe_3O_4$@PPy-MAA NC was investigated in batch equilibrium studies. The effect of the following parameters was investigated: adsorbent dosage (0.01-0.05 g), pH (1-5.6), initial $Ag^+$ concentration (50-600 mg/L) and temperature (25°C, 35°C, 45°C). The $Fe_3O_4$@PPy-MAA NC was contacted with 50 mL of $Ag^+$ solutions (Silver nitrate was dissolved in deionised water) in 100 mL glass bottles and placed in a thermostatic water bath shaker (Separations Scientific, SA) at 200 rpm for 24 h. The experiments were conducted at room temperature (25°C) unless otherwise stated. The pH was adjusted accordingly using sodium hydroxide (aq) and diluted nitric acid. Following optimisation, the adsorbent dose (0.025 mg) was kept constant throughout the study. The samples (10 mL) were filtered through 0.45 µm syringe filters and analysed for residual $Ag^+$ ion concentration using Inductively Coupled Plasma Mass Spectroscopy (ICP-MS, Thermo Fisher Scientific, USA). The adsorption efficiency was determined using the following equation:

$$adsorption\ efficiency\,\% = \frac{(C_0 - C_e)}{C_0} \times 100 \qquad (1)$$

The adsorbed amount (uptake) of the contaminant was determined using the following equation:

$$q_e(mg/g) = \frac{(C_0 - C_e)V}{W} \qquad (2)$$

where $q_e$ (mg/g) is the adsorption capacity at equilibrium; $C_0$ and $C_e$ are the initial and equilibrium concentrations (mg/L) of contaminant, respectively; $V$ is the experimental solution volume (L), and $W$ is the adsorbent weight (g).

The adsorption kinetics studies were carried out by varying the initial $Ag^+$ ion concentration (50, 100, 150 mg/L). The adsorbent and $Ag^+$ suspension was stirred in a 1L beaker for 8 h. Aliquot (~5 mL) samples were collected and filtered using a 0.45 µm syringe filter at predetermined time intervals. The filtrate was analysed for residual $Ag^+$ concentration. Thereafter, the adsorption capacities and removal percentages were determined. The amount of contaminant per unit mass of adsorbent at a given time, ($q_t$) was determined using the following equation:

$$q_t(mg/g) = \frac{(C_0 - C_t)V}{W} \qquad (3)$$

where $C_t$ is the concentration at a given time t.

Furthermore, to understand the adsorption kinetics of the $Fe_3O_4$@PPy-MAA NC towards $Ag^+$ removal, the experimental data were fitted to two models, namely: pseudo-first-order (eq.4) and pseudo-second-order (eq.5) kinetic models [34-35].

$$log(q_e - q_t) = log q_e - \frac{k_1}{2.303}t \qquad (4)$$

$$\frac{t}{q_t} = \frac{1}{k_2 q_e^2} + \frac{t}{q_e} \qquad (5)$$

where $q_e$ (mg/g) and $q_t$ (mg/g) is the adsorption at equilibrium and at a given time $t$ (min), respectively; $k_1$ (1/min) and $k_2$ (g/mg.min) are the pseudo-first-order and the pseudo-second-order rate constants, respectively.

### 4.2.5 Antimicrobial activity test with $Fe_3O_4$@PPy-MAA on cell cultures of *Escherichia coli (E. coli)*

Aliquots (~1 mL) of 15% w/v sodium thiosulfate and 0.9 mL of 0.9% saline water were prepared. 10-200 mg of NC was weighed into 50 mL centrifuge tubes containing 20 mL sterile deionised water. The tubes were inoculated with *Escherichia coli* (American Type Culture Collection®; ATCC 25922) at a final concentration of ~ $10^7$ CFU/mL. Two sets of tubes, 1 set with $Fe_3O_4$@PPy-MAA NC and another with just water and bacteria, were used as controls. The experiments were performed in triplicates. The tubes were sampled every 10 min for 60 min (starting from time 0, the time immediately following inoculation). The extracted samples were added to the sodium thiosulfate aliquots, to deactivate the Ag, and further diluted in 0.9% saline water. Then, 0.01 mL of the deactivated samples was plated on nutrient agar using the drop plate technique [36]. The plates were incubated for 24 h at 37°C. The colonies were counted using an aCOLade 2 manual colony counter (Synbiosis, UK) and the results were recorded in CFU/mL.

### 4.2.6 Catalytic activity of Ag-loaded $Fe_3O_4$@PPy-MAA for catalytic reduction of 4-nitrophenol

To evaluate the activity of the $Fe_3O_4$@PPy-MAA/Ag NC as an efficient catalyst, the reduction of 4-nitrophenol to 4-aminophenol was considered as a model reaction. In a typical reaction, 2.5 mg $Fe_3O_4$@PPy-MAA/Ag catalyst was added to 25 mL aqueous solution of 4-NP (1 mmol) under stirring condition at 25°C in a 50 mL round bottom flask. Next, freshly prepared 2.5 mL aqueous solution of $NaBH_4$ ($1\times10^{-1}$ M) was slowly added to the above reaction mixture. A sudden change in colour from light to dark yellow was experienced. The progress of the $-NO_2$ conversion was monitored by the change in absorbance at the wavelengths of 400 nm for 4-NP and 300 nm for newly formed 4-AP, at definite time intervals. The colour change from dark yellow to colourless happened within 45 min of reaction time. With a fixed concentration and volume of 4-NP and $NaBH_4$, the amount of catalyst was also varied from 2.5-7.5 mg, to evaluate the efficiency of the developed $Fe_3O_4$@PPy-MAA/Ag catalyst. Furthermore, to investigate the catalytic potentiality of Ag NPs, relative to $Fe_3O_4$ NPs, Both $Fe_3O_4$@PPy-MAA and $Fe_3O_4$@PPy-MAA/Ag were equally employed for the same reaction without $NaBH_4$.

### 4.2.7 Catalytic reduction and degradation of organic dyes using silver loaded $Fe_3O_4$@PPy-MAA

For this study, two water-soluble organic dyes, namely, methyl orange (MO) and methylene blue (MB) were chosen as model for the reduction and degradation using $Fe_3O_4$@PPy-MAA/Ag in the presence of reducing agent $NaBH_4$. In a typical degradation process, different amount of the as-prepared $Fe_3O_4$@PPy-MAA/Ag (1.0 to 5.0 mg) was added to 25 mL of aqueous dye solution ($1\times10^{-4}$ M). Subsequently, 1 mL freshly prepared $NaBH_4$ solution ($1\times10^{-1}$ M) was injected into the above mixture and the reaction was stirred at 25°C. The catalytic activity was recorded by using UV-vis absorption spectra ($\lambda_{max}$: 464 nm for MO;

$\lambda_{max}$: 664 nm for MB) of supernatant at definite time intervals. Samples were also analysed using the UPLC QTOF.

## 4.3 RESULTS AND DISCUSSION

### 4.3.1 Characterisation of thiol-modified magnetic polypyrrole nanocomposite ($Fe_3O_4$@PPy-MAA)

The surface morphology of the $Fe_3O_4$@PPy-MAA NC before and after adsorption was studied using FE-SEM (Figure 4-1). The NC appeared as spherical aggregates with a relatively uniform shape before the addition of $Ag^+$ (Figure 4-1a). However, the surface of the $Fe_3O_4$@PPy-MAA NC was modified after $Ag^+$ adsorption (Figure 4-1b). The formation of crystal clumps along with aggregation of spherical $Fe_3O_4$@PPy-MAA NC is an indication of $Ag^+$ adsorption onto the magnetic NCs surface. The presence of elements on the $Fe_3O_4$@PPy-MAA NC before and after $Ag^+$ adsorption experiments was determined through EDX spectra. The existence of C, N, O, S and Fe in the developed magnetic NC was confirmed by EDX spectra (Figure 4-1c), and the addition of an Ag peak (Figure 4-1d) indicated successful adsorption of $Ag^+$ onto $Fe_3O_4$@PPy-MAA NC surface.

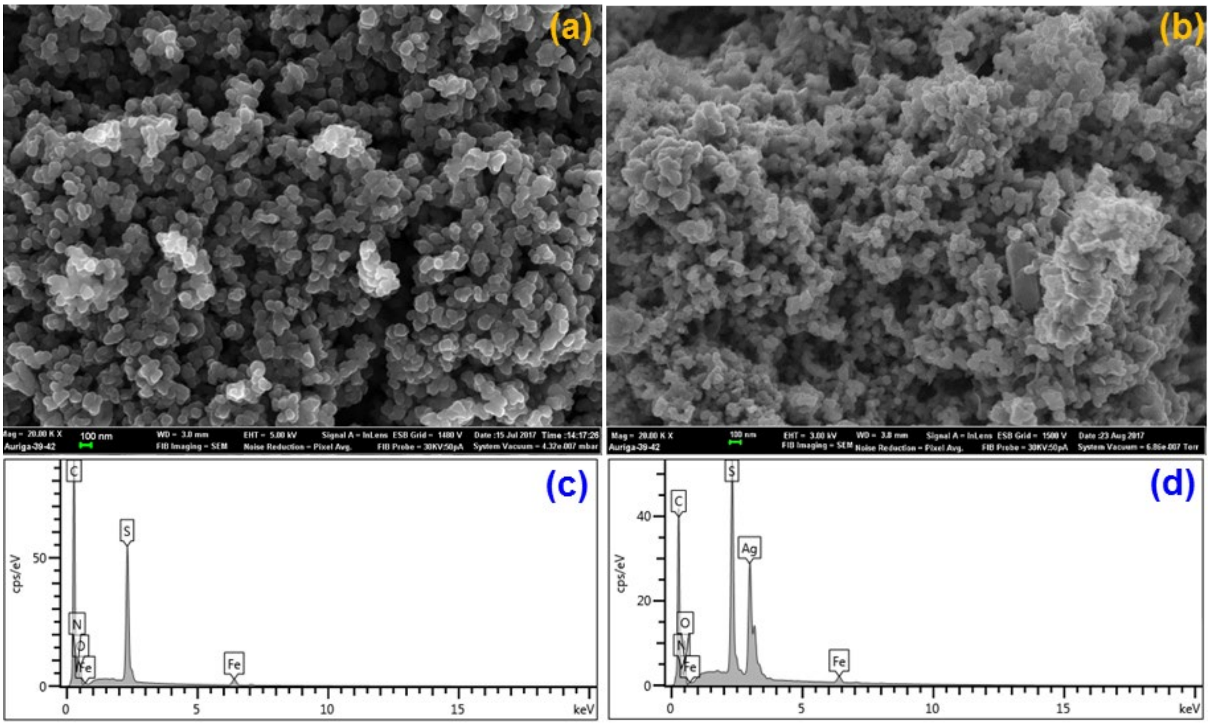

**Figure 4-1: FE-SEM micrographs of $Fe_3O_4$@PPy-MAA (a) before and (b) after $Ag^+$ adsorption; EDX spectra of $Fe_3O_4$@PPy-MAA (c) before, (d) after adsorption.**

Also, elemental mapping of $Fe_3O_4$@PPy-MAA/Ag NC (Figure 4-2a) and the separate distribution of C, O, S, Fe and Ag are shown in Figure 4-2(b-f). The surface modification of the NC with MAA and adsorption $Ag^+$ were thus confirmed.

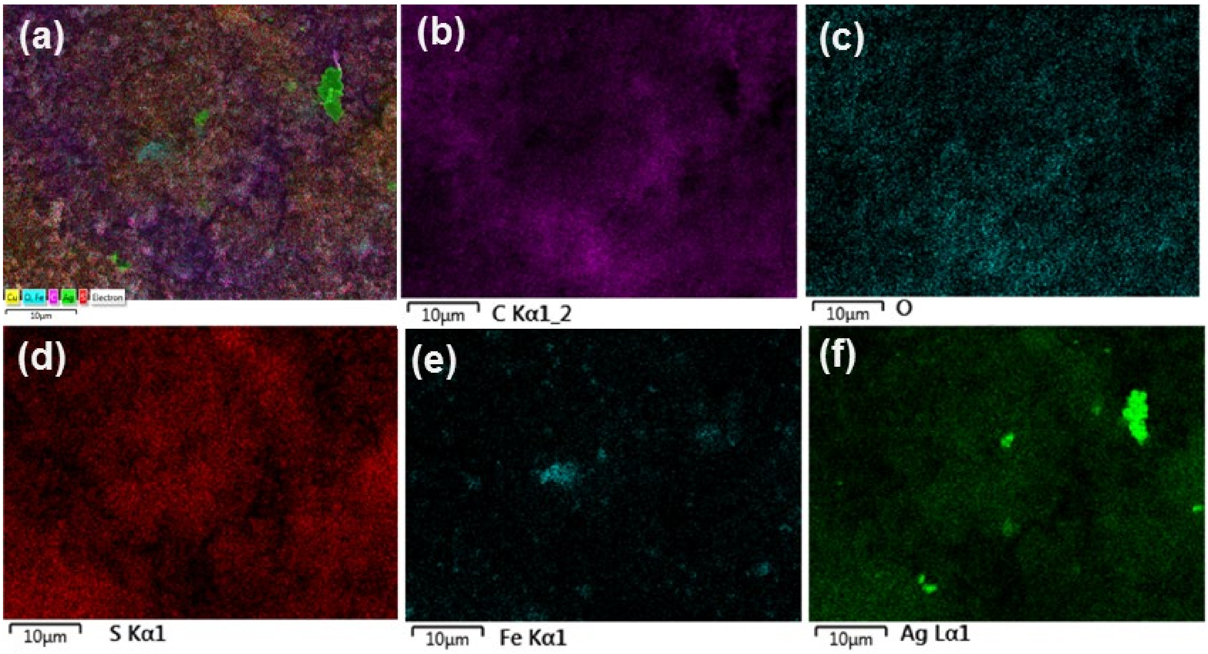

**Figure 4-2: (a) Elemental mapping of PPy-MAA@$Fe_3O_4$/Ag NC and separate distribution of (b) C, (c) O, (d) S, (e) Fe and (f) Ag.**

The morphology of the $Fe_3O_4$@PPy-MAA NC before and after $Ag^+$ adsorption was further examined using the HR-TEM. Figure 4-3a displays the spherical morphology of the as-prepared magnetic NC. In comparison to the $Fe_3O_4$@PPy-MAA NC (Figure 4-3a), the surface of the NC after Ag adsorption has a relatively different morphology. The TEM image (Figure 4-3b) shows that Ag NPs were embedded on the surface of the NC. Lattice fringes were measured to confirm the presence of $Fe_3O_4$ and Ag NPs. The lattice fringes of $Fe_3O_4$ and Ag NPs present in the magnetic NC are shown in Figure 4-3c. The interfering distance attributed to the (111) plane of the Ag NPs was measured to be 0.23 nm, and that of $Fe_3O_4$ was measured to be 0.49 nm, which has been attributed to the (111) plane for both metals [37, 38].

A nearly uniform dispersion of Ag NPs onto the $Fe_3O_4$@PPy-MAA NC after adsorption was observed on the HR-TEM, through STEM-EDS (Figure 4-4). Therefore, it was evident that PPy was successfully doped with MAA and $Ag^+$ was reduced to Ag NPs in the following adsorption process.

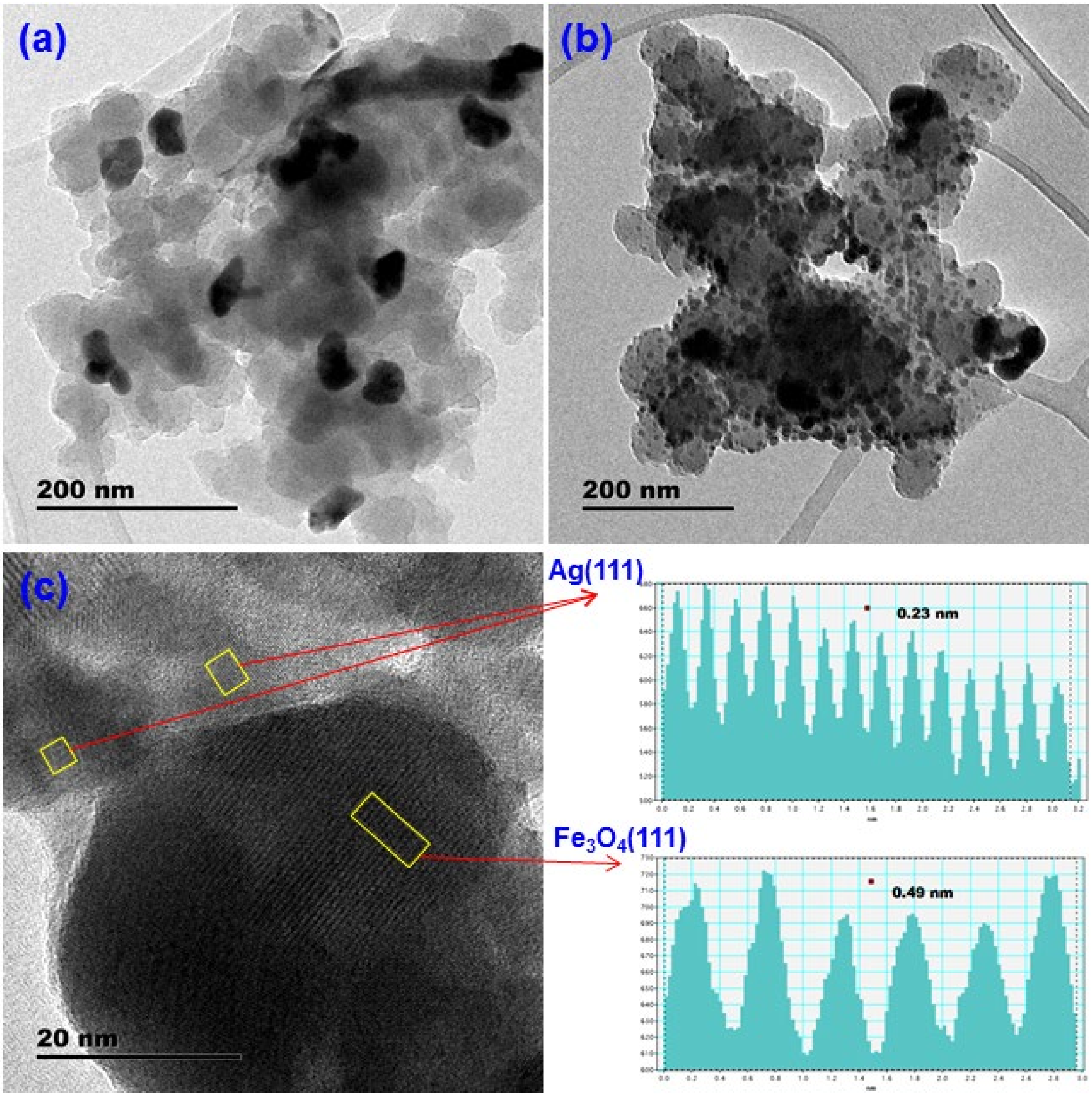

**Figure 4-3: HR-TEM image of the $Fe_3O_4$@PPy-MAA NC (a) before and (b) after $Ag^+$ adsorption; (c) lattice fringes of the adsorbed Ag.**

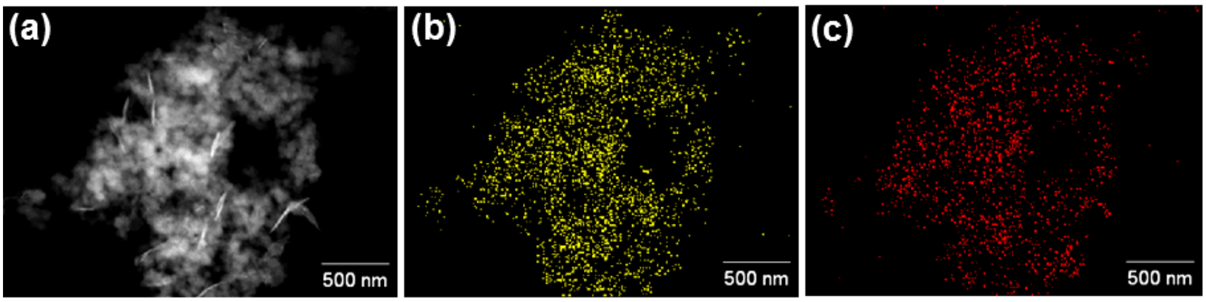

**Figure 4-4: HR-TEM (a) STEM micrograph of $Fe_3O_4$@PPy-MAA /Ag NC and EDS mapping (b) sulphur (c) silver.**

The ATR-FTIR spectra of $Fe_3O_4$@PPy-MAA and $Fe_3O_4$@PPy-MAA/Ag showing the functional groups present on the NCs are shown in Figure 4-5a. In the case of the $Fe_3O_4$@PPy-MAA NC, the intense peak at 1557 and 1488 cm$^{-1}$ can be ascribed to the antisymmetric and symmetric C=C stretching vibration of the PPy backbone [39]. The sharp peaks at 1367 and 1266 cm$^{-1}$ are assigned to C-N and C-O stretching vibrations, respectively. The introduction of broad bands around 3135 and 2640 cm$^{-1}$ reflect the characteristic stretching vibrations O-H and S-H of MAA [33]. The sharp characteristic peak at 1703 cm$^{-1}$ demonstrates vibrations of C=O of thioglycolic acid. The peaks at 2919 and 1050 cm$^{-1}$ are attributed to C-H stretching and deformation vibrations of ring, respectively [40]. The peaks at 1190 and 924 cm$^{-1}$ are assigned to typical bands for doped PPy [39]. The FTIR spectrum of $Fe_3O_4$@PPy-MAA NC showed significant changes in the above functional groups after Ag$^+$ adsorption, which was proof that Ag$^+$ adsorption was successful.

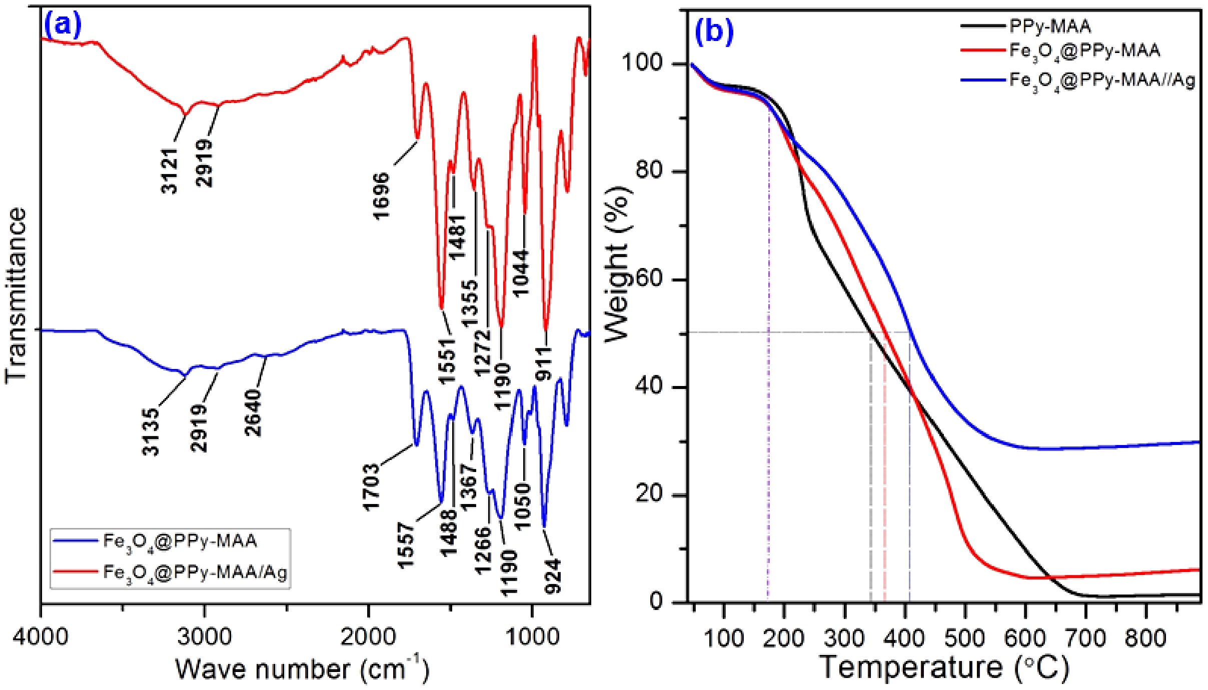

**Figure 4-5: (a) FTIR spectra and (b) Thermogravimetric analysis of $Fe_3O_4$@PPy-MAA before and after Ag$^+$ adsorption.**

The thermal stability of the developed PPy-MAA, $Fe_3O_4$@PPy-MAA and $Fe_3O_4$@PPy-MAA/Ag were determined via the TGA analysis under air with a heating rate of 10°C/min up to 900°C (Figure 4-5b). The weight loss region at 100°C for all the samples was due to the evaporation of surface adsorbed water molecules [13]. To analyse the thermal stability of the NCs, $T_{50\%}$ values (the temperature at which 50% of the total mass loss occurs) were considered for all the tested samples. The results (Figure 4-5b) suggest that the $T_{50\%}$ value of PPy-MAA composite increased from 345°C to 367°C after incorporation of $Fe_3O_4$ NPs into the polymer matrix. Furthermore, after Ag$^+$ adsorption, the Ag-loaded NC ($Fe_3O_4$@PPy-MAA/Ag) showed a higher $T_{50\%}$ value (410°C) than the PPy-MAA composite and $Fe_3O_4$@PPy-MAA NC. Therefore, the thermal decomposition result (Figure 4-5b) indicates that the addition of NPs ($Fe_3O_4$ and Ag) to PPy-

MAA NC enhances the thermal stability of the NC [15, 16]. It was also observed that the degradation of the NCs started at temperatures above ~175°C. Therefore, the synthesized NCs could be subjected to apply for the removal toxic metal ions from aqueous medium up to experimental temperature at 175°C without any chemical change of the NCs.

XRD patterns have been used to clarify the phase and structural parameters of PPy-MAA, $Fe_3O_4$@PPy-MAA and $Fe_3O_4$@PPy-MAA/Ag composites. Figure 4-6i(a) indicates the amorphous nature of the PPy-MAA composite with a broad band at 2θ = 21.84° [17]. The incorporation of $Fe_3O_4$ into the polymer matrix is shown by six strong diffraction peaks (Figure 4-6i(b)) that can be seen in the $Fe_3O_4$@PPy-MAA NC. The positions of the characteristic diffraction peaks are matched with the value of 2θ at 30.3, 35.5, 43.3, 53.7, 57.1 and 62.5°. The above located diffraction peaks correspond to (220), (311), (400), (422), (511) and (440) lattice planes of $Fe_3O_4$, respectively [17, 18]. The XRD pattern of the $Fe_3O_4$@PPy-MAA/Ag (Figure 4-6 i(c)) shows a broad peak in the spectrum at 2θ = 15-26° corresponding to the amorphous phase of the PPy matrix. The other five strong peaks in this spectrum match with the face-centred cubic (fcc) structure of metallic Ag with the crystalline peaks appearing at 37.8, 44.1, 64.4, 77.3 and 81.4° corresponding to (111), (200), 220), (311) and (222) lattice planes, respectively [19]. The presence of peaks attributed to the $Fe_3O_4$ and Ag NPs in the $Fe_3O_4$@PPy-MAA/Ag spectrum is indicative of their incorporation being successful.

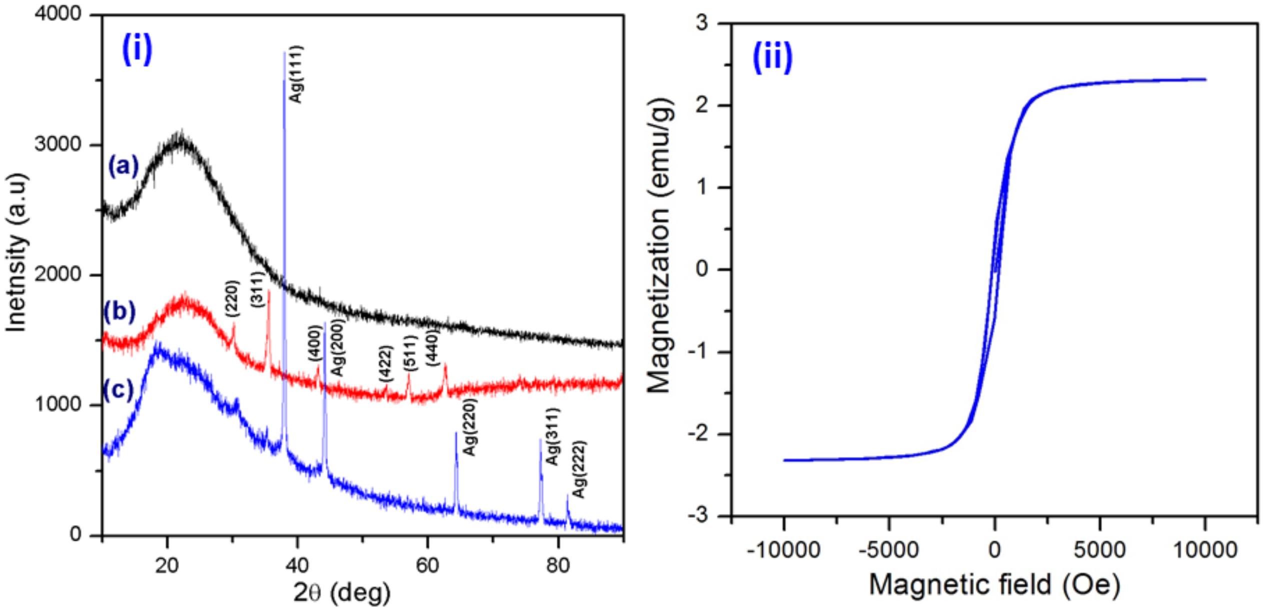

**Figure 4-6: (i) XRD spectra of (a) PPy/MAA, (b) and (c) $Fe_3O_4$@PPy-MAA NC before and after $Ag^+$ adsorption and, (ii) magnetisation curve of $Fe_3O_4$@PPy-MAA NC as a function of applied field.**

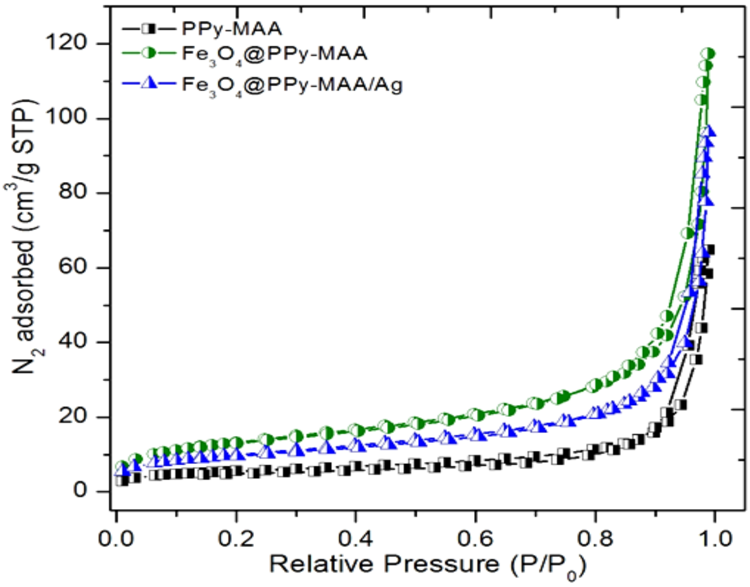

**Figure 4-7: BET surface area measurements of Fe$_3$O$_4$@PPy-MAA NC before and after Ag$^+$ adsorption.**

The BET specific surface area, average pore diameter and average pore volume of the PPy-MAA, Fe$_3$O$_4$@PPy-MAA and Fe$_3$O$_4$@PPy-MAA/Ag NC were determined using N$_2$ adsorption-desorption isotherms obtained from the BET method (Figure 4-7). The results obtained in Figure 4-7 show that the incorporation of Fe$_3$O$_4$ NPs into the polymer matrix led to an increase in surface area, from 20.67 to 48.48 m$^2$/g. It was also noted that the surface area decreased after Ag$^+$ adsorption (35.69 m$^2$/g) (Table 4.1), which was due to the Ag$^+$ adsorbed on the surface of the Fe$_3$O$_4$@PPy-MAA NC, as expected. The same trend was observed with the average pore volume, and pore diameter (Table 4-1). These trends further prove the effective incorporation and adsorption of Fe$_3$O$_4$ and Ag NPs in the polymer matrix. The magnetic properties of the Fe$_3$O$_4$@PPy-MAA NC were studied using a vibrating sample magnetometer, and the magnetization curve is shown in Figure 4-6 (ii). Weak ferromagnetic responses were observed in the hysteresis loop. The saturation magnetization ($\sigma_s$) value was found to be 2.32 emu/g. The $\sigma_s$ value was significantly lower compared to the bulk iron oxide value between 84.00 and 92.00 emu/g. The low $\sigma_s$ value is associated with the low content of iron oxide in the NC [20]. Additionally, the electroconductivity of PPy can lead to shielding of the magnetization of iron oxide, thus resulting in the lower $\sigma_s$ values [21].

**Table 4-1: BET Surface area measurements result of PPy-MAA, Fe$_3$O$_4$@PPy-MAA and Fe$_3$O$_4$@PPy-MAA/Ag NCs**

| Materials | Surface area (m$^2$/g) | Pore Volume (cm$^3$/g) | Pore diameter (nm) |
|---|---|---|---|
| PPy-MAA | 20.67 | 0.0825 | 15.97 |
| Fe$_3$O$_4$@PPy-MAA | 48.48 | 0.149 | 19.66 |
| Fe$_3$O$_4$@PPy-MAA/Ag | 35.69 | 0.120 | 13.48 |

### 4.3.2 Adsorption of $Ag^+$

#### *4.3.2.1 Effect of initial pH on $Ag^+$ adsorption*

The effect of pH plays a major role in the adsorption process due to the surface chemistry of the adsorbent. It is therefore, important to know at which pH is adsorption most favourable and it is shown in Figure 4-8. The effect of pH on the removal efficiency of $Ag^+$ ions from aqueous solutions was studied. The removal efficiency increased from 33.4 to 97.9% with an increase in pH from 1 to 5.6, respectively (Figure 4-8 a). The study was limited to the solution pH 5.6, because $Ag^+$ ions precipitates at pH higher than 6 [33]. The low removal efficiency at low pH could be due to the presence of high concentration of $H^+$ ions in solution, thus creating competition with the active sites [21]. On the other hand, the increase in $Ag^+$ ions removal efficiency indicates the relation of pH and the surface charge of the $Fe_3O_4$@PPy-MAA NCs (Figure 4-8b). The NCs were negatively charged from pH 3, with an isoelectric point at pH 2.3. The increase in pH (2 to 5.6) resulted in an increase in the negative charge on their surfaces (7.3 to -43.8 mV), which further explains the gradual increase in the removal efficiency of the $Ag^+$ ions. These observations suggest that an increase in surface charge increases the likelihood of the electrostatic interactions between the negatively charged (deprotonated) adsorbent surface and the positively charged $Ag^+$ ions [41].

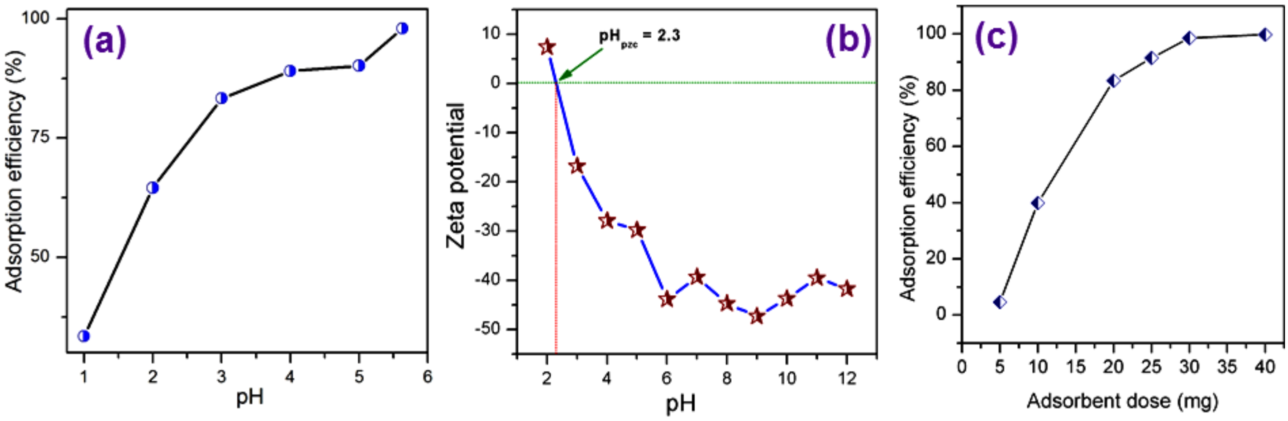

**Figure 4-8: Influence of pH on (a) absorption efficiency and (b) zeta potential of $Fe_3O_4$@PPy-MAA NC; (c) influence of adsorbent dose (mg) on adsorption efficiency.**

#### *4.3.2.2 Effect of the $Fe_3O_4$@PPy-MAA NC dosage*

The effect of the $Fe_3O_4$@PPy-MAA NC dosage on the removal efficiency of $Ag^+$ ions from aqueous solutions was investigated (Figure 4-8c). To perform this experiment, the adsorbent dosage was varied between 5 and 40 mg, while the initial $Ag^+$ ions concentration was 200 mg/L, at solution pH of 5.63 and an experimental temperature of 298 K. It was observed that the $Ag^+$ ions removal efficiency increased with an increase in adsorbent dosage. The removal efficiency increased from 4.60 to 39.84 and 83.41% for 5 mg, 10 mg and 20 mg, respectively. The increase in $Ag^+$ ions removal efficiency was due to the increase in surface active sites as the adsorbent dosage increased. The increase in adsorbent dosage led to a marginal removal efficiency of 98.3, 98.5 and 99.8% at 25, 30 and 40 mg, respectively. This was a result of limited exposure of the surface active sites to the volume (50 mL). Since, the removal efficiency was almost similar between 25 to 40 mg adsorbent dosages; the dose chosen going further was 25 mg.

### *4.3.2.3 The adsorption kinetics of $Ag^+$ removal*

The relationship between contact time and adsorbed $Ag^+$ ions at varying initial concentrations (50, 100, 150 mg/L) is shown in Figure 4-9a. The experimental result exposed that the longer time required for adsorption equilibrium with increasing the initial $Ag^+$ concentration. For example, at 50 mg/L $Ag^+$ initial concentration, it took 20 min for the system to reach equilibrium compared. However, for 100 and 150 mg/L $Ag^+$ concentration took 180 and 480 min, respectively to reach equilibrium adsorption condition. The adsorption process was initially rapid and steadily increased closer to reaching equilibrium condition. The fast adsorption at initial stage implies the ready availability of active sites on the $Fe_3O_4$@PPy-MAA NC surface.

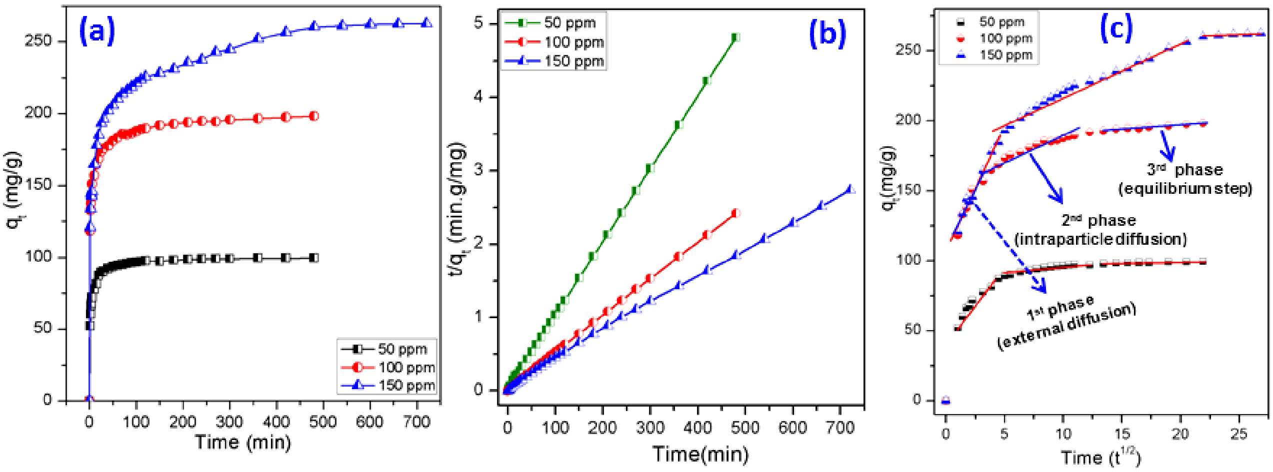

**Figure 4-9: Effect of contact time at (a) different initial concentrations, (b) linear plot of pseudo-second-order and, (c) intraparticle diffusion model of $Ag^+$ adsorption onto $Fe_3O_4$@PPy-MAA NC.**

The rate constants $k_1$ and $k_2$ of the two kinetics equations (pseudo-first-order and pseudo-second-order) were obtained from the slopes of linear plots of $\log(q_e-q_t)$ versus $t$ (Figure 4-10) and $t/q_t$ vs $t$ (Figure 4-9b), respectively. Table 4-2 summarises the calculated value of kinetics parameters $k$, $q_e$ and associated correlation coefficient $R^2$ initial $Ag^+$ concentration.

**Table 4-2: Kinetics parameters for $Ag^+$ adsorption onto $Fe_3O_4$@PPy-MAA NC.**

| Initial metal concentration ($C_0$)(mg/L) | Pseudo-first-order kinetic model | | | Pseudo-second-order kinetics model | | |
|---|---|---|---|---|---|---|
| | $k_1$(1/min) | $q_e$(mg/g) | $R^2$ | $k_2$(mg/g.min) | $q_e$(mg/g) | $R^2$ |
| 50 | $0.9 \times 10^{-2}$ | 18.5 | 0.7936 | $0.3 \times 10^{-3}$ | 99.9 | 0.9999 |
| 100 | $1.1 \times 10^{-2}$ | 41.6 | 0.8724 | $1.4 \times 10^{-3}$ | 198.1 | 0.9998 |
| 150 | $5.9 \times 10^{-2}$ | 100.8 | 0.9605 | $33.2 \times 10^{-3}$ | 264.5 | 0.9983 |

| | Weber-Morris model (Intraparticle diffusion model) | | | | | | | | |
|---|---|---|---|---|---|---|---|---|---|
| | Initial phase | | | Secondary phase | | | Third phase | | |
| $C_0$(mg/L) | $K_{ip1}$ | $C_1$ | $R^2$ | $K_{ip2}$ | $C_2$ | $R^2$ | $K_{ip3}$ | $C_3$ | $R^2$ |
| 50 | 9.58 | 47.12 | 0.9007 | 1.45 | 82.24 | 0.9503 | 0.21 | 95.04 | 0.8047 |
| 100 | 17.48 | 106.19 | 0.8798 | 3.04 | 157.35 | 0.9305 | 0.63 | 184.66 | 0.9674 |
| 200 | 18.32 | 108.57 | 0.9831 | 3.63 | 182.88 | 0.9859 | 0.68 | 249.19 | 0.9577 |

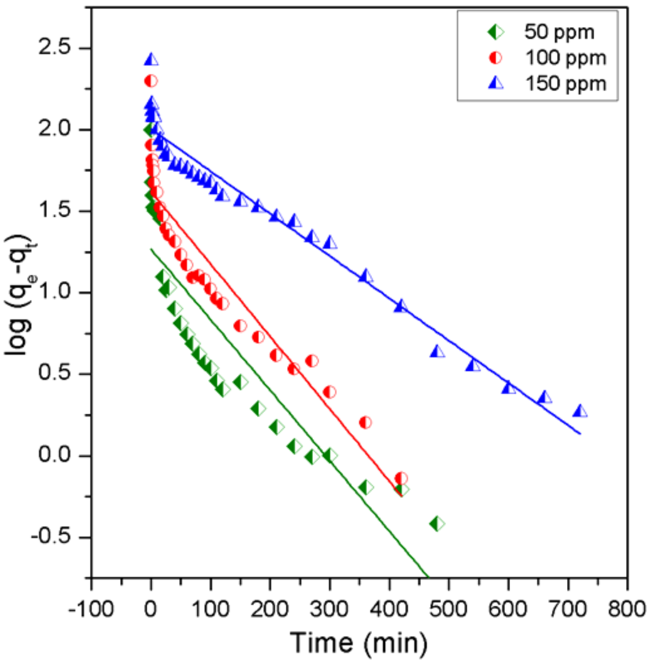

**Figure 4-10: Pseudo-first-order kinetics for $Ag^+$ adsorption on $Fe_3O_4$@PPy-MAA NC.**

The $R^2$ values of the pseudo-second-order rate equation were closer to 1(0.9983-0.9999) as compared to those of the pseudo-first-order rate equation (0.7936-0.9605) for all initial $Ag^+$ concentrations. The estimated $q_e$ (mg/g) values from pseudo-second-order kinetics were greater than those obtained from the pseudo-first-order equation. These experimental outcomes (Table 4-2) confirmed the suitability of the pseudo-second-order kinetics for describing the removal of $Ag^+$ ions from an aqueous medium. The adsorption data were further analysed to determine the rate-controlling step by Weber-Morris Intraparticle Diffusion model. It is clear from Figure 4-9c that the $Ag^+$ uptake process followed multilinear plots, suggesting that more than one step were involved in the mechanism of $Ag^+$ adsorption onto $Fe_3O_4$@PPy-

MAA NC surface. The first rapid step is characteristic of surface or film diffusion, whereby the $Ag^+$ ions moved towards the surface of the $Fe_3O_4$@PPy-MAA NC. The second region is attributed to the intraparticle diffusion of the $Ag^+$ ions, where gradual adsorption was observed. The third step describes the equilibrium phase of the adsorption study. The intraparticle diffusion parameters ($k_{id}$ and $C$) were calculated from the slope and intercept of the Weber-Morris intraparticle model (eq. 6), and the results are summarised in Table 4-2. The results (Table 4-2) indicate that both the linear steps (1st and 2nd) of the Weber-Morris intraparticle model did not pass through the origin, suggesting that intraparticle diffusion was not the only rate-limiting step of the whole $Ag^+$ adsorption process. Therefore, it can be concluded that both external diffusion, as well as intraparticle diffusion, are responsible for the adsorption of $Ag^+$ onto $Fe_3O_4$@PPy-MAA NC surface.

### *4.3.2.4 Equilibrium adsorption isotherms of $Ag^+$*

The effect of the initial $Ag^+$ concentration towards the adsorption efficiency and capacity at a fixed adsorbent dosage (0.5 g/L) is shown in Figure 4-11a. The adsorption capacity of the $Fe_3O_4$@PPy-MAA NC increased in proportion to the initial $Ag^+$ concentration and reached a plateau. On the other hand, adsorption efficiency decreased sharply with increasing initial $Ag^+$ ions concentration. The results (Figure 4-11a) indicate that the adsorption capacity of the magnetic NC was gradually enhanced from 99.5 to 653.7 mg/g with increasing initial $Ag^+$ concentrations of 50 to 600 mg/L, respectively. The increase in $Ag^+$ ions increased the driving force to which the ions could be attracted towards the adsorbent surface.

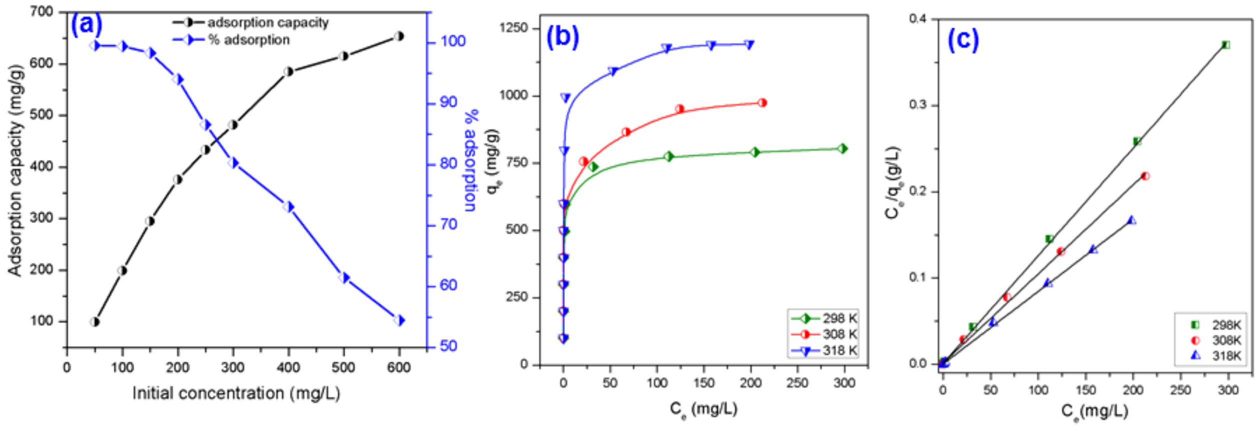

**Figure 4-11: (a) effect of initial metal concentration on the adsorption capacity of $Ag^+$ by the NC (b) adsorption equilibrium isotherms for removal of $Ag^+$ and fit of data to non-linear Langmuir and Freundlich isotherm models; (b) Fit of data to linearized Langmuir isotherm model.**

The effect of temperature on the adsorption of $Ag^+$ ions onto $Fe_3O_4$@PPy-MAA NC was investigated and the results are presented in Figure 4-11b. The adsorption isotherms studied were carried out at three different temperatures [298 (25°C), 308 (35°C) and 318 (45°C) K], with the initial $Ag^+$ concertation varied between 50 and 600 mg/L, at a constant adsorbent dosage of 0.5 g/L. The amounts of the $Ag^+$ taken up by the $Fe_3O_4$@PPy-MAA NC increased with an increase in $C_e$ and finally reached saturation. It was seen that the increase in temperature resulted in an increase in $Ag^+$ adsorption by the $Fe_3O_4$@PPy-MAA NC, indicating that the process was endothermic. Furthermore, increasing the temperature could have increased the driving force of the $Ag^+$ ions towards the surface active sites of the $Fe_3O_4$@PPy-MAA NC.

The relationship between the adsorbed $Ag^+$ ions per unit gram of adsorbent and the equilibrium $Ag^+$ concentration at a fixed temperature was studied using the Langmuir and Freundlich isotherm models (The details of the model is given in Appendix A). The favourability of the adsorption process is given by the dimensionless separation factor, $R_L$. The linear plots of two adsorption isotherm models (Langmuir and Freundlich) at three different temperatures (298, 308 and 318 K) and their fitting results are shown in Figure 4-11c, Figure 4-12a and Table 4-3, respectively.

**Table 4-3: Langmuir and Freundlich isotherm constants for $Ag^+$ adsoption onto the $Fe_3O_4$@PPy-MAA NC.**

| Temperature | Langmuir | | | | Freundlich | | |
|---|---|---|---|---|---|---|---|
| (K) | $q_m$ (mg/g) | b (L/mg) | $R_L$ | $R^2$ | $k_F$ (mg/g ) | 1/n | $R^2$ |
| 298 | 806.45 | 1.39 | 0.0035 | 0.9997 | 480.86 | 0.102 | 0.9428 |
| 308 | 975.6 | 1.07 | 0.0046 | 0.9980 | 571.60 | 0.121 | 0.7972 |
| 318 | 1191.9 | 0.64 | 0.0076 | 0.9996 | 606.86 | 0.146 | 0.7275 |

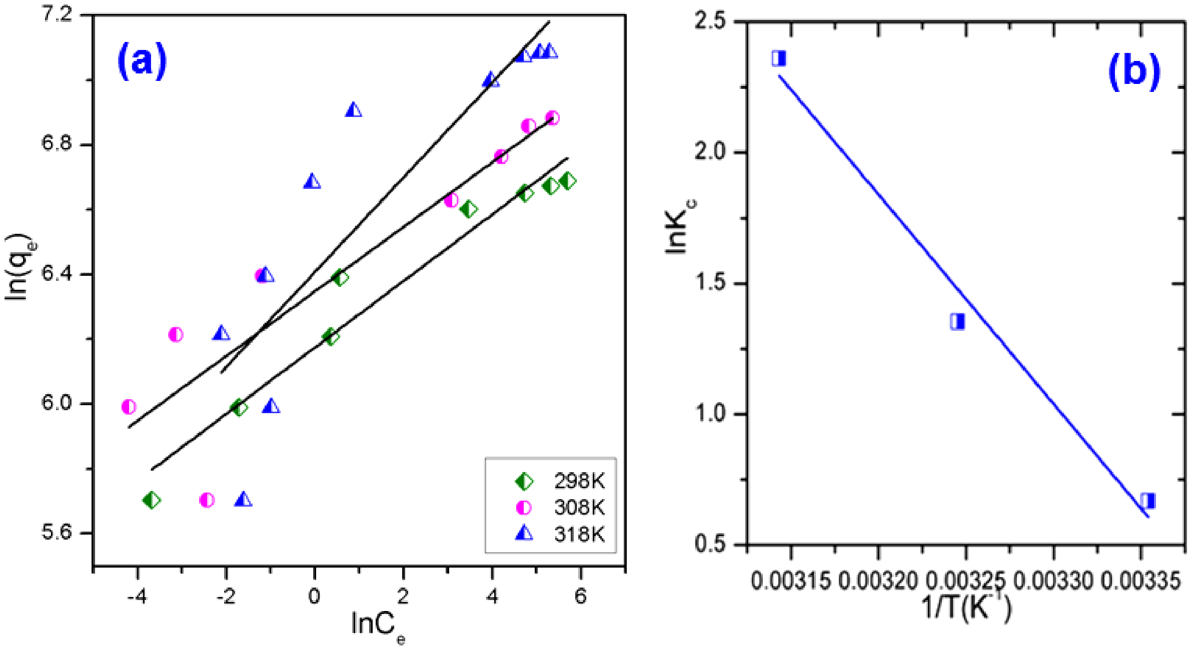

**Figure 4-12: (a) Freundlich adsorption isotherm of $Ag^+$ removal using $Fe_3O_4$@PPy-MAA NC and (b) Linear plot of $\ln K_c$ vs 1/T for thermodynamic properties of $Ag^+$ onto $Fe_3O_4$@PPy-MAA NC.**

The Langmuir isotherm could better describe the adsorption behaviour with higher correlation coefficients ($R^2 \approx 0.9998$, 0.9983 and 0.999) compared to those of the Freundlich isotherm ($R^2 \approx 0.6649$, 0.5241 and 0.6131). The Langmuir model assumes that the adsorption takes place on a homogenous surface of the adsorbent, with the active sites being uniform [42]. The maximum adsorption capacities increased from 806.45 to 1191.9 mg/g with an increase in temperature from 298 to 318 K, respectively. This indicates a better correlation between the experimental data and the Langmuir model, thus indicating that the adsorption process was homogenous with the formation of a monolayer on the surface of the adsorbent. The $R_L$ values also suggested that the adsorption process was favourable, with values being 0.0035, 0.0046 and 0.0076 for temperatures of 298, 308 and 318K respectively. Table 4-4 is a comparative table, which indicates the performance of the developed NC in comparison to other adsorbents that were synthesised for the removal of $Ag^+$ in aqueous solutions. It can be deduced from Table 4-4 that the $Fe_3O_4$@PPy-MAA NC is an effective adsorbent for the removal of $Ag^+$ ions from an aqueous medium in comparison to most of the reported adsorbents [42-49].

**Table 4-4: A comparison of adsorbent performance towards $Ag^+$ sorption.**

| Adsorbent | $q_m$ (mg/g) | Initial pH | Temperature (ºC) | Ref |
|---|---|---|---|---|
| Poly (Styrene-Alternative-Maleic Anhydride) nanoparticles | 75 | 6 | 25 | [43] |
| Verdelodo clay | 55.55 | - | 20 | [42] |
| Sulfoethyl functionalized silica nanoparticle | 21.9 | 6 | 25 | [44] |
| Magnetic Photocatalytic Ion-Imprinted Polymer | 35.475 | 6 | 25 | [45] |
| Halloysite nanotubes | 109.79 | 6 | 20 | [46] |
| Cliptonolite (Zeolite) | 33.23 | 4 | 25 | [47] |
| 4-vinyl pyridine -N,N-ethylene bisacrylamide | 75.64 | 6.5 | 25 | [48] |
| 1-vinyl imidazole-N,N-ethylene bisacrylamide | 74.18 | 6.5 | 25 | [48] |
| Carbon nanospheres | 152 | - | 25 | [49] |
| $Fe_3O_4$@PPy-MAA | 833.33 | 5.63 | 25 | This study |

### *4.3.2.5 Adsorption thermodynamics*

To understand the spontaneity as well as the detailed information about the internal energy changes during adsorption process, thermodynamic analysis was carried out using Van't Hoff equation (Appendix A). From the thermodynamic study, $\Delta H$ and $\Delta S$ were obtained from the slope and intercept of the linear Van't Hoff plots of ln $K_c$ vs 1/T shown in Figure 4-12b.

**Table 4-5: Thermodynamic properties of $Ag^+$ adsorption onto $Fe_3O_4$@PPy-MAA NC.**

| Temperature (K) | *ΔG* (KJ/mol) | *ΔH* (KJ/mol) | *ΔS* (KJ/mol.K) | $R^2$ |
|---|---|---|---|---|
| 298 | -1.656 | | | |
| 308 | -3.469 | 24.54 | 0.22 | 0.9839 |
| 318 | -6.241 | | | |

The parameters were calculated using eq S7 and eq S8 and are presented in Table 4-5. The positive *ΔH* (24.54 KJ/mol) and negative *ΔG* values (-1.65 to -6.24 KJ/mol) suggest that the adsorption of the $Ag^+$ onto the $Fe_3O_4$@PPy-MAA NC was endothermic and spontaneous [50]. The gradual decrease in *ΔG* values with rising temperatures also indicates that the adsorption spontaneity increased with increasing temperature (Table 4.5 [51]. A positive *ΔS* value (0.22 kJ/mol. K) means that the $Fe_3O_4$@PPy-MAA NC had an affinity for $Ag^+$, which also infers to the increased randomness at the solvent-solute interface [43].

### *4.3.2.6 Effect of co-existing ions*

The selectivity of $Fe_3O_4$@PPy-MAA NC was tested by studying the effect of co-existing ions in Figure 4-13. Nickel, cobalt and copper ions were mixed including silver ions with same concentration (200 mg/L) in an aqueous solution to test the uptake efficiency of $Fe_3O_4$@PPy-MAA NC for different metal ions. The competiveness of these co-existing ions for the removal of $Ag^+$ ions was shown in Figure 4-13. The experimental results exhibited superior adsorption efficiency (98.7%) of developed magnetic nanocomposite towards removal of $Ag^+$ ions in compare to other metal ions ($Ni^{+2}$, $Co^{+2}$ and $Cu^{+2}$). The developed nanocomposite showed very less adsorption efficiency 15, 12 and 2% for the removal of $Ni^{+2}$, $Co^{+2}$ and $Cu^{+2}$ ions, respectively. The relative high adsorption efficiency of $Fe_3O_4$@PPy-MAA NC may be arising due to the presence of thiol group into the nanocomposite which has strong affinity towards binding the silver ions.

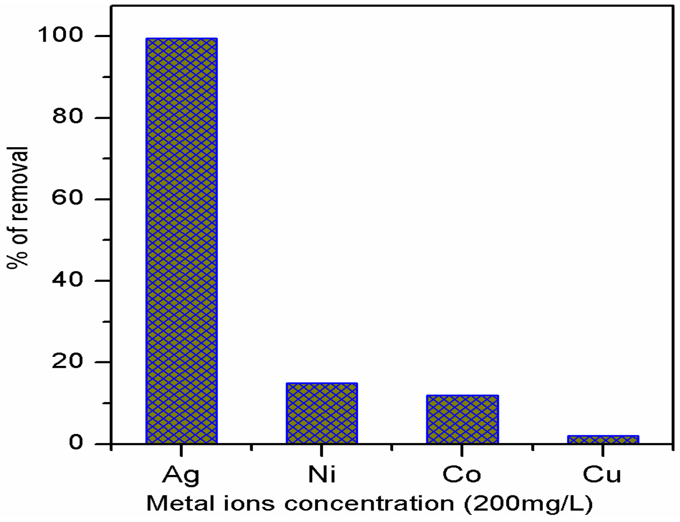

**Figure 4-13: Effect of co-existing ions on adsorption of $Ag^+$ ions**

#### *4.3.2.7 Adsorption mechanism*

According to the above characteristic evidence, the adsorption of $Ag^+$ onto the $Fe_3O_4$@PPy-MAA NC surface generally proceeds through physical adsorption followed by complex/redox adsorption [51]. At the initial stage, the physical adsorption occurred through an electrostatic interaction between positive $Ag^+$, with electron-rich nanocomposite functionalities (-SH, COO-, -NH). Heavy metal ions like $Ag^+$, with high standard reduction potential, could be readily reduced to their metallic state ($Ag^0$) in the presence of electron rich polymers, followed by -SH, COO- and -NH groups through the complex/redox adsorption. The effect of pH (Figure 4-8a) showed maximum adsorption efficiency at pH=5.6, which correlates with the zeta potential value of the NC (Figure 4-8b), indicating the maximum physical interaction between the negative surface charge of the NC and the positive $Ag^+$ ions. To provide further evidence for the generation of silver nanoparticles through redox adsorption mechanism, X-ray diffraction and TEM analysis of the $Fe_3O_4$@PPy-MAA NC were carried out after the adsorption of $Ag^+$ ions from the aqueous solution. Compared with the XRD pattern of the $Fe_3O_4$@PPy-MAA NC, the silver-adsorbed NC ($Fe_3O_4$@PPy-MAA/Ag) exhibited face-centred cubic (FCC) metallic $Ag^0$ crystals having five sharp diffraction peaks at 37.8, 44.1, 64.4, 77.3 and 81.4°, exactly belonging to the (111), (200), 220), (311) and (222) crystal planes of silver, respectively. In the typical TEM micrograph (Figure 4-3b) of the $Fe_3O_4$@PPy-MAA/Ag, the Ag NPs were decorated on the magnetic NC. The high-resolution TEM image (Figure 4-3c) showed the lattice fringes of $Ag^0$ together with magnetic $Fe_3O_4$ NPs on the adsorbent surface, which was an indication of the formation of metallic $Ag^0$ after surface adsorption. Therefore, it can be concluded from the above results that silver ions can be successfully removed from an aqueous medium through surface physical adsorption and subsequent reduction of $Ag^+$ to metallic silver ($Ag^0$) onto the NC is the major adsorption mechanism.

To further explore the adsorption mechanism, the binding energy of the elements (C 1s, S 2p, O 1s, N 1s and Ag 3d) was calculated from the XPS analysis. The full survey scan spectra and high resolution XPS spectra of various elements present in $Fe_3O_4$@PPy-MAA and $Fe_3O_4$@PPy-MAA/Ag composite was shown in the Figure 4-14. The survey scans spectrum of $Fe_3O_4$@PPy-MAA (Figure 4-14a) displayed clear signals of S 2p, C 1s, N 1s and O 1s at 164, 284, 400 and 530 eV, respectively. Along with all the above energy signals, the presence of Ag 3d energy peak at 368 eV in the survey scan of $Fe_3O_4$@PPy-MAA/Ag confirmed the successful adsorption of $Ag^+$ ion and reduction to its metallic Ag Nps onto the composite surface. The deconvolution of the high resolution XPS spectrum of Ag 3d exhibited two peaks at binding energy 368.1 eV and 374.1 eV (Figure 4-14b) with spin-orbit splitting of 6.0 eV for Ag $3d^{5/2}$ and Ag $3d^{3/2}$, respectively [28]. In Figure 4-14c, the high-resolution XPS spectrum of C 1s showed the characteristic binding energy at 283.7, 284.8, 286.2, 287.6 and 288.8 eV due to presence of -C-H, -C-C, -C-N/-C-O/-C-S, -C=O and O=C-O binding environment, respectively [52]. The high resolution XPS spectra of S 2p (Figure 4-14(i)) showed two deconvoluted peaks at 163.2 and 164.1 eV for S $2p^{3/2}$ and S $2p^{1/2}$, respectively. Additionally, the sulphur attributed to -C-SOx is observed at 167.6 eV [30]. After $Ag^+$ ions adsorption (Figure 4-14d(ii)) the S $2p^{3/2}$ and S $2p^{1/2}$ signal shifted to lower energy value at 162.4 and 163.5 eV, respectively and signal intensity also decreased significantly. Therefore, S atom has a definite role for the adsorption of the $Ag^+$ ion from the medium. Figure 4-14e exposed the three major energy peaks of the O 1s atom located at 531.0, 532.1 and 533.4 eV, are corresponded to oxygen of oxide ($O^{2-}$), -C-O and O-C=O, respectively [31].

Figure 4-14f showed the binding energy peak of polypyrrole ring N at 399.6 eV and after $Ag^+$ adsorption the peak intensity decreased significantly which also confirmed that the polypyrrole matrix plays a vital role to adsorb $Ag^+$ ions onto its surface.

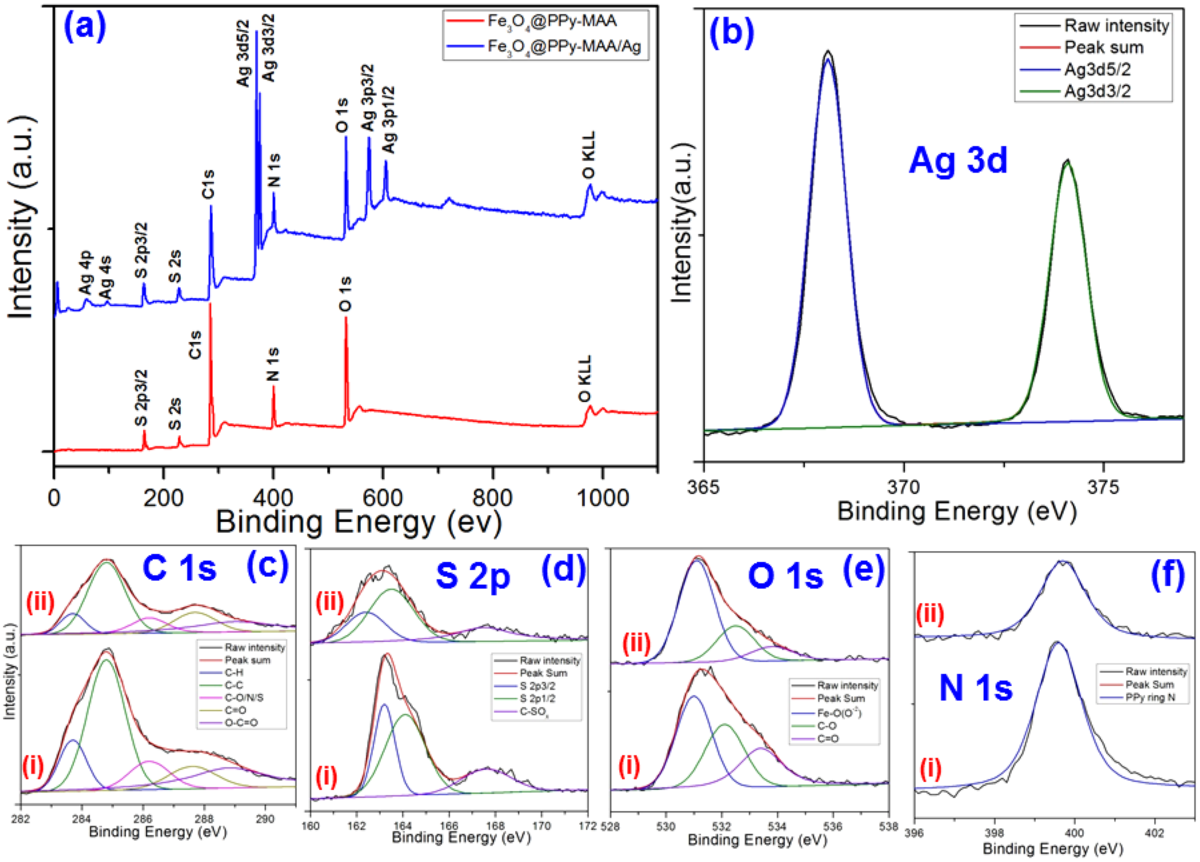

**Figure 4-14: (a) XPS total spectral survey of $Fe_3O_4$@PPy-MAA and $Fe_3O_4$@PPy-MAA/Ag; high resolution spectra of (b) Ag 3d (c) C 1s (d) S 2p, (e) O 1s and (f) N 1s of (i) $Fe_3O_4$@PPy-MAA, (ii) $Fe_3O_4$@PPy-MAA/Ag, respectively.**

### 4.3.3 Applications of post adsorbed Ag-loaded $Fe_3O_4$@PPy/MAA

#### *4.3.3.1 Catalytic reduction of p-nitrophenol (4-NP) using $Fe_3O_4$@PPy-MAA/Ag NC*

To evaluate the catalytic activity of the prepared $Fe_3O_4$@PPy-MAA/Ag NC, the reduction of 4-NP has been chosen as a model reaction in the presence of excess $NaBH_4$. The reduction experiments were studied at 25°C using different catalyst dosages (1.0 to 7.5 mg), 25 mL of 1 mmol aqueous 4-NP solution and 2.5 mL of freshly prepared $1×10^{-1}$M $NaBH_4$. The progress of the catalytic reduction was monitored by the UV-vis absorption spectroscopy. During experiment, after addition of freshly prepared $NaBH_4$ solution the maximum UV absorption of aqueous solution of 4-NP shifted with higher intensity from 318 to 400 nm. The initial colour change (light to intense yellow) associated with red shift after addition of the $NaBH_4$ solution is certainly attributed to the formation of 4-nitrophenolate ion with more pronounced π-conjugated donor-acceptor property [51]. Interestingly, the UV absorption peak of 4-NP at 400 nm and bright yellow colour disappeared with the addition of $Fe_3O_4$@PPy-MAA/Ag catalyst after a certain time interval. The progress of the reaction is further confirmed by the appearance, as well as gradual increase in the intensity of a new peak at 300 nm, due to the formation of 4-AP.

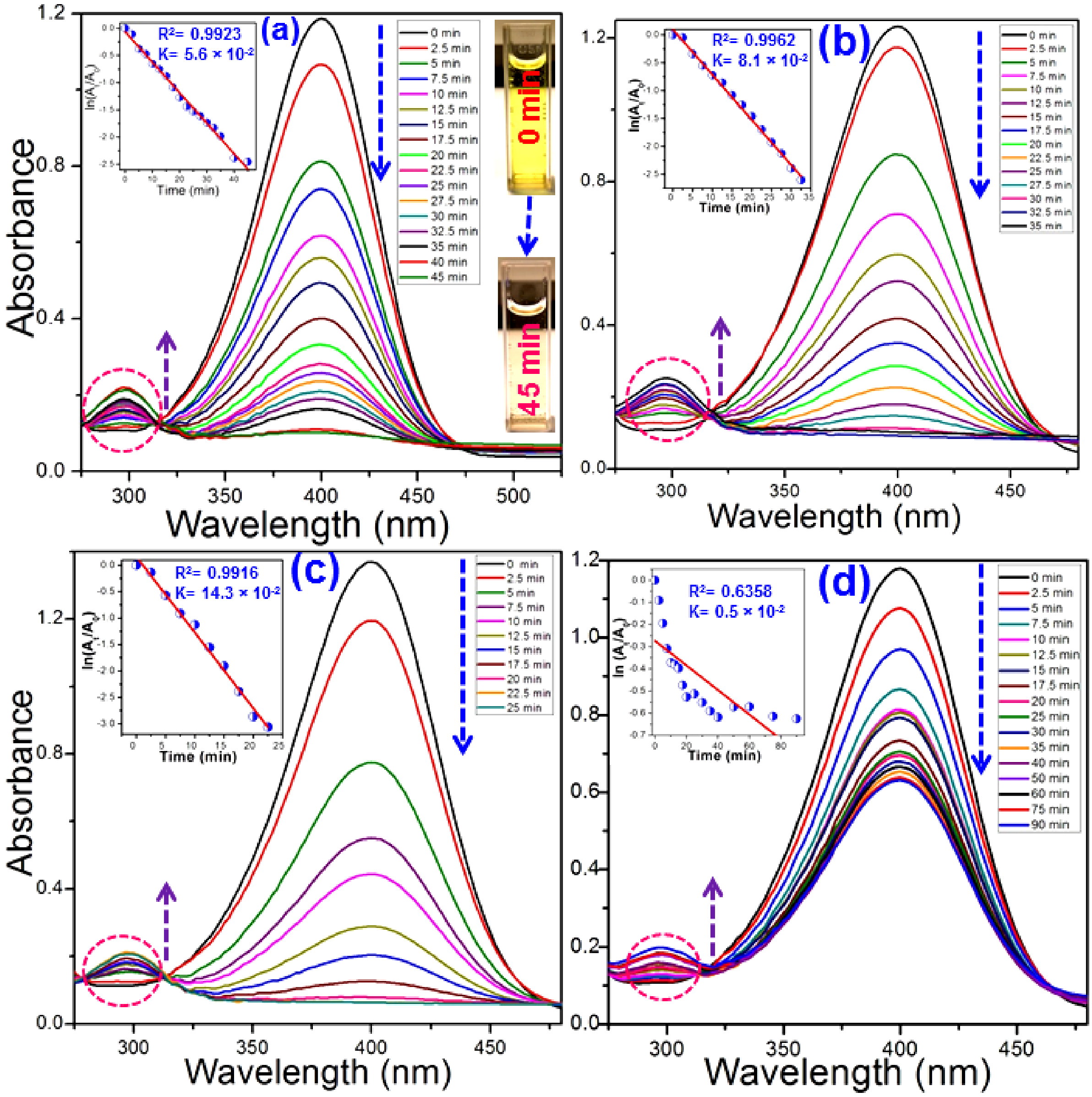

**Figure 4-15: Time dependent UV-vis spectra for the reduction of 4-nitrophenol and inset shows the plot of ln($A_t$/$A_0$) vs time in presence of different amount of catalyst (a) 1 mg (b) 2.5 mg, (c) 5.0 mg and (d) 7.5 mg.**

It is clear that with increasing catalyst dosage in the reaction medium, the time required for the conversion of 4-NP to 4-AP decreased. In the presence of 2.5 mg $Fe_3O_4$@PPy-MAA/Ag complete reduction of 4-NP was achieved within 45 min of reaction time period with noticeable change of colour from bright yellow to colourless (Figure 4-15.15a). Under the same reaction conditions (25 mL of 1 mmol 4-NP aqueous solution at 25°C), using 5.0 and 7.5 mg of silver loaded catalyst, the time required for the transformation of 4-NP to 4-AP was found to be 35 and 25 min, respectively (Figure 4-15.15b and c). However, at very low catalyst concentration (1.0 mg/27.5 mL), the reaction was not completed after 90 min (Figure 4-15.15d). The linear correlation between $\ln(A_t/A_0)$ and reaction time (t) under diverse operation procedure is shown in Figure 4-16.

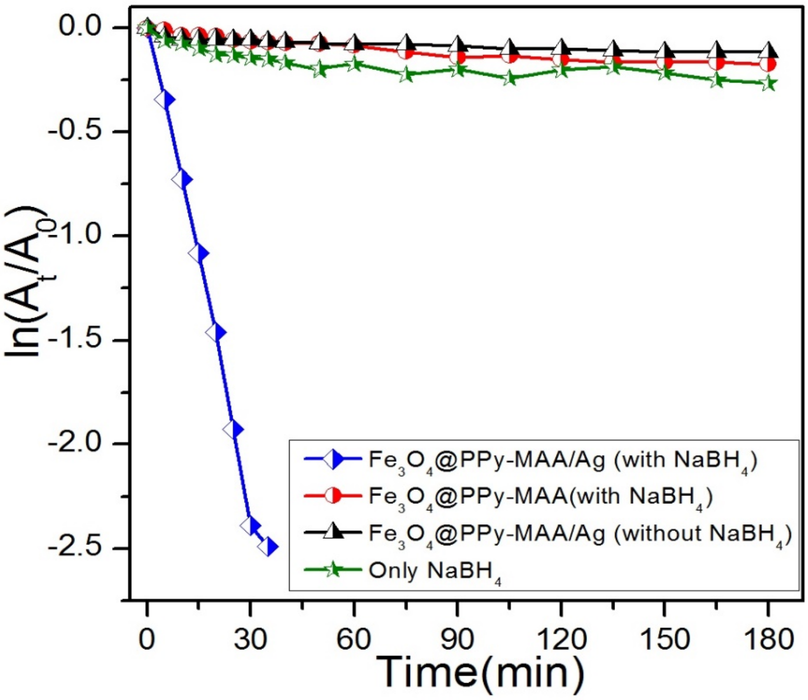

**Figure 4-16: Kinetics result of 4-nitrophenol reduction in various reaction conditions.**

The absence of catalyst, in the presence of $NaBH_4$, the absorption peak of 4-NP at 400 nm remains almost unaltered after 180 min. Likewise, when performed in the presence of catalyst and without $NaBH_4$ as reducing agent, the progress of 4-NP reduction was very difficult. These events indicate that the presence of both catalyst and reducing agent ($NaBH_4$) are indispensable for the development of the reaction. The $Fe_3O_4$@PPy-MAA adsorbent was equally tested for possible catalytic activity in the presence of $NaBH_4$ under similar conditions as described for $Fe_3O_4$@PPy-MAA/Ag. It was observed that absorption peak intensity at 400 nm remains nearly unchanged to that of initial 4-NP after 180 min reaction time. Therefore, Ag NPs played a key role for $-NO_2$ transformation.

As excess amount of $NaBH_4$ was employed for the catalytic reduction of 4-NP, the pseudo-first-order kinetics can be considered as a most appropriate equation to evaluate the rate constant of the reaction [28, 51-52]. The apparent rate coefficients were obtained using the following equation:

$$\ln\frac{C_t}{C_0} = \ln\frac{A_t}{A_0} = -kt \qquad (6)$$

where $C_0$ and $C_t$ are the concentration of 4-NP at time t = 0 and t = t, values related to the absorbance of 4-NP, $A_0$ and $A_t$, respectively. The rates of the reaction were quantitatively determined from the slopes of the linear plots of $\ln(A_t/A_0)$ against time (t), as shown in Figure 4-15(a-d) inset. It is obvious that the insets in Figure 4-154.15(a-c) show good linear correlations for the catalytic reduction of 4-NP using 2.5, 5.0 and 7.5 mg of $Fe_3O_4$@PPy-MAA/Ag catalyst. Moreover, increased mass of catalyst led to an improved reduction rate. The estimated pseudo-first-order rate constants were 0.5 × $10^{-2}$, 5.6 × $10^{-2}$, 8.1 × $10^{-2}$ and 14.3 × $10^{-2}$ min.$^{-1}$ for the reduction of 4-NP using 1.0, 2.5, 5.0 and 7.5 mg of $Fe_3O_4$@PPy-MAA/Ag NC, respectively.

### *4.3.3.2 Antimicrobial activity of silver adsorbed waste material*

The application of used adsorbent is of paramount importance, especially in adsorption technology. Thus, the antimicrobial activity of the $Fe_3O_4$@PPy-MAA/Ag NC was evaluated, using *E. coli* as the indicator bacterium (Figure 4-17). The chosen magnetic NC were from these adsorption conditions: 200 mg/L $Ag^+$ solution, 0.5 g/L NC, solution pH 5.63, 25°C, whereby the $Ag^+$ loading was 29 wt% (measured with ICP-MS). The initial *E. coli* concentration was kept at 1 x $10^7$ CFU/mL whilst varying NC dosage (50-200 mg). The effect of the $Fe_3O_4$@PPy-MAA/Ag NC dosage on the antimicrobial activity is shown in Figure 4-17.17a. The controls consisted of the pristine $Fe_3O_4$@PPy-MAA NC ($S_0$) and *E. coli* in sterilised deionised water. It was observed that the bacterial growth inhibition increased with an increase in the NC dose. Following exposure of *E. coli* cells to 100 mg of NCs, the concentration was reduced to 1.4 × $10^3$ CFU/mL, within 60 min.

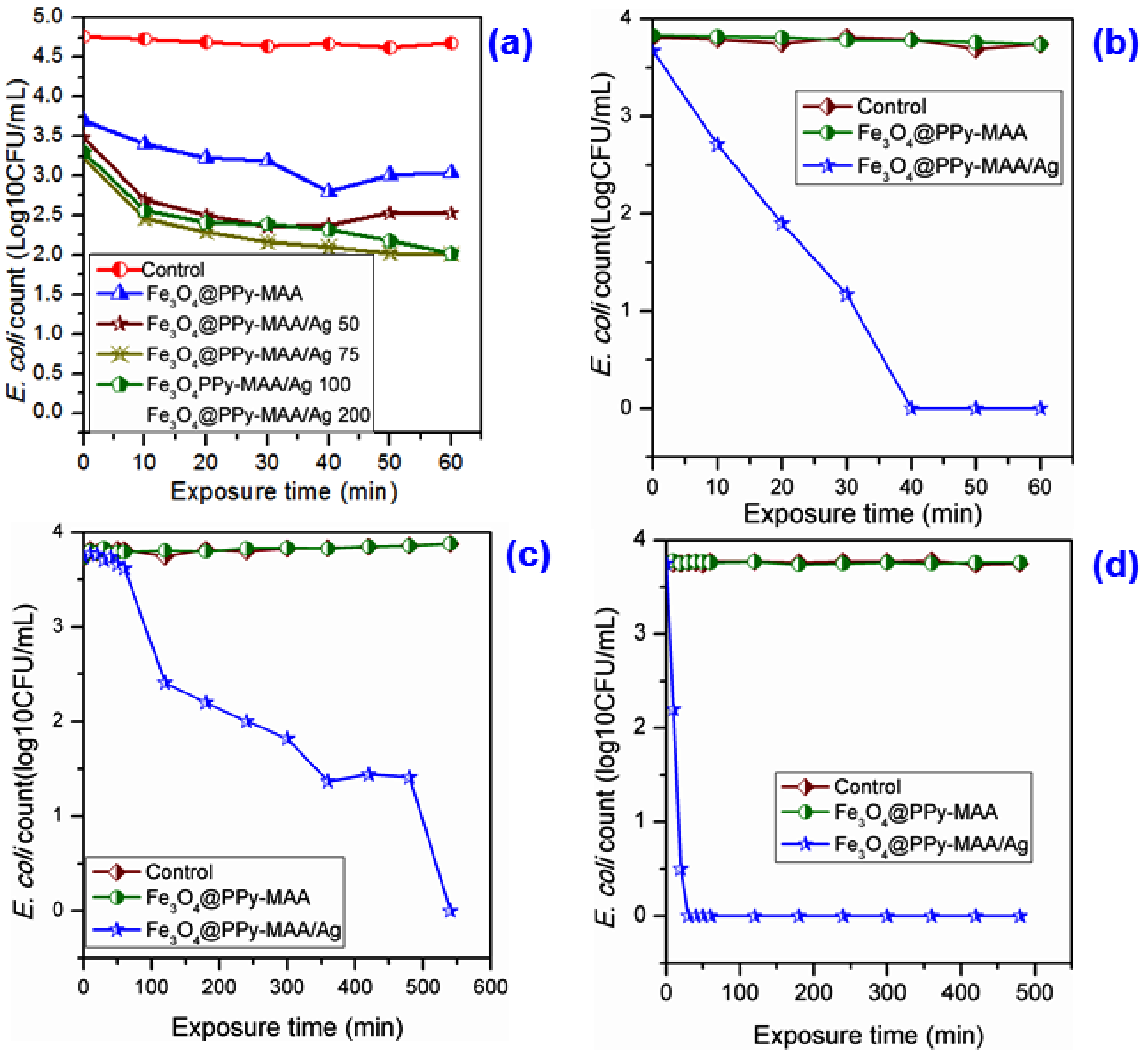

**Figure 4-17: Graphical representation of *E. coli* disinfection of (a) $Fe_3O_4$@PPy-MAA/Ag dose optimization; and *E. coli* disinfection in different water types: (b) synthetic water; (c) river water; and (d) ground water.**

The antimicrobial effect was seen to reach saturation at 200 mg NC dose. This could have been due to the *E.coli* attaching to the surface of the NC, inhibiting the release of elemental $Ag^+$ from the Ag NPs that are embedded on the NC surface [32]. Following the dose optimisation, the initial *E. coli* concentration in sterile deionised water (Figure 4-17.17b) was of ~6 × $10^3$ CFU/mL, and complete growth inhibition was observed after 30 min exposure. These results suggest that the disinfection time was concentration dependent; however the bactericidal effect of the NC was not compromised.

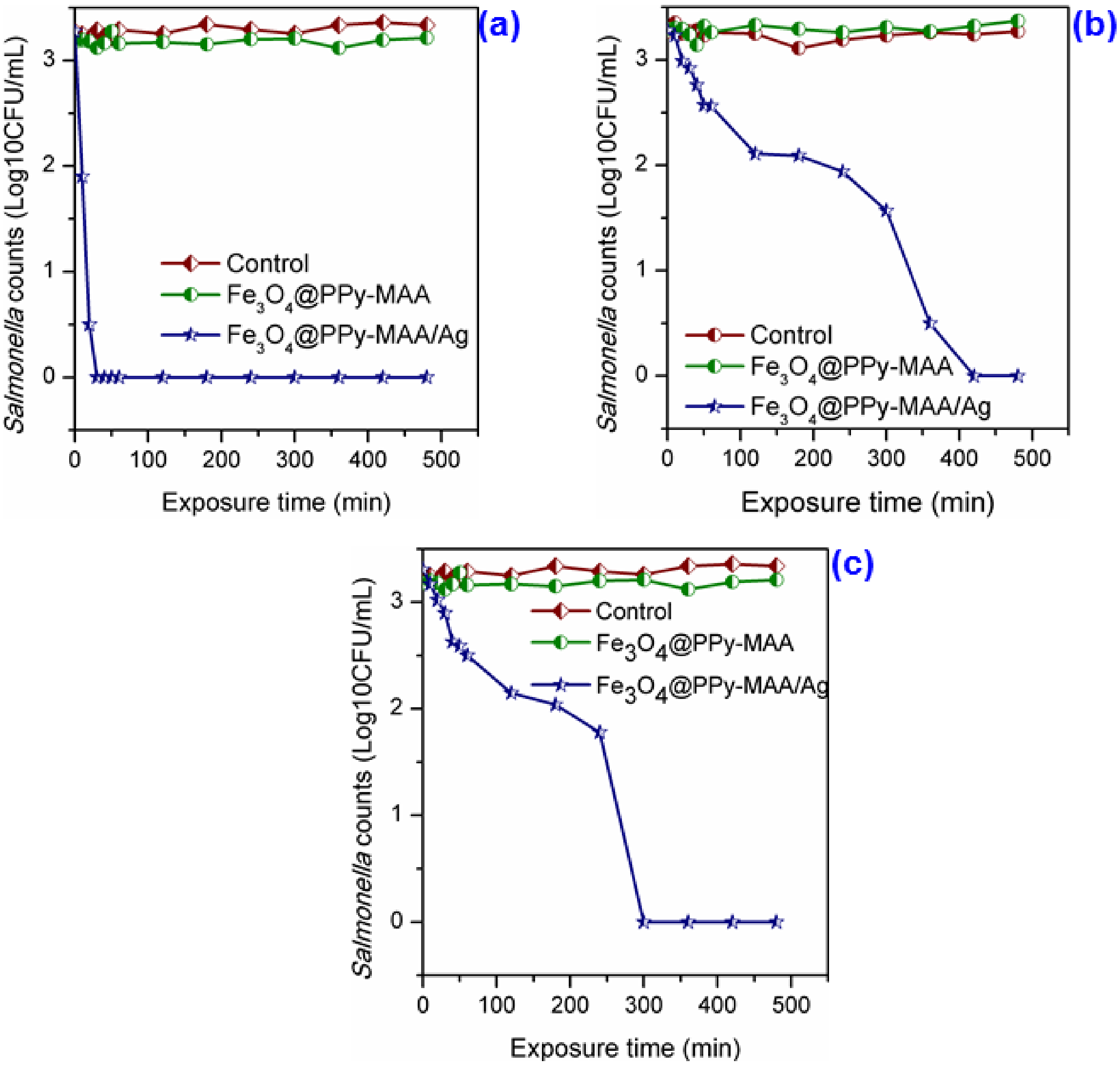

**Figure 4-18: Graphical representation of *Salmonella* disinfection of (a) synthetic water, (b) river water and (c) ground water, using $Fe_3O_4$@PPy-MAA/Ag.**

The bactericidal properties of $Fe_3O_4$@PPy-MAA/Ag NC were also tested on *Salmonella S.P* and the results are shown in Figure 4-18. *Salmonella*-spiked water (20mL), with an initial concentration of the *Salmonella* was ~2 × $10^3$ CFU/mL, was treated with 100 mg of $Fe_3O_4$@PPy-MAA/Ag NC. It was observed that complete growth inhibition occurred within the first 30 min of treatment with $Fe_3O_4$@PPy-MAA/Ag NC (Figure 4-18a). The control concentrations remained unchanged, thus also attributing the disinfection to the Ag-loaded NC. The antimicrobial activity of the $Fe_3O_4$@PPy-MAA/Ag NC was also tested using river and groundwater (borehole) collected from Pretoria North, Gauteng Province, South Africa. The water was characterised and the following specifications were established: river water – pH: 7.10 ± 0.01, total coliform count: 390 CFU/100 mL and *E. coli*: 38 CFU/100 mL; groundwater (borehole) – pH: 6.40 ± 0.01, total coliform count: 0 CFU/100 mL, *E. coli*: 0 CFU/100 mL. The river and borehole water were sterilised by autoclaving and then inoculated with *E. coli* to make up an initial concentration of ~6 × $10^3$ CFU/mL. 100 mg of $Fe_3O_4$@PPy-MAA/Ag NC (29% Ag-loaded) was used. The river water studies showed that there was a gradual decrease in bacterial growth over a period of 9 h (Figure 4-17.18c). The results obtained from testing the groundwater (borehole) showed that bacterial growth inhibition took place much faster than that of river water. Total growth inhibition was observed at 40 min (Figure 4-17.18d). This could be attributed to the less complex matrix of groundwater (borehole) water when compared to that of river water.

The testing of real field water samples continued, varying the bacterial species. River and ground water were spiked with ~2 x $10^3$ CFU/mL of *Salmonella* and treated with 100 mg of $Fe_3O_4$@PPy-MAA/Ag NC. In river water (Figure 4-18.18b), there was a gradual decrease in Salmonella cells as the exposure time increased, until complete growth inhibition was observed after 400 min. A similar trend was observed with groundwater, except that there was a sharp decrease in Salmonella cells between 200 and 300 min (Figure 4-18.18c). The prolonged disinfection in real water samples, compared to synthetic water, could be due to the complexity of real water samples such as turbidity and other components present in real water. It was also noted that the adsorption of $Ag^+$ was performed in clean water sources and that in real samples, there may be a more complex matrix, leading to a decrease in the NC's performance. This will be addressed in the follow up study, whereby real industrial samples are treated with $Fe_3O_4$@PPy-MAA.

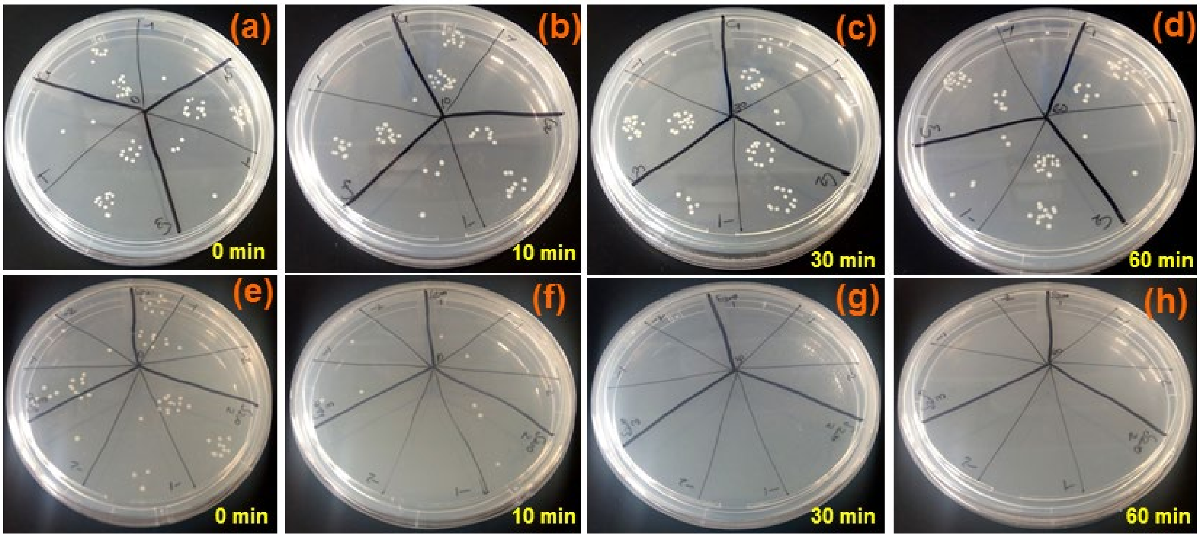

**Figure 4-19: Photographs of *E. coli* colonies incubated on nutrient agar plates obtained from inoculated suspensions with [(a)-(d)] Control (C1, C2, C3) and [(e)-(h)] $Fe_3O_4$@PPy-MAA/Ag 200 ($S_1$200, $S_2$200, $S_3$200) films.**

The pictorial evidence of the bactericidal properties of $Fe_3O_4$@PPy-MAA/Ag NC is shown in Figure 4-19. It is noted that the $Ag^+$, in this study, is primarily removed from clean water sources and in real samples there may be a more complex matrix, leading to a decrease in the NC's performance. This will be addressed in the follow up study, whereby real industrial samples are treated with $Fe_3O_4$@PPy-MAA and further disinfection is tested.

#### 4.3.3.3 *Catalytic reduction and/or removal of organics*

As the prepared $Fe_3O_4$@PPy-MAA/Ag NC exposed excellent catalytic behaviour for the reduction of 4-NP, the next step was to examine the performance of the NC towards the degradation of hazardous organic dyes. To investigate the catalytic degradation activity of the developed NC, methyl orange (MO) was initially chosen as a model organic dye. The study was performed using $NaBH_4$ as a reducing agent. The progress of the MO catalytic degradation process was monitored with a change in intensity of the UV absorption peak at $\lambda_{max}$ = 464 nm [53,30]. The time dependent change in the deep orange colour of the solution, concomitant with the modification in the absorption spectrum of MO is shown in Figure 4-20(a-d).

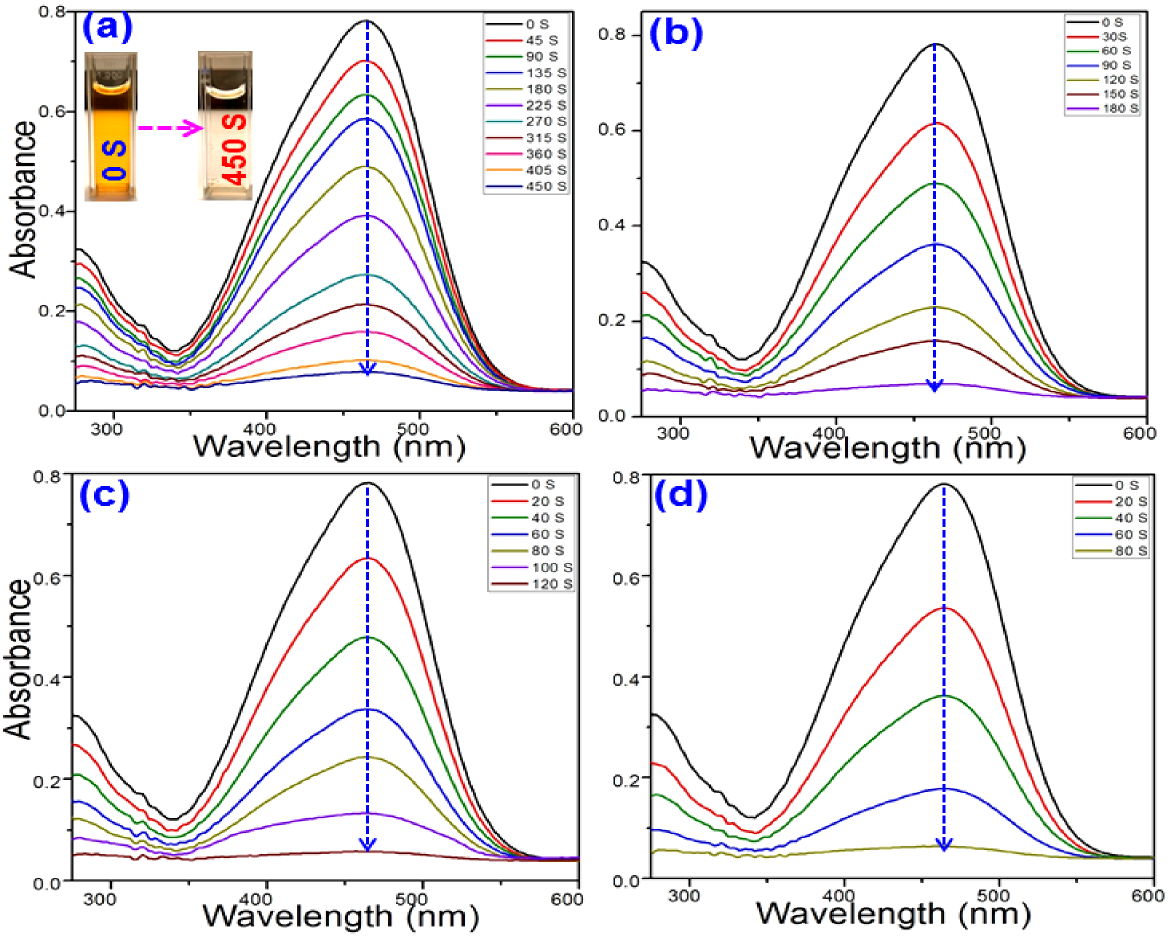

**Figure 4-20: UV-vis absorption spectral changes for the reduction of MO dye by $NaBH_4$ at various time intervals in the presence of (a) 1.0 mg (b) 2.0 mg, (c) 4.0 mg and (d) 5.0 mg $Fe_3O_4$@PPy-MAA/Ag catalyst.**

The complete decolourisation of MO dye occurred within 450 to 80 second with increasing amount of $Fe_3O_4$@PPy-MAA/Ag (1.0 to 5.0 mg) in different catalytic reaction conditions. The rate constants (k) for the degradation of MO dye using different operation procedure were also derived from the pseudo-first-order kinetics. From the linear graphs of ln($C_t/C_0$) vs degradation time (Figure 4-21(a-d)), the rate constant was found to be 0.52 × $10^{-2}$ $S^{-1}$ when using 1.0 mg catalyst dosage. However, the estimated rate constant values were 10.7 × $10^{-2}$, 17.3 × $10^{-2}$ and 24.2 × $10^{-2}$ $S^{-1}$ for the degradation study of MO when exposed to

2.0, 4.0 and 5.0 mg $Fe_3O_4$@PPy-MAA/Ag NC, respectively. To gain insight into the catalytic efficiency of $Fe_3O_4$@PPy-MAA/Ag, a correlation study (variation of In($A_t$/$A_0$) over a time period of 60 min was carried out by altering both the catalyst and reducing agent. Practically, null degradation of MO was experienced with no reductant, as represented in Figure 4-21e (green line). In the presence of $NaBH_4$ and with no Ag NPs deposition, a very slow MO degradation was observed after 60 min, as revealed by the red plot. Likewise, the use of reductant only did not achieve significant MO degradation, relative to a combine application of Ag deposited on $Fe_3O_4$@PPy-MAA NC and $NaBH_4$. Therefore, $Fe_3O_4$@PPy-MAA/Ag NC has a significant catalytic effect for the degradation of MO dye due to presence of Ag NPs at the surface.

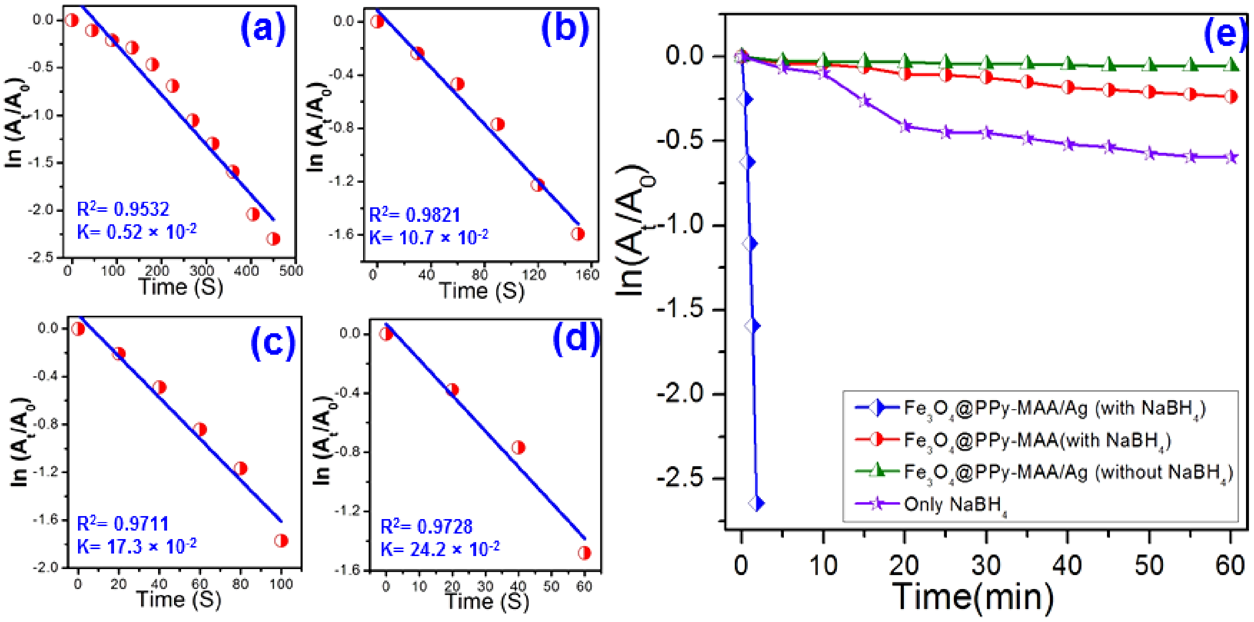

**Figure 4-21: In($A_t$/$A_0$) versus reaction time for reduction of MO in presence of $Fe_3O_4$@PPy MAA/Ag catalyst a) 1.0 mg (b) 2.0 mg, (c) 4.0 mg and (d) 5.0 mg; (e) Kinetics result for the reduction of MO**

The catalytic efficiency of the prepared Ag deposited NC was as well considered for the reduction of methylene blue (MB) in aqueous solution. For this study, 25 mL of 1× $10^{-4}$ M MB solution was treated with the prepared catalyst and reducing agent ($NaBH_4$). The change in UV-vis absorption maxima at λmax = 664 nm was employed to monitor the entire reduction process.

Figure 4-22 displays a series of UV-vis absorption spectra at various time (s) intervals for the degradation of MB using different amount of $Fe_3O_4$@PPy-MAA/Ag catalyst.

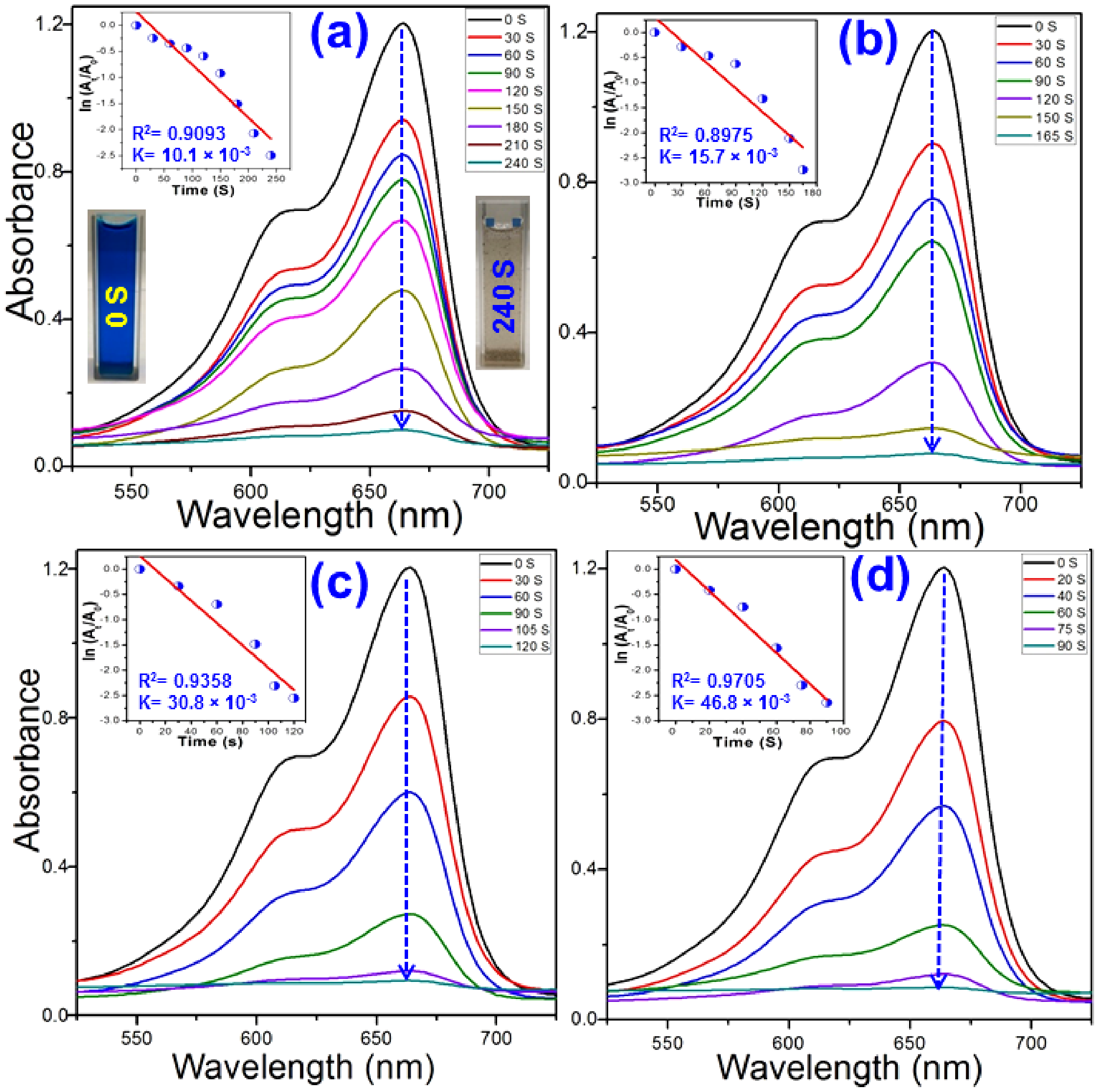

**Figure 4-22: Time dependent UV-vis spectra for the reduction of MB with the amount of (a) 1.0 mg (b) 2.0 mg, (c) 4.0 mg and (d) 5.0 mg catalyst. Inset shows the corresponding plot of ln($A_t$/$A_0$) vs reaction time (t).**

With the progress of the reduction, the characteristic peak (λmax = 664 nm) intensity was found to drop remarkably and nearly disappeared within 4 minutes. Figure 4-22(a-d) indicates that less time (s) was required for complete disappearance of the intense blue colour (MB) to colourless leuco-methylene blue (LMB) when using higher amount of catalyst [31-32]. Loadings of 1.0, 2.0, 4.0 and 5.0 mg $Fe_3O_4$@PPy-MAA/Ag catalysts effect complete decolourisation within 240, 165, 120 and 90 s, respectively. The rate constants of the reduction kinetics were also calculated from the linear plot of ln($A_t$/$A_0$) *vs* reduction time (t), and these are presented in the inset of Figure 4-22(a-d). These values were 10.1 × $10^{-3}$, 15.7 × $10^{-3}$, 30.8 × $10^{-3}$ and 46.8 × $10^{-3}$ $S^{-1}$ for the MB reduction using 1.0, 2.0, 4.0 and 5.0 mg of catalyst, respectively.

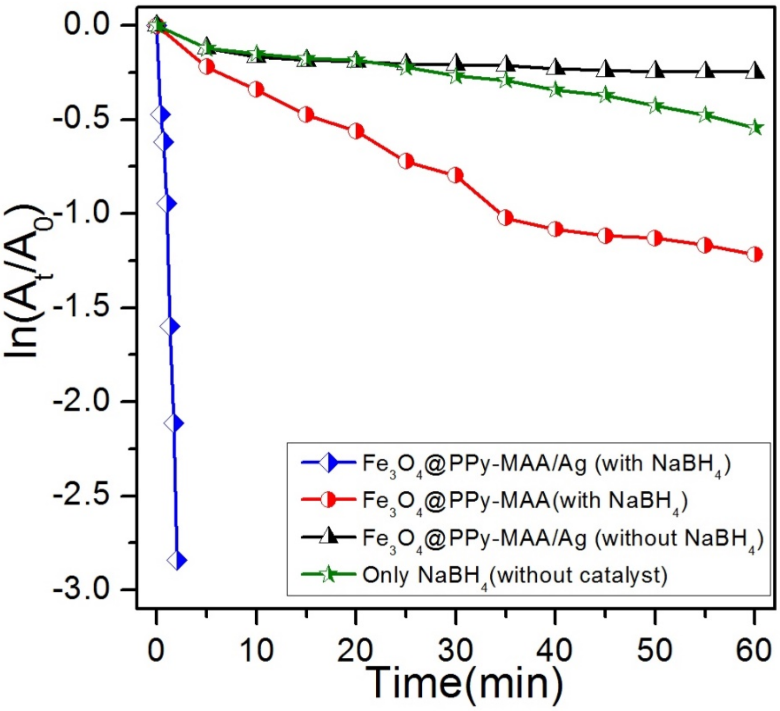

**Figure 4-23: Kinetics result of MB reduction in various reaction conditions.**

Moreover, the reduction of MB was found to proceed in a similar manner than that of MO, when varying both the catalyst and reductant, as shown in the correlation of $\ln(A_t/A_0)$ against reduction time (Figure 4-23). After 60 min of exposure time, there was no major change in the characteristic absorption peak of MB, with only $NaBH_4$ (no $Fe_3O_4$@PPy-MAA/Ag catalyst) or $Fe_3O_4$@PPy-MAA/Ag, exclusively (no $NaBH_4$). A plausible catalytic reduction pathway has been discussed before.

#### *4.3.3.4 Reduction mechanism of organic pollutant (4-M, MO and MB)*

Based on the above experimental results, a possible mechanism for reduction of 4-NP and organic dyes using the developed $Fe_3O_4$@PPy-MAA/Ag catalyst in the presence of $NaBH_4$ has been proposed and exemplified in Scheme 4.1. The experimental results show that in the presence of $NaBH_4$ exclusively, the reduction rate is very slow. To overcome this, Ag metal has been employed into the reaction medium to accelerate the reduction rate. The general mechanism for the catalytic reduction of 4-NP was proposed by Langmuir-Hinshelwood model (L-H model) [54]. In aqueous solution $NaBH_4$ gets dissociate to produce $BH_4^-$ ions which are a key species for the reduction to occur. The reaction between borohydride ions and organic species (4-NP, MO and MB) and their decomposition takes place at the surface of the metal catalyst. Herein, the metal NPs acts as an electron carrier from $BH_4^-$ species to organic pollutant (4-NP, MO and MB). The adsorption of the borohydride onto the surface of metal catalyst is well-reported as fast and reversible in nature. Therefore, the organic species (4-NP, MO and MB) get activated by capturing the electrons from $BH_4^-$ through the metal nanoparticles [55-56]. Adsorbed borohydride ion reacts with metal nanoparticle and transfers a surface-hydrogen species to the surface of the metal nanoparticle (Ag NP). The reduction of adsorbed organic species (4-NP, MO and MB) occurs through the shifting of surface-hydrogen species into the activated groups of the target organic species. This step is considered as the rate determining step of the reduction reaction.

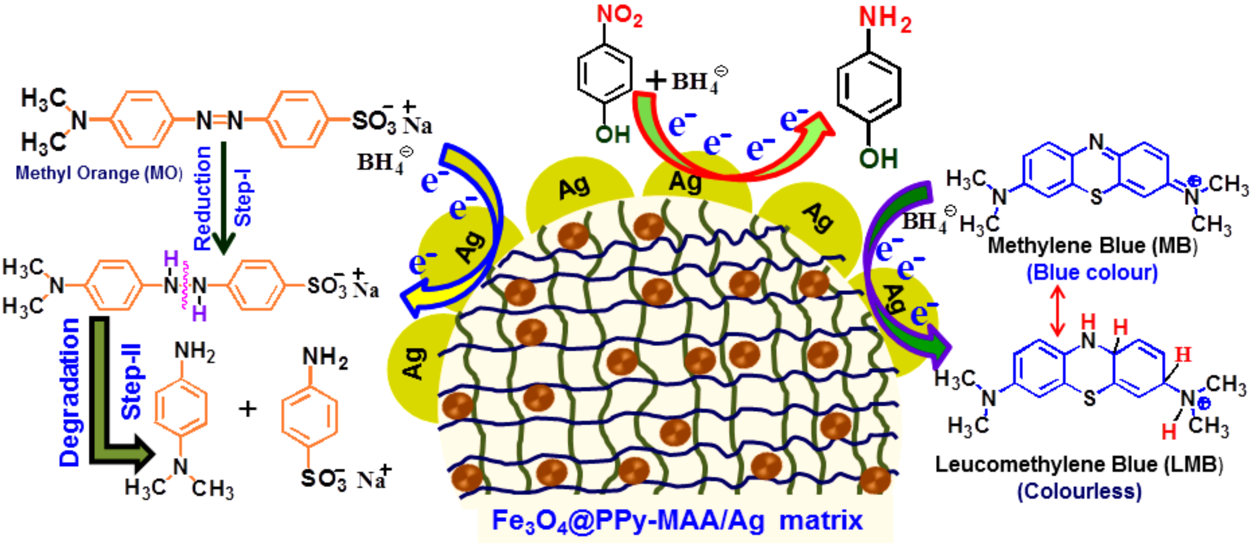

**Scheme 4-1: Plausible mechanism for the reduction of 4-nitrophenol and organic dyes (MO and MB) by $Fe_3O_4$@PPy-MAA/Ag nanocatalyst.**

Detachment of the reduced molecules (4-AP, LMB, reduced MO) results into free metal catalyst surface for subsequent catalytic cycle. Remarkably, in the case of MB experiment, the colourless reduced form of MB (LMB) was found to undergo slow aerial oxidation in open atmosphere after 3-4 hour. However, upon shaking, this blue colour characteristic of MB in the solution was once again reduced, certainly as a result of the excess $NaBH_4$ present in solution. Similar observation has been previously reported and referred as ‘clock’ reaction [57]. Reduced solution of MO, on the hand, did not show any colour change even after several days, revealing no subsequent re-oxidation process. The dye degraded products were analysed using UPLC-QTOF-MS. UPLC chromatograms of the pure MO (time 0 min.) and degraded sample at 2 min in electrospray positive (ESI+) and negative ions (ESI-) modes are displayed in Figure 4-24(a & b).

In both ESI+ and ESI-, two peaks were detected after 2 min of catalytic degradation using $Fe_3O_4$@PPy-MAA/Ag with no peak at the retention time for the untreated MO standard in the UPLC chromatogram. In the ESI- mode, the MO (retention time 4.46 min.) was characterised with an *m/z* 304.0758 $[M-Na]^-$ corresponding to $C_{14}H_{14}N_3O_3S^-$ (calculated 304.0756). N,N-dimethyl-benzene-1,4-diamine (retention time 0.63 min) was identified as a breakdown product of MO based on its *m/z* 136.0997 $[M]^-$ corresponding to molecular formula $C_8H_{12}N_2O_3$ (calculated 136.1000) (Figure 4-24e) based on the cleavage of the azo bond, responsible for the absorbance in the visible region at 464 nm. The ESI- mode also had a peak at retention time 0.72 min. which was identified as 4-amino-benzenesulfonate based on its *m/z* 172.0071 $[M]^-$ corresponding to molecular formula $C_6H_6NO_3S^-$ (calculated 172.0068) (Figure 4-24f). Further, the mass spectrograms of degraded MO after 5 min did not show any change relative to that after 2 min. Hence, the MO decolourisation products were N,N-dimethyl-benzene-1,4-diamine and 4-amino-benzenesulfonate, formed through hydrogenation and subsequently -NH-NH- bond dissociation as shown in Scheme 1 [58].

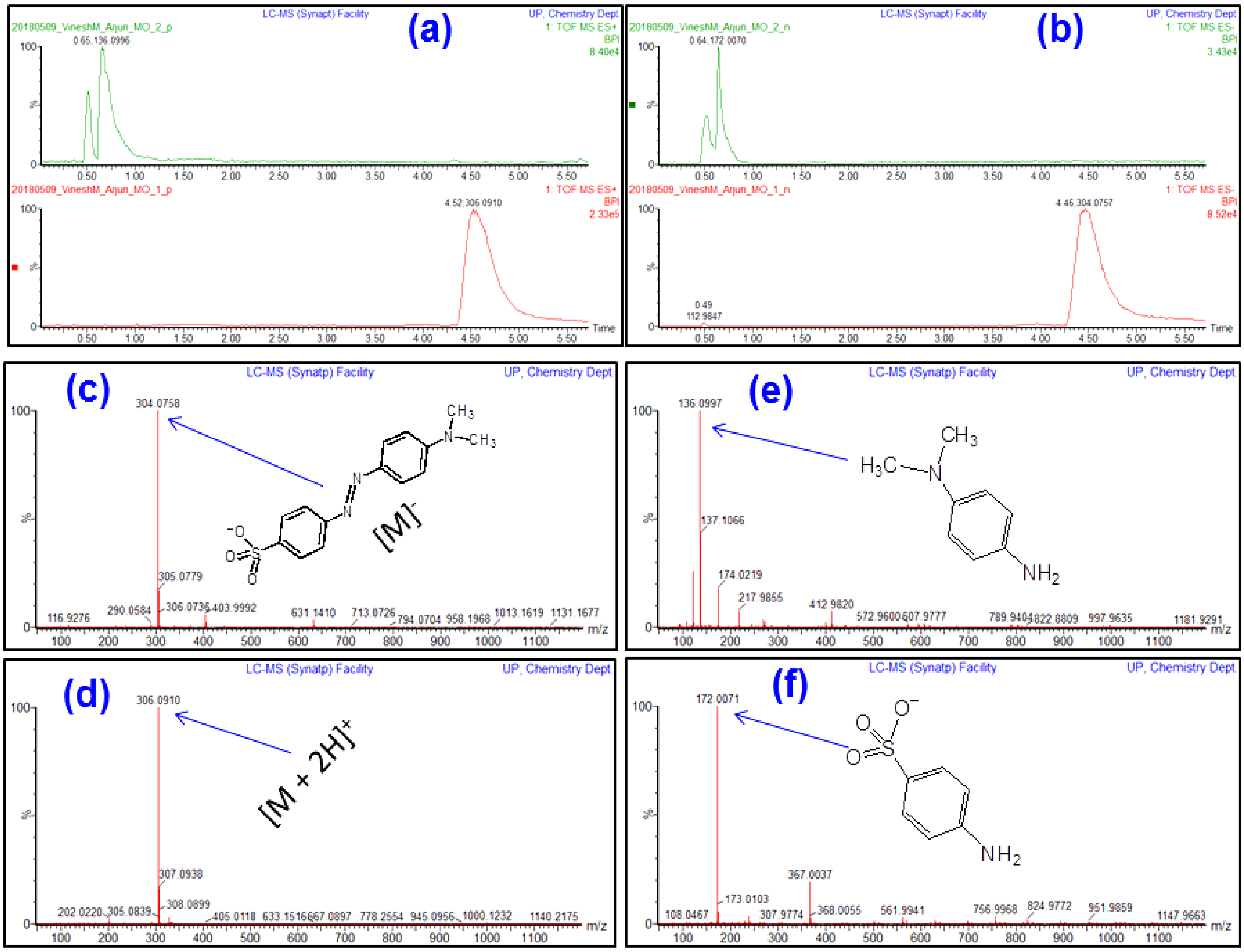

**Figure 4-24: LC-MS spectra of pure MO and degradation products in (a) positive (b) negative modes. Mass spectra of MO in two different modes (c) and (d); Mass spectra of two degradation products (e) N,N-dimethyl-benzene-1,4-diamine and (f) 4-amino-benzenesulfonate.**

### *4.3.3.5 Reusability of the catalyst*

For practical application of the catalysts, it is important to elucidate the reusability of the developed catalyst. Therefore, the reduction of 4-NP was chosen as a model reaction to examine the reusability of the developed magnetic nanocatalyst. The catalyst was separated from the reaction mixture after the reduction of 4-NP and washing five times with distilled water for further use in recycling performance. The reusability of the nanocatalyst is expressed in Figure 4-25. The $Fe_3O_4$@PPy-MAA/Ag has been successfully reused in eight repeated cycles for the reduction of 4-NP after 30 min. of reaction time. It has been noticed that after 7th cycles, the catalyst did not exhibit any significant loss of its activity. The conversion of 4-NP to 4-AP with >90% after 7th cycle indicates high stability and excellent recyclability of the catalyst. The reusability experiment of 8th cycles displayed ~81% conversion of 4-NP after 30 min of catalytic reduction. The above recyclability (8th cycle) showed >95% conversion of 4-NP with increasing the reaction time from 30 to 60 minutes. Therefore, these results demonstrate that the synthesized nanocatalyst exhibits excellent stability as well as robustness towards the multiple cycle of application.

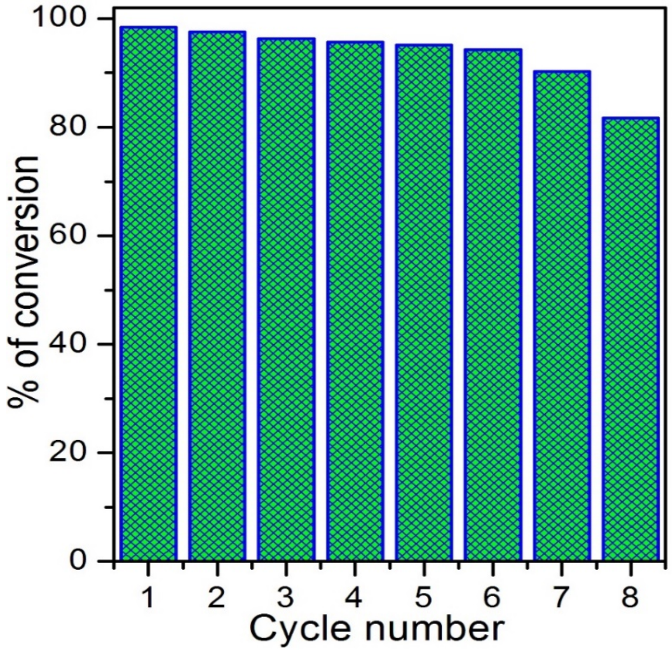

**Figure 4-25: Reusability of $Fe_3O_4$@PPy-MAA/Ag nanocatalyst over eight successive cycles for reduction of 4-NP.**

### *4.3.3.6 Leaching test of $Fe_3O_4$@PPy-MAA/Ag*

Leaching tests were done to determine how much of the $Ag^+$ ions were leached into the aqueous media. Disinfected synthetic and real water samples were filtered using a 0.45 μm syringe filter, and the supernatant was tested for residual $Ag^+$ using the ICP-MS. $Ag^+$ leachate was 0.09 mg/L, which is below the allowable limit of 0.1 mg/L. This this application is suitable for drinking water.

## 4.4 SUMMARY

In the current study, the magnetic NC ($Fe_3O_4$@PPy-MAA) was derived successfully from PPy doped with MAA and incorporated $Fe_3O_4$ NPs. TEM revealed that the $Fe_3O_4$ was encapsulated in the polymer matrix and that Ag NPs were also formed on the $Fe_3O_4$@PPy-MAA NC surface. The thermal stability of the NCs was subsequently increased due to the addition of $Fe_3O_4$ and the adsorption of $Ag^+$. It was established via VSM that the NC was ferromagnetic, following the observation of the hysteresis loop. The saturation magnetization ($\sigma_s$) value was 2.32 emu/g. The adsorption phenomenon was well described by pseudo-second-order rate equation and Langmuir isotherm model, with a maximum adsorption capacity of 833.3 mg/g at 25°C. The isotherm studies also confirmed that the adsorption process was endothermic and favourable. The Ag-containing magnetic NC demonstrated excellent antimicrobial activities against *E. coli*.

Although it was established that the antimicrobial activity of the $Fe_3O_4$@PPy-MAA/Ag NC was influenced by the nature of water being treated, the antimicrobial activity was realised within a working day. This is significant in water treatment practices since time is an important factor. Thus, like most chemical treatment methods, any pre-treatment that would reduce the turbidity of the water could greatly enhance the disinfection ability of the $Fe_3O_4$@PPy-MAA/Ag NC. Therefore, the $Fe_3O_4$@PPy-MAA NC is a promising agent for the remediation of $Ag^+$ in aqueous media and the secondary Ag-loaded waste material ($Fe_3O_4$@PPy-MAA/Ag) could be subsequently used for disinfection of microbially polluted waters.

Furthermore, the as-prepared nanocatalyst was also found to exhibit excellent catalytic activity towards the reduction of 4-NP to 4-AP in the presence of $NaBH_4$, with reaction rate constants of 0.5-14.3 × $10^{-2}$ $min.^{-1}$ In addition, the $Fe_3O_4$@PPy-MAA/Ag nanocomposite appeared to be a promising catalyst for quick reduction and decolourisation of toxic organic dyes (MO and MB) within few minutes (1.0-7.5) using very low catalyst amount (1-5 mg). Kinetics study revealed that the rate constant of the catalytic reaction improved with increased catalyst dose. The Ag NPs, developed and deposited at the surface of the prepared catalyst acted as an intermediate to transfer electron and hydrogen from $BH_4^-$ ions to the organic species (4-NP, MO and MB). Therefore, $Fe_3O_4$@PPy-MAA/Ag can serve as a promising catalyst with potential ability in the reduction of organic toxic pollutants (4-NP, MO and MB) from waterbodies.

## 4.5 REFERENCES

[1] M. R. Huang, S. Li, X. G. Li. Longan shell as novel biomacromolecular sorbent for highly selective removal of lead and mercury Ions. *J. Phys. Chem. B* **2010**, *114*, 3534-3542.

[2] S. E. Bailey, T. J. Olin, R. M. Bricka, D. D. Adrian. A review of potentially low-cost sorbents for heavy metals. *Water Res.* **1999**, *33*, 2469-2479.

[3] C. J. Vörösmarty, P. B. McIntyre, M. O. Gessner, D. Dudgeon, A. Prusevich, P. Green,; S. Glidden,; S. E. Bunn,; C. A. Sullivan,; C. Reidy Liermann, P. M. Davies. Global threats to human water security and river biodiversity. *Nature* **2010**, *467*, 555-561.

[4] S. Jagtap, M. K. Yenkie, N. Labhsetwar, S. Rayalu. Fluoride in drinking water and defluoridation of water. *Chem. Rev*. **2012**, *112*, 2454-2466.

A. Lewandowska, L. Falkowska, J. Jóźwik, Factors determining the fluctuation of fluoride concentrations in PM10 aerosols in the urbanized coastal area of the Baltic Sea (Gdynia, Poland). *Environ. Sci. Pollut. Res*. **2013**, *20*, 6109-6118.

[5] S. Ayoob, A. K. Gupta. Fluoride in drinking water: A review on the status and stress effects. *Crit. Rev. Environ. Sci. Technol*. **2006**, *36*, 433-487.

[6] Z. Mandinic; M. Curcic; B. Antonijevic; M. Carevic; J. Mandic; D. Djukic-Cosic. Fluoride in drinking water and dental fluorosis. *Sci. Total Environ*. **2010**, *408*, 3507-3512.

A. Wang, B. Luo, M. H. Liang, A. L. Wang, J. Wang, Y. Fang, Y. Chang, L. Zhi. Chemical amination of graphene oxides and their extraordinary properties in the detection of lead Ions. *Nanoscale* **2011**, *3*, 5059-5066.

[7] L. Liu, L. Ding, X. Wu, F. Deng, R. Kang, X. Luo. Enhancing the Hg(II) removal efficiency from real wastewater by novel thymine-grafted reduced graphene oxide complexes. *Ind. Eng. Chem. Res.* **2016**, *55*, 6845-6853.

[8] B. Yan, B. Li, F. Kunecke, Z. Gu, L. Guo. Polypyrrole-based implantable electroactive pump for controlled drug microinjection. *ACS Appl. Mater. Interfaces* **2015**, *7*, 14563-14568.

[9] H. Wang, X. Yuan, Y. Wu, X. Chen, L. Leng, H. Wang, H. Li, G. Zeng. Facile synthesis of polypyrrole decorated reduced graphene oxide-$Fe_3O_4$ magnetic composites and its application for the Cr(VI) removal. *J. Chem. Eng.* **2015,** *262,* 597-606*.*

[10] K. T. Vadiraj, S. L. Belagali. Characterization of polyaniline for optical and electrical properties. *IOSR J. Appl. Chem. Ver. II*. **2015**, *8*, 53-56.

[11] H. N. M. E. Mahmud, A. K. O. Huq, R. B. Yahya. The removal of heavy metal ions from wastewater/aqueous solution using polypyrrole-based adsorbents: A review. RSC Adv. 2016, 6, 14778-14791.

[12] W. Bai, F. Nie, J. Zheng, Q. Sheng. Novel silver nanoparticle manganese oxyhydroxide graphen oxide nanocomposite prepared by modified silver mirror reaction and Its application for electrochemical sensing. *ACS Appl. Mater. Interfaces* **2014**, *6*, 5439-5449.

[13] J. Huang, R. B. Kaner. A general chemical route to polyaniline nanofibers. J. Am. Chem. Soc. 2004, 126, 851-855.

[14] J. Huang, S. Virji, B. H. Weiller, R. B. Kaner. Polyaniline nanofibers: Facile synthesis and chemical sensors. J. Am. Chem. Soc. 2003, 125, 314-315.

[15] M. Bhaumik, R. I. McCrindle, A. Maity, S. Agarwal, V. K. Gupta. Polyaniline nanofibers as highly effective re-usable adsorbent for removal of reactive black 5 from aqueous solutions. *J. Colloid Interface Sci*. **2016**, *466*, 442-451.

[16] M. Bhaumik, H. J. Choi, R. I. McCrindle, A. Maity. Composite nanofibers prepared from metallic iron nanoparticles and polyaniline: High performance for water treatment applications. *J. Colloid Interface Sci*. **2014**, *425*, 75-82.

[17] M. Karthikeyan, K. K. Satheeshkumar, K. P. Elango. Defluoridation of water via doping of polyanilines. *J. Hazard. Mater*. **2009**, *163*, 1026-1032.

[18] M. Karthikeyan, K. K. S. Kumar, K. P. Elango. Batch sorption studies on the removal of fluoride ions from water using eco-friendly conducting polymer/bio-polymer composites. *Desalination* **2011**, *267*, 49-56.

[19] M. Karthikeyan, K. K. Satheesh Kumar, K. P. Elango. Conducting polymer/alumina composites as viable adsorbents for the removal of fluoride ions from aqueous solution. *J. Fluor. Chem*. **2009**, *130*, 894-901.

[20] R. A. Sheldon. Fundamentals of green chemistry: efficiency in reaction design. *Chem. Soc. Rev*. **2012**, *41*, 1437-1451.

[21] S. L. Y. Tang, R. L. Smith, M. Poliakoff. Principles of green chemistry: productively. *Green Chem*. 2005, *7*, 761-762.

[22] G. Centi, S. Perathoner. Catalysis and sustainable (green) chemistry. *Catal. Today* **2003**, *77*, 287-297.

A. Kästner, A. F. Thünemann. Catalytic reduction of 4-Nitrophenol using silver nanoparticles with adjustable activity. *Langmuir* **2016**, *32*, 7383-7391.

[23] M. Kaloti, A. Kumar, N. K. Navani. Synthesis of glucose-mediated Ag-γ-$Fe_2O_3$ multifunctional nanocomposites in aqueous medium-a kinetic analysis of their catalytic activity for 4-Nitrophenol reduction. *Green Chem.* **2015**, *17*, 4786-4799.

[24] X. Yuan, H. Wang, Y. Wu, G. Zeng, X. Chen, L. Leng, Z. Wu, H. Li. One-pot self-assembly and photoreduction synthesis of silver nanoparticle-decorated reduced graphene oxide/MIL-125(Ti) photocatalyst with improved visible light photocatalytic activity. *Appl. Organometal. Chem.* **2016**, *30*, 289-296.

A. Leyva-perez, A. Corma. Similarities and differences between the “Relativistic” triad gold, platinum, and mercury in catalysis. *Angew. Chem. Int. Ed*. **2012**, *51*, 614-635.

B. A. Ragachev, M. A. Yarmolenko, J. Xiaohong, R. Shen, A.P. Luchnikov, A. V. Rogachev. Molecular structure, optical, electrical and sensing properties of PANI-Based coatings with silver nanoparticles deposited from the active gas phase. *Appl. Surf. Sci.* **2015**, *351*, 811-818.

[25] X. Li,; Y. Gao,; J. Gong,; L. Zhang,; L. Qu. Polyaniline/Ag composite nanotubes prepared through UV rays irradiation via fiber template approach and their $NH_3$ gas sensitivity. *J. Phys. Chem. C* **2009**, *113*, 69-73.

[26] W. Shao, X. Liu, H. Min, G. Dong, Q. Feng, S. Zuo. Preparation, characterization, and antibacterial activity of silver nanoparticle-decorated graphene oxide nanocomposite. *ACS Appl. Mater. Interfaces* **2015**, *7(12)*, 6966-6973.

[27] K. Chauhan, R. Sharma,; R. Dharela, G. S. Chauhan, R. K. Singhal. Chitosan-thiomer stabilized silver nano-composites for antimicrobial and antioxidant applications. *RSC Adv.* **2016**, *6*, 75453-75464.

[28] Y. L. Xu, Q. Zhong, X. Y. Liu. Elemental mercury oxidation and adsorption on magnesite powder modified by Mn at low temperature. *J. Hazard. Mater*. **2015**, *283*, 252-259.

[29] P. Huttenloch, K. E. Roehl, K. Czurda. Use of copper shavings to remove mercury from contaminated groundwater of wastewater by amalgamation. Environ. Sci. Technol. 2003, 37, 4269-4273.

[30] R. Stolle, H. Koeser, H. Gutberlet. Oxidation and reduction of mercury by SCR DeNOx catalysts under flue gas conditions in coal fired power plants. Appl. Catal. B. 2014, 144, 486-497.

A. M. Berkovic, S. G. Bertolotti, L. S. Villata, M. C. Gonzalez, R. Pis Diez, D. O. Mártire. Photoinduced reduction of divalent mercury by quinones in the presence of formic acid under anaerobic conditions. Chemosphere 2012, 89, 1189-1194.

B. Yan, B. Li, F. Kunecke, Z. Gu, L. Guo. Polypyrrole-based implantable electroactive pump for controlled drug microinjection. ACS Appl. Mater. Interfaces 2015, 7, 14563-14568.

[31] H. Wang, X. Yuan, Y. Wu, X. Chen, L. Leng, H. Wang, H. Li, G. Zeng, Facile synthesis of polypyrrole decorated reduced graphene oxide-$Fe_3O_4$ magnetic composites and its application for the Cr(VI) removal. J. Chem. Eng. 2015, 262, 597-606.

[32] K. T. Vadiraj, S. L. Belagali. Characterization of polyaniline for optical and electrical properties. IOSR J. Appl. Chem. Ver. II. 2015, 8, 53-56.

[33] S. A. Idris, S. R. Harvey, L. T. Gibson. Selective extraction of mercury(II) from water samples using mercapto functionalised-MCM-41 and regeneration of the sorbent using microwave digestion. J. Hazard. Mater. 2011, 193, 171-176.

[34] X. Dou, D. Mohan, C. U. Pittman, S. Yang. Remediating fluoride from water using hydrous zirconium oxide. *Chem. Eng. J.* **2012**, *198*, 236-245.

A. Pan, J. Xu, B. Wu, Z. Li, X. Liu. Enhanced removal of fluoride by polystyrene anion exchanger supported hydrous zirconium oxide nanoparticles. Environ. Sci. Technol. 2013, 47, 9347-9354.

[35] H. Hu, J. H. Xin, H. Hu. PAM/graphene/Ag ternary hydrogel: Synthesis, characterization and catalytic application. J. Mater. Chem. A 2014, 2, 11319-11333.

[36] L. H. Velazquez-Jimenez, E. Vences-Alvarez, J. L. Flores-Arciniega, H. Flores-Zuñiga, J. R. Rangel-Mendez. Water defluoridation with special emphasis on adsorbents-containing metal oxides and/or hydroxides: A review. Sep. Purif. Technol. 2015, 150, 292-307.

A. Xu, J. Li, F. He, Y. Cui, C. Huang, H. Jin. $Al_2O_3$ -$Fe_3O_4$ -expanded graphite nano-sandwich structure for fluoride removal from aqueous solution. RSC Adv. 2016, 6, 97376-97384.

[37] R. A. Sheldon. Fundamentals of green chemistry: efficiency in reaction design. Chem. Soc. Rev. 2012, 41, 1437-1451.

[38] S. L. Y. Tang, R. L. Smith, M. Poliakoff. Principles of green chemistry: Productively. Green Chem. 2005, 7, 761-762.

[39] Centi, G.; Perathoner, S. Catalysis and sustainable (green) chemistry. Catal. Today 2003, 77, 287-297.

A. Kästner, A. F. Thünemann. Catalytic reduction of 4-Nitrophenol using silver nanoparticles with adjustable activity. Langmuir 2016, 32, 7383-7391.

[40] M. Kaloti, A. Kumar, N. K. Navani. Synthesis of glucose-mediated Ag-γ-$Fe_2O_3$ multifunctional nanocomposites in aqueous medium-a kinetic analysis of their catalytic activity for 4-Nitrophenol reduction. Green Chem. 2015, 17, 4786-4799.

[41] X. Yuan, H. Wang, Y. Wu,; G. Zeng, X. Chen, L. Leng, Z. Wu, H. Li. One-pot self-assembly and photoreduction synthesis of silver nanoparticle-decorated reduced graphene oxide/MIL-125(Ti) photocatalyst with improved visible light photocatalytic activity. Appl. Organometal. Chem. 2016, 30, 289-296.

A. A. Ragachev, M. A. Yarmolenko, J. Xiaohong, R. Shen, P. A. Luchnikov, A. V. Rogachev. Molecular structure, optical, electrical and sensing properties of PANI-Based coatings with silver nanoparticles deposited from the active gas phase. Appl. Surf. Sci. 2015, 351, 811-818.

[42] M. Berkovic, S. G. Bertolotti, L. S. Villata, M. C. Gonzalez, R. Pis Diez, D. O. Mártire. Photoinduced Reduction of Divalent Mercury by Quinones in the Presence of Formic Acid Under Anaerobic Conditions. Chemosphere 2012, 89, 1189-1194.

[43] M. Bhaumik, C. Noubactep, V. K. Gupta, R. I. McCrindle, A. Maity, Polyaniline/$Fe^0$ composite nanofibers: An excellent adsorbent for the removal of arsenic from aqueous solutions. Chem. Eng. J. 2015, 271, 135-146.

[44] M. Bhaumik, T. Y. Leswifi, A. Maity, V. V. Srinivasu, M. S. Onyango. Removal of fluoride from aqueous solution by Ploypyrrole/$Fe_3O_4$ magnetic nanocomposite. J. Hazard. Mater. 2011, 186, 150-159.

[45] S. Machida, S. Miyata, Chemical synthesis of highly electrically conductive, Polypyrrole. Synth. Met. 1989, 31, 311-318.

[46] Saha, A. Ghosh, D. Nandi, K. Gupta, D. Chatterjee, U. C. Ghosh. β-Cyclodextrin modified hydrous zirconium oxide: Synthesis, characterization and defluoridation performance from aqueous solution. Chem. Eng. J. 2015, 263, 220-230.

[47] S. Muthu Prabhu, S. Meenakshi. Chemistry of defluoridation by one-pot synthesized dicarboxylic acids mediated polyacrylamide-zirconium complex. Chem. Eng. J. 2015, 262, 224-234.

## 4.6 APPENDIX

**Weber-Morris Intraparticle Diffusion equation:**

The Weber-Morris Intraparticle Diffusion model was used, whereby the relationship between $q_t$ and *t* was evaluated (eq. S1)

$$q_t = k_{id}t^{1/2} + C \qquad \text{(S1)}$$

where, $k_{id}$ (mg/g.min$^{1/2}$) is an intraparticle diffusion rate constant, and *C* is a parameter related to the thickness of the boundary layer.

**Equilibrium adsorption isotherms**

The linear and non-linear Langmuir isotherm equations are depicted by eq. S2 and S3, respectively.

$$\frac{C_e}{q_e} = \frac{1}{bq_m} + \frac{C_e}{q_m} \qquad \text{(S2)}$$

$$q_e = \frac{bq_m\,C_e}{1+bC_e} \qquad \text{(S3)}$$

where $C_e$ (mg/L) is the equilibrium concentration of adsorbate ions in solution. $q_e$ and $q_m$ (mg/g) are the amount of ions adsorbed per unit mass of adsorbent at equilibrium and maximum adsorption capacity, respectively. *b* (L/mg) is the Langmuir constant related to the affinity of the binding sites for adsorbed ions. The non-linear and linear forms of the Freundlich isotherms are depicted by eq. S4 and eq. S5, respectively.

$$q_e = K_f\,{C_e}^{1/n} \qquad \text{(S4)}$$

$$\ln q_e = \ln k_F + \frac{1}{n}\ln C_e \qquad \text{(S5)}$$

where, $C_e$ is the concentration of adsorbate at equilibrium (mg/L) and $q_m$ is the maximum adsorption capacity, and b is the Langmuir constant related to the binding energy of adsorption. The Freundlich constants $k_F$ (mg/g) and $1/n$ signify the adsorption capacity and adsorption intensity, respectively. Values of $1/n$ range from 0 to 1 and if close to zero denote more surface homogeneity. On the other hand, $n$ values between 1 and 10 signify favourable adsorption [37]. $K_f$ and 1/n values were determined and are summarized in Table 2. The values of $n$ ranged between 0 and 10 for linear Freundlich isotherm, also indicate favourable adsorption.

**The mathematical expression of Separation factor ($R_L$):**

$$R_L = \frac{1}{1+C_0 b} \tag{S6}$$

where, $C_0$ is the initial concentration (mg/L). If the calculated $R_L$ value lies between 0 and 1, then the adsorption process is favourable.

**Adsorption thermodynamics**

Thermodynamic parameters ($\Delta G$, $\Delta H$ and $\Delta S$) were determined applying Van't Hoff equation. The following equations were used:

$$\Delta G = -RT\ \ln K_c \tag{S7}$$

$$lnK_c = \frac{\Delta S}{R} - \frac{\Delta H}{RT} \tag{S8}$$

where $\Delta G$ is Gibbs free energy change, $\Delta H$ is the enthalpy change, $\Delta S$ is the entropy change, R is the universal gas constant (8.314 J/mol/K), T is the temperature (K), and $K_c$ ($q_e/C_e$) is the equilibrium constant (L/g).

**Adsorption Kinetics**

Pseudo-first-order and pseudo-second-order kinetic models were employed to investigate the adsorption kinetics and understand the mechanism involved. These are represented by Eq. (S9) to (S10).

$$q_t = q_e(1 - exp\ (^{-k_1\, t} \tag{S9}$$

$$log(\ q_e\ -\ q_t\ ) = log(q_e\ ) - \frac{k_1}{2.303}\ t \tag{S10}$$

$$q_t = \frac{k_2 q_e 2\ t}{1+\ k_2\ q_e\ t} \tag{S11}$$

$$\frac{t}{q_t} = \frac{1}{k_2 q_e 2} + \frac{t}{q_e} \tag{S12}$$

where $k_1$ (1/min) and $k_2$ (g/mg.min) are pseudo-first-order and second-order-rate constants, respectively. $q_e$ and $q_t$ (mg/g) are adsorption capacities at equilibrium and time $t$ (min), respectively.

# CHAPTER 5: SYNTHESIS OF HCEFE NANOFIBERS AND BIMETAL-OXIDES-BASED ADSORBENTS AND THEIR APPLICATION FOR GROUNDWATER DEFLOURIDATION

## 5.1 INTRODUCTION

Groundwater, which represents approximately 97 percent of the global fresh water, is often regarded as an economical source of drinking water in developing countries [1]. However, owing to anthropogenic and natural activities, the quality of groundwater can be affected by pollutants such as fluoride ions ($F^-$). High concentration of $F^-$ in water is mainly due to the weathering of fluoride rich minerals and volcanic activity, alongside many anthropogenic actions [2,3]. Although low concentration of $F^-$ (below 1.5 mg/L) in drinking water has prophylactic influence over dental and bone health, as endorsed by the World Health Organization (WHO), prolonged exposure to high $F^-$ ions concentration may result in dental and skeletal fluorosis, infertility as well as neurological disorders [4]. Literature reports that over 24 countries including South Africa are harshly affected by high $F^-$ ions concentration in drinking water [5]. Hitherto an assortment of technologies, including coagulation, membrane filtration, electrochemical methods and adsorption has been developed for their remediation from groundwater [1].

Amongst the aforementioned technologies, adsorption is frequently regarded as superior because of its simplicity, high efficiency and cost-effectiveness [6-8]. Moreover, several studies have been conducted on the $F^-$ uptake from water, with emphasis on biosorbents, industrial wastes, cellulose fibers, resins, clays, activated carbon, carbon nanotubes, calcium-based materials and alumina [9-11]. However, drawbacks such as relatively high cost, low selectivity, narrow pH ranges, low efficiency and high sludge generation have been encountered in the application of some of these materials [6,9,12]. Nano-metal oxides are also noteworthy materials in scavenging $F^-$ ions from water and several studies have been conducted for their application. These include Ce-Mg [13], Mn-Ce [14], Ce-Fe [15,16], Ce-Al [17], Al-Mg [18], Fe-Zr [19], Al-Fe [20] and Mn-Al [21] oxides. Their main advantages are fast adsorption, shorter diffusion routes, high surface area to volume ratio and low sludge generation [15,21-23]. Nevertheless, despite these merits they still present major shortcomings, including loss of activity due to agglomeration, low adsorption capacity, reduced selectivity and difficulty of isolation from aqueous medium [22,23].

These limitations may be alleviated by embedding nano-metal oxide particles onto porous active supports of larger surface area like polymers, which make adsorbents separable. Furthermore, the selection of a suitable polymer matrix with particular functional groups can afford materials with highly improved adsorption properties [12,24]. A literature survey on the adsorption behaviour of conducting polymer-based nanomaterials revealed that polyaniline (PANI) exhibits desired properties like large surface area, modifiable surface chemistry, chemical stability and high affinity for anionic pollutants [12,25]. However, pristine PANI, obtained by an extensive mixing procedure, has been previously applied for $F^-$ removal from aqueous solution but showed very low adsorption capacity in batch mode [26]. PANI adsorbent is generally aggregated in solution, which depresses its adsorption capacity. PANI-$CeO_2$ and PANI-$Fe_3O_4$ mesoporous silica nanocomposites, on the other hand, were reported to demonstrate high capacity for the removal of toxic chromium (VI) [24,27]. Likewise, hydrous $ZrO_2$-deposited PANI NFs was found to exhibit fast and high adsorption capacity towards $F^-$ ions [25]. Since oxides of iron are prevalent in nature and ceria is among the cheapest of the rare earth metal oxides with high $F^-$ adsorption ability, the current study endeavoured to fabricate hydrous $CeO_2$-$Fe_3O_4$ deposited PANI nanofibers (HCeFe NFs) by a simple co-precipitation deposition of the nano-metal oxides onto PANI NFs network using the corresponding metal salt precursors. The yielded hybrid nanomaterial was characterised using a combination of microscopic and spectrometric techniques such as SEM-EDS, HR-TEM, BET, XRD, XPS, DMA and TG-DTA. The effect of various adsorption parameters, including, temperature, adsorbent dose, pH and contact time were evaluated. In addition, the influence of co-existing ions on the uptake performance of HCeFe NFs was tested. The desorption studies as well as mechanical assay were equally conducted to assess the long-term viability of HCeFe NFs after multiple uses and its strain, respectively. Ultimately, the real environmental application of this novel nanomaterial for $F^-$ remediation in groundwater samples was assessed.

## 5.2 MATERIALS AND METHODS

### 5.2.1 Materials

Sodium fluoride (NaF > 99%), cerium nitrate ($Ce(NO_3)_3.6H_2O$) (> 99%), iron (III) chloride anhydrous ($FeCl_3$ > 97%), iron (II) sulphate ($FeSO_4.7H_2O$), aniline (ANI, 99%) and all other chemicals of analytical grade were acquired from Sigma-Aldrich, USA. A 1000 mg/L stock solution of $F^-$ ions was prepared by dissolving 0.221 g of NaF in 100 mL of deionised water. 0.1M NaOH (> 99.9% grade) and 0.1M HCl (Sigma-Aldrich, USA) aqueous solutions were used to adjust the pH.

### 5.2.2 Preparation of hydrous HCeFe NFs composites

#### *5.2.2.1 Synthesis of polyaniline nanofibers*

Polyaniline nanofibers were synthesised using a method reported elsewhere [25]. 6 g of $FeCl_3$ was dissolved into 80 mL of deionised water under vigorous stirring, followed by a rapid addition of 0.8 mL of aniline monomer. The mixture was stirred for 5 minutes, left unstirred for 48 hours, filtered and washed with acetone and deionised water. The obtained nanofibers were dried at 60°C for 12 hours.

#### *5.2.2.2 Synthesis of the nanofibers composites*

Previous investigation on the defluoridation potential of hydrous Ce-Fe nano-metal oxides adsorbent revealed that Ce:Fe molar ratios 0.4:1, 0.5:1, 0.6:1 and 1:1 exhibited almost equivalent adsorption capacities [15]. In the current study Ce: Fe ratio of 1:1 was adopted for the preparation of hydrous $CeO_2$-

$Fe_3O_4$ bimetal oxides (HCeFe) and HCeFe NFs. 0.53 g of $FeCl_3$, 0.26 g of $FeSO_4.7H_2O$ and 2.17 g of $Ce(NO_3)_3.6H_2O$ were dissolved in 80 mL of deionised water. 2M NaOH was then added dropwise with magnetic stirring under ambient temperature until pH 8.0, and the resulting precipitate was vigorously stirred for 1 hour, aged for 24 hours, centrifuged, washed four times with deionised water, oven dried for extra 24 hours at 60°C and ground to afford HCeFe bimetal oxides. With regards to the preparation of the desired HCeFe NFs, 0.53 g of $FeCl_3$, 0.26 g of $FeSO_4.7H_2O$ and 2.17 g of $Ce(NO_3)_3.6H_2O$ were dissolved in 80 mL of deionised water with stirring, followed by the addition of 0.1, 0.2 and 0.3 g of PANI NFs in three separate mixtures and sonication for 15 minutes. Next, in each reaction mixture, 2M NaOH was added dropwise with magnetic stirring under ambient temperature until pH 8. The resulting precipitates were treated as for the synthesis of HCeFe bimetal oxides. The products were denoted HCeFe NFs-1, HCeFe NFs-2 and HCeFe NFs-3, respectively. To determine the ideal adsorbent for $F^-$ ions adsorption, optimisation study was carried out using the as-synthesised adsorbents under the following conditions; 50 mL aqueous solution of 20 mg/L $F^-$ ions, pH 6.0 ± 0.2 and adsorbent dose of 0.03 g.

### 5.2.3 Characterization

The FTIR spectra of the prepared pristine PANI nanofibers, HCeFe NFs and $F^-$ loaded HCeFe NFs were acquired using a Perkin Elmer Spectrum 100 Spectrometer (Perkin Elmer USA) in the range of 500-4000 $cm^{-1}$. The surface morphology and microstructure of the HCeFe NFs were studied by FE-SEM and HR-TEM using the microscopes, Zeiss Auriga Cobra FIB, Germany and a high resolution TEM (JEOL-JEM 2100, Japan) with LaB6 filament operated at 200 kV, respectively. TGA and DTA experiments were performed in air flowing at 50 mL/min and 10°C/min heating on a TGA Q500 (TA Instruments, USA). A Micrometrics ASAP 2020 gas adsorption instrument (Micromeritics, USA) using low-temperature (-198.50°C) $N_2$ adsorption-desorption technique was used for BET surface area measurements. A PANalytical X'Pert PRO-X-ray diffractometer (PANalytical, The Netherlands) using CuKα radiation with a wavelength of 1.5505 Å with adjustable slits at 45 kV/30 mA for 2θ values ranging from 5 to 90 was used for XRD characterisation. XPS studies were conducted on Kratos Axis Ultra device with Al monochromatic X-ray source (1486.6 eV) to establish the elemental composition of the HCeFe NFs before and after $F^-$ adsorption. The mechanical assay was executed using a DMA 8000 dynamic mechanical analyser (Perkin Elmer), operated at the frequency of 1 Hz and amplitude of oscillation 0.05 mm. The temperature ranged from 0 to 150°C, with a heating rate of 2°C/min. The mean dimensions of the samples plaques were 1.15 x 7.36 x 12.61, 0.96 x 7.36 x 12.29 and 0.96 x 7.36 x 12.27 $mm^3$ for PANI NFs, HCeFe NFs-2 and bimetal oxides HCeFe NPs, respectively. The temperature dependent behaviour was investigated by observing the variation in force and phase angle at steady amplitude of oscillation. The point-of-zero charge was measured using a change in pH approach with a Thermo Scientific pH meter as reported in other studies [15].

### 5.2.4 Batch adsorption experiments

Test solutions for $F^-$ removal were prepared by suitable dilutions from the stock solution. Adsorption studies were conducted in triplicate in plastic containers using 50 mL of 20 mg/L $F^-$ ions solution at pH 6.0 ± 0.2 and 0.03 g of adsorbent, followed by shaking in a thermostatic water bath shaker at 200 rpm for 24 hours. The pH influence was established by varying the initial pH (2-12) using 20 mg/L of $F^-$ ions solution. The pH adjustment was done using 0.1M HCl and 0.1M NaOH solution. The determination of residual $F^-$ ions in filtrate samples was conducted using an ion selective electrode (ThermoORION) in the form of conductance, as described elsewhere [28-30]. The fluoride electrode was calibrated using 10.0, 1.0 and 0.1 mg/L $F^-$ ion solutions by mixing these with an equivalent volume of Total Ionic Strength Adjustment Buffer (TISAB II). The buffer was made by dissolving 58 g of NaCl and 57 mL of 99.99% glacial acetic acid in 500 mL of deionised water, adjusting the pH to 5.5 using 5M NaOH and subsequently adding deionised water to 1L [8,25]. The percentage removal of $F^-$ ions was estimated using Eq.1:

$$\% \, removal = \left(\frac{C_o - C_e}{Co}\right) \times 100 \qquad (1)$$

where $C_o$ and $C_e$ are the initial and equilibrium $F^-$ ions concentration, respectively.

The influence of the adsorbent dose was investigated by changing the amounts of the adsorbent from 0.05 to 0.1 g using 20 mg/L of $F^-$ ions solution at the optimised pH 6.0 ± 0.2. The equilibrium adsorption capacity of the adsorbent is given by Eq. (2)

$$q_e = \left(\frac{C_o - Ce}{m}\right) V \qquad (2)$$

where $q_e$ (mg/g) and $V$ (L) denote the equilibrium amount of $F^-$ ions per unit mass of adsorbent and the solution volume, respectively.

To understand the adsorption accomplishment and adsorption mechanism, adsorption isotherms were investigated at pH 6.0 ± 0.2 for different temperatures (15, 25, 35 and 45°C) with initial $F^-$ ions concentration ranging from 5-100 mg/L and 0.03 g adsorbent dose. The experiment was done in triplicate. The isotherm data associated with the adsorption process were used to determine the thermodynamic parameters such as Gibbs free energy *($\Delta G°$)*, enthalpy *($\Delta H°$)* and entropy *($\Delta S°$)* change. Adsorption kinetics is essential for the prediction of the rate and modelling of water treatment system. This was studied using 50 mL solutions of different initial $F^-$ ions concentrations (10, 20, 30 and 40 mg/L) at 25°C, 0.03 g adsorbent dose and pH 6.0 ± 0.2 for 0 to 180 minutes shaking. The adsorption capacity of the adsorbent *($q_t$)* at time *t* was obtained using Eq. (3):

$$q_t = (\frac{C_o - C_t}{m}) V \qquad (3)$$

where $q_t$ (mg/g) and $C_t$ (mg/L) represent the quantity of $F^-$ taken per unit mass of adsorbent and the concentration of $F^-$ ions at time *t*, respectively.

The influence of co-existing ions is fundamental because no single ion is found sequestrated in natural water bodies. Hence this was performed by dissolving precursor salts of the selected ions ($Cl^-$, $SO_4^{2-}$, $NO_3^-$, $HCO^-_3$, $PO_4^{3-}$) together with $F^-$ ions at 0, 10, 20 and 40 mg/L concentrations in deionised water. The resultant solutions were shaken using the optimised adsorbent dose at pH 6.0 ± 0.2 for 24 hours followed by analysis for the residual F$^-$ ions. Typically, 0.03 g of adsorbent was added to 50 mL of 20 mg/L F$^-$ ions solution at pH of 6.0 ± 0.2. The F$^-$ loaded adsorbent was treated with 0.05, 0.025, 0.05, 0.075 and 0.1M NaOH solutions and it was found that 0.1M NaOH solution produced the highest desorption ability. This was then adopted for three consecutive desorption cycles. 2M HCl was employed for regeneration of the adsorbent.

## 5.3 RESULTS AND DISCUSSION

### 5.3.1 Optimisation study

The as-prepared three nanofibers composite adsorbents with different amounts of polyaniline fibers (HCeFe NFs-1, HCeFe NFs-2 and HCeFe NFs-3) along with PANI NFs and HCeFe were compared for their F$^-$ adsorption at pH 6.0 ±0.2 using 0.03 g adsorbent dose in 50 mL of 20 mg/L F$^-$ solution. The results are presented in Fig. 5.1(a). The percentage F$^-$ removal of HCeFe NFs-1(26.20% PANI NFs loading) and HCeFe NFs-3 (78.4% PANI NFs loading) were 70.3 and 59.5, values lower than that of 91.4 removal percentage by HCeFe NFs-2 (52.4% PANI NFs loading). Relatively high amount of PANI NFs loading as compared to metal oxides causes a decrease in F$^-$ uptake.

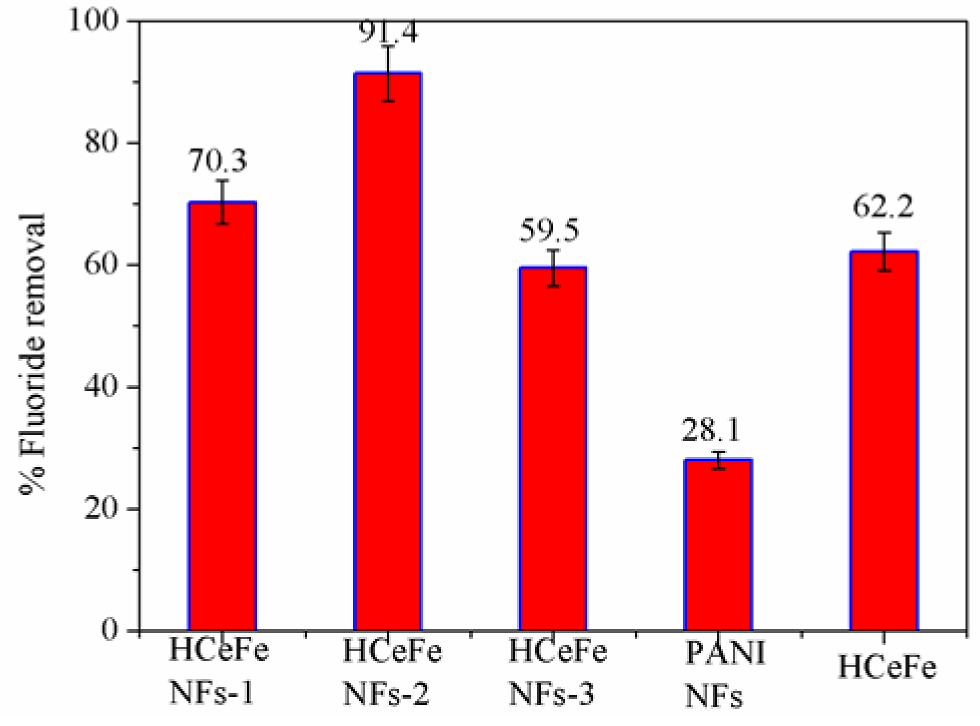

**Figure 5-1: Comparison of adsorption efficiency of nanocomposites at different loading in PANI NFs (HCeFe NFs-1, HCeFe NFs-2 and HCeFe NFs-3), PANI NFs and HCeO$_2$-Fe$_3$O$_4$ for fluoride ions adsorption using 0.03 g adsorbent, 50 mL of 20 mg/L F$^-$ solution at pH 6.0 ± 0.2 and temperature of 25°C.**

This observation could be ascribed to the optimal structure of hydrous cerium iron bimetal oxide deposited polyaniline with the maximum accessibility of binding sites of all components. Therefore, HCeFe NFs-2 with the highest adsorptive capacity (See Fig. 5.1) was adopted as the ideal adsorbent and further compared with pristine PANI NFs and hydrous $CeO_2$-$Fe_3O_4$. As illustrated in Fig. 5.1, HCeFe NFs-2 showed the highest percentage removal of $F^-$ (91.4%), relative to PANI NFs (28.1%) and HCeFe (62.2%) counterparts.

### 5.3.2 Physico-chemical characterization

The FTIR spectrum of pristine PANI NFs is shown in Fig. 5.2(A)(a). The bands at 1554 and 1478 $cm^{-1}$ are ascribed to the C=N and C=C vibration of benzenoid/quinonoid moieties of the polymer chain. Those at 1281 and 1220 $cm^{-1}$ are attributed to the C-N and C-H stretching vibration of the aromatic amine [12,27]. Fig. 5.2(A)(b), on the other hand, represents the spectrum of the HCeFe NFs-2 adsorbent. The bands at 3227 and 1644 $cm^{-1}$ correspond to stretching and bending vibration of $H_2O$ and surface-bonded OH groups. The bands at 1118 and 1076 $cm^{-1}$ correspond to bending vibration of OH groups of the metal oxides [13,16]. Those at 778, 685 and 658 $cm^{-1}$ can be attributed to the Fe-O/Ce-O bonds [15,27]. There is evidence of incorporation of hydrous metal oxide in HCeFe NFs-2 adsorbent, owing to the bands at 3227, 1644, 1076, 685 and 658 $cm^{-1}$, which are absent in the spectrum of pristine PANI NFs. In addition, the observed shift of the bands at 1554 and 1478 $cm^{-1}$, initially present in the FTIR spectrum of PANI NFs, to 1481 and 1309 $cm^{-1}$ in HCeFe NFs-2 adsorbent spectrum suggests strong interaction between $CeO_2$/$Fe_3O_4$ nanoparticles and the PANI NFs [28]. In the spectrum of HCeFe NFs-2 after adsorption procedure (Fig. 5.2(A)(c)), the bands at 3227, 1118 and 1076 $cm^{-1}$ shifted to 3204 $cm^{-1}$, 1090 $cm^{-1}$ and 1067 $cm^{-1}$, respectively and the intensity of the band at 1644 $cm^{-1}$ decreased. These observations are attributed to the adsorption of $F^-$ ions onto the prepared adsorbent.

Fig. 5.2(B) shows the XRD of the PANI NFs, $HCeO_2$-$Fe_3O_4$, HCeFe NFs-2 before and after $F^-$ adsorption. The pattern in Fig. 5.2(B)(a) reveals the characteristic peaks of PANI NFs at 2θ of 7.39, 15.51, 20.40 and 25.47° [12,27,29]. Characteristic peaks of $CeO_2$ at 28.90 (111), 33.70 (200), 47.94 (220), 56.80 (311) and 76.60° (331) are shown in Fig. 5.2(B)(b) [13,14,15,30]. The absence of the peaks corresponding to $Fe_3O_4$ may be attributed to the formation of $Fe_3O_4$-$CeO_2$ solid solution, in analogy with literature precedent [14,15]. Relative to XRD spectrum of pristine PANI NFs and HCeFe bimetal oxides, Fig. 5.2(B)(c) revealed the coexistence of both components in HCeFe NFs-2 with a PANI characteristic peak at 25.47°. The specific surface area is a significant parameter for the evaluation of textural properties of an adsorbent. This was calculated by means of the BET method. The BET surface area of HCeFe NFs-2 adsorbent was 66 $m^2/g$, much higher than that of previously reported pristine PANI NFs (39 $m^2/g$) [31]. This might be due to the prevention of π-π aggregation in PANI NFs and their decoration with nano-metal oxides. As shown in Fig. 5.2(C), the $N_2$ adsorption-desorption isotherm is of type IV with hysteresis loop of nature H3, according to the IUPAC classification [16]. The estimated pore size and volume were 4.18 nm and 0.077 $cm^3/g$, respectively (Fig. 5.2(D)). Since this pore size was larger than that of $F^-$ ions (0.133 nm), we envisaged that $F^-$ ions will be able to access the mesoporous material easily.

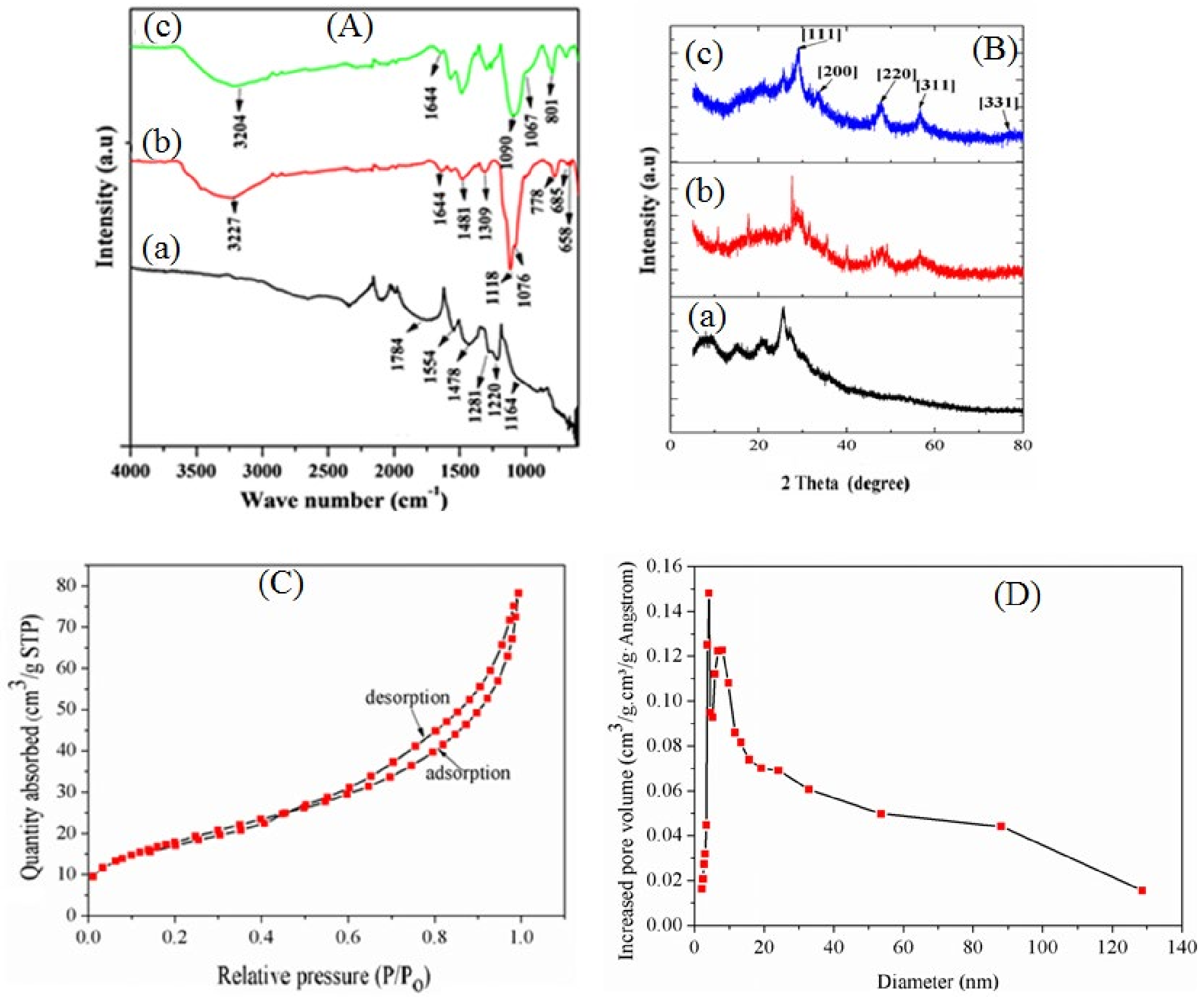

**Figure 5-2: (A) FTIR spectra of (a) pristine PANI NFs, (b) and (c) HCeFe NFs-2 adsorbent before and after F$^-$ ions uptake; (B) XRD patterns for (a) PANI NFs, (b) HCeO$_2$-Fe$_3$O$_4$ and (c) HCeFe NFs-2; (C) N$_2$ adsorption-desorption isotherm of HCeFe NFs-2 composite; and (D) pore size distribution curve.**

Figs. 5.3(A)(a) and (b) show the XPS wide scan spectra of HCeFe NFs-2 before and after F$^-$ adsorption, repectively. Energy bands due to Cl 2p (198.04 eV), C1s (283.98 eV), N1s (398.64 eV), O1s (529.77 eV), Fe 2p (710.12 and 723.66 eV) and Ce 3d (883.37 and 901.11 eV) are noticed [16]. The N 1s and C 1s peaks are associtated with the quinonoid imine, benzenoid amine, doped imine electronic states and the C chain which characterise the backbone of PANI NFs in HCeFe NFs-2 [12,23]. In addition, the two peaks at binding energies 710.12 and 723.66 eV correspond to Fe 2p$_{3/2}$ and Fe 2p$_{1/2}$, as a result of Fe element arising from Fe$_3$O$_4$, in correlation with literature precedent [32]. A new F 1s core level peak in the XPS wide spectrum at 684.3 eV binding energy is clearly observed in Fig. 5.3(A)(b) after adsorption, confirming the uptake of F$^-$ ions onto the adsorbernt [16]. Furthermore, there is a reduction in the intensity of Cl 2p core level peak after F$^-$ adsorption, indicating possible replacement of doped Cl$^-$ ions from PANI NFs.

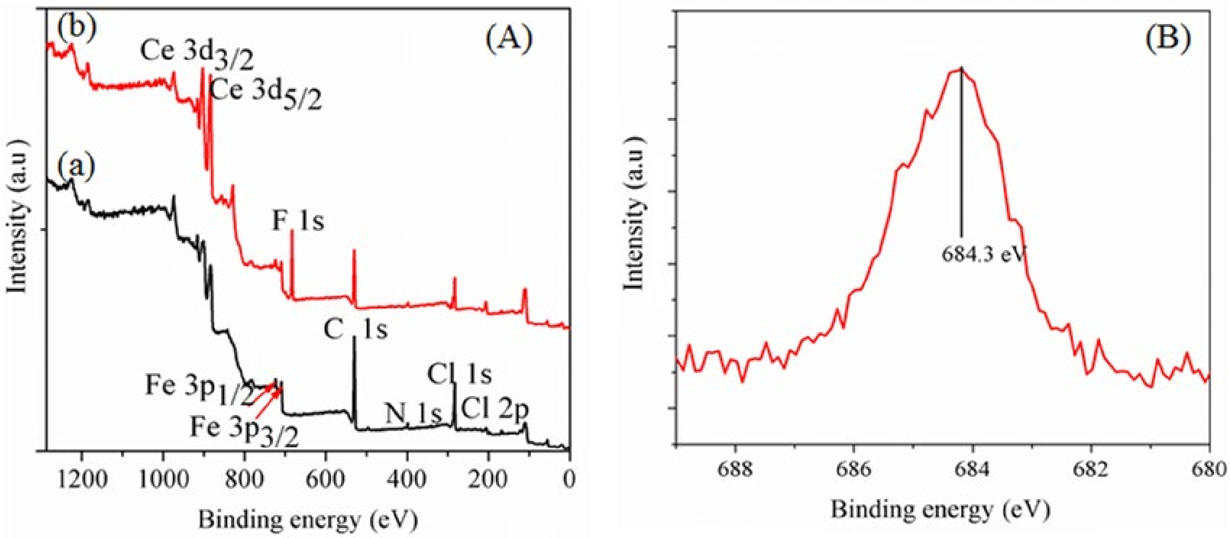

**Figure 5-3: (A) Wide scan XPS spectra of HCeFe NFs-2 (a) before and (b) after F$^-$ ions adsorption; (B) core level XPS spectrum of F 1s.**

The TG-DTA thermograms of HCeFe and HCeFe NFs-2 are shown in Fig. 5.4(A) and (B). These two materials went through different thermal decomposition patterns with different percentages of weight loss being observed. With regards to HCeFe, there was an initial weight loss of 10.43% in the range of 50-100°C due to surface-attached water, followed by a weight loss of 4.66% associated with the exothermic effect around 222°C as a result of the absorbed water molecules. Thereafter, a final weight loss step amounting to 7.11% up to 693°C was noticed, most likely as a result of phase transition [15]. Likewise, HCeFe NFs-2 indicated an early weight loss of about 10.86% owing to the loss of surface water in the temperature range of 50-105°C and subsequent 6.38% weight loss around 206°C. The observed high weight loss of 30.52% around 350-435°C is certainly attributed to the thermal decomposition of the PANI NFs skeleton in HCeFe NFs-2 [27,28]. The phase transition, on the other hand, occurred at around 700°C. Thus HCeFe NFs-2 can be used as highly stable material for water remediation in adsorption process.

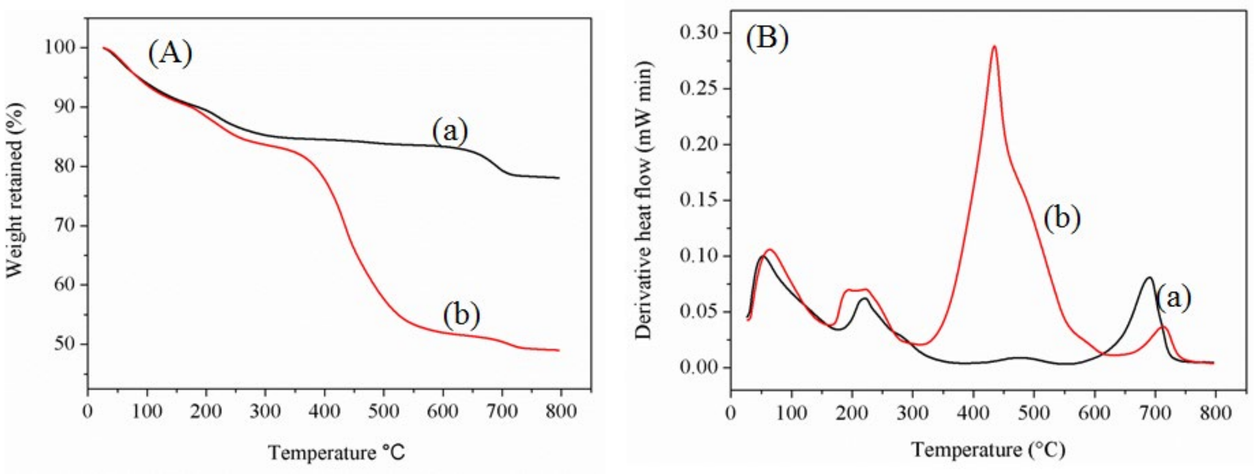

**Figure 5-4: (A) TGA and (B) DTA plots of (a) HCeO$_2$-Fe$_3$O$_4$ and (b) HCeFe NFs-2 composite.**

The SEM image of HCeFe NFs-2 is displayed in Fig. 5.5(a). HCeFe NFs-2 morphology consists of nanofibers with agglomerated spherical particles of $HCeO_2$-$Fe_3O_4$. The HR-TEM image of HCeFe NFs-2 (Fig. 5.5(b)) revealed that the material is made up of two different components with the black spots indicating the nano-metal oxides and the light-coloured layer indicating PANI NFs. This observation confirms that the agglomerated metal oxides are facilely deposited onto PANI NFs matrix. Fig. 5.5(c) shows the HR-TEM images of HCeFe NFs-2 composite at higher magnification. The metal oxides on the PANI NFs exhibited the lattice fringe with 0.31-0.32 nm spacing corresponding to the (111) crystallography plane of $CeO_2$ [16,17]. Moreover, the amorphous nature of some of the particles could be attributed to the presence of solid solution of $CeO_2$ and $Fe_3O_4$ [15]. These TEM results are in good agreement with XRD analysis where the $Fe_3O_4$ peaks could hardly be observed due to their amorphous behaviour in this material [16].

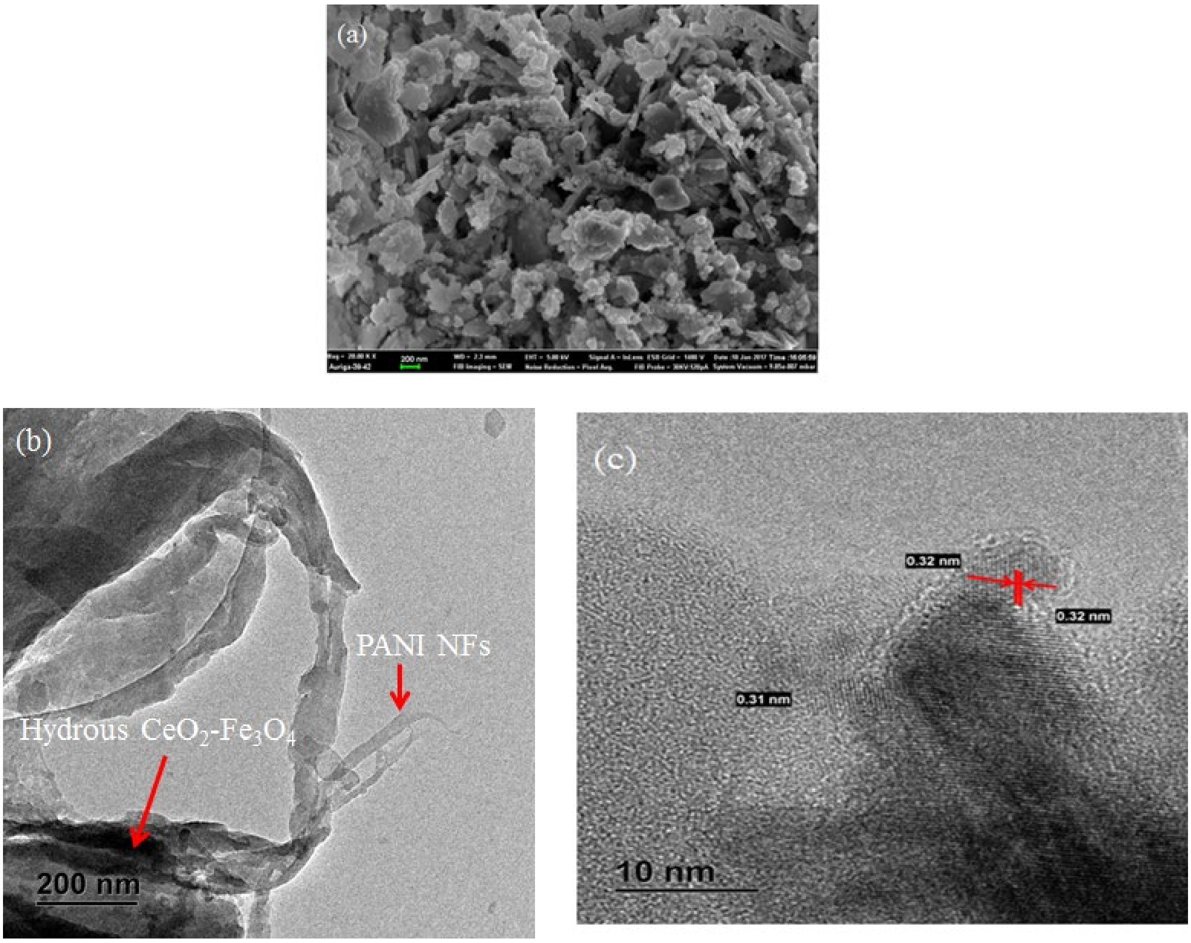

**Figure 5-5: (a) SEM, (b) and (c) HR-TEM images of HCeFe NFs-2.**

TEM mapping was accomplished to consolidate the presence of hydrous Ce and Fe oxides in the HCeFe NFs-2 structure as well as its $F^-$ ions uptake ability. Fig. 5.6 shows a uniform distribution of C, N, O, Ce , Fe, Cl and F elements at the surface of HCeFe NFs-2 after treatment.

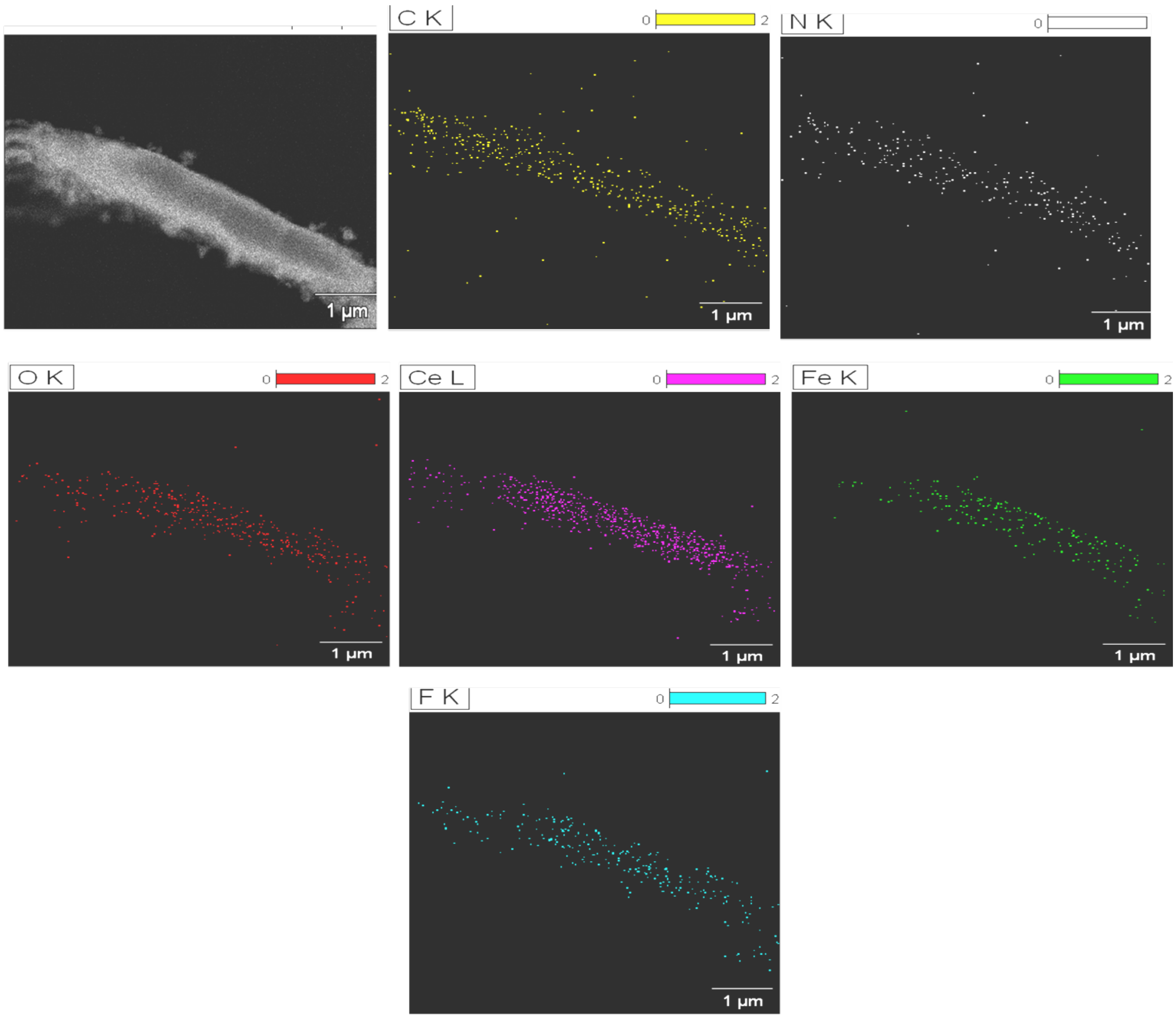

**Figure 5-6: STEM elemental mapping (C, N, O, Ce, Fe and F) of HCeFe NFs-2 composite after fluoride adsorption.**

The EDX analysis of SEM image of HCeFe NFs-2 adsorbent shown in Fig. 5.7(b) clearly revealed the existence of Ce and Fe besides C, N and O elements. Peaks corresponding to C, O, N, Cl, Ce and Fe elements were detected at energy values of 0.277, 0.525, 0.525, 2.667, 4.667 and 6.404 keV, respectively. This enlightes the presence of Ce and Fe on the polyaniline nanofiber. Nevertheless, the EDX spectrum of pristine PANI NFs only revealed peaks for C, N and Cl as presented in Fig. 5.7(a). The specrtrum after adsorption of $F^-$ ions is shown in Fig. 5.7(c). Comparing Fig. 5.7(b) with 5.7(c), a new peak corresponding to F element appears at energy value 0.667 keV, revealing $F^-$ ions uptake onto the adsorbent.

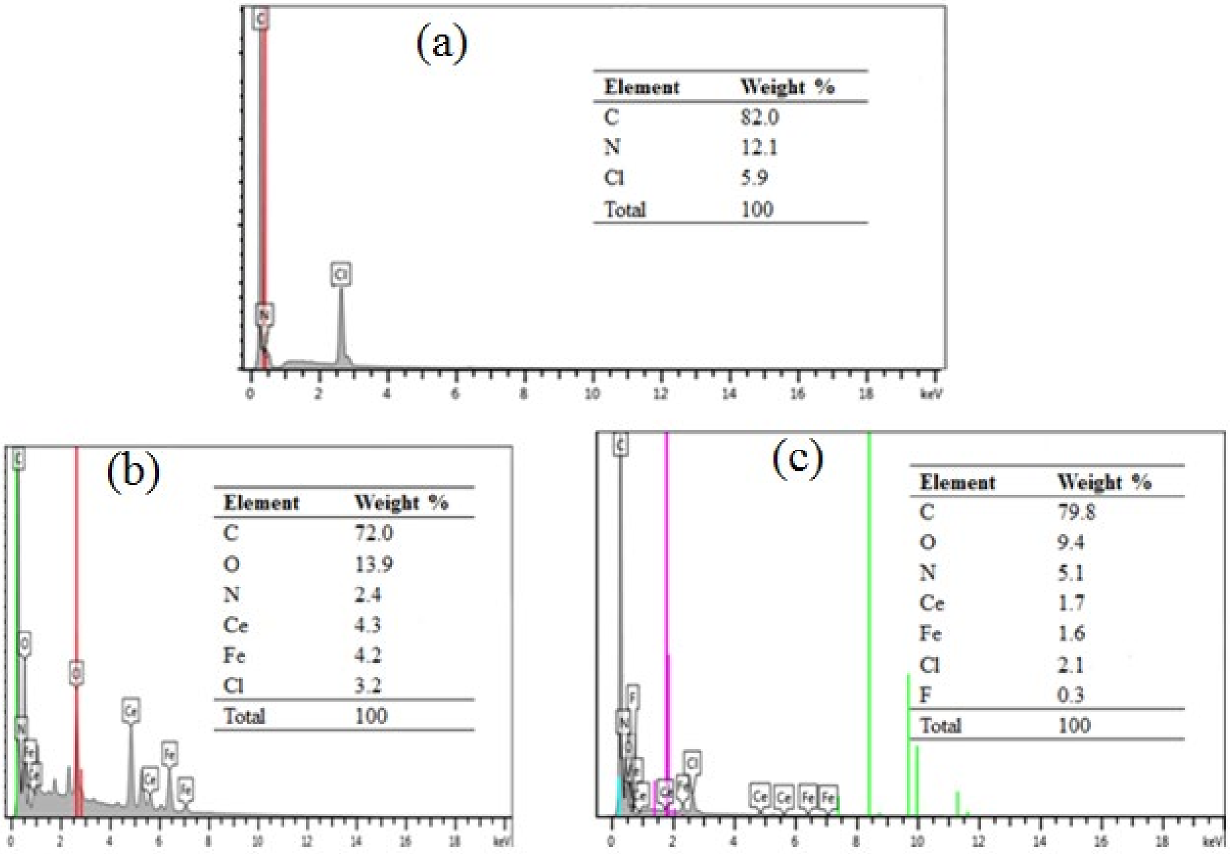

**Figure 5-7: EDX spectra of (a) PANI NFs (b) and (c) HCeFe NFs-2 composite before and after $F^-$ ions adsorption.**

The pH at the point-of-zero charge ($pH_{pzc}$) is a parameter which indicates the zero electrostatic potential of a surface at that particular pH, hence it was investigated. The $pH_{pzc}$ of HCeFe NFs-2 was found to be around 6.6, as shown in Fig. 5.8(a). Thus, at pH < 6.6 the surface of HCeFe NFs-2 is predominantly positive and above, it is expected to be predominantly negative. Therefore $F^-$ ions can be attracted to the surface of the prepared adsorbent at pH < 6.6 through electrostatic interactions among other mechanisms.

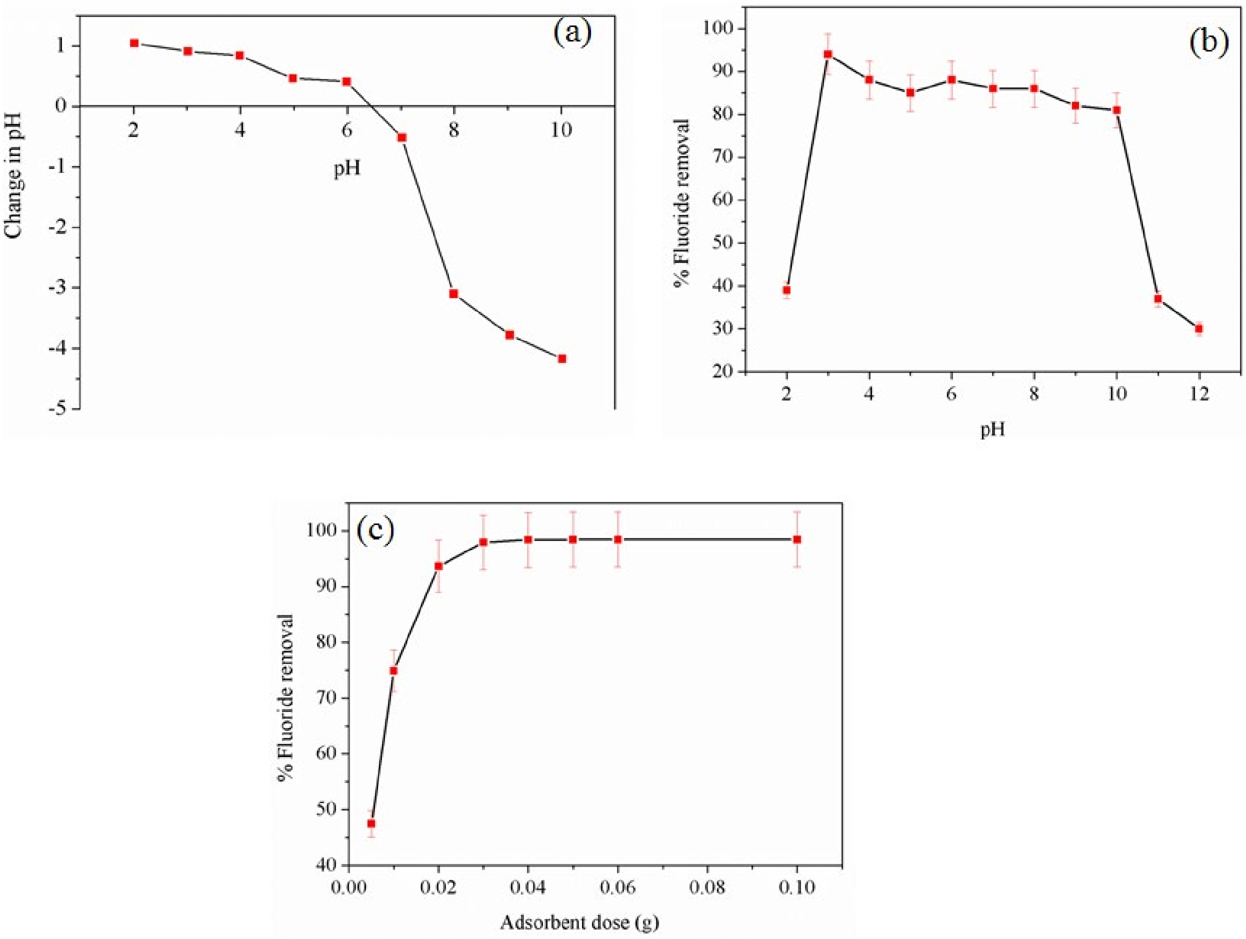

**Figure 5-8: (a) Determination of pH at the point-of-zero charge of HCeFe NFs-2 composite; Influence of (b) pH using 0.03 g dose and (c) HCeFe NFs-2 dose on $F^-$ ions adsorption at pH 6.0 ± 0.2 for 24 hours shaking time.**

### 5.3.3 Batch adsorption studies

#### *5.3.3.1 Effect of pH on the removal of $F^-$ ions*

Solution pH is a principal factor that affects adsorption at the solute/solid interface. Its influence on $F^-$ ions removal was studied from pH 2 to 12. As shown in Fig. 8(b) the sorption occurred over a range of pH 3-10 from which the percentage removal was almost constant between 94.00 and 80.61%. Maximum adsorption was observed at pH 3 (94.00%) and gradually decreased to 38% as the pH increased to 11. This could be attributed to the fact that at pH 2, Most of $F^-$ exits as neutral hydrogen fluoride which limits its adsorption. In addition, at very high pH 11-12 the solution has more hydroxyl than hydrogen ions, leading to competitive adsorption between hydroxyl and $F^-$ ions on the active sites [15,33,34]. The effect of pH is regarded as related to point-of-zero charge ($pH_{zc}$) of an adsorbent. At pH < $pH_{pzc}$, there is protonation of the nitrogen atoms on PANI NFs and hydrous metal oxides, giving rise to an overall positive charge of the adsorbent's surface, resulting in possible electrostatic interactions and thereby adsorption of $F^-$ ions [6,15,19]. The adsorbent surface being negatively charged when pH was over 6.6, this may serve as another reason for the decrease in adsorption capacity with increasing pH. In that regard, electrostatic repulsion exists between $F^-$ and hydroxyl groups on the adsorbent surface and only anionic exchange is expected to take place [20]. This demonstrates the applicability of HCeFe NFs-2 adsorbent for the removal of $F^-$ over a wide pH range of 3-10.

### *5.3.3.2 Effect of adsorbent dose*

The influence of HCeFe NFs-2 adsorbent amount on the adsorption of $F^-$ was investigated at pH 6.0 ± 0.2 and at 25°C and the results are presented in Fig. 5.8(c). The percentage of $F^-$ removal increased from 47.44% to 98.00% with increasing the dose from 0.005 to 0.03 g as more active sites for $F^-$ adsorption became available [30]. The removal proficiency remained constant as adsorbent amount increased from 0.04 to 0.1 g. This could be because at high dosage, active sites overlap or agglomerate and this lead to less available sites for adsorption [35]. Consequently, 0.03 g dose was adopted for the entire adsorption investigations.

### *5.3.3.3 Adsorption isotherms*

Adsorption isotherms are important in appreciating the interaction between adsorbent and pollutant for the planning and operation of a tangible adsorption system. The effect of temperature on the adsorption of $F^-$ ions by HCeFe NFs-2 was therefore studied at 15, 25, 35 and 45°C and the results are presented in Fig. 5.9(a), (b) and (c).

The adsorption of $F^-$ decreases with increase in temperature, suggesting an exothermic nature of the process. The increase in temperature has previously been reported to decrease the attachment tendency of $F^-$ ions onto Ce-Fe bimetal oxides surface and thereby weakening the degree of adsorption [15,16]. The adsorption data were analysed using two common isotherm models, the Langmuir and the Freundlich. The Langmuir model simulates monolayer exposure and that all the active sites at the surface of the adsorbent have equivalent affinity for the adsorbates with no lateral interaction between molecules [36,37]. The Langmuir linear and nonlinear forms are represented by Eq. (4) and (5) respectively.

$$\frac{C_e}{q_e} = \frac{1}{q_m b} + \frac{C_e}{q_m} \qquad (4)$$

$$q_e = \frac{b q_m C_e}{1 + b C_e} \qquad (5)$$

where $C_e$ (mg/L) and $q_e$ (mg/g) are the equilibrium concentration of $F^-$ ions in solution and the amount of $F^-$ ions adsorbed per unit mass of adsorbent at equilibrium, respectively. $q_m$ is the maximum adsorption capacity; $b$ (L/mg) is the Langmuir constant related to the $F^-$ ions affinity for the binding sites [9,35]. The fit of the isotherm data by nonlinear and linear form of the Langmuir model is presented in Fig. 9(b) and (c) and the calculated isotherm parameters are summarised in Table 1. The Langmuir parameters $q_m$ and $b$ at different temperatures were evaluated for linear and nonlinear Langmuir model fit and are also presented in Table 5.1. The $q_m$ values evaluated from the data, ranged from 117.64 to 93.46 mg/g for linear and 110.20 to 89.17 mg/g for nonlinear fit.

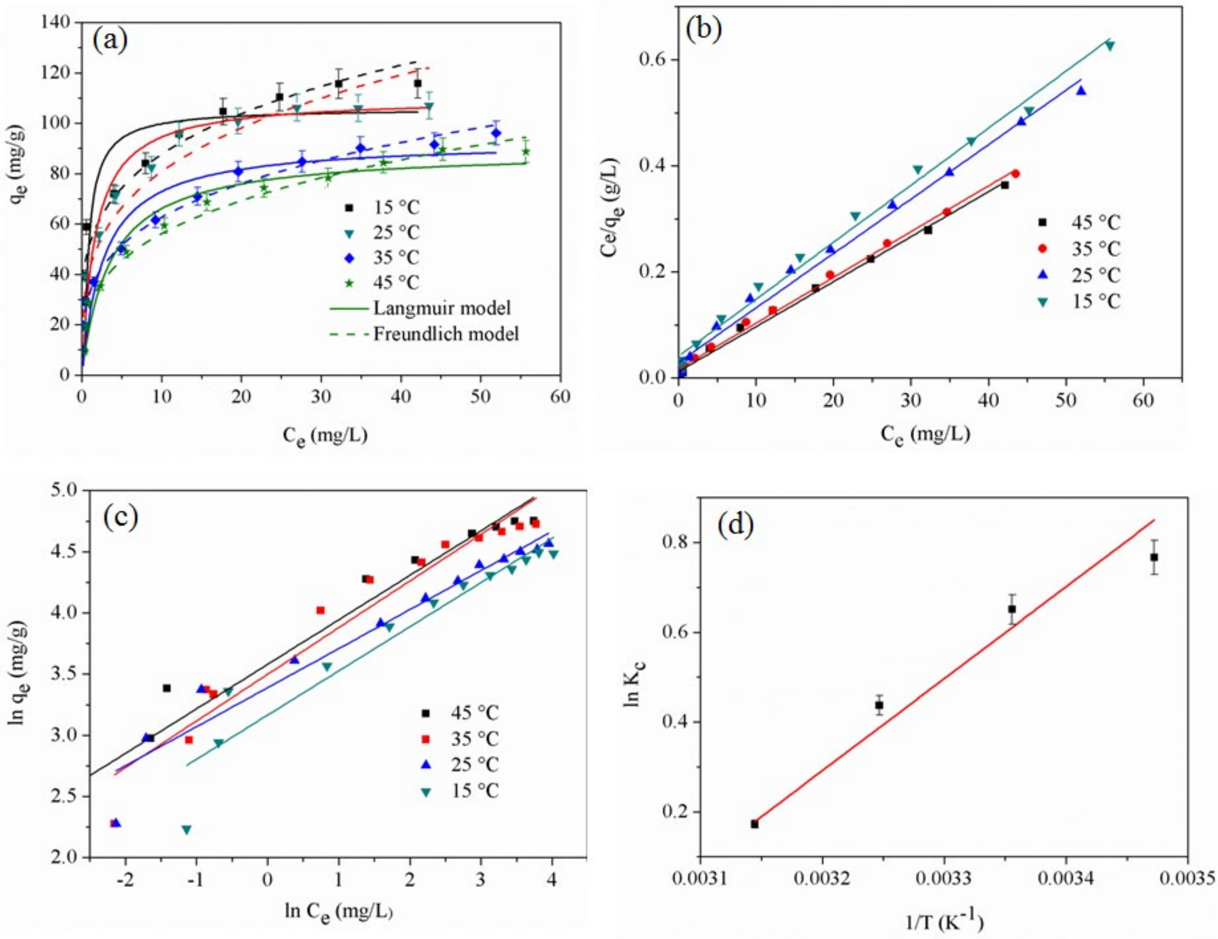

**Figure 5-9: (a) Adsorption equilibrium isotherms for $F^-$ ions removal by HCeFe NFs-2 composite and the data fit to Langmuir and Freundlich nonlinear models; Fit of data to linearized (b) Langmuir and (c) Freundlich models; (d) Van't Hoff's plot for the determination of thermodynamic parameters.**

**Table 5-1: Langmuir and Freundlich parameters for the sorption of $F^-$ ions onto HCeFe NFs-2 composite.**

| Isotherm models | Temperature /K | | | |
|---|---|---|---|---|
| | 288 | 298 | 308 | 318 |
| *Langmuir linear model* | | | | |
| $q_m$ (mg/g) | 117.64 ± 5.882 | 116.28 ± 5.814 | 97.08 ± 4.854 | 93.46 ± 4.673 |
| $b$ (L/mg) | 0.692 ± 0.034 | 0.494 ± 0.024 | 0.335 ± 0.016 | 0.258 ± 0.013 |
| $R_L$ | 0.0588 ± 0.003 | 0.0787 ± 0.004 | 0.109 ± 0.005 | 0.123 ± 0.006 |
| $R^2$ | 0.9950 | 0.9970 | 0.9906 | 0.9922 |
| *Non-linear* | | | | |
| Best-fit values | | | | |
| $q_m$ | 110.2 | 105.9 | 92.90 | 89.17 |
| $b$ | 0.604 | 1.683 | 0.365 | 0.287 |
| Std. Error | | | | |
| $q_m$ | 4.107 | 5.134 | 5.753 | 4.557 |
| $b$ | 0.1174 | 0.4799 | 0.1255 | 0.073 |
| 95% Confidence Intervals | | | | |
| $q_m$ | 101.0 to 119.3 | 94.46 to 117.3 | 80.08 to 105.7 | 79.02 to 99.32 |
| $b$ | 0.342-0.865 | 0.613-2.752 | 0.086-0.645 | 0.124-0.449 |
| Goodness of Fit | | | | |
| Degrees of Freedom | 10 | 10 | 10 | 10 |
| $R^2$ | 0.965 | 0.917 | 0.912 | 0.940 |
| Absolute Sum of Squares | 548.9 | 1376 | 892.3 | 520.5 |
| *Sy.x* | 7.408 | 11.73 | 9.446 | 7.214 |
| Number of points Analyzed | 12 | 12 | 12 | 12 |

| | | | | |
|---|---|---|---|---|
| *Freundlich linear model* | | | | |
| $K_f$ (mg/g) | 35.90 ± 1.79 | 33.09 ± 1.65 | 29.67 ± 1.48 | 23.71 ± 1.19 |
| *1/n* | 0.364 ± 0.018 | 0.5123± 0.026 | 0.319 ± 0.016 | 0.361 ± 0.018 |
| $R^2$ | 0.9520 | 0.9412 | 0.9455 | 0.9136 |
| *Non-linear model* | | | | |
| Best-fit values | | | | |
| $K_f$ | 49.29 | 42.46 | 32.95 | 27.95 |
| *n* | 4.041 | 3.575 | 3.579 | 3.300 |
| Std. Error | | | | |
| $K_f$ | 3.784 | 3.274 | 1.629 | 1.981 |
| *n* | 0.4180 | 0.3240 | 0.1932 | 0.2307 |
| 95% Confidence Intervals | | | | |
| $K_f$ | 40.86 to 57.72 | 35.17 to 49.75 | 29.32 to 36.58 | 23.54 to 32.36 |
| *n* | 3.109 to 4.972 | 2.853 to 4.296 | 3.148 to 4.009 | 2.786 to 3.814 |
| Goodness of Fit | | | | |
| Degrees of Freedom | 10 | 10 | 10 | 10 |
| $R^2$ | 0.9455 | 0.9569 | 0.9860 | 0.9749 |
| Absolute Sum of Squares | 909.9 | 671.6 | 142.0 | 219.8 |
| *Sy.x* | 9.539 | 8.195 | 3.768 | 4.688 |
| Number of points Analyzed | 12 | 12 | 12 | 12 |

The decrease in $q_m$ with temperature further validates the exothermic nature of the adsorption and the general decrease in $b$ with temperature indicates lesser energy of binding at higher temperatures [7]. The dimensionless constant $R_L$ is an essential parameter which indicates favourability or non-favourability of adsorption of Langmuir isotherm model. It is expressed by Eq. (6)

$$R_L = \frac{1}{1+bCo} \qquad (6)$$

$R_L$ values within the range $0 < R_L < 1$ for each of the different initial concentrations indicate favourable adsorption. Whereas, $R_L = 1$, $R_L = 0$ and $R_L > 1$ suggest linear, irreversible and unfavourable adsorption process, respectively. For this study, the $R_L$ values were established to be between 0 and 1, defining favourable adsorption process (Table 5.1).

The nonlinear [7] and linear [39] forms of Freundlich isotherm were also evaluated for the isotherm applicability of the data and these are represented in Eq. (7) and (8)

$$q_e = K_f C_e^{1/n} \tag{7}$$

$$lnq_e = lnK_f + \frac{1}{n}\, lnC_e \tag{8}$$

where $K_f$ denotes the Freundlich isotherm constant related to adsorption capacity. The coefficient *1/n*, on the other hand, is associated with the heterogeneity of the adsorption site energies and adsorption intensity [33].

The higher the $K_f$ value, the greater will be the adsorption efficiency. Moreover, $n$ values within the range 0 and 10 indicate stronger adsorbate/adsorbent interaction and thereby better adsorption process [38,39]. The $K_f$ and *1/n* values were evaluated and are shown in Table 5.1. The values of *1/n*, obtained using the curve plotted ln $q_e$ against ln $C_e$ are as follows; 0.364, 0.512, 0.319 and 0.361 for the temperatures 15, 25, 35 and 45°C, respectively. The smallest value of $1/n$, that is, 0.32 and higher value of $n$ (3.12) indicates active interaction between HCeFe NFs-2 and $F^-$ ions [6,37]. Fig. 5.9(b) and (c) show the linear fit of the equilibrium data for the Langmuir and Freundlich models. Comparing both models, it is observed that the $R^2$ values for the Langmuir ($R^2_{linear}$ = 0.9906-0.9970) were higher than those obtained from the Freundlich model ($R^2_{linear}$ = 0.9136-0.9520) for all temperatures. Based on this comparison, the Langmuir isotherm best described the adsorption process and the evaluated $q_m$ values ranged from 117.64-93.46 mg/g for 15 to 45°C. These obtained $q_m$ values were far much higher than those for previously reported hydrous Ce-Fe binary metal oxides 24.80 mg/g [15] and pristine PANI 0.77 mg/g [12]. Furthermore, the performance of HCeFe NFs-2 for the adsorption of $F^-$ ions was also assessed by comparison with other related adsorbents in the literature as shown in Table 5.2. It is evident that HCeFe NFs-2 has very high adsorption capacity and can therefore be seen as good material for application in water defluoridation.

**Table 5-2: Comparative assessment of F$^-$ ions adsorption capacity of HCeFe NFs-2 composite with other reported materials.**

| Adsorbent | Adsorption Capacity (mg/g) | Optimum pH | Ref. |
|---|---|---|---|
| Polypyrrole+ hydrous $TiO_2$ | 31.95 | 6.5 | [2] |
| $Fe_3O_4$@Alg-La | 45.23 | 4.0 | [7] |
| $Fe_3O_4$ polypyrrole | 17.6-22.3 | 6.5 | [8] |
| PANI-Aluminium oxide | 6.60 | 3.0 | [12] |
| Hydrous cerium-iron(III) oxide | 24.80 | 5.0-7.0 | [15] |
| $Fe_3O_4$@$Al(OH)_3$ magnetic material | 88.48 | 6.5 | [20] |
| β-Cyclodextrin modified hydrous $ZrO_2$ | 17.73 | 6.9 | [35] |
| Hydrous Zirconium oxide | 124.00 and 68.00 | 4.0 and 7.0 | [40] |
| $CeO_2$-$ZrO_2$ nanocages | 175.00 | 4.0 | [41] |
| Zr(IV)-ethylenediamine | 37.03 | 7.0 | [42] |
| HCeFe NFs-2 nanocomposite | 116.28 | 6.0 | Present work |

### *5.3.3.4 Thermodynamic parameters for F$^-$ adsorption by HCeFe NFs-2*

The thermodynamic characteristic parameters, $\Delta G°$, $\Delta H°$ and $\Delta S°$ were evaluated from adsorption isotherm data using Eq. (9) and (10):

$$\Delta G° = -RT \ln K_c = -RT \ln \left(m\frac{q_e}{C_e}\right) \quad (9)$$

$$\ln \left(m\frac{q_e}{C_e}\right) = \frac{\Delta S°}{R} - \frac{\Delta H°}{RT} \quad (10)$$

where $R$ (J/mol K), $T$ (K) and $K_c$ are the molar gas constant, temperature and the equilibrium constant, respectively. The ratio $mq_e/C_e$ is the adsorption affinity. The values of $\Delta H°$ and $\Delta S°$ were computed from the slope and intercept of the plot of ln ($mq_e/C_e$) versus $1/T$, respectively as shown in Fig. 5.9(d). The values of $\Delta G°$ were calculated by using Eq. (9). The thermodynamic parameters are presented in Table 5.3. The negative value of $\Delta H°$ confirms the feasibility of an exothermic adsorption process, as reported previously on the use of metal oxide-based nanoadsorbents [7,15,16]. The negative value of $\Delta S°$ indicates decrease in amount of species at the solid-liquid interface and hence randomness. The negative values of $\Delta G°$ (-1.835 to -0.455 kJ/mol) suggest a spontaneous F$^-$ adsorption process through physical sorption under the experimental conditions. Moreover, its decrease in magnitude with increase temperature indicates that the process was more favourable at low temperatures.

**Table 5-3: Thermodynamic parameters from temperature dependent adsorption.**

| Temperature (°C) | ∆$G°$ (kJ/mol) | ∆$H°$ (kJ/mol) | ∆$S°$ (kJ/mol/K) | $R^2$ |
|---|---|---|---|---|
| 15 | -1.835 ± 0.09 | -15.10 | -0.0458 | 0.999 |
| 25 | -1.612 ± 0.08 | | | |
| 35 | -1.190 ± 0.06 | | | |
| 45 | -0.455 ± 0.02 | | | |

#### 5.3.3.5 *Adsorption kinetics*

Kinetics studies are useful in predicting the adsorption rate that gives insight into design and modelling for adsorption based water treatment processes [8]. An adsorbent must have rapid adsorption kinetics to be considered feasible for industrial application. The effect of contact time for $F^-$ adsorption on HCeFe NFs-2 adsorbent was studied for four initial $F^-$ ions concentrations 10, 20, 30 and 40 mg/L at 25°C as shown in Fig. 5.10(a).

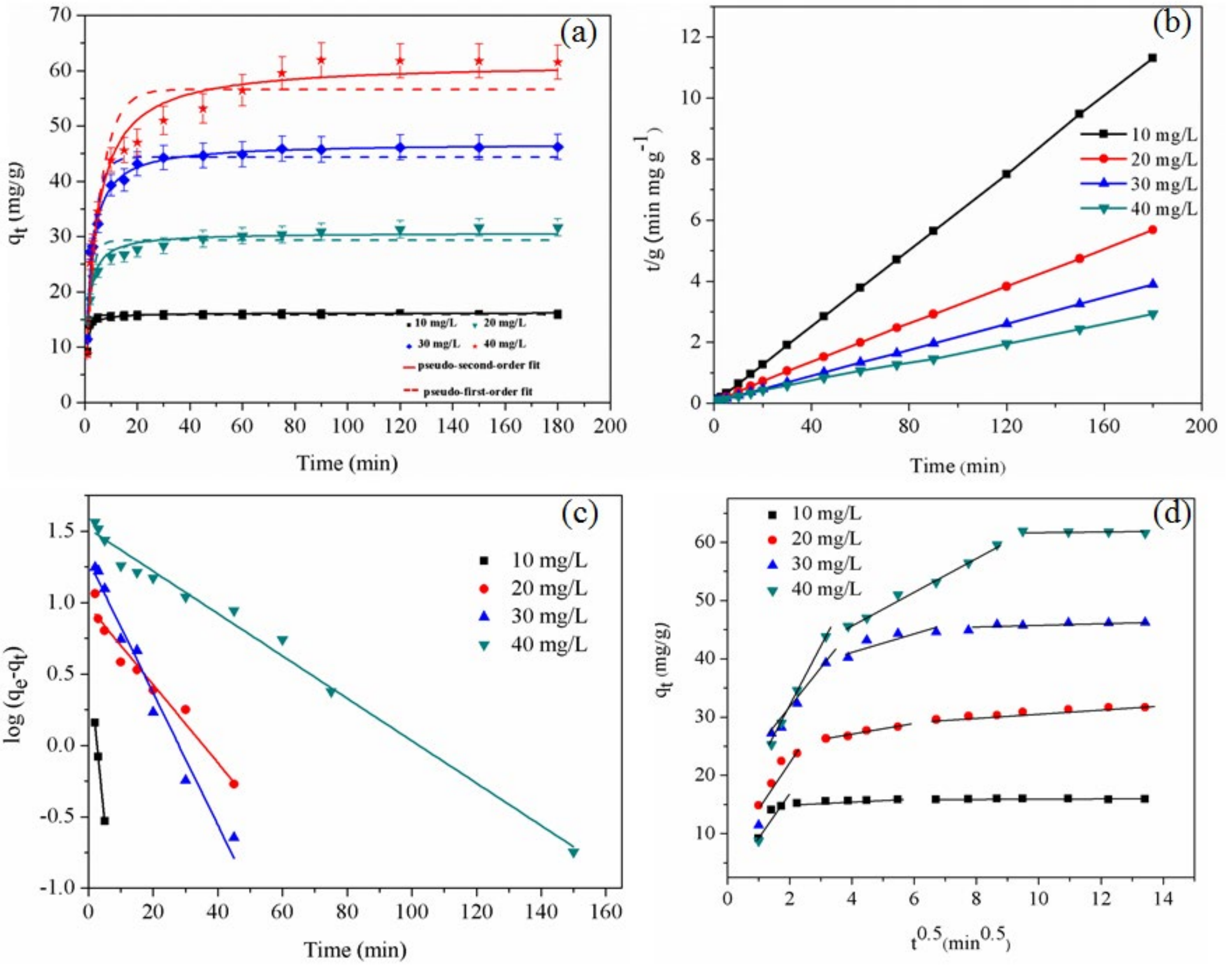

**Figure 5-10: (a) Effect of contact time on the adsorption of $F^-$ ions onto HCeFe NFs-2 composite and fit of kinetic data to (a) pseudo-first-order and pseudo-second-order nonlinear, (b) pseudo-second-order linear, (c) pseudo-first-order linear kinetic models: at pH 6.0 ± 0.2, adsorbent dose 0.03 g, contact time 24 hours and temperature 25°C; (d) Intra-particle diffusion model.**

$F^-$ ions adsorption increased with contact time and was relatively rapid, with most of the adsorption taking place in the first 10, 45, 75 and 90 minutes, respectively. This time range is shorter as compared to some reported adsorbent contact times in literature [38,40,41]. To study the kinetic mechanism of the adsorption, the nonlinear and linear pseudo-first-order and pseudo-second-order kinetic models, were employed and these are represented by Eq. (11) to (14)

$$q_t = q_e(1 - \exp(^{-k_1 \mathrm{t}}) \tag{11}$$

$$\log(q_e - q_t) = \log(q_e) - \frac{k_1}{2.303}\, t \tag{12}$$

$$q_t = \frac{k_2 q_e 2\ t}{1 + k_2 q_e t} \tag{13}$$

$$\frac{t}{q_t} = \frac{1}{k_2 q_e 2} + \frac{t}{q_e} \tag{14}$$

where $k_1$ ($\mathrm{min}^{-1}$) and $k_2$ (g/mg.min) are the pseudo-first-order and pseudo-second-order-rate constants respectively. $q_e$ and $q_t$ (mg/g) are the adsorption capacities at equilibrium and time $t$ (min), respectively. The non-linear and linear plots of the pseudo-second-order and pseudo-first kinetics models are illustrated in Fig. 5.10(a), (b) and (c). The values for the rate constants and other parameters computed from linear and non-linear regression plots are shown in Table 5.3. The $R^2$ values obtained from the pseudo-second-order model ($R^2_{linear}$ = 0.9999-1.000 and $R^2_{nonlinear}$ = 0.8800-0.9685) are greater than those from the pseudo-first-order model ($R^2_{linear}$ = 0. 0.9609-0.9998 and $R^2_{nonlinear}$ = 0.8377-0.9739). Furthermore, the $q_e$ values acquired from the pseudo-second-order model were in close concurrence with the experimental values. Consequently, it can be deduced that the $F^-$ ions adsorption onto HCeFe NFs-2 followed the pseudo-second-order kinetics model. The values of $k_2$ generally decreased from 0.2471 to 0.0302 (g/mg.min) with surge in initial $F^-$ ions concentration, owing to the increase in the rate of adsorption with decrease in concentration. Moreover, to understand the nature of the rate controlling step in the adsorption of $F^-$ ions, the Webber-Morris intra-particle diffusion model was employed and the equation is as follows:

$$q_t = k_{int}\, t^{0.5} + C_i \tag{15}$$

where $k_{int}$ (mg/g $\mathrm{min}^{0.5}$) and $C_i$ (mg/g) are the intra-particle diffusion rate constant and constant linked to the magnitude of the boundary layer thickness, respectively. Plots of $t^{0.5}$ against $q_t$ produced for different initial $F^-$ ions concentrations are shown in Fig. 5.10(c). The initial part may be governed by boundary layer diffusion and the second part by intra-particle diffusion. The values of $k_{int}$ for the four different concentrations of $F^-$ ions were acquired from the slopes of the initial linear part of the curves and displayed in Table 5.4, together with the $R^2$ values. The values of $k_{int}$ increased from 7.7319 to 19.9730 mg/g.$\mathrm{min}^{0.5}$ as the initial concentration increased from 10 mg/L to 40 mg/L. The deviation of the straight lines from the origin could be attributed to the variance between the rate of mass transfer in the initial and final stages which indicates a complex situation in which both film diffusion and intra-particle diffusion contribute to the rate determining step [2].

**Table 5-4: Kinetics parameters for the sorption of $F^-$ ions by HCeFe NFs-2 composite at different concentrations.**

| Kinetic models | Initial concentration (mg/L) | | | |
|---|---|---|---|---|
| | 10 | 20 | 30 | 40 |
| *Pseudo- first-order linear* | | | | |
| *k₁* (g/mg min) | 0.527 ± 0.026 | 0.063 ± 0.003 | 0.106 ± 0.005 | 0.03408 ± 0.002 |
| *qₑ* (mg/g) | 4.095 ± 0.205 | 9.304 ± 0.465 | 19.56 ± 0.978 | 32.878 ± 1.644 |
| $R^2$ | 0.9998 | 0.9609 | 0.9767 | 0.9877 |
| *Non-linear* | | | | |
| Best-fit values | | | | |
| $q_e$ | 15.81 | 29.33 | 44.38 | 56.62 |
| $k_1$ (1/min) | 0.9376 | 0.5083 | 0.3328 | 0.1876 |
| Std. Error | | | | |
| $q_e$ | 0.0834 | 0.6314 | 0.8082 | 1.790 |
| $k_1$ | 0.0371 | 0.0640 | 0.0326 | 0.0297 |
| 95% Confidence Intervals | | | | |
| $q_e$ | 15.63 to 15.99 | 27.97 to 30.69 | 42.63 to 46.12 | 52.75 to 60.48 |
| $k_1$ | 0.8574-1.018 | 0.3700-0.6466 | 0.2624-0.4033 | 0.1234-0.2517 |
| Goodness of Fit | | | | |
| Degrees of Freedom | 13 | 13 | 13 | 13 |
| $R^2$ | 0.9739 | 0.8377 | 0.9374 | 0.8948 |
| Absolute Sum of Squares | 1.098 | 57.91 | 88.84 | 378.7 |
| *Sy.x* | 0.2906 | 2.111 | 2.614 | 5.397 |
| Number of points | | | | |
| Analyzed | 15 | 15 | 15 | 15 |
| *Pseudo-second - order linear* | | | | |
| $k_2$ (g/mg. min) | 0.247 ± 0.0302 | 0.142 ± 0.0071 | 0.112 ± 0.0056 | 0.0302 ± 0.0015 |
| $q_e$ *(mg/g)* | 15.94 ± 0.797 | 30.30 ± 1.515 | 44.82 ± 2.241 | 63.78 ± 3.189 |
| $R^2$ | 1 | 1 | 1 | 0.999 |

| Kinetic models | Initial concentration (mg/L) | | | |
|---|---|---|---|---|
| | 10 | 20 | 30 | 40 |
| *Non-linear* | | | | |
| Best-fit values | | | | |
| $k_2$ | 0.1215 | 0.0261 | 0.0105 | 0.0040 |
| $q_e$ | 16.18 | 30.65 | 46.85 | 61.39 |
| Std. Error | | | | |
| $k_2$ | 0.0180 | 0.0024 | 0.0009 | 0.0005 |
| $q_e$ | 0.2010 | 0.3478 | 0.6084 | 1.249 |
| 95% Confidence Intervals | | | | |
| $k_2$ | 0.0826 to 0.1604 | 0.0209 to 0.0314 | 0.0083 to 0.0126 | 0.0029 to 0.0051 |
| $q_e$ | 15.74-16.61 | 29.90-31.40 | 45.53-48.16 | 58.69-64.08 |
| Goodness of Fit | | | | |
| Degrees of Freedom | 13 | 13 | 13 | 13 |
| $R^2$ | 0.8800 | 0.9635 | 0.9753 | 0.9685 |
| Absolute Sum of Squares | 5.053 | 13.04 | 35.06 | 113.5 |
| *Sy.x* | 0.6234 | 1.001 | 1.642 | 2.955 |
| Number of points Analyzed | 15 | 15 | 15 | 15 |
| *Intraparticle diffusion* | | | | |
| $k_{int}$ (mg/g. min)$^{1/2}$ | 7.732 ± 0.387 | 7.442 ± 0.387 | 11.147 ± 0.557 | 19.973± 0.999 |
| $C_i$ (mg/g) | 1.971 ± 0.0985 | 8.039 ± 0.401 | 6.461 ± 0.323 | 7.4874 ± 0.374 |
| $R^2$ | 0.885 | 0.929 | 0.877 | 0.879 |

#### *5.3.3.6 Desorption studies and mechanical stability of HCeFe NFs-2*

Regeneration of the utilised adsorbent is very important to assess its potential and costs effectiveness [43]. The adsorbent regeneration efficiency of HCeFe NFs-2 was evaluated by employing desorption-adsorption experiments. The adsorbent maintained its original efficiency up to two cycles as illustrated in Fig. 5.11(a).

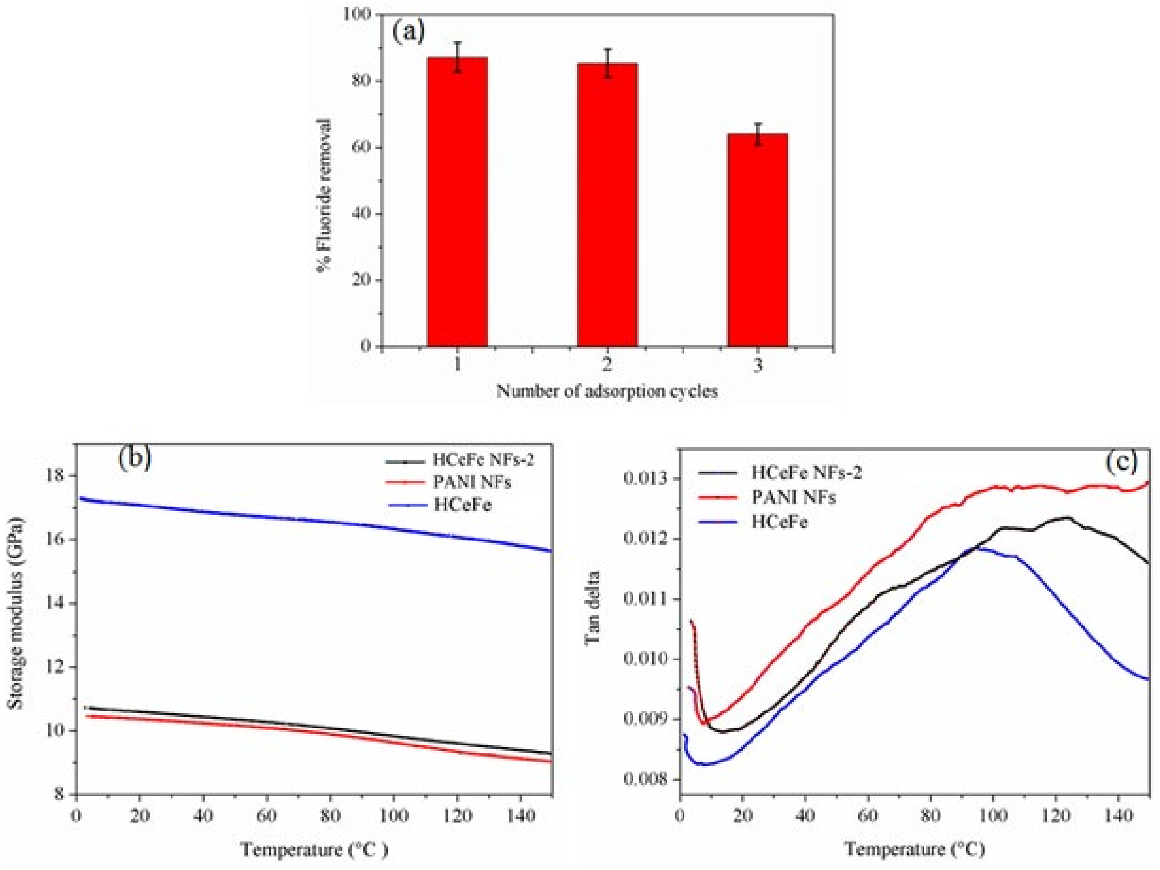

**Figure 5-11: (a) Adsorption and desorption cycles of HCeFe NFs-2 composite; Variation of (b) storage modulus and (c) tan δ against temperature for PANI NFs, HCeFe NFs-2 and HCeO$_2$-Fe$_3$O$_4$ adsorbents.**

In the third cycle a reduction to 64.2% is observed. This suggests that HCeFe NFs-2 can be used for 3 consecutive adsorptions-desorption cycles. The dynamic mechanical analysis of PANI NFs, HCeFe NFs-2 and bimetal oxides HCeFe NPs is shown in Fig. 5.11(b) and (c). The results revealed that HCeFe NFs-2 displays better mechanical properties than PANI NFs. For the complete temperature array tested, the storage modulus of HCeFe NFs-2 was slightly higher relative to PANI NFs [Fig. 5.11(b)]. This observation is attributed to the presence of nanometal oxides, which restrict the mobility of PANI macromolecular chains in HCeFe NFs-2 [44,45]. An opposite trend to the variation in storage modulus was observed for the loss factor, tan δ as shown in Fig. 5.11(c). The tan δ, represents the proportion of the loss modulus to the storage modulus and is strongly related to structural transformations. The tan δ data of HCeFe NFs-2 were found to be lower than those of PANI NFs, indication that the presence of metal oxides in HCeFe NFs-2 serves as reinforcement in the PANI matrix and decreases damping behaviour [46].

### *5.3.3.7 Effect of co-existing ions*

Numerous ions are simultaneously present in natural water and wastewater systems. The effect of several anions like sulphate ($SO_4^{2-}$), chloride ($Cl^-$), bicarbonate ($HCO_3^-$), phosphate ($PO_4^{3-}$) and nitrate ($NO_3^-$) on the $F^-$ adsorption onto HCeFe NFs-2 is illustrated in Fig. 5.12(a). The sorption of $F^-$ ions is influenced by

$SO_4^{2-}$, $HCO_3^-$ and $PO_4^{3-}$ ions, with $PO_4^{3-}$ ions having the greatest effect. $F^-$ uptake decreased from 84.47 to 35.80% when phosphate ions increased from 0 to 40 mg/L. The order of interference was $PO_4^{3-} > HCO_3^- > SO_4^{2-} > NO_3^- > Cl^-$. The $Cl^-$ and $NO_3^-$ ions had very little interference as they are well known as low affinity ligands, forming outer-sphere complexes with active sites on the surface of the adsorbent [2]. This order of interference is closely related to the Z/R (charge/radius) values of the anions $PO_4^{3-}$ (3/3.40) > $SO_4^{2-}$ (2/2.40) > $Cl^-$ (1/1.18) > $NO^{-}_{3}$ (1/2.81). Fortunately, the concentration of $PO_4^{3-}$ ions in drinking water is ordinarily depressed hence its competitive impact on $F^-$ ions removal may be minimal [43,47,48].

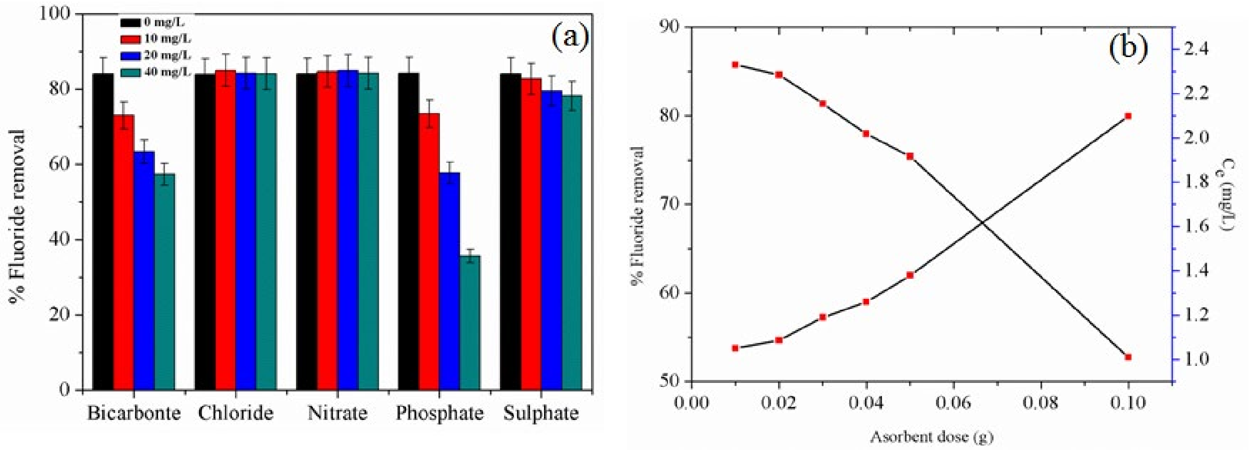

**Figure 5-12: (a) Effect of co-existing ion on the adsorption of $F^-$ ions at pH = 6.0 ± 0.2, adsorbent dose of 0.03 g per 50 mL of solution at 25°C and (b) Effect of adsorbent dose on % $F^-$ ions removal and equilibrium $F^-$ ions concentration using field collected fluoride-containing water sample.**

#### *5.3.3.8 Performance on natural water samples*

The potential applicability of HCeFe NFs-2 composite for real $F^-$ containing samples from a shallow well at Nemutenzi village (444785E/7828266N), in Nyanyadzi/Hot Spring area of Manicaland Province of Zimbabwe was evaluated. This was done by spiking well water to increase its concentration of $F^-$ ions from 2.96 mg/L to 5.0 mg/L. Other characteristics of this water were pH = 7.4, $PO_4^{3-}$ 1.31 mg/L, $SO_4^{2-}$ 12.67 mg/L, $NO_3^-$ 1.70 mg/L and electrical conductivity 750 µS/cm. The adsorbent mass was varied from 0.01 to 0.1 g, using 50 mL $F^-$ ions solution at pH 7.4 and 25°C for 24 hours in batch adsorption. Fig. 5.12(b) shows the influence of adsorbent dose on % $F^-$ ions removal and equilibrium $F^-$ ions concentration. It was found that 0.1 g of HCeFe NFs-2 achieved $F^-$ ions removal up to a concentration of 1.00 mg/L, below the stipulated standard permissible limit of 1.5 mg/L [15,49].

#### *5.3.3.9 Adsorption mechanism*

The $pH_{pzc}$, FTIR and XPS results were employed to provide the plausible adsorption mechanism. From Fig. 5.8(b), it was observed earlier that the percentage of $F^-$ ions removal was high from pH 3 to10. However, a drastic decrease was experienced with further increase in pH. At pH < $pH_{pzc}$, protonation encourages development of positively charged $MOH_2^+$ and $NH^+$ groups, hence $F^-$ ions adsorption is probably occurring through coulombic attractions [15,25,50]. Solution pH measurements before and after adsorption showed an increase in pH, implying that hydroxyl groups were perhaps being released as a result of ionic exchange [51]. At high solution pH > $pH_{pzc}$ the adsorbent surface is predominantly negatively charged and electric repulsion is set to take place. Thus, the only conceivable $F^-$ removal arising is through ions exchange between $F^-$ and surface-bonded OH groups [15,49,52], together with $Cl^-$ counter ions doping the PANI NFs moiety [42].

These proposed mechanisms are in agreement with the FTIR spectrum and XPS data. FTIR spectrum of HCeFe NFs-2 after adsorption (Fig. 5.2(B)(c)), showed that the bands at 3227, 1118 and 1076 $cm^{-1}$ shifted to 3204, 1090 and 1067 $cm^{-1}$, respectively. In addition, the weakening of these bands indicates reduction in the amount of surface hydroxyl groups after $F^-$ ions adsorption, certainly as a result of substitution during the adsorption process. The XPS spectra of Ce 3d in Fig. 5.13(a) and (b) show the presence of both Ce(VI) and Ce(III) in HCeFe NFs-2 adsorbent. Before adsorption, as shown in Fig. 5.13(a), peaks at 882.5, 885.3, 898.5 and 903.8 eV are observed. The peaks at 882.5 and 898.5 eV are ascribed to Ce(IV) $3d_{5/2}$ and $3d_{3/2}$, respectively. The peaks at 885.3 and 903.8 eV are attributed to Ce(III) $3d_{5/2}$ and $3d_{3/2}$ [14,16,50].

After fluoride adsorption, the peaks at 882.5, 885.3 and 903.8 eV shifted to higher energy 883.1, 886.7 and 905.5 eV, respectively. This exposes a possibility of OH bonded to Ce(III) and Ce(IV) contributing to the $F^-$ ions adsorption [14,15,48,50]. The binding of electronegative fluoride onto Ce leads to a decrease in its electron density, hence a shift in the Ce(IV) $3d_{5/2}$ and Ce(III) $3d_{3/2}$ binding energies [48]. The Fe 2p core level spectrum for HCeFe NFs-2, on the other hand, exhibits contribution of $2p_{1/2}$ and $2p_{3/2}$ components with binding energies of 710.3, 713.7, 723.6 and 725.8 eV, corresponding to $Fe^{2+}$ $2p_{3/2}$, $Fe^{3+}$ $2p_{3/2}$, $Fe^{2+}$ $2p_{1/2}$ and $Fe^{3+}$ $2p_{1/2}$, respectively as shown in Fig. 5.13(c) [16,53]. Hence, this analysis reveals the stability of $Fe_3O_4$ chemical states in the HCeFe NFs-2 adsorbent. Although no significant change was observed on the Fe 2p core level spectrum after adsorption, this ferroferric oxide is set to form solid solution with $CeO_2$. This effect leads to increased surface area as well as the amount of binding sites for $F^-$ ions adsorption.

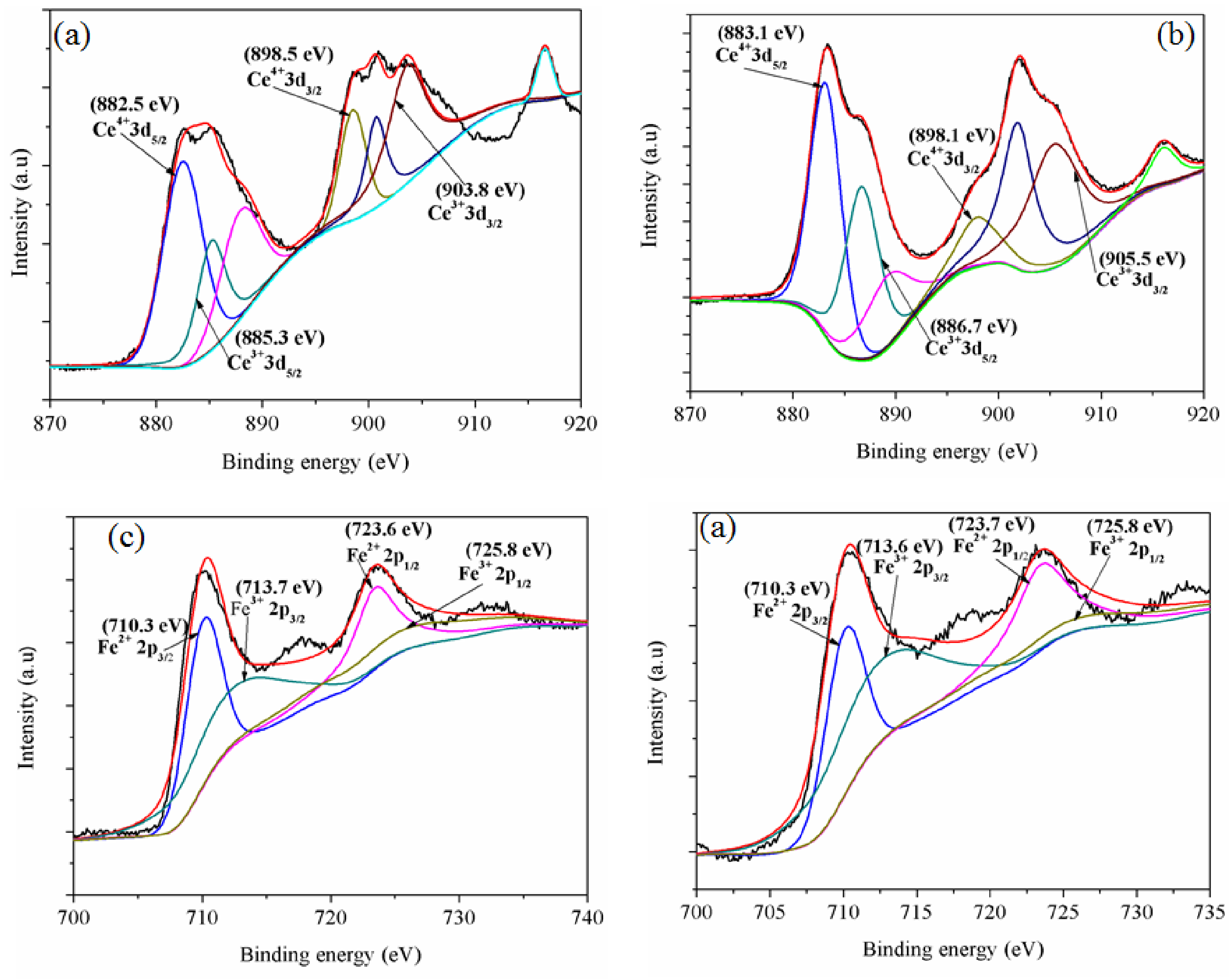

**Figure 5-13: XPS core level spectra of (a) and (b) Ce 3d before and after adsorption; (c) and (d) Fe 2p before and after adsorption.**

A step further, the N 1s core level spectra of HCeFe NFs-2 adsorbent before and after the adsorption procedure are presented in Fig. 5.14(a) and (b). The spectrum before adsorption shows binding energies at 398.3, 399.1 and 400.0 eV, ascribed to the quinonoid imine (=N-), benzenoid amine (- NH-) and positively charged doped imine ($-NH^{+\cdot}$), respectively. There is a noteworthy change in the positively charged doped imine binding energy from 400.0 to 400.3 eV. The latter exerts an attractive interaction to the counter ion $Cl^-$ ions which are substituted by the extremely electronegative $F^-$ ions during adsorption [25,54]. This statement is in good agreement with the reduction in Cl 2p peak intensity in the wide scan spectrum of HCeFe NFs-2, after $F^-$ adsorption (Fig. 5.3(A)(b)). The deconvoluted spectra of O 1s before and after adsorption are shown in Fig. 5.14(c) and (d). The peaks corresponding to oxygen of Ce/Fe oxides (M-O), adsorbent surface hydroxyl groups (M-OH) and $H_2O$ are evidenced [14,16,49,50]. Moreover, the peak area of M-O increased from 23.35 to 31.12% whilst that of M-OH decreased from 58.77 to 41.90%.

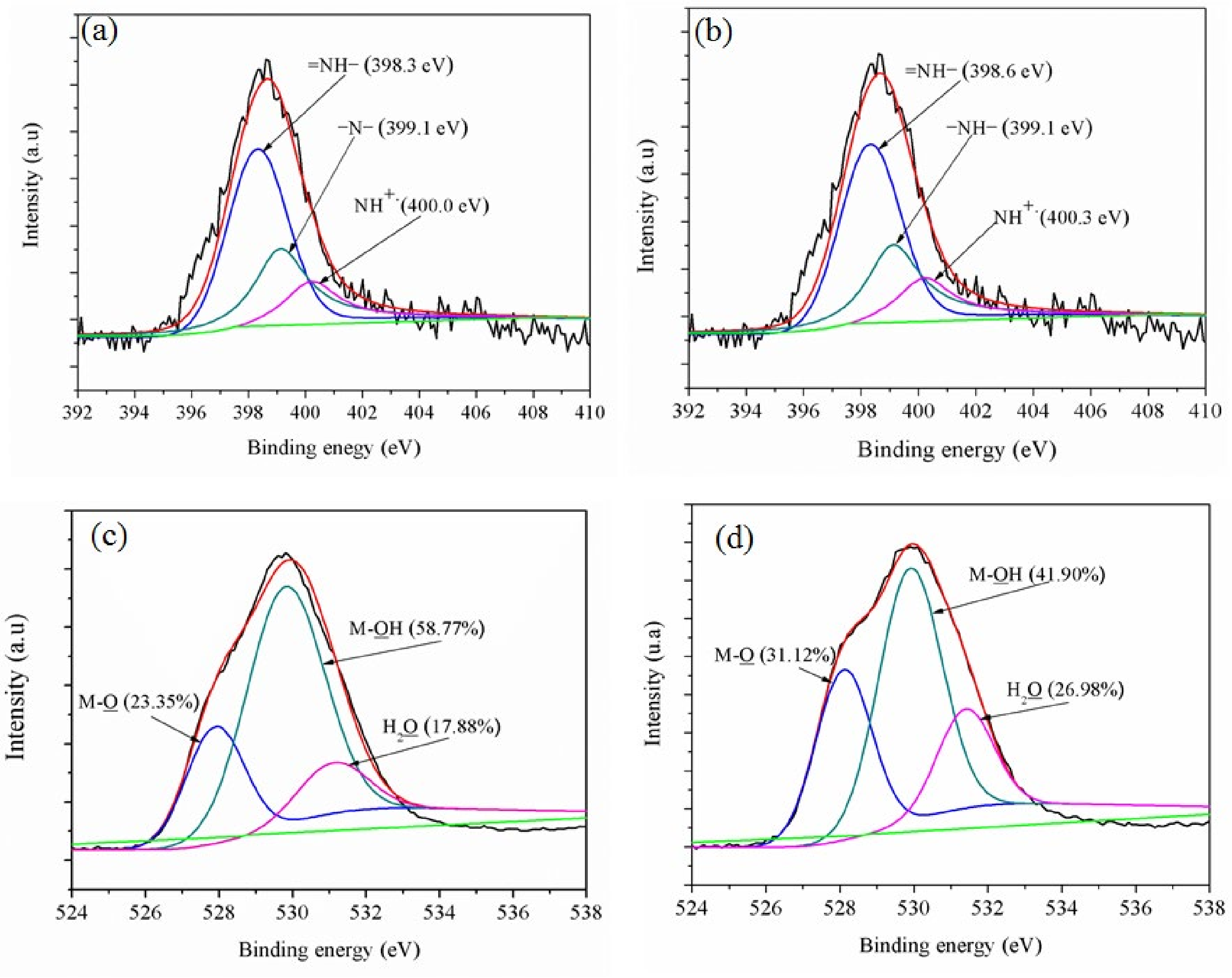

**Figure 5-14: XPS spectra of (a) and (b) N 1s before and after adsorption; (c) and (d) O 1s before and after adsorption.**

The decrease in M-OH peak area is certainly attributed to the participation of these hydroxyl groups in the adsorption of $F^-$ ions. This reaffirms an ionic exchange mechanism [41,43,54].

Therefore, the plausible reaction mechanisms are as follows:

$$\left[\begin{array}{lcl} MOH_2^+ + F^- & \longrightarrow & MOH_2^+..F^- \\ NH^+ + F^- & \longrightarrow & NH^+..F^- \end{array}\right] \quad \textbf{Electrostatic attraction}$$

$$\left[\begin{array}{lcl} MOH + F^- & \longrightarrow & MF + OH^- \\ NH^+Cl^- + F^- & \longrightarrow & NH^+F^- + Cl^- \end{array}\right] \quad \textbf{Ion exchange}$$

## 5.4 SUMMARY

In this study, a series of HCeFe NFs was prepared by fast polymerisation of aniline and subsequent co-precipitation deposition of $CeO_2$-$Fe_3O_4$ on the PANI NFs. The novel nanocomposites were tested for their potential to serve as adsorbents in water defluoridation process, as opposed to conventional PANI or well reported nanometal oxides. The optimized adsorbent HCeFe NFs-2 with 66 $m^2/g$ BET surface area exhibited good $F^-$ ions removal over a broad pH range 3-10. The Langmuir isotherm described the adsorption well and implied monolayer adsorption with maximum capacity of 116.28 mg/g at pH 6.0 ± 0.2 and 25°C. The thermodynamic parameters indicated to the exothermic and spontaneous nature of the process. The relatively rapid kinetics of $F^-$ ions adsorption onto HCeFe NFs-2 composite conformed to the pseudo-second-order model. According to FTIR and XPS spectra analysis, together with $pH_{pzc}$ measurement, the mechanism involved both electrostatic attraction and ion exchange. The regeneration study indicated that this material could be used in three consecutive cycles before being discarded. Batch treatment of 50 mL spiked groundwater samples with 0.1 g of HCeFe NFs-2 reduced the $F^-$ ions level from 5.00 mg/L to 1.00 mg/L, below the WHO permissible level. Henceforth, this material can serve as suitable alternative for defluoridation of drinking water. Further investigation on the application of HCeFe NFs-2 for large scale water treatment could be assessed in fixed-bed column dynamic system.

## 5.5 REFERENCES

[1] S. Ayoob, A.K. Gupta, V.T. Bhat, A conceptual overview on sustainable technologies for the defluoridation of drinking water, Crit. Rev. Environ. Sci. Technol. 38 (2008) 401-470.

[2] K. Parashar, N. Ballav, S. Debnath, K. Pillay, A. Maity, Hydrous titanium oxide@polypyrrole hybrid nanocomposite as an efficient selective scavenger for the defluoridation of drinking water, RSC Adv. 6 (2016) 99482-99495.

[3] G. Biswas, M. Kumari, K. Adhikari, S. Dutta, A Critical Review on Occurrence of Fluoride and Its Removal through Adsorption with an Emphasis on Natural Minerals, Curr. Pollution Rep. 3 (2017) 104-119.

[4] R.A. Fallahzadeh, M. Miri, M. Taghavi, A. Gholizadeh, R. Anbarani, A. Hosseini-Bandegharaei, M. Ferrante, G.O. Conti, Spatial variation and probabilistic risk assessment of exposure to fluoride in drinking water, Food Chem. Toxicol. 113 (2018) 314-321.

[5] S. Kumari, S. Khan, Defluoridation technology for drinking water and tea by green synthesized $Fe_3O_4/Al_2O_3$ nanoparticles coated polyurethane foams for rural communities, Sci. Rep. 7 (2017) 8070.

[6] K. Parashar, N. Ballav, S. Debnath, K. Pillay, A. Maity, Rapid and efficient removal of fluoride ions from aqueous solution using a polypyrrole coated hydrous tin oxide nanocomposite, J. Colloid Interface Sci. 476 (2016) 103-118.

[7] Y. Zhang, X. Lin, Q. Zhou, X. Lou, Fluoride adsorption from aqueous solution by magnetic core-shell $Fe_3O_4$@alginate-La particles fabricated via electro-coextrution, Appl. Surf. Sci. 389 (2016) 34-45.

[8] M. Bhaumik, T.Y. Leswifa, A. Maity, V.V. Srinivasu, M.S. Onyango, Removal of $F^-$ from aqueous solution by polypyrrole/$Fe_3O_4$ magnetic nanocomposite, J. Hazard. Mater. 186 (2011) 150-159.

[9] A. Bhatnagar, E. Kumar, M. Sillanpää, Fluoride removal from water by adsorption-a review, Chem. Eng. J. 171 (2011) 811-840.

[10] L.H. Velazquez-Jimenez, E. Vences-Alvarez, J.L. Flores-Arciniega, H. Flores-Zuñiga, J.R. Rangel-Mendez, Water defluoridation with special emphasis on adsorbents-containing metal oxides and/or hydroxides: A review, Sep. Purif. Technol. 150 (2015) 292-307.

[11] A.M. Rauchir, M.J. Basu, Adsorption of fluoride onto mixed rare earth metal oxides, Sep. Purif. Technol. 24 (2001) 122-127.

[12] M. Karthekeyan, K.S. Kumar, K.P. Elango, Conducting polymer/alumina composites as viable adsorbents of fluoride ions from aqueous solution, J. Fluorine Chem. 130 (2009) 894-901.

[13] M. Chigondo, H.K. Paumo, M. Bhaumik, K. Pillay, A. Maity, Rapid high adsorption performance of hydrous cerium-magnesium oxides for removal of fluoride from water, J. Mol. Liq. 265 (2018) 496-509.

[14] S. Deng, H. Liu, W. Zhou, J. Huang, G. Yu, Mn-Ce oxide as a high-capacity adsorbent for fluoride removal from water, J. Hazard. Mater. 186 (2011) 1360-1366.

[15] K. Mukhopadhyay, A. Ghosh, S.K. Das, B. Show, P. Sasikumar, U.C. Ghosh, Synthesis and characterisation of cerium(IV)-incorporated hydrous iron(III) oxide as an adsorbent for fluoride removal from water, RSC Adv. 7 (2017) 26037-26051.

[16] D. Tang, G. Zhang, Efficient removal of fluoride by hierarchical Ce-Fe bimetal adsorbent: thermodynamics, kinetics and mechanism, Chem. Eng. J. 283 (2016) 721-729.

[17] H. Liu, L. Deng, Z. Li, G. Yu, J. Huang, Preparation of Al-Ce hybrid adsorbent and its application for defluoridation of drinking water, J. Hazard. Mater. 179 (2010) 424-430.

[18] N. Chubar, New inorganic ion exchangers based on Mg-Al hydrous oxides: (Alkoxide-free) sol-gel synthesis and characterization, J. Colloid Interface Sci. 357 (2011) 198-209.

[19] X. Dou, Y. Zhang, H. Wang, T. Wang, Y. Wang, Performance of granular zirconium-iron oxide in the removal of fluoride from drinking water, Water Res. 45 (2011) 3571-3578.

[20] X. Zhao, J. Wang, F. Wu, T. Wang, Y. Cai, Y. Shi, G. Jiang, Removal of fluoride from aqueous media by $Fe_3O_4$@$Al(OH)_3$ magnetic nanomaterials, J. Hazard. Mater. 173 (2010) 102-109.

[21] S. Alemu, Mulugeta, F. Zewge, B.S. Chandravanshi, Water defluoridation by aluminium oxide-manganese oxide composite material, Environ. Technol. 35 (2014) 1893-1903.

[22] M. Hua, S. Zhang, B. Pan, W. Zhang, L. Lv, Q. Zhang, Heavy metal removal from water/wastewater by nanosized metal oxides: A review, J. Hazard. Mater. 211 (2012) 317-331.

[23] S. Sakar, E. Guibal, F. Quignard, A.K. Sen Gupta, Polymer-supported metals and metal oxide nanoparticles: synthesis, characterisation and applications, J. Nanopart. Res. 14 (2012) 715.

[24] L. Tang, Y. Fang, Y. Pang, G. Zeng, J. Wang, Y. Zhou, Y. Deng, G. Yang, Y. Cai, J. Chen, Synergistic adsorption and reduction of hexavalent chromium using highly uniform polyaniline-magnetic mesoporous silica composite, Chem. Eng. J. 254 (2014) 302-312.

[25] K. Parashar, N. Ballav, S. Debnath, K. Pillay, A. Maity, Hydrous $ZrO_2$ decorated polyaniline nanofibres: Synthesis, characterization and application as an efficient adsorbent for water defluoridation, J. Colloid Interface Sci. 508 (2017) 342-358.

[26] M. Karthekeyan, K.S. Kumar, K.P. Elango, Batch sorption studies on the removal of fluoride ions from water using eco-friendly conducting polymer/bio-polymer composites, Desalination 267 (2011) 49-56.

[27] S. Mandal, S.S. Mahapatra, R.K. Patel, Enhanced removal of Cr(VI) by cerium oxide polyaniline composite: Optimization and modeling approach using response surface methodology and artificial neural networks, J. Environ. Chem Eng. 3 (2015) 870-885.

[28] A.H. Elsayed, M.M. Eldin, A.M. Elsyed, A.H. Alazm, E.M. Younes, H.A. Motaweh, Synthesis and characterisation of polyaniline/ferrites nanocomposites, Int. J. Electrochem. Sci. 6 (2011) 206-209.

[29] S.B. Kondawar, S.P. Agrawal, S.H. Nimkar, H.J. Sharma, P.T. Patil, Conductive polyaniline-tin oxide nanocomposites for ammonia sensor, Adv. Mater. Lett. 3 (2012) 393-398.

[30] L. Liu, Z. Cui, Q. Ma. W. Cui, X. Zhang, One-step synthesis of magnetic iron-aluminium oxide/graphene oxide nanoparticles as selective adsorbent for fluoride removal form aqueous solution, RSC Adv. 8 (2016) 10783-10791.

[31] M. Bhaumik, R.I. McCrindle, A. Maity, S. Agarwal, V.K. Gupta, Polyaniline nanofibers as highly effective re-usable adsorbent for removal of reactive black 5 from aqueous solutions, J. Colloid Interface Sci. 466 (2016) 442-451.

[32] R. Li, Y. Wang, C. Zhou, C. Wang, X. Ba, Y. Li, X. Huang, J. Liu, Carbon-stabilized high-capacity ferroferric oxide nanorod array for flexible solid-state alkaline battery-supercapacitor hybrid device with high environmental suitability, Adv. Funct. Mater. 25 (2015) 5384-5394.

[33] S.K. Swain, T. Patnaik, P.C. Patnaik, U. Jha, R.K. Dey, Development of new alginate entrapped Fe(III)-Zr(IV) binary mixed oxide for removal of fluoride from water bodies, Chem. Eng. J. 215-216 (2013) 763-771.

[34] L. Liu, Z. Cui, Q. Ma. W. Cui, X. Zhang, One-step synthesis of magnetic iron-aluminium oxide/graphene oxide nanoparticles as selective adsorbent for fluoride removal form aqueous solution, RSC Adv. 8 (2016) 10783-10791.

[35] I. Saha, I. Ghosh, D. Nandi, K. Gupta, D. Chatterjee, U.C. Ghosh, β-Cyclodextrin modified hydrous zirconium oxide. Synthesis, characterization and defluoridation performance from aqueous solution, Chem. Eng. J. 263 (2015) 220-230.

[36] E. Vences-Alvarez, L.H. Velazquez-Jimenez, L.F. Chazaro-Ruiz, P.E. Diaz-Flores, J.R. Rangel-Mendez, Fluoride removal in water by a hybrid adsorbent lanthanum-carbon, J. Colloid Interface Sci. 455 (2015) 194-202.

[37] K.Y. Foo, B.H. Hameed, Insights into modelling of isotherm adsorption systems, Chem. Eng. J. 156 (2010) 2-10.

[38] H.M. Cai, G.J. Chen, C.Y. Peng, Z.Z. Zhang, Y.Y. Dong, G.Z. Shang, X.H. Zhu, H.J. Gao, X.C. Wan, Removal of fluoride from drinking water using tea waste loaded with Al/Fe oxides: A novel, safe and efficient biosorbent, Appl. Surf. Sci. 328 (2015) 34-44.

[39] N.H. Kera, M. Baumik, N. Ballav, K. Pillay, S.S. Ray, A. Maity, Selective removal of Cr(VI) from aqueous solution by polypyrrole/2.5-diaminobenzene sulfonic acid composite, J. Colloid Interface Sci. 475 (2016) 144-157.

[40] X. Dou, D. Mohan, C.U. Pittaman Jr, S. Yang, Remediating fluoride from water using hydrous Zirconium oxide, Chem. Eng. J. 198 (2012) 236-245.

[41] J. Wang, W. Xu, L. Chen, Y. Jia, X.J. Huang, J. Lui, Excellent fluoride removal performance by $CeO_2$ and $ZrO_2$ nanocages in water environment, Chem. Eng. J. 231 (2013) 195-205.

[42] S.K. Swain, S. Mishra, T. Patnaik, R.K. Patel, U. Jha, R.K. Dey, Fluoride removal performance of a new hybrid sorbent of Zr (IV)-ethylenediamine, Chem. Eng. J. 184 (2012) 72-81.

[43] A. Azari, R.R. Kalantary, G. Ghanizadeh, B. Kakavandi, M. Farzadkia, E. Ahmadi, Iron-silver oxide nanoadsorbent synthesized by co-precipitation process for fluoride removal from aqueous solution and its adsorption mechanism, RSC Adv. 5 (2015) 87377-87391.

[44] B.C. Anderson, P.D. Bloom, K.G. Baikerikar, V.V. Sheares, S.K. Mallapragada, Al-Cu-Fe quasicrystal/ultra-high molecular weight polyethylene composites as biomaterials for acetabular cup prosthetics, Biomaterials 23 (2002) 1761-1768.

[45] E. Kontou, M. Niaounakis, Thermo-mechanical properties of LLDPE/$SiO_2$ nanocomposites, Polymer 47 (2006) 1267-1280.

[46] T. Kuila, S. Bose, A.K. Mishra, P. Khanra, N.H. Kim, J.H. Lee, Effect of functionalized graphene on the physical properties of linear low density polyethylene nanocomposites, Polym. Test. 31 (2012) 31-38.

[47] Y. Zhang, M. Yang, X. Huang, Arsenic removal with Ce(VI) doped with Fe oxide adsorbent, Chemophore 51 (2003) 945-852.

[48] Z. Yu, C. Xu, K. Yuan, X. Gan, C. Feng, X. Wang, L. Zhu, G. Zhang, D. Xu, Characterization and adsorption mechanism of $ZrO_2$ mesoporous fibers for health-hazardous fluoride removal, J. Hazard. Mater. 346 (2018) 82-92.

[49] J. Zhu, X. Lin, P. Wu, Q. Zhou X. Luo, Fluoride removal from aqueous solution by Al(III)-Zr(VI) binary oxide adsorbent, App. Surf. Sci. 357 (2015) 91-100.

[50] A. Dhillon, S.K. Soni, D. Kumar, Enhanced fluoride removal performance by Ce-Zn binary metal oxide: Adsorption characteristics and mechanism, J. Fluorine Chem. 199 (2017) 67-76.

[51] L. Li, Q. Zhu, K. Man, Z. Xing, Fluoride removal from liquid phase by Fe-Al-La tri-metal hydroxides adsorbent prepared by iron and aluminium leaching from red mud, J. Mol. Liq. 237 (2017) 164-172.

[52] H.X. Wu, T.J. Wang, L. Chen, Y. Jin, Y. Zhang, X.M. Dou, The roles of the surface charge and hydroxyl group on a Fe-Al-Ce adsorbent in fluoride adsorption, Ind. Eng. Chem. Res. 48 (2009) 4530-4534.

[53] Q. Ke, C. Tang, Y. Liu, H. Liu, J. Wang, Intercalating graphene with clusters of $Fe_3O_4$ nanocrystals for electrochemical supercapacitors, Mater. Res. Express, 1 (2014) 025015.

[54] E. Binkauskienė, V. Jasulaitienė, A. Lugauskas, Effect of Aspergillus niger Tiegh. L-10 on the physical and chemical properties of a polyaniline coating in the growth substrate, Synth. Met. 159 (2009)1365-136

# CHAPTER 6: RAPID HIGH ADSORPTION PERFORMANCE OF HYDROUS CERIUM-MAGNESIUM OXIDES FOR REMOVAL OF FLUORIDE FROM WATER

## 6.1 INTRODUCTION

Fluoride ions ($F^-$) are abundantly present in drinking water and can either be beneficial or detrimental to the human health, depending on the concentration and amounts ingested [1,2]. For instance, $F^-$ concentrations of 0.8-1.0 mg/L can prevent tooth decay and contribute to the development of strong bones, especially in young children [3,4]. However, exposure to high levels of $F^-$ can result in health disorders such as dental and skeletal fluorosis [5]. The World Health Organization (WHO) has restricted acceptable $F^-$ limit concentrations in drinking water between 0.5 and 1.5 mg/L [6]. The main sources of fluoride pollution are naturogenic. However, anthropogenic sources, including wastewater discharge from manufacturing of coal, aluminium and zinc contribute significantly in fluoridation of water bodies [7,8]. A variety of methods that can be used to reduce the level of $F^-$ ions in aqueous solution have been developed. These include coagulation, precipitation, membrane process, electrochemical treatment, ion exchange and adsorption [9-13]. Of all these, adsorption has been identified as the most suitable technique because of the simple design, ease operation procedure and cost-effectiveness [14]. An array of adsorbents, ranging from activated charcoal, coal fly ash, chitosan, charcoal, shells, alumina brick powder, polymers, zeolites, agricultural waste, carbon nanotubes and many others, have also been employed [8,9,15]. However, besides being soluble in aqueous medium, some of these materials also display very low efficiency, resulting in secondary pollution [16].

Nano-metal oxides are one example of inorganic nanomaterials that have attracted much attention and appear to be very promising adsorbents for removing $F^-$ ions. They exhibit remarkable properties such as large surface areas, increased number of easily accessible binding sites, good acid-basic properties and high adsorption efficiencies [8,10,11,16,17]. The nano-sized metal oxides reported in the literature for defluoridation include Fe, Mn, Al, Ti, Ca, Mg, and Zr oxides [18–20]. It has also been observed that rare earth metal oxides have high sorption capacities for $F^-$ ions removal [18,20,21]. However, these metals are expensive to be used on their own as sole oxide adsorbents. Moreover, their optimum adsorption pH range is more acidic and may likely induce their dissolution [22-24]. To reduce the cost related with rare metal oxides, they are usually doped or combined with relatively less expensive metals oxides [18,22,23,24,25]. $CeO_2$, as the least soluble among rare metal oxides, has found wide applications in the removal of pollutants, including $F^-$ ions [24]. Although its preparation method in most reported cases involve energy consuming technique; cheap, limited aqueous solubility and nontoxic MgO has equally been reported as highly efficient adsorbent in defluoridation [18,26,27].

Taking into consideration the fact that the preparation cost of nano-metal oxides impacts the total cost of the treatment process, synthetic methods which required expensive reactants or high temperatures were not considered as models. Co-precipitation is a simple method that uses metal salts precursors rather than expensive metal alkoxides and organic solvents [27,28]. This study reports the synthesis of a series of Ce-Mg bimetal oxides by simple co-precipitation method and the application of the optimized nanocomposite in $F^-$ remediation. The effect of adsorbent dose, contact time, solution pH, initial concentration, temperature and competing ions on adsorption of $F^-$ onto the optimized adsorbent was studied. The kinetics and thermodynamics of the adsorption process were also investigated. Regeneration study as well as field feasibility assay were performed using the synthesized ideal adsorbent.

## 6.2 MATERIALS AND METHODS

### 6.2.1 Synthesis of hydrous cerium-magnesium oxides composite

A facile co-precipitation method was employed for the synthesis of hydrous Ce-Mg bimetal oxides (HCeMgO). In a typical synthetic procedure, 0.04 moles of $Ce(NO_3)_3{\cdot}6H_2O$ and 0.04 moles of $Mg(NO_3)_3{\cdot}6H_2O$ (analytical grade, Sigma-Aldrich, USA) were dissolved in 400 mL of deionized water. Then, 64 mL of 2M NaOH (analytical grade, Sigma-Aldrich, USA) aqueous solution was added dropwise under magnetic stirring to adjust the pH to 10 at ambient temperature. The resulting precipitate was vigorously stirred for 1 h, aged for 24 h, centrifuged, washed three times with deionised water, dried for additional 24 h in an oven set at 100°C, and finally ground into a fine powder to afford HCeMgO1:1. Likewise, stirred mixtures of $Ce(NO_3)_3{\cdot}6H_2O$ and $Mg(NO_3)_3{\cdot}6H_2O$ with Ce:Mg molar ratio 2:1, 1:2, 1:3 and 80, 56, 40 mL of 2M NaOH were treated separately as described above to achieve HCeMgO 2:1, HCeMgO 1:2, and HCeMgO 1:3, respectively. To determine the optimum composite, these adsorbents as well as pure hydrous cerium oxide ($HCeO_2$) and hydrous magnesium oxide (HMgO) were examined in the adsorption of 10 mg/L of $F^-$ ions solution at pH = 5.5 and adsorbent dose of 0.03 g in 50 mL. The experimental results suggested that HCeMgO1:1 composite, obtained with less cerium salt, was the optimum adsorbent.

### 6.2.2 Characterization of HCeMgO1:1

The HCeMgO1:1 composite was characterized by several techniques. The FTIR spectra of optimised HCeMgO1:1 composite and $F^-$ ions loaded binary metal oxide (HCeMgO1:1+F) were obtained using a Perkin Elmer Spectrum 100 Spectrometer (Perkin Elmer, USA) in the range of 500-4000 $cm^{-1}$ with 4 $cm^{-1}$ resolution and 32 scans. The surface morphology and microstructure of HCeMgO1:1 composite were studied by FE-SEM and HR-TEM using Zeiss Auriga Cobra FIB microscope and a high resolution transmission electron microscope (JEOL-JEM 2100, Japan) with LaB6 filament operated at 200 kV, respectively. TGA and DTA experiments were performed in air at a flow rate of 50 mL/min and a heating rate of 10°C/min on TG Q500 (TA Instruments, USA). A Micrometrics ASAP 2020 gas adsorption apparatus (Micrometics, USA) using low temperature (-198.50°C) $N_2$ adsorption-desorption technique was used for BET surface area measurements. A PANalytical X'Pert PRO-diffractometer (PANalytical, The Netherlands) using CuKα radiation with a wavelength of 1.5505 Å with slits at 45 kV/30 mA and 2ϴ values ranging from 5 to 90 was used for the XRD characterization of the adsorbent. XPS studies were carried out on Kratos Axis Ultra device with Al monochromatic X-ray source (1486.6 eV) to establish the elemental composition of HCeMgO1:1 before and after $F^-$ adsorption. The point-of-zero charge was determined using a change in pH method with a Thermo Scientific pH meter.

### 6.2.3 Batch adsorption experiments

A 1000 mg/L stock solution of $F^-$ ions was prepared by dissolving 0.221 g of oven dried NaF (analytical grade, Sigma-Aldrich, USA) in 100 mL of deionised water. Solutions of NaF required for the $F^-$ ions adsorption experiments were prepared by appropriate dilutions from the 1000 mg/L stock solution. Adsorption studies were conducted in batch mode using polypropylene plastic bottles containing 50 mL of 10 mg/L $F^-$ solution which was contacted with 0.03 g adsorbent. The $F^-$/adsorbent suspensions were agitated in a temperature controlled water bath shaker at 200 rpm for 24 h at 25°C. The effect of pH on $F^-$ adsorption was studied by adjusting the pH (from 2-11) of $F^-$ solution using 0.1M HCl (analytical grade, Sigma-Aldrich, USA) and 0.1M NaOH solutions. Real field water samples containing 5 mg/L $F^-$ ions concentration were also tested for the removal of $F^-$ ions.

Determination of F$^-$ ions in the filtered samples was conducted using a fluoride ion-selective electrode (ThermoORION) in the form of conductance, as described elsewhere [22,25,29]. Calibration of this electrode was performed using 10.0, 1.0 and 0.1 mg/L of F$^-$ ions solutions with Total Ionic Strength Adjustment Buffer (TISAB II) reagent. The buffer was made by dissolving 58 g of NaCl and 57 mL of 99.99% glacial acetic acid in 500 mL of deionised water, adjusting the pH to 5.5 using 5 M NaOH followed by addition of deionised water to 1 L. The adsorption efficiency for F$^-$ ions removal was calculated using Eq.1:

$$\% \, removal = \left(\frac{C_o - C_e}{Co}\right) \times 100 \quad (1)$$

where $C_o$ and $C_e$ are the initial and equilibrium F$^-$ ions concentrations, respectively.
In the adsorbent dosage study effect, the amounts of optimised HCeMgO1:1 adsorbent were varied from 0.05 to 0.1 g with the same procedure followed as for the pH effect investigation.

The adsorption capacity of the adsorbent at equilibrium was determined from Eq. (2).

$$q_e = \left(\frac{C_o - C_e}{m}\right) V \quad (2)$$

where $q_e$ (mg/g) is the amount of F$^-$ ions at equilibrium per unit mass of adsorbent. $C_o$, $C_e$, $m$ and $V$ are the initial F$^-$ ions concentration, equilibrium F$^-$ ions concentration, adsorbent mass and volume of the sample in L, respectively.

The adsorption performance was further studied by investigating adsorption isotherms at 15, 25, 35 and 45°C using a Sep. Sci MRC Refrigerated Shaker Bath, South Africa and varying the initial F$^-$ ions concentration from 5-100 mg/L. The data obtained from the adsorption isotherm studies were used to calculate the thermodynamic parameters of the adsorption process such as Gibbs free energy ($\Delta G°$), enthalpy ($\Delta H°$) and entropy ($\Delta S°$) change. The kinetics of adsorption was also studied to predict the adsorption rate and modelling of adsorption based water treatment. These were conducted at concentrations of 10, 15, 25 and 40 mg/L for 0 to 160 minutes shaking time at optimised pH 5.5 and adsorbent dose 0.03 g in 50 mL. The samples were filtered and analysed for residual F$^-$ ions after treatment.

The adsorption capacity of the adsorbent ($q_t$) at time $t$ was obtained using Eq. (3):

$$q_t = (\frac{C_o - C_t}{m})\mathrm{V} \quad (3)$$

where $q_t$ (mg/g) is the amount of F$^-$ adsorbed per unit mass of the adsorbent at time $t$ and $C_t$ (mg/L) is the concentration of the F$^-$ ions at time $t$.

### *6.2.3.1 Effect of competing ions*

The possible interference presented by competing ions is a fundamental study because no single ion is found in isolation in natural water bodies. A mixture of ions such as Cl$^-$, $SO_4^{2-}$, $NO_3^-$, $HCO^-_3$ and $PO_4^{3-}$ are usually encountered in polluted water. This study was achieved by dissolving the precursor salts of the above-mentioned ions together with F$^-$ ions at 10, 20 and 40 mg/L concentrations in deionised water. The resultant solutions were each treated with the optimised adsorbent dose at the optimised pH for 24 h, followed by analysis of the residual F$^-$ ions.

### *6.2.3.2 Desorption and regeneration studies*

Successive adsorption and desorption studies were conducted to establish the reusability of the spent adsorbent. This was done by contacting 50 mL of 10 mg/L F$^-$ ions-containing solution with 0.03 g dose of adsorbent at pH 5.5. The F$^-$ ions loaded adsorbent was then treated with 0.05, 0.025, 0.05 and 0.1M NaOH solution. It was found that 0.1M NaOH produced the highest desorption ability. Hence, the latter NaOH concentration was used for four adsorption-desorption consecutive cycles.

## 6.3 RESULTS AND DISCUSSION

### 6.3.1 Adsorbent optimisation

To achieve the best performing composition of HCeMgO for $F^-$ ions removal, adsorbent optimisation experiments were conducted. Fig. 6.1 shows that the Ce-Mg ratio had a significant influence on adsorption efficiency. The highest sorption efficiency (76.8%) for the bimetal oxide obtained with less rare metal, was achieved at Ce/Mg salt molar ratio of 1:1, denoted as HCeMgO1:1. This ideal nanocomposite was adopted for all studies as it was expected to produce high adsorption. Moreover, $F^-$ ions adsorption removal efficiency of the binary HCeMgO1:1 differs from that of $HCeO_2$ (96.8%) by a small margin. Thus cost effectiveness could be achieved with HCeMgO1:1 for all adsorption studies.

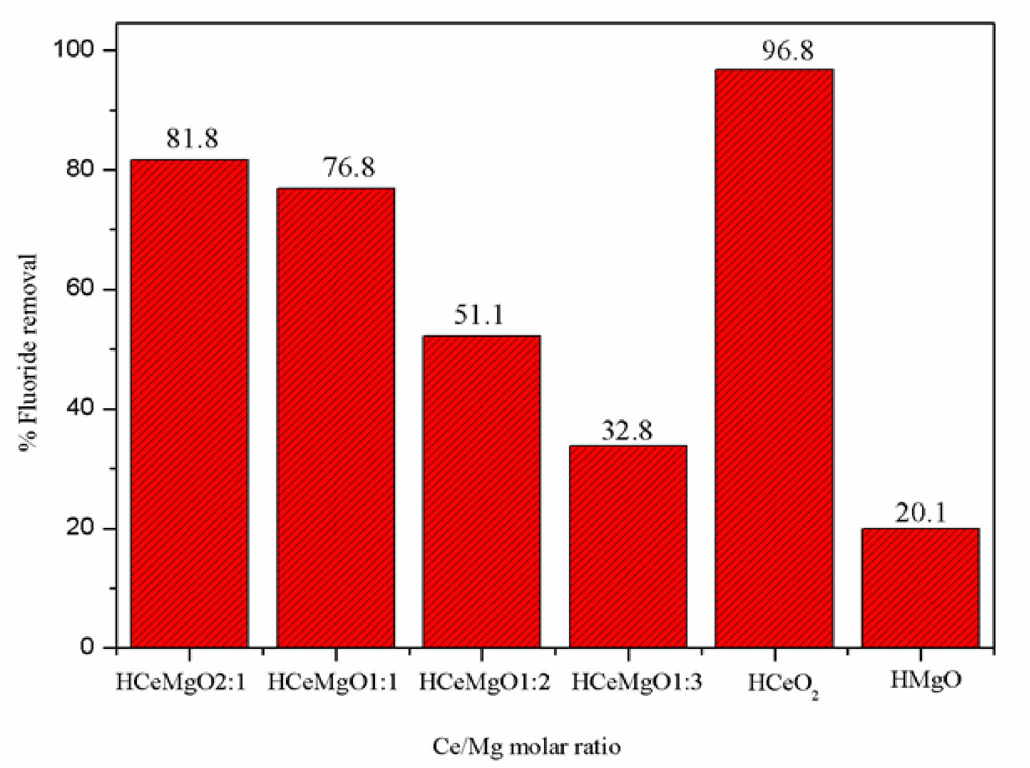

**Figure 6-1: Comparison of adsorption % of $F^-$ ions on hybrid adsorbent prepared at different Ce/Mg molar ratio. Sorption conditions: 0.03 g of adsorbent in 50 mL of 10 mg/L $F^-$ ions solution at pH 5.5 and 25°C for 24 h.**

### 6.3.2 Physico-chemical characterization

Fig. 6.2(A) shows the FTIR spectra of HCeMgO1:1 before and after $F^-$ ions adsorption. Observed bands at 657, 1358, 1635 and 3369 $cm^{-1}$ are signature bands of hydrous metal oxide present in HCeMgO1:1 [18, 22]. The bands at 3369 and 1635 $cm^{-1}$ are assigned to the stretching vibration of adsorbed water and bending vibration of hydroxyl groups, respectively [23]. The bands at 1512, 1412 and 1358 $cm^{-1}$ correspond to the lattice vibration of Ce-Mg mixed metals, while the band at 657 $cm^{-1}$ is attributed to metal-oxygen stretching [13]. After adsorption, bands at 3369 and 1635 $cm^{-1}$ shifted to 3410 $cm^{-1}$ and 1643 $cm^{-1}$, owing to the combined interaction of Ce-F and Mg-F bonds formation [21–23]. The disappearance of the band at 1358 $cm^{-1}$ after adsorption as well as the formation of a new band at 1309 $cm^{-1}$ affirms replacement of HCeMgO1:1 surface hydroxyl groups after $F^-$ ions adsorption process [2, 28]. XRD patterns of (a) HMgO (b) $HCeO_2$, (c) and (d) HCeMgO1:1 before and after $F^-$ ions adsorption are shown in Fig. 6.2(B). The diffraction peaks at 28.7, 33.1, 47.6 and 56.6° are characteristic of $CeO_2$ [20, 23, 24] and those at 20, 38, 50, 62.5 and 70° are typical peaks for HMgO [26-30]. The diffraction peaks of HCeMgO1:1 show a slight shift of patterns to wide angles (28.70, 33.70, 47.94, 56.78 and 76.89°), and high intensity relative to those of pristine $HCeO_2$, indicating the incorporation of $Mg^{2+}$ in the lattice structure of $CeO_2$ [23, 24].

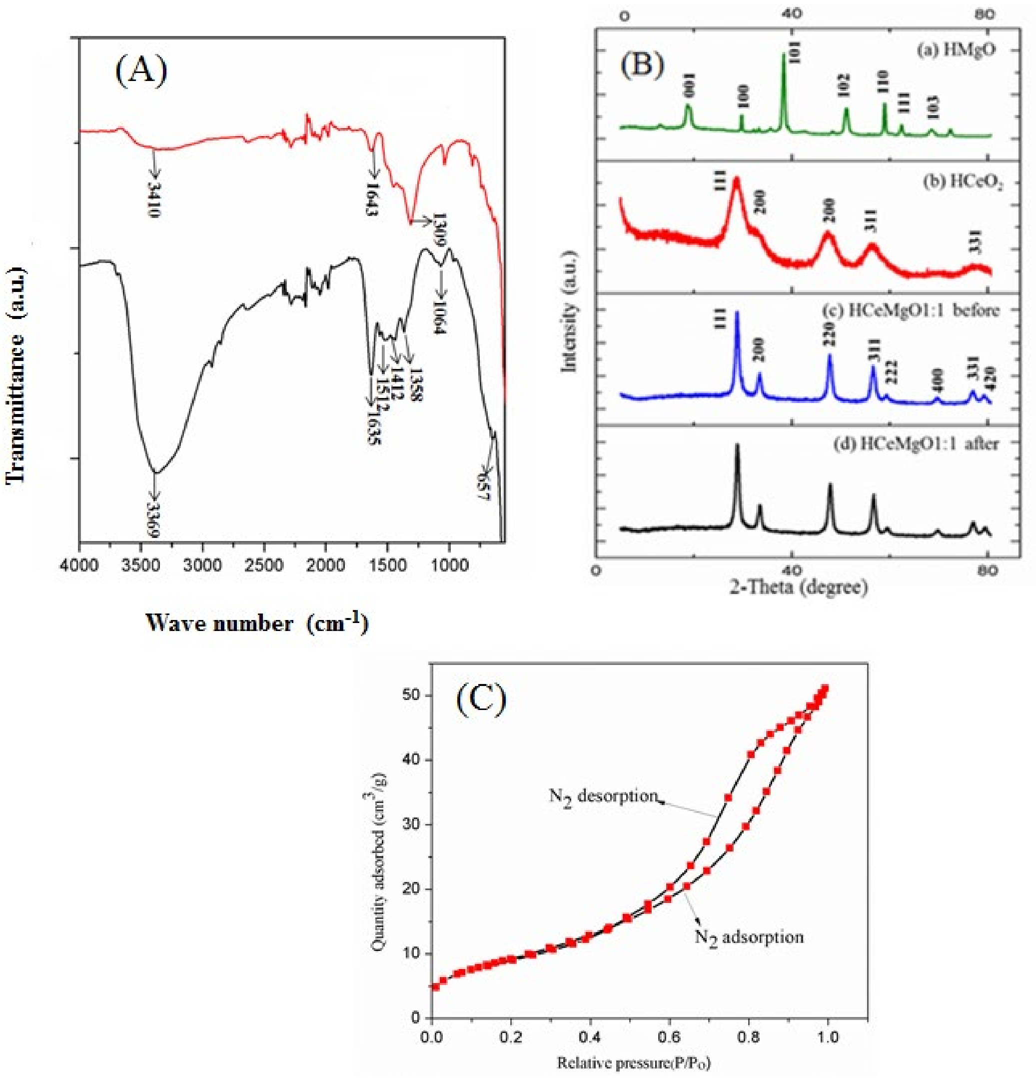

**Figure 6-2: FTIR spectra of (A) HCeMgO1:1 adsorbent before (a) and after (b) sorption (B) XRD patterns of (a) HMgO (b) $HCeO_2$ (c) and (d) HCeMgO1:1 before and after $F^-$ ions adsorption (C) $N_2$ adsorption-desorption isotherms of HCeMgO1:1.**

The HMgO peaks are hardly detected in the HCeMgO1:1 XRD pattern, probably as a result of the contraction of MgO unit cell after entering $CeO_2$ structure to form Ce-Mg solid solution and this can be attributed to the smaller ionic radius of $Mg^{2+}$ (0.072 nm) relative to that of $Ce^{4+}$ (0.097 nm) [20, 23, 28]. An amorphous phase of MgO may also have resulted in the HCeMgO1:1 adsorbent [23]. This analysis indicates that both HMgO and $HCeO_2$ are incorporated in the new structure. On the other hand, the XRD patterns of HCeMgO1:1 before [Fig. 6.2(B)(c)] and after [Fig. 6.2(B)(d)] adsorption did not display significant change. The specific surface area plays a crucial role for the evaluation of the textural properties of an adsorbent. Fig. 6.2(C) shows the $N_2$ adsorption-desorption isotherm of HCeMgO1:1. The BET surface area of the adsorbent was 34.07 $m^2/g$, value slightly higher than that of pristine HMgO (33.7 $m^2/g$). The $N_2$ adsorption-desorption isotherm of HCeMgO1:1 is type IV with a $H_2$ hysteresis loop, according to IUPAC classification [22]. The average pore diameter, estimated around 8.42 nm is larger than that of $F^-$ ions (0.133 nm), indicating that the latter are able to enter easily into the optimised adsorbent pores. The FE-SEM and HR-TEM images are shown in Figs. 6.3(A) and (B). The FE-SEM image in Fig. 6.3(A) shows large clusters of semi-spherical nanoparticles. The HR-TEM images in Figs. 6.3(B) and (C), on the other hand, disclose agglomerated nanoparticles with 0.311 nm spacing of the crystallography plane, value close to 0.32 nm for (111) facet of $CeO_2$ [24], but significantly smaller.

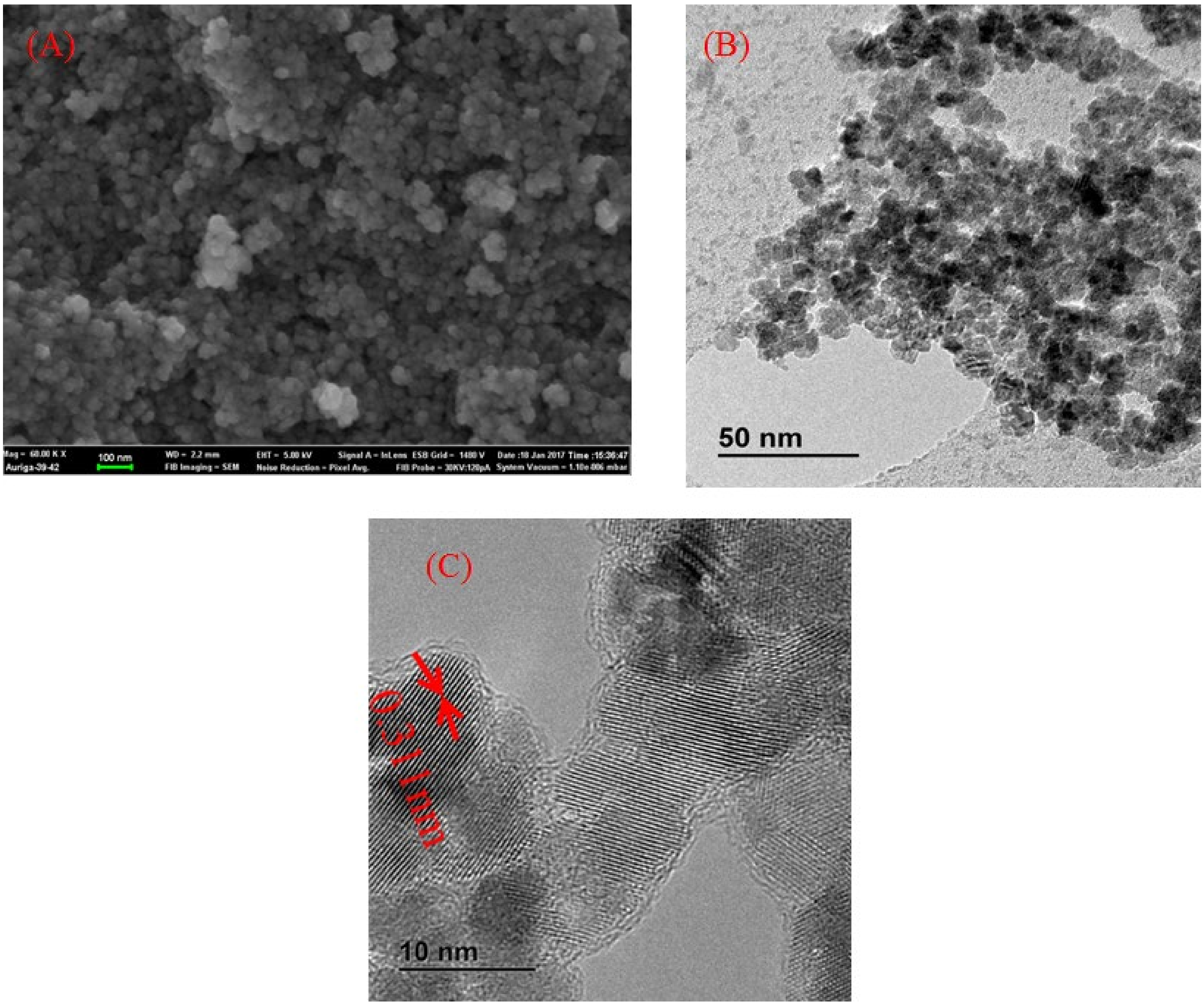

**Figure 6-3: (A) FE-SEM (B) TEM and (C) HR-TEM images of HCeMgO1:1 composite.**

This is probably due to displacement of large $Ce^{4+}$ by small $Mg^{2+}$ in the $CeO_2$ lattice structure and formation of solid solution. A Ce-Mg solid solution structure contributes to the formation of partly amorphous particles. These HR-TEM results are in good agreement with XRD analysis, where the $Ce^{4+}$ dominated the crystal structure. The presence of crystals with relatively large size is due to the preparation method of hydrous oxides. Co-precipitation enhances the degree of aggregation, owing to the difference in solubility of $Mg(OH)_2$ and $Ce(OH)_4$. $Ce^{4+}$ has higher reactivity and can also form stronger bond with hydroxide ions ($K_{sp}$ = 2.0 x$10^{-20}$) than $Mg^{2+}$ ion ($K_{sp}$ = 5.6 x $10^{-12}$). Consequently $Mg^{2+}$ may form more aggregation during reaction [22, 23] and this may explain its low XRD peaks in the bimetal oxide spectra. The EDS spectrum before adsorption in Fig. 6.4(A) clearly shows the presence of Ce, Mg and O elements within the structure of HCeMgO1:1 composite.

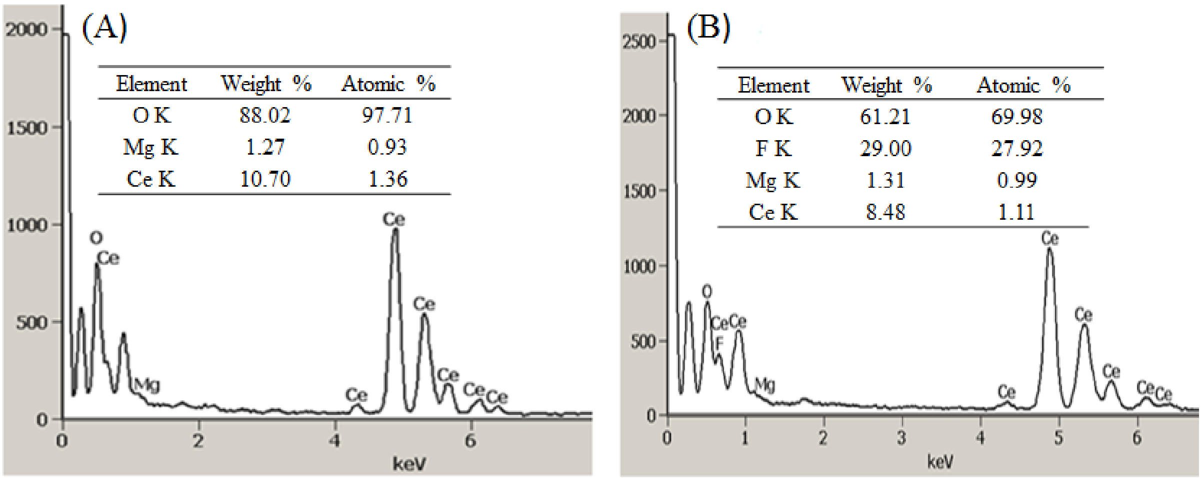

(A)

| Element | Weight % | Atomic % |
|---|---|---|
| O K | 88.02 | 97.71 |
| Mg K | 1.27 | 0.93 |
| Ce K | 10.70 | 1.36 |

(B)

| Element | Weight % | Atomic % |
|---|---|---|
| O K | 61.21 | 69.98 |
| F K | 29.00 | 27.92 |
| Mg K | 1.31 | 0.99 |
| Ce K | 8.48 | 1.11 |

**Figure 6-4: EDS spectra of HCeMgO1:1 (A) before and (B) after $F^-$ ions adsorption.**

Fig. 6.5, on the other hand, displays the HCeMgO1:1 STEM images elemental mapping of O, Ce, Mg, and F after adsorption and the corresponding EDS spectrum is presented in Fig. 6.5(B). It can be clearly observed from the mapping images that all the elements are well-distributed on the surface of the adsorbent. It is also evident that $F^-$ ions were incorporated in the HCeMgO1:1 adsorbent, since a fluoride peak is detected in the EDS after adsorption. Furthermore, analysis of the atomic percentage of Ce and Mg revealed a ratio 1:1, which confirms the co-precipitation proportion of the precursor salts during synthesis of HCeMgO1:1. Interestingly, the $F^-$ laden adsorbent reveals a reduced atomic ratio of O (69.98%) in Fig. 6.4(B), relative to 97.71% before adsorption [Fig. 6.4(A)]. This observation, in conjunction with FTIR analysis, reaffirms that oxygen atoms are replaced during adsorption process. An anion exchange adsorption mechanism by replacement of surface OH group with $F^-$ ions is therefore supported. The wide-scan XPS spectra of HCeMgO1:1 before and after adsorption were obtained to investigate changes in the elemental compositions of the adsorbent. Fig. 6.6(A) and Table 1 shows the XPS survey spectra and elementary composition of virgin and $F^-$ ions loaded adsorbent.

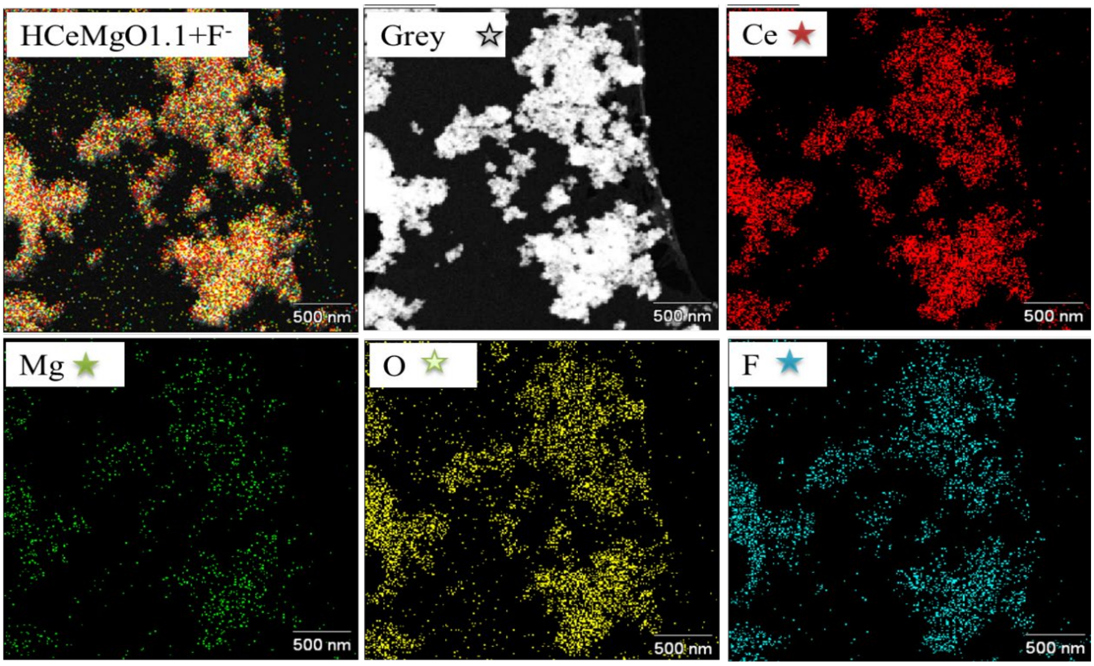

**Figure 6-5: STEM images of HCEMgO1:1 adsorbent after F$^-$ ions adsorption and mapping of O, Ce, Mg and F.**

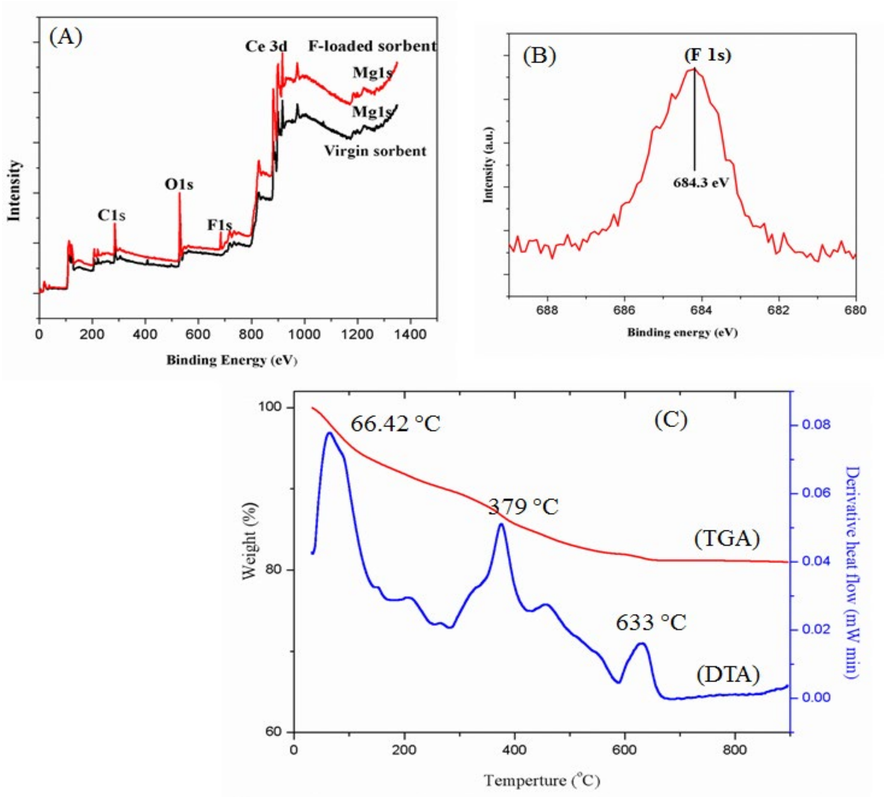

**Figure 6-6: (A) Wide-scan XPS spectra for HCeMgO1:1 before and after sorption (B) core-level XPS spectrum of F 1s (C) TGA and DTA plots for HCeMgO1:1 adsorbent.**

**Table 6-1: Summary of atomic ratio of HCeMgO1:1 before and after adsorption from XPS study.**

| Atomic ratio,% | Ce | Mg | O | F |
|---|---|---|---|---|
| Virgin sorbent | 0.71 | 1.03 | 98.26 | 0 |
| $F^-$ loaded sorbent | 0.56 | 0.87 | 88.61 | 9.96 |

The spectrum on HCeMgO1:1 before adsorption contains energy bands for O 1s (531 eV), Ce 3d (898.46-910 eV) and Mg 1s (1304.58 eV). The adsorption of $F^-$ ions on HCeMgO1:1 was confirmed by the appearance of a new F 1s core level peak in the XPS wide scan spectra after adsorption, at 684.3 eV binding energy as exposed in Fig. 6.6(B) [10, 24, 31]. TG-DTA was performed to determine the thermal stability of the HCeMgO1:1 adsorbent [Fig. 6.6(C)]. The weight loss occurred in three stages with the initial of about 10.04% being the loss of surface water in the temperature range of 30-250°C followed by the second weight loss (7.62%) associated with the exothermic effect around 379°C in the DTA spectrum due to lattice water molecules [29]. Further reduction in weight (1.22%) at 633°C is probably ascribed to phase transition from hydroxides to oxides [27]. This shows that HCeMgO1:1 is applicable for water treatment up to 250°C. The point-of-zero charge is a parameter which characterises the surface charge of an adsorbent, hence it was determined. The $pH_{pzc}$ of HCeMgO1:1 was found to be 5.8 as shown in Fig. 6.7(A). This information indicates that below pH 5.8, HCeMgO1:1 surface is positively charged and can therefore accommodate anions.

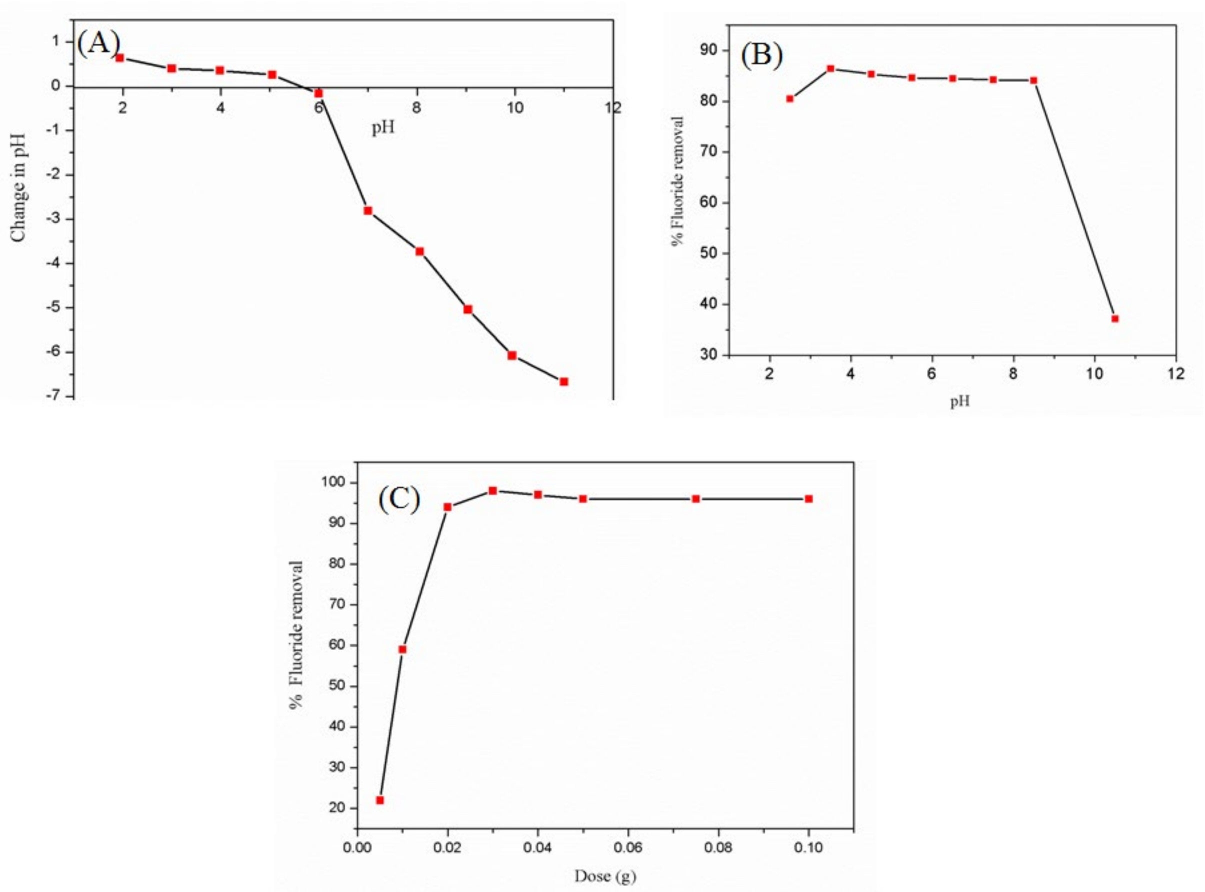

**Figure 6-7: (A) Determination of point-of-zero charge of HCeMgO1:1 (B) effect of pH using 10 mg/L $F^-$ ions solution (adsorbent dose: 0.03 g/50 mL of $F^-$ ions solution, contact time: 24 hr and temperature: 25°C) and (C) effect of adsorbent dose on adsorption of $F^-$ ions on HCeMgO1:1 using 10 mg/L $F^-$ ions solution at pH 5.5 and 25°C.**

### 6.3.3 Batch adsorption study

#### *6.3.3.1 Effect of pH on the removal of $F^-$ ions*

Solution pH is a key parameter affecting adsorption process. Its effect on $F^-$ ions removal was studied from pH 2 to 10.5 using 0.03 g of adsorbent mass in 50 mL of 10 mg/L $F^-$ ions solution. As shown in Fig. 6.7(B), the sorption occurred over a range of pH 2-8.5 from which percentage removal was between 80 and 88%, with optimum pH found at 3.5. Afterward, the percentage removal decreased to 38% as the pH increased. At pH above the $pH_{pzc}$ the adsorbent surface is negatively charged and induces coulombic repulsion to $F^-$ ions. Moreover, at relatively higher pH 9-11, the solution contains more hydroxyl ions than hydrogen ions, leading to competitive adsorption between hydroxyl and $F^-$ ions on the active sites. Hence, the decrease in absorption efficiency observed at relatively high pH [22,29,32,33].

#### *6.3.3.2 Effect of adsorbent dose*

The effect of HCeMgO1:1 dose on the removal of $F^-$ ions at pH 5.5 was investigated. Fig. 7(C) shows that the percentage removal increased from 22% to 98% when the adsorbent dose increased from 0.005 to 0.03 g. This is due to an increase in available active adsorption sites for $F^-$ ions uptake [30]. Thereafter no further increase in removal efficiency was observed as the adsorbent dose increased to 0.1 g. This could be attributed to the fact that at high dosage, active sites overlap, resulting in less available binding sites for adsorption [30]. Thus for the current study, 0.03 g dose was identified to serve as optimum adsorbent dosage for further experiments.

#### *6.3.3.3 Adsorption isotherms*

In order to design and operate an efficient adsorption system, the interactions between adsorbent and adsorbate need to be understood. This is often achieved by studying the adsorption isotherms. The temperature effect on the adsorption of $F^-$ ions onto HCeMgO1:1 was therefore studied at 15, 25, 35 and 45°C and Figs. 6.8(A), (B) and (C) show the isotherm experiments results. These results indicate that adsorption of $F^-$ ions increases with an increase in temperature, suggesting an endothermic process. The increase in temperature results in an increase in the binding ability of $F^-$ ions onto the adsorbent surface, thereby enhancing the extent of adsorption [30]. Two common analytical isotherm equations, namely, the Langmuir and the Freundlich isotherms were applied to model the data. The Langmuir model assumes monolayer coverage and the adsorbate can be equally adsorbed on all sorption sites. There is also no lateral interaction between ions [29,30].

The Langmuir linear and nonlinear forms are represented by Eq. (4) and (5), respectively.

$$\frac{C_e}{q_e} = \frac{1}{q_m b} + \frac{C_e}{q_m} \tag{4}$$

$$q_e = \frac{b q_m C_e}{1 + bC_e} \tag{5}$$

where $C_e$ (mg/L) is the equilibrium concentration of $F^-$ ions in solution. $q_e$ and $q_m$ (mg/g) are the amount of $F^-$ ions adsorbed per unit mass of adsorbent at equilibrium and maximum adsorption capacity, respectively. $b$ (L/mg) is the Langmuir constant related to the affinity of the binding sites for $F^-$ ions [29]. Both the nonlinear and linear fits of Langmuir model are shown in Figs. 6.8(A) and (B) and the calculated isotherm parameters are summarized in Table 6.2. These include $q_m$ and $b$ at different temperatures for linear and nonlinear Langmuir fits.

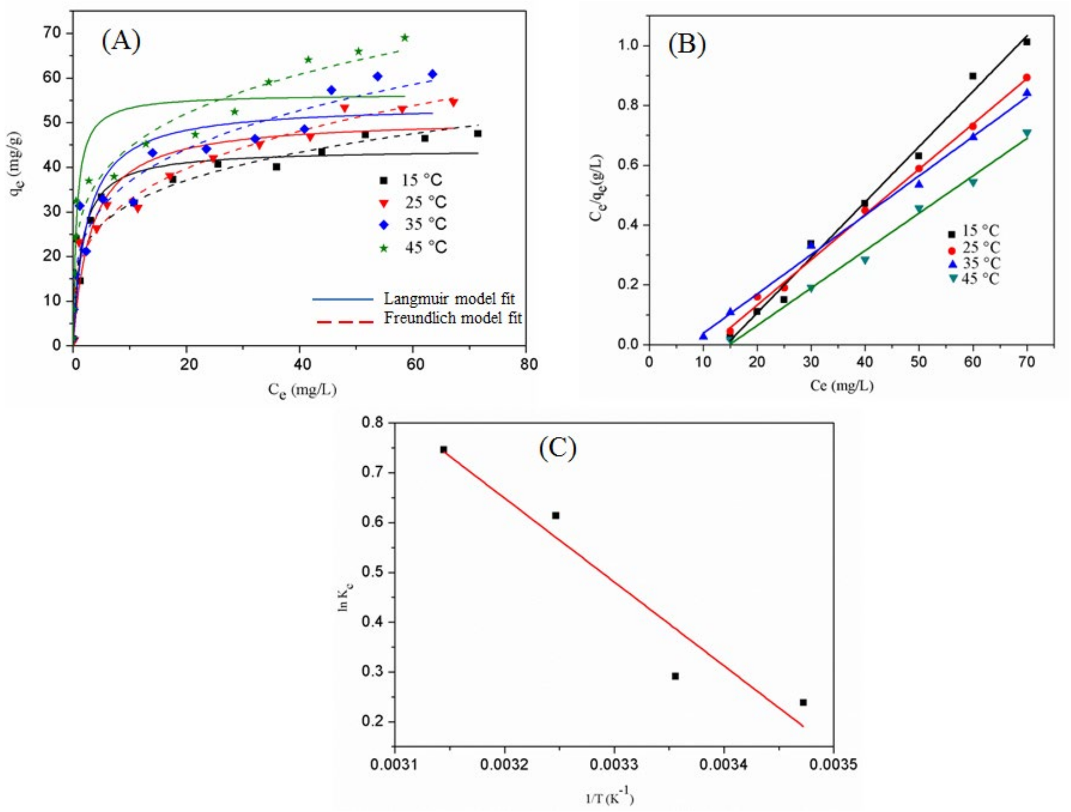

**Figure 6-8: (A) Adsorption equilibrium isotherms for $F^-$ ions removal by HCeMgO1:1 and the data fit to nonlinear Langmuir and Freundlich isotherm models; (B) Fit of data to linearized Langmuir model (C) Van't Hoff's plot for the determination of thermodynamic parameters.**

**Table 6-2: Langmuir and Freundlich isotherms parameters for the sorption of $F^-$ ions onto HCeMgO1:1.**

| Isotherm models | Temperature | | | |
|---|---|---|---|---|
| | 15°C | 25°C | 35°C | 45°C |
| Langmuir | | | | |
| Linear | | | | |
| $q_{max}$ (mg/g) | 54.05 | 66.23 | 75.76 | 80.00 |
| $b$ (L/mg) | 0.073 | 0.0894 | 0.1417 | 0.0675 |
| $R_L$ | 0.1227 | 0.1227 | 0.0882 | 0.1563 |
| $R^2$ | 0.9909 | 9976 | 0.9959 | 0.9931 |
| Non-linear model | | | | |
| Best-fit values | | | | |
| $q_m$ | 44.08 | 51.03 | 54.09 | 56.47 |
| $b$ | 0.6687 | 0.3189 | 0.4151 | 1.643 |
| Std. Error | | | | |

| Isotherm models | Temperature | | | |
|---|---|---|---|---|
| | 15°C | 25°C | 35°C | 45°C |
| $q_m$ | 2.103 | 3.501 | 3.796 | 3.202 |
| *b* | 0.2016 | 0.1233 | 0.1661 | 0.6209 |
| 95% Confidence Intervals | | | | |
| $q_m$ | 39.49 to 48.66 | 43.40 to 58.66 | 45.82 to 62.36 | 49.49 to 63.44 |
| *b* | 0.2295 to 1.108 | 0.05030 to 0.5875 | 0.05329 to 0.7769 | 0.2895 to 2.995 |
| Goodness of Fit | | | | |
| Degrees of Freedom | 12 | 12 | 12 | 12 |
| $R^2$ | 0.8978 | 0.8671 | 0.8481 | 0.8603 |
| Absolute Sum of Squares | 292.7 | 503.2 | 709.5 | 845.2 |
| *Sy.x* | 4.939 | 6.475 | 7.689 | 8.393 |
| Number of points Analyzed | 14 | 14 | 14 | 14 |
| | | | | |
| Freundlich | | | | |
| Linear | | | | |
| $K_f$ (mg/g) | 2.155 | 1.888 | 2.167 | 2.118 |
| *n* | 1.285 | 1.215 | 1.283 | 1.332 |
| $R^2$ | 0.9498 | 0.956 | 0.9640 | 0.9727 |
| Non-linear model | | | | |
| Best-fit values | | | | |
| $K_f$ | 1.883 | 1.729 | 2.031 | 2.650 |
| *n* | 4.424 | 3.606 | 3.868 | 4.441 |
| Std. Error | | | | |
| $K_f$ | 1.802 | 1.551 | 1.865 | 1.864 |
| *n* | 0.5361 | 0.3321 | 0.3990 | 0.4134 |
| 95% Confidence Intervals | | | | |
| $K_f$ | 1.490 to 2.275 | 1.391 to 2.067 | 1.624 to 2.437 | 2.243 to 3.056 |
| *n* | 3.256 to 5.592 | 2.882 to 4.329 | 2.999 to 4.738 | 3.541 to 5.342 |
| Goodness of Fit | | | | |
| Degrees of Freedom | 12 | 12 | 12 | 12 |
| $R^2$ | 0.9154 | 0.9527 | 0.9510 | 0.9597 |
| Absolute Sum of Squares | 24.23 | 17.91 | 22.88 | 24.40 |
| *Sy.x* | 4.494 | 3.863 | 4.366 | 4.510 |
| Number of points analyzed | 14 | 14 | 14 | 14 |

The increase in $q_m$ with temperature confirms that the adsorption process was endothermic in nature and the general increase in Langmuir constant (*b*) with temperature indicates greater binding energies at higher temperatures. The dimensionless constant $R_L$ is another important parameter of the Langmuir isotherm which reveals favourability or non-favourability of adsorption. This factor is expressed using Eq. (6)

$$R_L = \frac{1}{1+bCo} \tag{6}$$

where $C_o$ (mg/L) is the initial $F^-$ ions concentration. If $R_L$ is such that $0 < R_L < 1$ the adsorption process is favourable. $R_L > 1$, on the other hand, indicates unfavourable adsorption. Linear adsorption is articulated when $R_L = 1$ and irreversible adsorption when $R_L = 0$. In the present adsorption process, $R_L$ values were between 0 and 1 thus suggesting favourable adsorption [20,30].

The nonlinear [22] and linear [34] forms of Freundlich isotherm represented by Eq. (7) and (8), were also evaluated for isotherm data.

$$q_e = K_f\, C_e^{1/n} \tag{7}$$

$$ln\, q_e = lnK_f + \frac{1}{n}\, lnC_e \tag{8}$$

where $K_f$ (mg/g) and *1/n* are the Freundlich constants related to adsorption capacity and intensity of adsorption, respectively [35]. Values of *1/n* range from 0 to 1 and if close to zero denote more surface homogeneity. On the other hand, *n* values between 1 and 10 signify favourable adsorption [36]. $K_f$ and 1/n values were determined and are summarized in Table 6.2. The values of *n* ranged between 0 and 10 for linear Freundlich isotherm, also indicate favourable adsorption.

Figs. 6.8(A) and S1 (Supplementary information) show the nonlinear and linear fit of equilibrium data for Freundlich model, respectively. When comparing the two adsorption isotherm models, the $R^2$ values for Langmuir ($R^2_{linear}$ = 0.9909-0.9976) were higher than those for Freundlich ($R^2_{linear}$ = 0.9498-0.9727) for all temperatures. This specifies that $F^-$ ions adsorption onto HCeMgO1:1 surface was homogeneous and took place through monolayer coverage, as Langmuir isotherm best described the process [29,37,38]. The $q_m$ values evaluated from the data ranged from 54.05 to 80.00 mg/g for the linear isotherm. The performance of HCeMgO1:1 for $F^-$ ions adsorption was also assessed by comparison with other available materials in the literature (Table 6.3). Relative to the listed adsorbents, HCeMgO1:1 exhibited higher adsorption efficiency. As a result, this adsorbent has good prospect for treatment of groundwater with a high $F^-$ ions content.

**Table 6-3: Comparative assessment of $F^-$ ions adsorption capacity of HCeMgO1:1 with other reported materials.**

| Adsorbent | Adsorption capacity (mg/g) | Studied pH range | Ref. |
|---|---|---|---|
| Polypyrrole/$Fe_3O_4$ magnetic nanocomposite | 17.6-22.3 | 6.5 | [3] |
| $CeO_2$ and $ZrO_2$ mixed meta oxides | 12.4 | 5.8 | [20] |
| Fe-Ce bimetal oxides | 60.97 | na | [22] |
| Al-Ce mixed metal oxide | 27.5 | 6.0 | [23] |
| Mn-Ce bimetal oxides | 45.5 | 6.0 | [24] |
| $CeO_2$/MgO-Fe layered double hydroxides | 42.6 | na | [31] |

| Adsorbent | Adsorption capacity (mg/g) | Studied pH range | Ref. |
|---|---|---|---|
| Mg-Fe double hydroxides | 50.91 | 7.0 | [30] |
| Polypyrrole hydrous tin oxide nanocomposite | 28.99 | 6.5 | [29] |
| $Fe_3O_4$@$Al(OH)_3$ magnetic material | 88.48 | 6.5 | [35] |
| Ti-Fe oxide nano-adsorbent | 47.0 | na | [37] |
| $MnO_2$-$Al_2O_3$ composite material | 18.6 | 7.0 | [39] |
| Hydroxyapatite/MWCNTs | 30.22 | 7.0 | [40] |
| La oxide + activated carbon hybrid adsorbent | 9.98 | 7.0 | [41] |
| Fe-Sn bimetal oxide | 10.50 | 6.4 | [42] |
| Chitosan/montmorillonite/$ZrO_2$ composite | 23.0 | 4.0 | [43] |
| Fe doped $TiO_2$ nano-adsorbent | 53.22 | 7.0 | [44] |
| Hydrous $CeO_2$-MgO bimetal composite | 66.23 | 5.5 | This study |

*na- not available

#### 6.3.3.4 *Thermodynamic parameters for $F^-$ ions adsorption by HCeMgO1:1*

Change in Gibbs free energy ($\Delta G°$), enthalpy ($\Delta H°$) and entropy ($\Delta S°$) were evaluated from adsorption isotherm data using Eq. (9) and (10):

$$\Delta G° = -RT\ lnK_c = -RT\ ln\ (m\frac{q_e}{C_e}) \quad (9)$$

$$ln\ (m\frac{q_e}{C_e}) = \frac{\Delta S°}{R} - \frac{\Delta H°}{RT} \quad (10)$$

where $R$ (J/mol K) is the gas constant, $m$ (g) is the adsorbent dose in a volume of 1 L, and $K_c$ is the equilibrium constant. The ratio $mq_e/C_e$ is the adsorption affinity. The values of $\Delta H°$ and $\Delta S°$ were determined from the slope and intercept of the plot of $ln$ ($mq_e/C_e$) versus $1/T$, as shown in Fig. 6.8(C). The values of $\Delta G°$ were calculated by using Eq. (9). These calculated parameters are shown in Table 6.4. The positive $\Delta H°$ value indicates endothermic process during $F^-$ ions adsorption using HCeMgO1:1 composite [23,30,45]. The process also occurred with increasing entropy as indicated by the positive $\Delta S°$ values, suggesting an increase in randomness with an upsurge in number of $F^-$ ions. In addition, this process was spontaneous under the experimental conditions, as evidenced from the negative $\Delta G°$ values [23,30,46].

**Table 6-4: Thermodynamic parameters for $F^-$ ions adsorption onto HCeMgO1:1.**

| Temperature (°C) | $\Delta G°$ (kJ/mol) | $\Delta H°$ (kJ/mol) | $\Delta S°$ (kJ/mol/K) |
|---|---|---|---|
| 15 | -0.571 | +13.04 | +0.0473 |
| 25 | -0.721 | | |
| 35 | -1.570 | | |
| 45 | -1.972 | | |

### 6.3.3.5 *Adsorption kinetics*

Adsorption kinetics is useful in predicting the adsorption rate that gives more insight into design and modelling for adsorption based water treatment processes. An adsorbent must have rapid adsorption kinetics to be considered feasible for practical application. Fig. 6.9(A) shows the results from effect of contact time experiments for the adsorption of F$^-$ ions on HCeMgO1:1 adsorbent using four different initial F$^-$ ions concentrations: 10, 15, 25 and 40 mg/L.

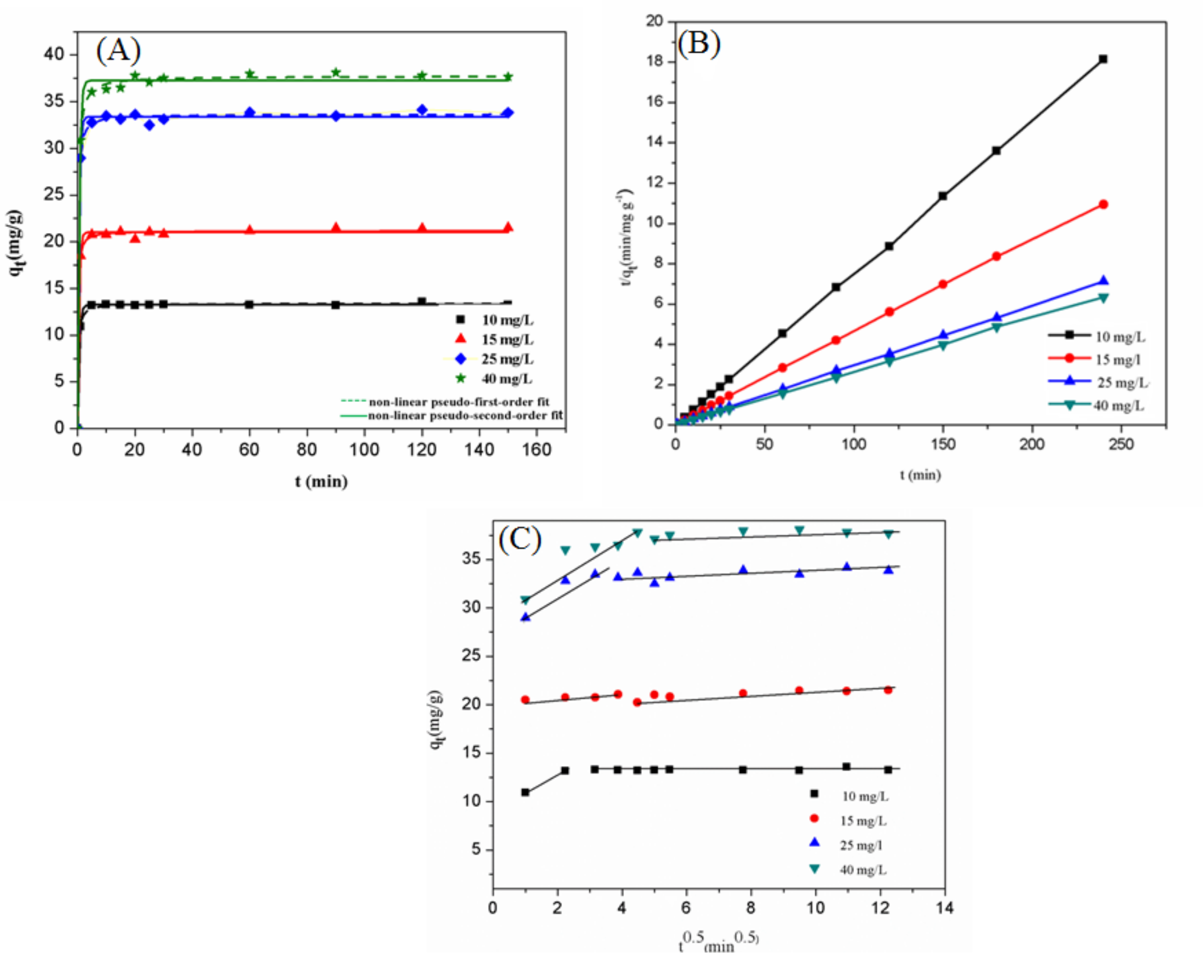

**Figure 6-9: Effect of contact time on the adsorption of F$^-$ ions onto HCeMgO1:1 (A) pseudo-first-order and pseudo-second-order nonlinear fitting; (B) fit of data to linearized pseudo-second-order kinetic model at pH 5.5 (adsorbent dose: 0.03 g/50 mL of F$^-$ ions solution, temperature: 25°C) and (C) intra-particle diffusion model for adsorption of F$^-$ ions by HCeMgO1:1.**

Within 5 to 20 min of contact time, the adsorption capacity increased rapidly to 12, 21, 33 and 37 mg/g for solution of initial F$^-$ ions concentrations 10, 15, 25 and 40 mg/L, respectively. The encountered contact time was much shorter than those reported for some adsorbents in the literature. This faster kinetics is attributed to the shorter diffusion routes associated with mixed metal oxides [8,23]. Pseudo-first-order and pseudo-second-order kinetic models were employed to investigate the adsorption kinetics and understand the mechanism involved. These are represented by Eq. (11) to (14).

$$q_t = q_e(1 - exp\,(^{-k_1\,t}\,) \qquad (11)$$

$$log(\, q_e \,-\, q_t\,) = log(q_e\,) - \frac{k_1}{2.303}\, t \tag{12}$$

$$q_t = \frac{k_2 q_e 2 \;t}{1 + k_2 \; q_e \, t} \tag{13}$$

$$\frac{t}{q_t} = \frac{1}{k_2 q_e 2} + \frac{t}{q_e} \tag{14}$$

where $k_1$ (1/min) and $k_2$ (g/mg.min) are pseudo-first-order and second-order-rate constants, respectively. $q_e$ and $q_t$ (mg/g) are adsorption capacities at equilibrium and time *t* (min), respectively.

Figs. 6.9(A) and (B) show both the linear and non-linear kinetic modelling of pseudo-second-order model. Fit of kinetic data to nonlinear pseudo-first-order model is shown in Fig. 6.9(A). The values of all kinetic parameters are reported in Table 6.5. The $R^2$ values obtained from the pseudo-second-order model ($R^2_{linear}$ = 0.9998-1.000 and $R^2_{non\text{-}linear}$ = 0.9984-0.9988) are higher than those from pseudo-first-order model ($R^2_{linear}$ = 0.1161-0.9853 and $R^2_{non\text{-}linear}$ = 0.9933-0.9977). Both the experimental and modelled $q_e$ values obtained from pseudo-second-order model correlated well. $F^-$ ions adsorption by HCeMgO1:1 therefore followed pseudo-second-order kinetics. There was also a general decrease in the values of $k_2$ with an increase in initial $F^-$ ions concentration (from 3.856 to 0.4422 g/mg/min).

This occurs because of faster adsorption from dilute solutions, as less $F^-$ ions migrate to the adsorption sites in contrast to concentrated solutions [20, 35, 47, 48]. In order to identify the rate determining step, the Webber-Morris intra-particle diffusion model was employed and the equation is as follows;

$$q_t \;=\; k_{int}\, t^{0.5} + C_i \tag{15}$$

where $k_{int}$ (mg/gmin$^{0.5}$) is the intra-particle diffusion rate constant and $C_i$ (mg/g), the constant related to the magnitude of the boundary layer thickness.

**Table 6-5: Kinetics parameters for the sorption of $F^-$ ions by HCeMgO1:1 at different concentrations.**

| Kinetic models | Initial concentration (mg/L) | | | |
|---|---|---|---|---|
| | 10 | 15 | 25 | 40 |
| **Pseudo-first order linear** | | | | |
| $k_1$(1/min) | 0.0170 | 0.0237 | 0.0210 | 0.0180 |
| $q_e$ (mg/g | 0.000762 | 0.9390 | 1.7500 | 1.9050 |
| $R^2$ | 0.1161 | 0.9534 | 0.9390 | 0.9853 |
| **Pseudo-first-order nonlinear** | | | | |
| Best-fit values | | | | |
| $q_e$ | 13.26 | 21.02 | 33.40 | 37.29 |
| $k_1$ | 1.724 | 2.122 | 2.023 | 1.758 |

| Kinetic models | Initial concentration (mg/L) | | | |
|---|---|---|---|---|
| | 10 | 15 | 25 | 40 |
| Std. Error | | | | |
| $q_e$ | 0.03263 | 0.1181 | 0.1534 | 0.2265 |
| $k_1$ | 0.04507 | 0.1540 | 0.1138 | 0.1152 |
| 95% Confidence Intervals | | | | |
| $q_e$ | 13.19 to 13.33 | 20.75 to 21.28 | 33.05 to 33.74 | 36.79 to 37.79 |
| $k_1$ | 1.623 to 1.824 | 1.779 to 2.465 | 1.769 to 2.277 | 1.502 to 2.015 |
| Goodness of Fit | | | | |
| Degrees of Freedom | 10 | 10 | 10 | 10 |
| $R^2$ | 0.9933 | 0.9965 | 0.9977 | 0.9960 |
| Absolute Sum of Squares | 0.1064 | 1.396 | 2.351 | 5.127 |
| *Sy.x* | 0.1031 | 0.3736 | 0.4849 | 0.7160 |
| Number of points Analysed | 12 | 12 | 12 | 12 |
| **Pseudo second order linear** | | | | |
| $k_2$ (g/mg.min) | 3.856 | 0.500 | 0.2086 | 0.4422 |
| $q_e$ (mg/g) | 13.26 | 21.14 | 33.54 | 37.30 |
| $R^2$ | 1.000 | 0.9998 | 0.9999 | 0.9998 |
| **Nonlinear best fits** | | | | |
| Best-fit values | | | | |
| $k_2$ | 0.3407 | 0.3229 | 0.1842 | 0.1161 |
| $q_e$ | 13.40 | 21.18 | 33.68 | 37.75 |
| Std. Error | | | | |
| $k_2$ | 0.02959 | 0.04778 | 0.02032 | 0.008769 |
| $q_e$ | 0.05481 | 0.1102 | 0.1406 | 0.1380 |
| 95% Confidence Intervals | | | | |
| $k_2$ | 0.2748 to 0.4067 | 0.2164 to0.4294 | 0.1390 to 0.2295 | 0.09660 to 0.1357 |
| $q_e$ | 13.28 to 13.53 | 20.94 to 21.43 | 33.36 to 33.99 | 37.44 to 38.06 |
| Goodness of Fit | | | | |
| Degrees of Freedom | 10 | 10 | 10 | 10 |
| $R^2$ | 0.9985 | 0.9975 | 0.9984 | 0.9988 |

| Kinetic models | Initial concentration (mg/L) | | | |
|---|---|---|---|---|
| | 10 | 15 | 25 | 40 |
| Absolute Sum of Squares | 0.2486 | 1.026 | 1.663 | 1.571 |
| *Sy.x* | 0.1577 | 0.3203 | 0.4077 | 0.3964 |
| Number of points Analyzed | 12 | 12 | 12 | 12 |
| **Intra-particle diffusion** | | | | |
| $k_{int}$ (mg/g/min $^{0.5}$) | 1.1350 | 1.1970 | 2.2193 | 2.16157 |
| $C_i$ (mg/g) | 10.024 | 20.411 | 27.199 | 28.830 |
| $R^2$ | 0.8424 | 0.8189 | 0.9139 | 0.8549 |

Fig. 6.9(C) represents a plot of $t^{0.5}$ against $q_t$ for different $F^-$ ions initial concentrations. There are two linear portion involved in the sorption of $F^-$ ions on HCeMgO1:1 adsorbent. The initial portion may be governed by boundary layer diffusion and the second by intra-particle diffusion [49]. From the slopes of the initial linear portion of the curves, the values of $k_{int}$ for the four different concentrations were obtained and presented in Table 4, together with the $R^2$ values. $k_{int}$ values increased from 1.1350 to 2.1616 mg/g min$^{0.5}$ as the initial concentration increased from 10 mg/L to 40 mg/L. However, the linear plots did not pass through the origin, denoting a complex situation in which both film diffusion and intra-particle diffusion contribute to the rate limiting step [49,50]. The magnitude of $C_i$ increases with increasing initial concentration of $F^-$ ions. This indicates an increase in boundary layer effects [29].

### *6.3.3.6 Effect of co-existing ions*

In general, drinking water can have a complex matrix, it may contain several anions along with $F^-$ ions like, $SO_4^{2-}$, $Cl^-$, $HCO_3^-$, $PO_4^{3-}$ and $NO_3^-$, which might compete for binding sites with $F^-$ ions, hence interfering with its adsorption [49,51]. The effect of various anions on the $F^-$ ions removal efficiency by HCeMgO1:1 adsorbent was investigated. The initial concentration of $F^-$ ions was kept constant at 10 mg/L whilst that of interfering ions was varied from 0 to 40 mg/L and pH adjusted to 5.5. The results are presented in Fig. 6.10(A) indicate that $Cl^-$ ions actually increases $F^-$ ions uptake and this is probably attributed to increased coulombic repulsive forces that occur during the process [29]. $NO_3^-$ and $HCO_3^-$ ions had very little effect on the $F^-$ ions removal whilst $SO_4^{2-}$ and $PO_4^{3-}$ ions caused a decrease in the adsorption of $F^-$ ions for all concentrations studied (10-40 mg/L). The $PO_4^{3-}$ ions, however, had the greater effect with the $F^-$ ions uptake decreasing from 90.70% to 62.29% when $PO_4^{3-}$ ions concentration increased from 0 to 40 mg/L. Thus the order of interference was $PO_4^{3-} > SO_4^{2-} > HCO_3^- > NO_3^- > Cl^-$. This is related to the formation of inner and outer sphere complexes associated with the different ions. $F^-$ ions are adsorbed through inner-sphere complexations which also happen to take place with $PO_4^{3-}$ ions, hence competitive adsorption [29,45]. In addition, the order of interference relatively compares to the Z/R (charge/radius) values of competitive anions: $PO_4^{3-}$ (3/3.40) > $SO_4^{2-}$ (2/2.40) > $Cl^-$ (1/1.18) > $NO_3^-$ (1/2.81). The greater the charge/radius, the more likely the anion is attracted to the adsorbent surface and hence the more it interferes with $F^-$ ions adsorption [35,45]. It is reported that the concentration of $PO_4^{3-}$ in drinking water is normally low thus its effect on $F^-$ ions removal may be minimal [20, 29].

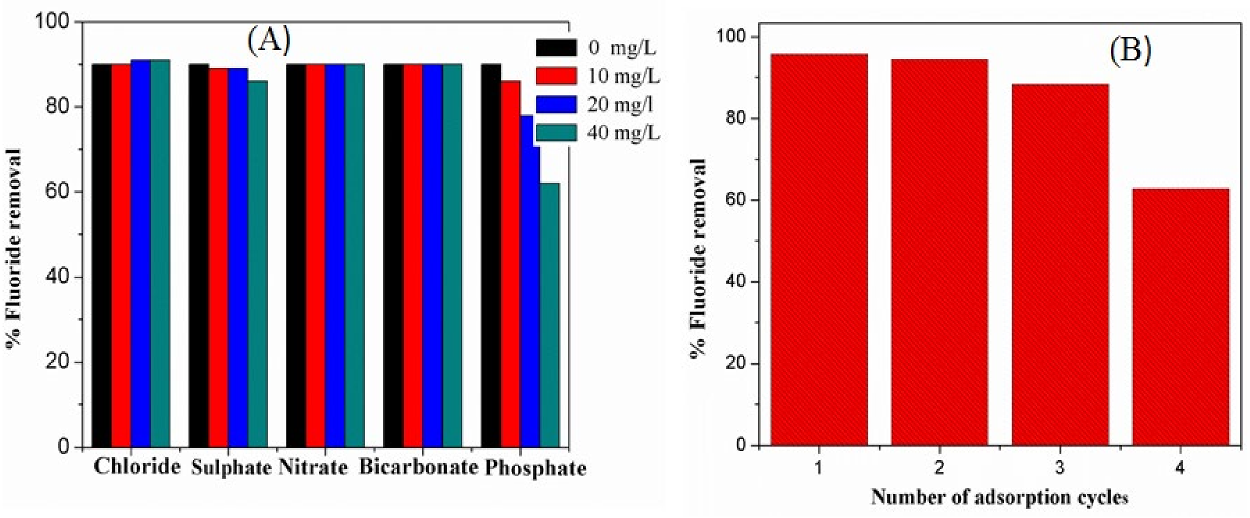

**Figure 6-10: (A) Effect of co-existing ions on F⁻ ions adsorption at pH 5.5 (adsorbent dose: 0.03 g/50 mL of F⁻ ions solution, contact time: 24 hr and temperature: 25°C) (B) F⁻ ions removal efficiency on the recycled HCeMgO1:1.**

#### *6.3.3.7 Desorption studies*

The reusability of an adsorbent is an important factor which affects its feasibility for large scale water treatment applications, and a high quality adsorbent must satisfy this factor. Various concentrations of NaOH ranging from 0.05 to 0.1M were used for desorption in order to find the best desorbing concentration. It was found that maximum regeneration of 97.50% was achieved by a 0.1M NaOH solution. This concentration of NaOH was then used for further adsorption-desorption experiments. The $F^-$ loaded HCeMgO1:1 adsorbent was subjected to four adsorption-desorption successive cycles. Fig. 6.10(B) illustrates the variation of the percentage removal with the number of adsorption-desorption cycles. The adsorbent maintained its higher efficiency up to three cycles, followed by a reduction to 62.4% in the 4th cycle, probably due to desorption and regeneration operations. This study suggests that HCeMgO1:1 can be used for four regeneration cycles.

#### *6.3.3.8 Performance on natural water samples*

To evaluate the $F^-$ ions removal efficiency of the HCeMgO1:1 adsorbent in natural water samples, fluoride-containing underground water from Moletjie village, Limpopo Province South Africa, was used. The water had a $F^-$ ions concentration of 0.416 mg/L and a pH of 7.88. The fluoride ions concentration was then increased to 5 mg/L by spiking, and its new pH was measured to be 8.3. Thereafter, the as-prepared natural water was contacted with doses of HCeMgO1:1 adsorbent ranging from 0.05 to 0.1 g in 50 mL of volume without adjusting the pH. An increase in HCeMgO1:1 dosage resulted in an increase of $F^-$ ions removal and a decrease in equilibrium $F^-$ ions concentration as shown in Figs. 6.11(A) and (B), respectively. This adsorbent was able to reduce the $F^-$ ions level to about 1.0 mg/L, value below the limit of 1.5 mg/L, as recommended by WHO.

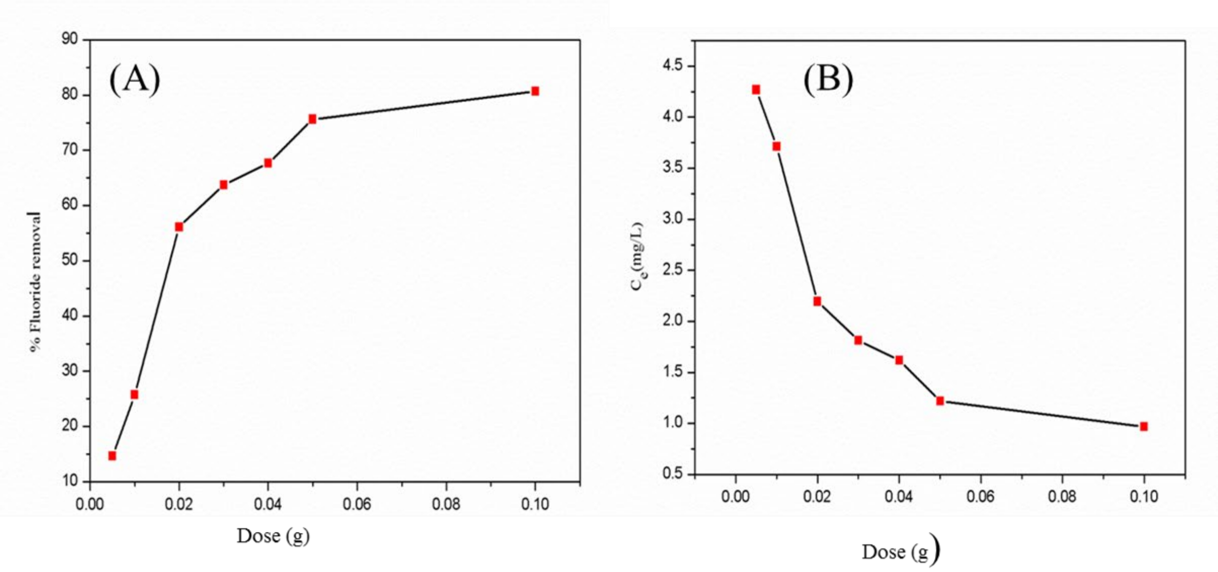

**Figure 6-11: Effect of adsorbent dosage on (A) % F⁻ ions removal and (B) equilibrium F⁻ ions concentration using groundwater samples.**

### 6.3.4 Adsorption mechanism

XPS and FTIR techniques were used to study the interaction between $F^-$ ions and the presence of functional groups on the adsorbent. Fig. 6.6(A) presents the XPS wide-scan spectra of the sorbent before and after adsorption. From the FTIR data [Fig. 6.2(A)], the HCeMgO1:1 surface hydroxyl groups were very proactive in the adsorption of $F^-$ ions. As observed in Fig. 6.12, the O 1s spectra of the virgin sorbent exhibit two signature peaks, with binding energies 529.71 and 531.96 eV, which can be assigned to oxygen ($O^{2-}$) of metal (Ce/Mg) oxide and surface hydroxyl groups, respectively [10, 22,35,50-52]. Further, the peak area ratio and peak intensity of $O^{2-}$ after adsorption are higher, comparative to the same peak before adsorption. The peak area ratio assigned to $O^{2-}$ of the adsorbent increases from 61.46% to 88.42%. However, the area of peaks assigned to OH group decreased from 38.54% to 11.58% after adsorption, pointing out that this group was involved in the $F^-$ ions adsorption [10,22,24].

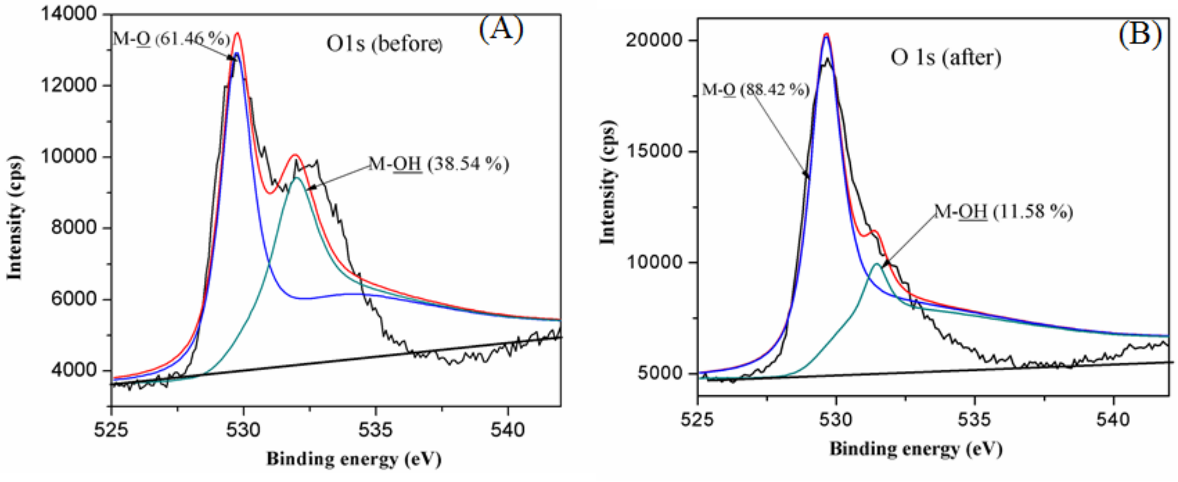

**Figure 6-12: XPS O 1s spectra (A) before and (B) after adsorption.**

This observation is consistent with FTIR analysis in terms of involvement of OH group in adsorption. The $pH_{pzc}$ (pH = 5.8) is an important parameter as discussed earlier. From Fig. 6.7(B), it can be observed that adsorption efficiency is high from pH 2 to 8.5, but decreases sharply as the pH increases further. When $pH < pH_{pzc}$, protonation leads to the formation of positively charged $MOH_2^+$ species (Eq.16), and there may be adsorption of anionic $F^-$ through electrostatic attractions and anionic exchange. With regard to $pH > pH_{pzc}$, the adsorbent surface of HCeMgO1:1 becomes negatively charged. Thus repulsion is set to take place with $F^-$ ions. In this case, adsorption process can only proceed through anionic exchange [23,29]. Both fluoride and hydroxyl ions are isoelectronic and the ability of the former to coordinate with $Ce^{4+}$ and $Mg^{2+}$ ions is relatively higher than that with $OH^-$, supporting the possibility of anion exchange at the surface of HCeMgO1:1 [51,53].

Therefore, the $F^-$ ions adsorption mechanism onto HCeMgO1:1 in aqueous matrix can be described as both electrostatic interactions and ion exchange. The following equations illustrate the possible adsorption mechanisms:

(a) Electrostatic attraction

$$M\text{-}OH_{(s)} + H^+_{(aq)} \rightarrow M\text{-}OH_2^+{}_{(s)} \qquad (16)$$

$$M\text{-}OH_2^+{}_{(s)} + F^-_{(aq)} \rightarrow M\text{-}OH_2^+\text{---}F_{(s)}^- \qquad (17)$$

(b) Ion exchange

$$M\text{-}OH_{(s)} + F^-_{(aq)} \rightarrow M\text{-}F_{(s)} + OH^-_{(aq)} \qquad (18)$$

## 6.4 SUMMARY

Hydrous Ce-Mg binary metal oxides were synthesised by a co-precipitation method and applied as an adsorbent for $F^-$ ions removal from water. HCeMgO adsorbent demonstrated rapid adsorption of $F^-$ ions within 5-20 minutes. This fast kinetics was attributed to shorter diffusion path associated with nano-metal oxides. The successful adsorption of $F^-$ ions on the fabricated hydrous binary nano-metal oxides was confirmed with the appearance of a fluoride peak on the EDS and XPS spectra. This adsorbent performed well over a wide pH range 2-8.5. Maximum adsorption capacity obtained from the best fitting Langmuir isotherm was 66.23 mg/g at 25°C, and the process seemed to involve both electrostatic and anion exchange. Thermodynamic data ($\Delta G°$ = -0.721 kJ/mol at 25°C and $\Delta H°$ = +13.04 kJ/mol) exposed a spontaneous and endothermic process. A pseudo-second-order model best described the adsorption kinetics and the process was hindered by phosphate and sulphate co-existing ions. The adsorbent maintained its relatively high adsorption efficiency over four cycles, comparable to those reported in literature. Additionally, treatment of 50 mL fluoride-spiked groundwater samples (5 mg/L $F^-$ ions concentrations) with 0.1 g of HCeMgO1:1 reduced the $F^-$ ions level to 1.00 mg/L. Hence, this material can serve as alternative adsorbent for removal of $F^-$ ions from drinking water.

## 6.5 REFERENCES

[1] S. Ali, S.K. Thakur, A. Sarkar, S. Sheka, Worldwide contamination by fluoride ions, Environ. Chem. Lett. 14 (2016) 291-315.

[2] Fluorides. Environmental Health Criteria 227, World Health Organization (WHO): Geneva, Switzerland 2002, 1-268.

[3] M. Bhaumik, T.Y. Leswifa, A. Maity, V.V. Srinivasu, M.S. Onyango, Removal of $F^-$ from aqueous solution by polypyrrole/$Fe_3O_4$ magnetic nanocomposite, J. Hazard. Mater. 186 (2011) 150-159.

[4] D. Dayananda, V.R. Sarva, S.V. Prasad, J. Arunachalam, N.N. Ghosh, Preparation of CaO loaded mesoporous $Al_2O_3$: Efficient adsorbent for $F^-$ removal from water, Chem. Eng. J. 248 (2014) 430-439.

[5] S. Blagojevic, M. Jakovljevic, M. Radulovic, Content of fluorine in soils in the vicinity of aluminium plant in Podgorica, J. Agric. Sci. 47 (2002) 1-8.

[6] K. Biswas, K. Gupta, A. Goswami, U.C. Ghosh, $F^-$ removal efficiency from aqueous solution by synthetic iron(III)-aluminium(III)-chromium (III) ternary mixed oxide, Desalination 255 (2010) 44-51.

[7] N. Esmaeeli, H. Faghihian, S. Naeimi, Magnetization and modification of ETS-4 titanosilicate for removal of fluoride from aqueous solutions, J. Alloys Compd. 744 (2018) 271-280.

[8] J. Hu, J.H. Shipley, Evaluation of desorption of Pb (II), Cu (II) and Zn (II) from titanium dioxide nanoparticles, App. Clay Sci. 103 (2015) 20-27.

[9] M. Chiban, M. Zerbet, G. Carja, F. Sinami, Application of low-cost adsorbents for arsenic removal: A review, J. Environ. Chem. Ecotoxicol. 4 (2011) 91-102.

[10] J. Wang, D. Kang, X. Yu, M. Ge, Y. Chen, Synthesis and characterization of Mg-Fe-La tri-metal composite as an adsorbent for $F^-$ removal, Chem. Eng. J. 26 (2015) 506-513.

[11] M.H. Stannic, M.E. Ravančić, A. Flanagan, Review on adsorption of $F^-$ from aqueous solution, Materials 7 (2014) 6317-6366.

[12] A.E. Chávez-Guajardo, J.C. Medina-Llamas, L. Maqueira, C.A.S. Andrade, K.G.B. Alves, C.P. de Melo, Efficient removal of Cr (VI) and Cu (II) ions from aqueous media by use of polypyrrole/maghemite and polyaniline/maghemite magnetic nanocomposites, Chem. Eng. J. 281 (2015) 826-836.

[13] T. Mahmood, S.U. Din, A. Naeem, S. Mustafa, M. Waseem, M. Hamayun, Adsorption of arsenate from aqueous solution on binary mixed oxide of iron and silicon, Chem. Eng. J. 192 (2012) 90-98.

[14] Z. Jin, Y. Jia, K.S. Zhang, L.T. Kong, B. Sun, W. Meng, J. Liu, Effective removal of fluoride by porous MgO nanoplates and its adsorption mechanism, J. Alloys Compd. 675 (2016) 292-300.

[15] I. Saha, A. Ghosh, D. Nandi, K. Gupta, D. Chatterjee, U.C. Ghosh, Beta-cyclodextrin modified hydrous zirconium oxide: Synthesis, characterization and defluoridation performance from aqueous solution, Chem. Eng. J. 263 (2015) 220-230.

[16] M.G. Sujana, S. Anand, Iron and aluminium based hydroxides: A novels sorbent for the removal of $F^-$ from water, Appl. Surf. Sci. 7 (2010) 6956-6962.

[17] T. Basu, U.C. Gosh, Nano-structured iron (III)-cerium (IV) mixed oxide: Synthesis, characterization and arsenic sorption kinetics in the presence of co-existing ions aiming to apply for high arsenic ground water treatment, Appl. Surf. Sci. 2 (2013) 471-481.

[18] R.R. Devi, I.M. Umlong, P.K. Raul, B. Das, S. Banerjee, L. Singh, Defluoridation of water using nanomagnesium oxide, J. Exp. Nanosci. 9 (2012) 512-524.

[19] A.A. Markeb, A. Alonso, A. Sánchez, X. Font, Adsorption process of fluoride from drinking water with magnetic core-shell Ce-Ti@ $Fe_3O_4$ and Ce-Ti oxide nanoparticles, Sci. Total Environ. 598 (2017) 949-958.

[20] A. Gosh, S. Chakrabarti, K. Biswas, U.C. Gosh, Agglomerated nanoparticles of hydrous Ce(IV) and Zr(IV) mixed oxide: Preparation, characterization and physicochemical aspects on $F^-$ adsorption, Appl. Surf. Sci. 307 (2014) 665-676.

[21] A.M. Rauchir, M.J. Basu, Adsorption of $F^-$ onto mixed rare earth metal oxides, Sep. Purif. Technol. 24 (2001) 121-127.

[22] D. Tang, G. Zhang, Efficient removal of $F^-$ by hierarchical Ce-Fe bimetal adsorbent: Thermodynamics, kinetics and mechanism, Chem. Eng. J. 283 (2016) 721-729.

[23] H. Liu, S. Deng, Z. Li, J. Huang, Preparation of Al-Ce adsorbent and its application for deflouridation of drinking water, J. Hazard. Mater. 179 (2010) 424-430.

[24] S. Deng, H. Liu, J. Huang, G. Yu, Mn-Ce oxide as a high capacity adsorbent for $F^-$ removal from water, J. Hazard. Mater. 186 (2011) 1360-1366.

[25] X. Wang, G. Zhang, H. Lan, R. Liu, J. Qu, Preparation of hollow Fe-Al binary oxyhydroxide for efficient removal of fluoride ions, Colloids Surf. A Physicochem. Eng. Asp. 520 (2017) 580-589.

[26] Z. Jin, Y. Jia, T. Luo, L.T. Kong, B. Sun, W. Shen, F.L. Meng, J.H. Liu, Efficient removal of $F^-$ by hierarchical MgO microspheres: Performance and mechanism study, Appl. Surf. Sci. 357 (2015) 1050-1088.

[27] N. Chubar, New inorganic ion exchangers based on Mg-Al hydrous oxides: (Alkoxide-free) sol-gel synthesis and characterization, J. Colloid Interface Sci. 357 (2011) 198-209.

[28] J. Wang, W. Xu, L. Chen, Y. Jia, L. Wang, X.J. Huang, J. Lui, Excellent $F^-$ removal performance by $CeO_2$ and $ZrO_2$ nanocages in water environment, Chem. Eng. J. 231 (2013) 195-205.

[29] K. Parashar, N. Ballav, S. Debnath, K. Pillay, A. Maity, Rapid and efficient removal of $F^-$ from aqueous solution using polypyrrole coated hydrous tin oxide composite, J. Colloid Interface Sci. 476 (2016) 103-118.

[30] D. Kang, X. Yu, S. Tong, M. Ge, J. Zuo, C. Cao, C. Song, Performance and mechanism of double layered hydroxides for $F^-$ and arsenate removal from aqueous solution, Chem. Eng. J. 228 (2013) 731-740.

[31] T. Zhang, Q. Li, H. Xiao, Z. Mei, H. Lu, Y. Zhou, Enhanced $F^-$ removal from water by non-thermal plasma $CeO_2$/Mg-Fe layered doubled hydroxides, Appl. Clay Sci. 72 (2013) 117-123.

[32] K. Mukhopadhyay, A. Ghosh, S.K. Das, B. Show, P. Sasikumar, U.C. Ghosh, Synthesis and characterisation of cerium (IV)-incorporated hydrous iron (III) oxide as an adsorbent for fluoride removal from water, RSC Adv. 7 (2017) 26037-26051.

[33] S.K. Swain, P. Patnaik, P.C. Patnaik, U. Jha, R.K. De, Development of new alginate entrapped Fe(III)-Zr(IV) binary mixed oxide for removal of fluoride from water bodies, Chem. Eng. J. 215-216 (2013) 763-771.

[34] K.Y. Foo, B.H. Hammed, Insights into modelling of isotherm adsorption systems, Chem. Eng. J. 156 (2010) 2-10.

[35] X. Zhao, J. Wang, F. Wu, T. Wang, Y. Cai, Y. Shi, G. Jiang, Removal of $F^-$ from aqueous media by $Fe_3O_4$ @ $Al(OH)_3$ magnetic nanomaterials, J. Hazard. Mater. 173 (2010) 102-109.

[36] M. Mohapatra, D. Harisprasad, L. Mohapatra, S. Annand, B.K. Mishra, Mg-doped nanoferrydrite-A new adsorbent for $F^-$ removal from aqueous solution, Appl. Surf. Sci. 258 (2012) 4228-4236.

[37] L. Chen, B.Y. He, S. He, T.J. Wang, C.L. Su, Y. Jin, Fe–Ti oxide nano-adsorbent synthesized by co-precipitation for $F^-$ removal from drinking water and its adsorption mechanism, Powder Technol. 227 (2012) 3-8.

[38] X. Dou Y. Zhang, H. Wang, T. Wang, Y. Wang, Performance of granular zirconium-iron oxide in the removal of $F^-$ from drinking water, Water Res. 45 (2011) 3571-3578.

[39] S. Alemu, S. Mulugeta, F. Zewge, B.S. Chandravanshi, Water defluoridation by aluminium oxide-manganese oxide composite material, Environ. Technol. 15 (2014) 1893-1903.

[40] Z. Ruan, Y. Tiana, J. Ruan, G. Cui, K. Iqbal, H. Ye, Z. Yang, S. Yana, Synthesis of hydroxyapatite/multi-walled carbon nanotubes for the removal of fluoride ions from solution, App. Surf. Sci. 412 (2017) 578-590.

a. Alvarez, L.H. Velazquez-Jimenez, L.P. Chazaro-Ruiz, P.E. Diaz-Flores, J.R. Rangel-Mendez, $F^-$ removal in water by a hybrid adsorbent lanthanum-carbon, J. Colloid Interface Sci. 455 (2015) 194-202.

[41] K. Biswas, K. Gupta, U.C. Ghosh, Adsorption of $F^-$ by hydrous iron (III) tin (IV) bimetal mixed oxide from the aqueous solution, Chem. Eng. J. 149 (2009) 196-206.

a. Teimouri, S.G. Nasab, S. Habibollahi, H.M. Fazel Najafabadi, A.N. Chermahini, Synthesis and characterization of a chitosan/montmorillonite/$ZrO_2$ nanocomposite and its application as an adsorbent for removal of $F^-$, RSC Adv. 5 (2015) 6771-6781.

[42] L. Chen, S. He, B.Y. He, T.J. Wang, C.L. Su, C. Zhang, Y. Jin, Synthesis of iron doped titanium oxide nanoadsorbent and its adsorption characteristics for $F^-$ in drinking water, Ind. Chem. Res. 51 (2012) 13150-13156.

[43] L. Liu, Z. Cui, Q. Ma, W.C. Cui, X. Zhang, One-step synthesis of magnetic iron-aluminium oxide/graphene oxide nanoparticles as selective adsorbent for $F^-$ removal form aqueous solution, RSC Adv. 8 (2016) 10783-10791.

[44] S. Kanra, S. Debnath, P. De, K. Parashar, K. Pillay, P. Sasikumar, U.C. Gosh, Preparation characterization, and evaluation of adsorption efficiency of Iron-Aluminium oxide-graphene oxide composite material, Chem. Eng. J. 306 (2016) 269-279.

[45] H.R. Mahmoud, S.A. El-Molla, M. Saif, Improvement of physicochemical properties of $Fe_2O_3$/MgO nanomaterials by hydrothermal treatment for dye removal from industrial wastewater, Powder Technol. 249 (2013) 225-233.

[46] Y. Zhang, X. Lin, Q. Zhou, X. Lou, Fluoride adsorption from aqueous solution by magnetic core-shell $Fe_3O_4$@alginate-La particles fabricated via electro-coextrution, Appl. Surf. Sci. 389 (2016) 34-45.

[47] S.D. Meenakshi, M. Rajaran, S. Rajendram, Z.R. Kennedy, G. Brindha, Synthesis and characterization of magnesium oxide nanoparticles, Elixier Nanotechnol. 50 (2012) 10618-10620.

[48] S. Debnath, M. Kitinyu, M. Onyango, Removal of Congo red from solution using two variant calcium and iron based mixed oxides nano-particle agglomerates, J. Ind. Chem. Eng. 20 (2014) 2119-2129.

[49] J. Zhu, X. Lin, P. Wu, Q. Zhou X. Luo, Fluoride removal from aqueous solution by Al(III)-Zr(VI) binary oxide adsorbent, App. Surf. Sci. 357 (2015) 91-100.

[50] Y. Yu, J.P. Chen, Key factors for optimum performance phosphate removal from contaminated water by Fe-Mg-La tri-metal composite sorbent, J. Colloid interface Sci. 445 (2015) 300-311.

[51] S.K. Swain, S. Mishra, T. Patnaik, R.K. Patel, U. Jha, R.K. Dey, Fluoride removal performance of a new hybrid sorbent of Zr(IV)-ethylenediamine, Chem. Eng. J. 184 (2012) 72-8.

# CHAPTER 7: CONCLUSIONS AND RECOMMENDATIONS

The silver-loaded $Fe_3O_4$@PPy/MAA NC has shown great potential in *E. coli* disinfection under continuous flow conditions. The NC performed optimally at a flow rate of 2 mL/min, bed mas of 2 g and initial *E. coli* concentration of $1.82 \times 10^2$ CFU/mL. It was evident that the performance of the bed was dependent on the bed mass, flow rate and initial contaminant concentration. Sigmoidal breakthrough curves were observed for the parameters that were tested. Increased bed masses prolonged the disinfection time of the NC whilst increased initial *E. coli* concentrations and flowrate, decreased the breakthrough and saturation time. The experimental data were fit to sigmoidal models and there was no superior model, all the models were competitive, with $R^2$ values of over 0.97. The experimental data were fitted perfectly even though in some instances the lag phase was under and overestimated. The stationary phase was fitted with great precision.

Various characterization techniques were successfully used in the characterization of the HCNS as well as the templates which were used in the synthesis of these HCNS. FT-IR confirmed the different functional groups which were obtained in the polystyrene templates, sulfonated polystyrene templates, conducting polymer-based nanocomposite as well as the resultant HCNS adsorbent. The ZIES-SEM images confirmed that the HCNS retained the spherical shape of the polystyrene templates as well as the successful deposition of the polyaniline on the surface of the spheres. HR-TEM confirmed the successful removal of the polystyrenes templates by carbonization at 680°C from the hollow core of the HCNS which was observed on the HR-TEM images. The different diffraction peaks and crystallography of the templates as well as the graphitic planes of the HCNS were obtained and confirmed by XRD. The BET surface area of the resultant HCNS was obtained as 286.14 $m^2/g$ and the mixed IUPAC type I an IV curves which resulted, confirmed the presence of micropores as well as mesopores in the synthesized HCNS.

Furthermore, batch adsorption studies were carried out for the removal of $Co^{2+}$ and $Ni^{2+}$ from aqueous media. Diverse spectro analytical techniques such as FT-IR, BET, SEM, EDX, TEM, STEM, and zeta potential analysis confirmed the adsorption of $Co^{2+}$ and $Ni^{2+}$ onto the HCNS. Adsorption studies were carried out and maximum adsorption was observed at adsorbent dosage of 0.03 g and at a pH of 4 for $Co^{2+}$ removal whereas maximum adsorption was observed at adsorbent dosage of 0.03 g and at a pH of 5 for $Ni^{2+}$ removal. However, the pH results for both $Co^{2+}$ and $Ni^{2+}$ showed that the HCNS adsorbent was negatively charged over a wider pH range and this made this adsorbent more suitable for the adsorption of these metal cations via electrostatic interactions. Adsorption kinetics studies were carried out and they revealed that the adsorption process was well fitted by the pseudo-second-order kinetic model for both $Co^{2+}$ and $Ni^{2+}$ adsorption. Furthermore, the resultant metal-loaded (Co-HCNS, Ni-HCNS) as well as the virgin HCNS adsorbents were applied in the sensing of gases such as $C_3H_6O$, $CH_4$, $H_2S$, $NO_2$ and $SO_2$. The evaluation of selectivity of the HCNS, Co-HCNS and Ni-HCNS revealed that the HCNS and Co-HCNS were mostly selective towards $NO_2$ and $SO_2$ while Ni-HCNS was mostly selective towards $H_2S$. Upon evaluation of the effect of temperature on gas sensor response, it was observed that the sensor response decreased with increasing temperature, with maximum sensor response observed at 50°C.

In summary, proof of concept has been proven with all the materials that were synthesized and tested since the conception of this project. Therefore, commercialization opportunities should be explored, where product development is possible.

# APPENDICES

---

## LIST OF PUBLICATIONS EMANATING FROM THIS PROJECT

### Journal articles

[1] Das R, Giri S, King Abia AL, Dhonge B, Maity A (2017). Removal of Noble Metal Ions ($Ag^+$) by Mercapto Group-Containing Polypyrrole Matrix and Reusability of Its Waste Material in Environmental Applications. *ACS Sustainable Chemistry & Engineering.*; 5(3), 2711-24.

[2] Das R, Giri S, Muliwa AM, Maity A. (2017) High-Performance Hg (II) Removal Using Thiol-Functionalized Polypyrrole (PPy/MAA) Composite and Effective Catalytic Activity of Hg (II)-Adsorbed Waste Material. *ACS Sustainable Chemistry & Engineering.* 5(9), 7524-36.

[3] Giri S, Das R, van der Westhuyzen C, Maity A (2017). An efficient selective reduction of nitroarenes catalyzed by reusable silver-adsorbed waste nanocomposite. *Applied Catalysis B: Environmental*. 209, 669-78.

[4] Parashar K, Ballav N, Debnath S, Pillay K, Maity A. Hydrous $ZrO_2$ decorated polyaniline nanofibres: Synthesis, characterization and application as an efficient adsorbent for water defluoridation. *Journal of Colloid and Interface Science*. 2017 Dec 15; 508:342-58.

[5] Mahlangu, T., Das, R., Abia, L. K., Onyango, M., Ray, S. S., & Maity, A. (2019). Thiol-modified magnetic polypyrrole nanocomposite: An effective adsorbent for the adsorption of silver ions from aqueous solution and subsequent water disinfection by silver-laden nanocomposite. *Chemical Engineering Journal*, *360*, 423-434.

[6] Das, R., Sypu, V. S., Paumo, H. K., Bhaumik, M., Maharaj, V., & Maity, A. (2019). Silver decorated magnetic nanocomposite ($Fe_3O_4$@ PPy-MAA/Ag) as highly active catalyst towards reduction of 4-nitrophenol and toxic organic dyes. *Applied Catalysis B: Environmental*, *244*, 546-558.

[7] Chigondo, M., Paumo, H. K., Bhaumik, M., Pillay, K., & Maity, A. (2018). Rapid high adsorption performance of hydrous cerium-magnesium oxides for removal of fluoride from water. *Journal of Molecular Liquids*.

[8] Chigondo, M., Paumo, H. K., Bhaumik, M., Pillay, K., & Maity, A. (2018). Hydrous $CeO_2$-$Fe_3O_4$ decorated polyaniline fibers nanocomposite for effective defluoridation of drinking water. *Journal of colloid and interface science*, *532*, 500-516.

[9] M Bhaumik, R Kumar, I Arunachellan, T Ludwig, K Mkhulu, A Maity and S Mathur, High-performance supercapacitors based on S-doped polyaniline nanotubes decorated with Ni(OH)2 nanosponge and onion-like carbons derived from used car tyres, *Electrochimica Acta*, 342, 2020, 136111.

[10] $Ni(OH)_2$ nanoparticles decorated sulfur doped polyaniline nanotubes as efficient catalyst for nitroarenes reduction, Venkata Satyanarayana Sypu, **Madhumita Bhaumik**, Kumar Raju, Arjun Maity, ***Journal of Colloid Interface***, Under Revision, 2020.

[11] Efficient catalytic reduction of nitroaromatics by recyclable $NiFe_2O_4$ nanoparticles decorated polyaniline nanotubes, Venkata Satyanarayana Sypu, Nazia H Kera, **Madhumita Bhaumik**, Kumar Raju, Arjun Maity, ***Materials Today Communication***, Under Revision, 2020.

[12] Cu nanoparticles decorated polyaniline nanotubes as catalysts for the reduction of nitroarenes under mild conditions, Venkata Satyanarayana Sypu, Nazia H Kera, **Madhumita Bhaumik**, Kumar Raju, Arjun Maity, ***Applied Surface Science***, Submitted, 2020.

## Book Chapters

[1] Fluoride toxicity and recent advances in water defluoridation with specific emphasis on nanotechnology, Kamya Parashar, Kriveshini Pillay, **Arjun Maity**, Springer book entitled "***Emerging Nanostructured Materials for Energy and Environmental Science***" *at* SPRINGER NATURE http://www.springer.com/series/11480, 2019, pp395-442.

[2] Surface-modified conducting polymer based-nanostructured materials for removal of toxic heavy metals from wastewater, Raghunath Das, Kamdem Paumo Hugues, **Arjun Maity**, Springer book entitled "***Advanced Nanostructured Materials for Environmental Remediation***" *at* SPRINGER NATURE http://www.springer.com/series/11480, 2019, pp111-144.

## HUMAN CAPITAL DEVELOPMENT

Thembisile Mahlangu, D. Tech. student, TUT- Thesis submitted, 2019.
Iviwe Arunachellan, Ph. D. student, UJ- Thesis will be submitted, 2020.
Venkata Satya Narayana Sypu, Ph. D. student, UJ-Thesis will be submitted, 2020.
Lindiwe Skosana, M. Sc. student, UJ- Thesis evaluated and awarded.

## CONFERENCES

[1] T. Mahlangu, A. Maity and S. Shina Ray, Silver remediation and subsequent water disinfection using thiol-modified nanocomposites. **Poster presentation**, Emerging Researchers' Symposium, CSIR, South Africa, 28-29 June 2018 (Best poster presentation award).

[2] Lindiwe A. Skosana, Arjun Maity, Kriveshini Pillay and Suprakas Sinha Ray, Carbonaceous nanomaterials and their conducting polymer-based nanocomposites for the removal of heavy metals from water. **Poster Presentation:** DST Nanotechnology Innovation Centres' 10 Year Anniversary Workshop, CSIR International Convention Centre, Pretoria, 14-16 October 2018

[3] L. A. Skosana, A. Maity, K. Pillay and S. Sinha Ray, Carbonaceous nanomaterials and their conducting polymer-based nanocomposites for the removal of heavy metals from water and the use of metal-loaded adsorbents for gas sensing applications. **Oral Presentation**: 8th South African Nanotechnology Initiative – Nano sciences Young Researchers' Symposium (SANI-NYRS), Vaal University of Technology, Vanderbijlpark, 16 November 2018

[4] L. Skosana, A. Maity, K. Pillay, and S. Sinha Ray, **Poster presentation:** Carbonaceous nanomaterials for the removal of $Co^{2+}$ and $Ni^{2+}$ from water and the application of metal-loaded adsorbents as gas sensors, 6th South African Young Water Professionals Biennial Conference, Durban, 20- 23 October 2019.

[5] T. Mahlangu, Removal of silver from water and subsequent re-use of secondary waste for bacteria inactivation. **Oral presentation**, 6th South African Young Water Professionals Biennial Conference, Durban, South Africa, 20-23 October 2019

[6] T. Mahlangu, A. Maity and S. Shina Ray, Silver remediation and subsequent water disinfection using thiol-modified nanocomposites. **Poster presentation**, PPS Europe-Africa 2019 Regional Conference, CSIR, South Africa, 18-21 November 2019.

[7] Iviwe Arunachellan, A. Maity and K. Pillay, Carbonaceous materials from waste material for the treatment of copper ion containing water and their re-use in organic transformations, **Oral presentation**, International workshop on porous materials and their applications, 2018.

[8] Iviwe Arunachellan A. Maity, and K. Pillay, Carbonaceous materials from waste material for the treatment of copper ion containing water and their re-use in organic transformations, **Oral presentation**, 6th South African Young Water Professionals Biennial Conference, 2019.

[9] Iviwe Arunachellan A. Maity, and K.Pillay, Carbonaceous materials from waste material for the treatment of copper ion containing water and their re-use in organic transformations, **Oral presentation**, TBD Water show Africa, 2020.